Gas Chromatographic Microsystems
for Airborne and Aqueous Volatile Organic Compound Determinations

by

Junqi Wang

A dissertation submitted in partial fulfillment
of the requirements for the degree of
Doctor of Philosophy
(Chemistry)
in the University of Michigan
2019

Doctoral Committee:

Professor Edward T. Zellers, Chair
Assistant Professor Andrew Ault
Professor Stephen Maldonado
Adjunct Research Investigator Joseph A. Potkay

Junqi Wang

wjunqi@umich.edu

ORCID iD: 0000-0002-0006-0332

DEDICATION

This dissertation is dedicated to my parents and my wife Fengyao for their unconditional and continuous support!

ACKNOWLEDGEMENTS

First and foremost, I would like to thank my primary research advisor, Professor Edward T. Zellers, for his guidance and support over the past five years. I also want to sincerely thank Dr. Joseph A. Potkay for his guidance and mentoring of my Chapter 2 work as the co-principal investigator. The scientific knowledge and attitude to the research from both of them significantly helped me to grow up as a capable scientist. I would like to thank my other committee members, Professor Andrew Ault, and Professor Stephen Maldonado, for their instrumental commentary to the milestones of my research.

I would aslo like to thank the current and former members of the Zellers research group, as well as the numerous collaborators, who made particular contributions to this work: Dr. William Collin for his training on gas chromatography (GC) operations, μcolumn coating and charterization; Dr.Jonathan Bryant-Genevier for their training on the first generation Personal Exposure Monitoring Microsystem (PEMM-1) μGC instrument operations; Mr. Nicolas Nuñovero for his significant work on the design and implementation of the electronic software and hardware for the PEMM-1 systems, help on mock field testing of the second generation of PEMM (PEMM-2), coting thens sensor array for PEMM-2, help to resolve the electronic problems in PEMM instruments; Dr. Lindsay K. Wright Dr. Chengyi Zhang for preparing the MPN films and coating sensor arrays for PEMM-1; Dr. Kee Scholten and Mr. Changhua (Henry) Zhan for their fabrication of the sensor array devices; Dr. Jialiu Ma from Matzger group for his help in MPN synthesis and

characterization of adsorbent materails; Dr. Zhijin Lin for this initial efforts to PEMM-2 mock field testings; Dr. Robert Nidetz for fabricating the μPCF and μcolumn devices used in the PEMM systems, Sanketh Buggaveeti for his work optimizing the design of the μPCF heaters; Dr. Katsuo Kurabayashi for providing valuable guidance on the design and fabrication of PEMM devices; Dr. William H. Steinecker and his co-workers Seth J. Peterson, Bryan M. Brookover at Targeted Compound Monitoring, LLC for PEMM-2 insturment assembly; Ms. Clementine Kornder for her tireless efforts to help and smooth everything in the last semeter of my graduate study.

The Chapter 2 work was supported by seed funding from the Center for Wireless Integrated MicroSensing & Systems ($WIMS^2$) and Grant T42 OH008455 from the Centers for Disease Control and Prevention (NIOSH-CDCP) through University of Michigan Center for Occupational Health & Safety Engineering (COHSE) program. Chapter 3 and 4 work was supported by the NIOSH-CDCP Grant R01-OH-010297. The work described in Chapter 5 was supported by the Office of the Director of National Intelligence (ODNI) and Intelligence Advanced Research Projects Activity (IARPA) by Contract 2017-17012600004. Devices were fabricated in the Lurie Nanofabrication Facility.

Finally, I would like to thank my Mom Ziying Liu, and Dad Shenqing Wang, for their constant love and support. Without their support, I would not be able to come to the US to pursue my undergraduate training at the University of Nebraska-Kearney. Dad, you will win the fight with the Esophageal cancer. To my wife Fengyao Li, your love and support made me keep moving when things got tough. I am the luckiest man in the world to meet and got married to you. To my daughter, Arianna Wang, thanks for choosing me as your father. I love you so much and your Mom and I wish you grow up happily and healthily! I also want to thank my parents-in-law, who have continuously support my young family, particularly in finance. To my undergraduate research

advisor Professor Haishi Cao, thank you so much! You are the first person leading me to the research world. I will not be able to come to the University of Michigan without your mentoring and support! To my two elder brothers, thank you so much to help take care of our parents when I was away from home. To my sister-in-law, Zhongyao Li, thank you so much for everything you did in the past 2 years as a responsible sister and aunt. To all of you, my accomplishments are your accomplishments and I feel most successful when I have made you proud.

Table of Contents

List of Tables

List of Figures

Abstract

New technologies offering sensitive, selective, and near-real-time identification and quantification of the individual components of complex mixtures of volatile and semi-volatile organic compounds (S/VOCs) are greatly needed in applications such as personal (worker) exposure assessment, air and water pollution monitoring, disease diagnosis, and homeland security. This dissertation describes the characterization of two prototype instruments containing core gas chromatographic microsystems (μGCs); the development and characterization of a microscale vapor extractor (μVE), and its integration with a μGC; and the development of adsorbent materials providing selective preconcentration of polar S/VOCs for use in certain μGC applications. Following a review of the background and significance of the research (Chapter 1), this dissertation then describes the design, modeling, and preliminary characterization of the μVE, which is a passive device containing microchannels and a polymer membrane that transfers dissolved VOCs from aqueous samples passed through the device to the gas phase for analysis by a downstream μGC (Chapter 2). In a proof-of-concept experiment, a hybrid μVE-μGC microsystem extracted four VOCs from a 700 μL sample of synthetic urine in 3.5 min, and then separated, identified, and quantified each VOC in ~80 sec with a projected detection limit as low as 660 parts-per-billion. The hybrid μVE-μGC microsystem may eventually permit rapid field/clinical analyses of water contaminants and urinary biomarkers of exposure and disease. Chapters 3 and 4 describe prototype μGC instruments that are referred to as Personal Exposure

Monitoring Microsystems (PEMM-1 and PEMM-2, respectively). PEMM-1 is a laptop-controlled, AC-powered, compact, bench-top unit and PEMM-2 is a battery-powered, belt-mounted unit with embedded controll. Both contain analytical microsystems made from Si-microfabricated components: a dual-adsorbent μpreconcentrator-focuser, a single- or dual-μcolumn separation module, and a μsensor-array detector. The μsensor-array consists of 4-5 chemiresistors (CR) coated with various monolayer-protected Au nanoparticles (MPN), which collectively yield partially selective response patterns that can enhance the recognition/discrimination of VOCs. Other key components include a pre-trap for low-volatility interferences, a split-flow injection valve, and an onboard He carrier-gas canister. In laboratory tests, PEMM-1 demonstrated the determination of 17 VOCs in the presence of 7 background interferences in 8 min. Detection limits were below the corresponding Threshold Limit Values (TLV) of the VOCs. PEMM-2 demonstrated the direct, autonomous determination of 21 VOCs in 6 min, with detection limits ranging from 16−600 ppb, well below TLV levels. A chemometric strategy involving retention time windows was implemented that greatly facilitated vapor recognition and discrimination via the μsensor-array response patterns. Results from a "mock" field test, in which personal exposures to time-varying concentrations of a mixture of five VOCs were measured autonomously, agreed closely with those from a reference GC. Chapter 5 describes the use of a trigonal-tripyramidal room-temperature ionic liquid (RTIL) as a surface modifier for the graphitized carbons, Carbopack B (C-B) and Carbopack X (C-X), used as μpreconcentrator adsorbents. The goal was to impart selectivity for polar compounds, particularly organophosphates and their precursors. Results showed that the capacities for five organophosphorus vapors were consistently enhanced ~2.5-fold with the RTIL-treated adsorbents relative to the untreated adsorbents. Furthermore, the capacities for several non-polar reference vapors were reduced 11 to

26-fold with the modified adsorbents. Implementation in next-generation μpreconcentrator devices is planned.

Background and Significance

1.1. Dissertation Overview

This dissertation presents four projects concerned with gas chromatographic microsystem (μGC) technologies for determining airborne and aqueous volatile organic compounds (VOCs). Those projects involve modeling, design, fabrication, and characterization Si-based microfluidic chip for aqueous VOC extraction; system integration and performance evaluations; material synthesis, characterization, and implementation. The application of this work includes personal VOC exposure assessment, air and water pollution monitoring, disease diagnosis, and homeland security.

There are six chapters in this dissertation. Chapter 1 describes the background of this study including VOCs, airborne and aqueous VOC sample preconcentration and extraction, VOC analysis by gas chromatography (GC) instruments, chromatographic separation theory, VOC detectors in GC system, critical μGC analytical components, and state-of-the-art instrumentation of micro gas chromatography prototypes, adsorption theory, the Wheeler model and the linear solvation energy relationship (LSER) model. Chapter 2 presents the first project which involves development and characterization a microfabricated vapor extractor (μVE) for aqueous analysis by GC and μGC. The passive μVE chip has a sandwich structure with a Si substrate etched with liquid channels, a glass substrate etched with a gas channel and a thin layer of polydimethylsiloxane (PDMS) membrane in between to extract VOCs from liquid to the gas phase. Its performance when interfaced to a μGC prototype was demonstrated.

Chapter 3 describes the first generation Personal Exposure Monitoring Microsystem (PEMM) μGC (i.e. PEMM-1). PEMM-1 is a benchtop prototype instrument containing a gas chromatographic microanalytical system designed for the determination of multiple airborne volatile organic compounds (VOCs) at concentrations in the vicinity of recommended occupational exposure limits. The core microsystem in PEMM-1 consists of a set of discrete Si-microfabricated devices: a dual-cavity, adsorbent-packed micro-preconcentrator-focuser (μPCF) chip that quantitatively captures and thermally desorbs/injects VOCs with vapor pressures between ~ 0.03 and 13 kPa; tandem separation microcolumns (μSC) chips with cross-linked PDMS wall-coated stationary phases capable of temperature-programmed separations; and an integrated array of five μchemiresistors (μCR) coated with different thiolate-monolayer protected gold nanoparticle (MPN) interface films that quantify and further differentiates among the analytes by virtue of the response patterns generated. PEMM-1 was designed as the precursor of the second generation PEMM μGC (i.e. PEMM-2), and its results were used to guide the adaptation of the microsystem.

Chapter 4 describes PEMM-2 which is a belt-mountable prototype instrument containing a gas chromatographic microsystem capable for near-real-time recognition and quantification of volatile organic compounds (VOCs) in moderately complex mixtures at concentrations encountered in industrial workplace environments. The μPCF and μCR-array devices in PEMM-2 are of the same design as those developed for PEMM-1, but a more power-efficient, monolithic μSC replaced the PEMM-1 dual-μSC module. Additional innovative features of the PEMM-2 (some also developed and validated via the PEMM-1) include a pretrap comprising a short wall-coated capillary for excluding intractable low volatility interferences, a split-flow injector for increasing chromatographic resolution of early eluting VOCs, a streamlined fluidic layout, improved circuitry for sensor signal amplification and conditioning, on-board microcontrol of

system functions and data acquisition, and a companion Raspberry Pi module for wireless communication. The improvements of PEMM-2 resulted in lower limits of detection (LODs), more complex mixture analyses, enhanced vapor recognition, and lower operating power.

Most adsorbent materials used for trapping and thermally desorbing VOCs in portable or "micro" analytical systems preferentially trap non-polar or moderately polar VOCs relative to more polar VOCs. Chapter 5 explores the use of a trigonal-tripyramidal room-temperature ionic liquid (RTIL) as a surface modifier for the graphitized carbons, Carbopack B (C-B, 100 m^2/g) and Carbopack X (C-X, 240 m^2/g) with the broad goal of imparting selectivity for polar VOCs in preference to non-polar VOCs. The RTIL demonstrated a unique selectivity to polar compounds over nonpolar compounds when coated to graphitized carbon black, C-B and C-Xa, for airborne VOC sample collection.

1.2. Volatile Organic Compounds and Their Health Effects

1.2.1. Volatile Organic Compounds

Volatile organic compounds (VOCs) have diverse definitions. The U.S. Environmental Protection Agency (EPA) defines VOCs as any compounds of carbon, excluding carbon monoxide, carbon dioxide, carbonic acid, metallic carbides or carbonates and ammonium carbonate, which participate in atmospheric photochemical reactions.[1,2] The European Union designates a VOC to be any organic compound with a boiling point ≤ 250 °C measured at a standard atmospheric pressure of 101.3 kPa.[3] The World Health Organization (WHO) also describes VOC by using boiling points but categorizes them into three sub-groups as summarized in Table 1.1. As the reference, the n-alkanes are listed in Table 1.1 as well in each of the group. In general, the definition that VOCs are organic chemical compounds whose composition makes it possible for them to evaporate under normal indoor atmospheric conditions of temperature and

pressure has been used a lot in the scientific literature [4] and this dissertation also uses the broad definition of VOC as encompassing mean all compounds from VVOC to SVOC.

Table 1.1.Classification of VOCs by WHO in ref.3

Description	Abbreviation	Boiling Point Range (°C)	Reference n-alkane
Very volatile organic compounds	VVOC	< 0 to 50-100	n-C_1--n-C_7
Volatile organic compounds	VOC	50-100 to 240-260	n-C_8-- n-C_{12}
Semi volatile organic compounds	SVOC	240-260 to 380-400	n-C_{13}--n-C_{30}

1.2.2. Airborne VOCs and Their Health and Environmental Effects

VOCs are omnipresent and are found in both the indoor and outdoor environment. VOCs can have severe human health effects and environmental consequences. Indoor VOCs mainly come from personal products, household products, building materials, and furniture. Their concentration is usually in the ~μg/m^3 or part-per-billion (ppb) range.[6,7] In the industrial workplace, workers are commonly exposed to VOCs in the part-per-million (ppm) range which is considered a much higher concentration level. Depending on the concentrations of VOC and exposure time, VOCs can have the following health effects: eye, nose and throat irritation, and headaches in short-time exposure; loss of coordination and nausea, damage to the liver, kidney and central nervous system caused by long-time exposur.[8]

Three major organizations, the Occupational Safety and Health Administration (OSHA), the American Conference of Governmental Industrial Hygienists (ACGIH), and the National Institute for Occupational Safety and Health (NIOSH) regulate (by OSHA) or recommend (by ACGIH and NIOSH) the occupational exposure limits (OELs) of VOCs in the US.[9] They establish Permissible Exposure Limits (PELs), Threshold Limit Values (TLVs), and Recommended Exposure Limits (RELs), respectively, to prevent the employee from the adverse health effects of work exposure. These exposure limits are usually in the low ppb to the high ppm range collectively

spanning ~4 orders of magnitudes [9-11] The OELs are usually given as time-weighted average (TWA), short-term exposure limits (STEL) or ceiling limits (CL). A TWA is the average concentration value of the exposure over a specified period, usually an eight-hour work shift. The STEL is the maximum acceptable average concentration value over a short period of time, usually 15 minutes in one work shift. The CL is the concentration limit that may not be exceeded for any time. The work described Chapter 3 and 4 uses industrial chemicals and their TLV-TWA and TLV-STEL recommended by ACGIH as the chemical target and concentration guideline for instrument design and performance evaluation.

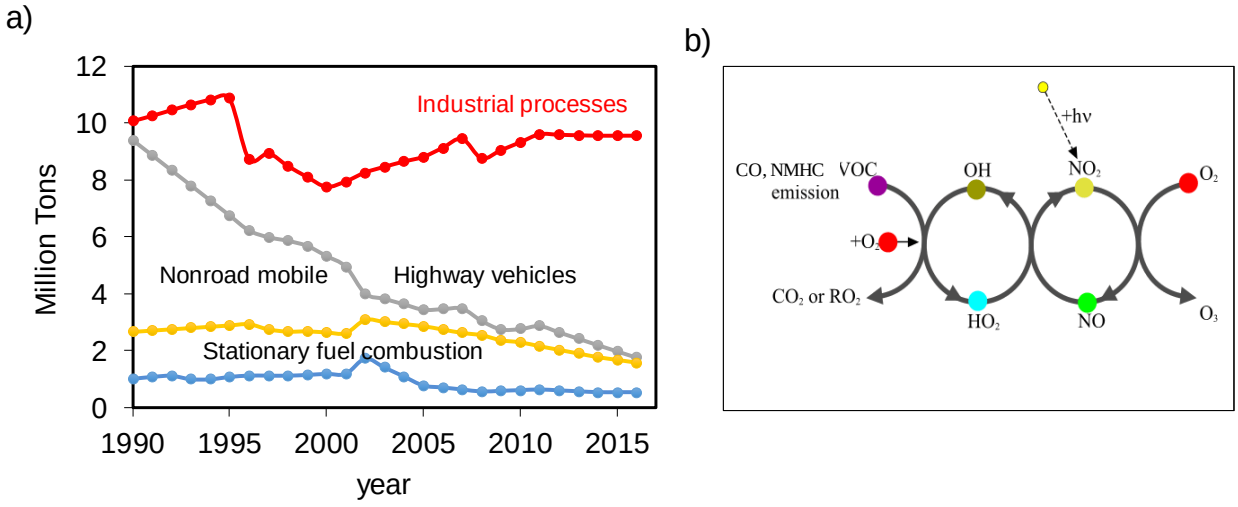

Figure 1.1. a) US outdoor VOC emissions from different sources between1990 and 2017 (data from reference 11); b) the photochemical reactions of VOCs for ozone formation (in ref.13).

Outdoor VOCs are mainly from industrial activities and vehicle emissions. Figure 1.1a shows the anthropogenic source categories.[11] The outdoor VOC concentration is usually lower than indoor VOC by 2-5 fold.[7] EPA regulates outdoor VOC emissions because they participate in atmospheric photochemical reactions that contribute to ozone formation (see Figure 1.1b) and play

a role in the formation of secondary organic aerosols.[12] Monitoring outdoor VOC is out of the scope of this work, thus, no further discussion is processed here.

1.2.3. Aqueous VOCs and VOC Biomarkers

VOCs are not only present in the air, but also in the water, urine, and blood. VOCs are important water contaminants that can cause adverse effects on human health. The water VOC contamination is usually caused by industrial effluents, waste disposal, gasoline or oil spills on the ground surface, pesticides and herbicides used in agriculture, and disinfection processes.[13] To protect the public from contaminated water, the Environmental Protection Agency (EPA) established the maximum contaminant level (MCL), which is the highest level of a contaminant allowed in drinking water. For example, toluene and trichloroethylene and have a 1 ppm and 0.005 ppm MCL, respectively. The full list of these water VOC contaminants and their MCLs can be found on the EPA website.[14]

Table 1.2. VOC and its BEIs examples in the aqueous biological media of urine or blood from ref. 8

Compound	BEI (mg/L)	urine (u)/blood(b)
cyclohexanone (as cyclohexanol)	8	u
dichloromethane	0.3	u
n-hexane (as 2,5-hexanedione)	0.4	u
methyl chloroform (as trichloroethanol)	30	u
2-hexanone (as 2,5-hexanedione)	0.4	u
4-methyl-2-pentanone	1	u
2-butanone	2	u
styrene	0.04	b
trichloroethylene (as trichloroethanol)	0.5	b
tetrachloroethylene	0.5	b
tetrahydrofuran	2	u
toluene	0.03	u

Another type of important aqueous VOCs is VOCs or their metabolites in blood or urine.

They are recommended by the ACGIH for industrial worker exposure monitoring. The Biological Exposure Indices (BEIs) of the corresponding VOCs are used as the guidelines for safe exposure level evaluation.[8] Table 1.2 lists examples of VOCs and their BEIs in blood or urine.

Research also finds certain VOCs are biomarkers of cancers. The research in ref. 15 found the VOCs in the urine could be successfully used as the biomarker to the lung cancer diagnosis. Some of VOC biomarkers in urine they found were 2-heptanone, 5-hepten-2-one and o-toluidine.

Thus, on-site analysis of VOC concentration levels in liquid media facilitates assessments of water pollution, biomonitoring of exposures to toxic chemicals, and disease diagnosis. Traditionally, VOC collection from liquid media has entailed purge-and-trap, headspace sampling, or solid-phase microextraction (SPME) followed by analysis by GC with a flame ionization detection (FID) or a mass spectrometer (MS).[17] Such approaches are not well suited for on-site analysis either because of low extraction efficiencies, poor precision, or because the analysis system is too cumbersome. Inspired by the artificial lung technology,[16] the μVE in Chapter 2 overcome the shortcoming of the traditionally aqueous VOC collection. By integrating with the μGC in Chapter 3, the hybrid μVE- μGC analytical system showed the great potential for the rapid field/clinical analyses of water contaminants and urinary biomarkers of exposure and disease.

1.3. VOC Monitoring by GC

The quantitative determination of VOCs usually involves sample collection (and preconcentration), separation, and detection, which is illustrated in Figure 1.2. The total volatile organic compound (TVOC) is usually used to investigate indoor and outdoor air quality problems. The TVOC concentration determination process usually skips the separation step and directly measures VOC mixture together by photoionization detector (PID) or flame ionization detector (FID).[17] The limitations of TVOC are apparent. It cannot differentiate the identity and quantity of

VOC component in the air. And the measurement is not accurate enough low because TVOC measurement is based on the single calibration compound data to represent to whole VOC complex. Thus TVOC concentration cannot be used to protect people from the exposure of toxic VOCs especially whose TLVs are very low. Thus, the individual VOC monitoring is essential.

For personal exposure monitoring, the inhalation sample is collected by passing the air sample in the worker's personal breathing zone through an adsorbent-packed tube. The sampling method, for instance, adsorbent material, sample volume, and sampling duration, is often dependent on the physical properties of the analytes, for example, vapor pressure (p_v) and polarity, the nature of the health outcome, like acute or chronic, and the detector. Usually, 15 mins and 8 hours sampling are collected to meet ACGIH short term exposure limits (STELs) and work-shift time-weighted averages (TWAs) requirements, respectively.[8]

Classic aqueous VOC sampling by extracting VOC from fluids through purge-and-trap, headspace sampling, and solid-phase microextraction,[18-21] each of the sampling technology will be reviewed and discussed with more details in *Sections of 1.3.1.2 and 1.3.1.3.* the collected sample is then separated by gas chromatography (GC) and analyzed by FID or mass spectrometer (MS) detectors. More details of VOC analysis will be discussed in *Section 1.3.2.*

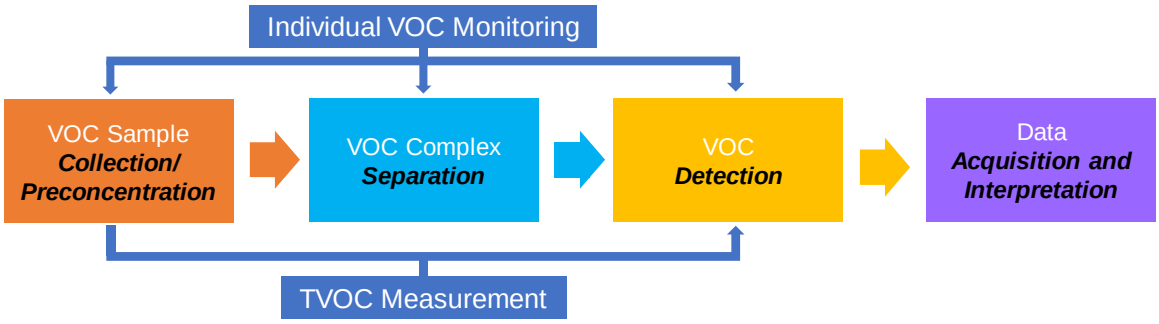

Figure 1.2. The block diagram of a typical VOC analysis which involves sample collection, separation and detection. The sample collection is usually on-site, but the separation and detection are usually conducted off-site in a laboratory.

1.3.1. VOC Sample Collection Review

1.3.1.1. The Fundamentals of Adsorption and Extraction

The first step of the VOC analysis is sample collection. Different methods have been developed to either directly collect the air sample or trap VOC on the adsorbent materials (airborne and aqueous VOCs). Although the direct collection of air sample in a canister and Tedlar bag for VOC analysis is recommended in some of EPA and NIOSH methods,[22,23] these methods suffer many limitations and shortcomings including vapor condensation on the canister or bag surface, vapor permeation through the bag, and humidity issues for GC analysis. And thus, this method is not recommended for low vapor pressure sample collection. As a better approach, the adsorbent material, such as porous carbon,[22,24] zeolite,[22] carbon nanotube,[24,25] Tenax,[26] metal-organic framework (MOF) [27,28] and polymer (i.e. PDMS)[21] have been used to capture or extract VOC from air or liquid. Both pore filling adsorption (Figure 1.3a) and membrane extraction (figure 1.3b) involves the process of molecule transportation between phases and chemical potential-driven process which involves the molecule transport between phases. The fundamental principles of chemical transportation between phases are discussed in the following.

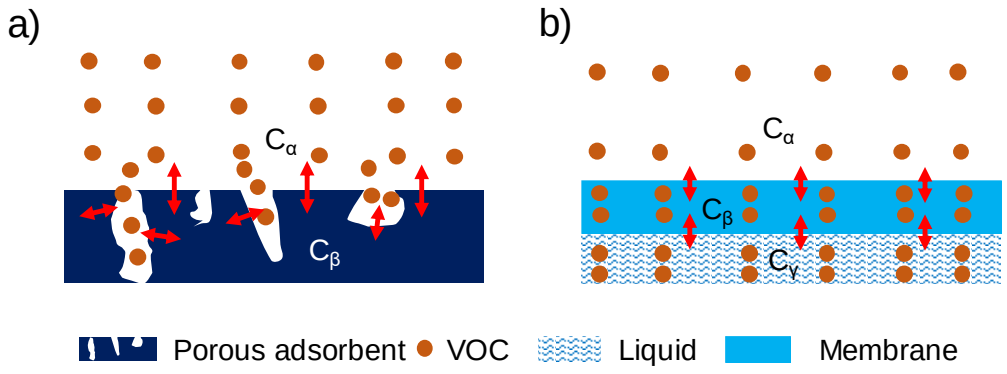

Figure 1.3. a) The VOC adsorption on the porous materials; b) VOC extraction by the membrane from the liquid phase to the gas phase.

For a given molecule in a given phase *x*, its chemical potential μ_α can be described by the equation

$$\mu_x=\mu_x^\circ+RT\,lnC_x \qquad \text{(Eq. 1.1)}$$

where μ_x is the chemical potential of VOC in phase *x*; μ_x° the standard state chemical potential in phase *x*; *R* is the gas constant; *T* is the temperature in Kelvin; and C_x is the concentration of the VOC in phase α. For the Eq. 1.1, the first part μ_x° is mainly depends on the intermolecular interactions in the standard state. Thus, it majorly related to enthalpy and its value is lowest when the intermolecular interactions are greatest.[29] The second part $RT\,lnC_x$ in which the concentration presents the entropy term.[29] For the adsorption process as depicted in Figure 1.3a, the chemical potential of VOC in gas phase α and solid phase β, respectively, is

$$\mu_\alpha=\mu_\alpha^\circ+RT\,lnC_\alpha \qquad \text{(Eq. 1.2)}$$

$$\mu_\beta=\mu_\beta^\circ+RT\,lnC_\beta \qquad \text{(Eq. 1.3)}$$

To compare, $\mu_\alpha^\circ > \mu_\beta^\circ$, $C_\alpha > C_\beta$, and thus $\mu_\alpha > \mu_\beta$. So, the adsorption is a chemical potential driving process in which VOC transfers from the higher potential phase to the lower chemical potential phase until the chemical potentials reach to the equal in both phases when an equilibrium is established. At the equilibrium steady state $\mu_\alpha = \mu_\beta$, thus

$$K=\frac{C_\beta}{C_\alpha}=\exp\left(\frac{-\Delta\mu^\circ}{RT}\right) \qquad \text{(Eq. 1.4)}$$

where *K* is the partition coefficient of VOC between phase α and β; $\Delta\mu^\circ=\mu_\beta^\circ-\mu_\alpha^\circ$ is the standard chemical potential changes when chemicals transferring from phase α to β and it is also be recognized as ΔG°, the standard state Gibbs free energy changed when the VOC sample transferring from phase α to β. The partition coefficient is also usually written as

$$K=\frac{C_\beta}{C_\alpha}=\exp\left(\frac{-\Delta G^\circ}{RT}\right) \qquad \text{(Eq. 1.5)}$$

Now, if taking consider the Gibbs free energy change this adsorption process, $\Delta G^{\circ}=\mu_{\beta}^{\circ}-\mu_{\alpha}^{\circ}$ <0, and thus, the adsorption process is spontaneous, and VOCs are favoring to transfer to the adsorbent phase than the gas phase.

Membrane extraction of VOC from the liquid phase to the gas phase as illustrated in figure 1.3b undergoes similar transferring process but it is composed of the VOC transfer from liquid phase γ to membrane phase β, and VOC pass through from membrane β to gas phase α. Each of the VOC transferences between two phases is spontaneous and the details of the transferring process are comparable to the process the adsorption process from gas to adsorbent phase.

1.3.1.2 Adsorbent-Based Airborne VOC Sample Collections

Sampling VOC from atmospheric air is usually engaged with passing the air sample through a tube packed with a bed of one or multiple adsorbent materials by a suction pump which is usually more favorable than sampling atmospheric air directly in a canister and a Tedlar bag, because this adsorbent tube or preconcentrator can significantly enhance the concentration of the trapped vapors. The number of adsorbents in a sampling tube is mainly determined by the volatility range of the VOC analytes. In some applications, a single adsorbent can meet the requirement; while in many other practices, multiple adsorbents are needed to sufficiently capture all kinds of VOCs and also exhaustively release them by thermal desorption. Usually, a stronger adsorbent (i.e. the adsorbent has a larger surface area) are suitable for higher volatile compound sampling to avoid breakthrough problem and the low vapor pressure compound residues retention during thermal desorption; a weaker adsorbent (i.e. the adsorbent has a smaller surface area) is used for lower volatile organic compound for a better thermal desorption. The wider the volatility range, the more adsorbent beds are needed. Figure 1.5a shows the diagram of a multi-adsorbent tube. When sampling, the air sample passes through the beds in the order of the weak adsorbent to the

strongest adsorbent. The trapped VOC is usually thermally released from the bed but with an opposite flush flow. Figure 1.5b and 1.5c are examples of commercial multi-adsorbent and single adsorbent tube from SKC[30] and PerkinElmer[31], respectively. There are more other materials have been used as the adsorbent. The materials include porous polymers, graphitized carbon, molecular sieves, activated carbon, and their applications are summarized in Table 1.3. This method is constrained by the large dead volume which broadens the injection band width and the high-power consumption because of the large thermal mass.

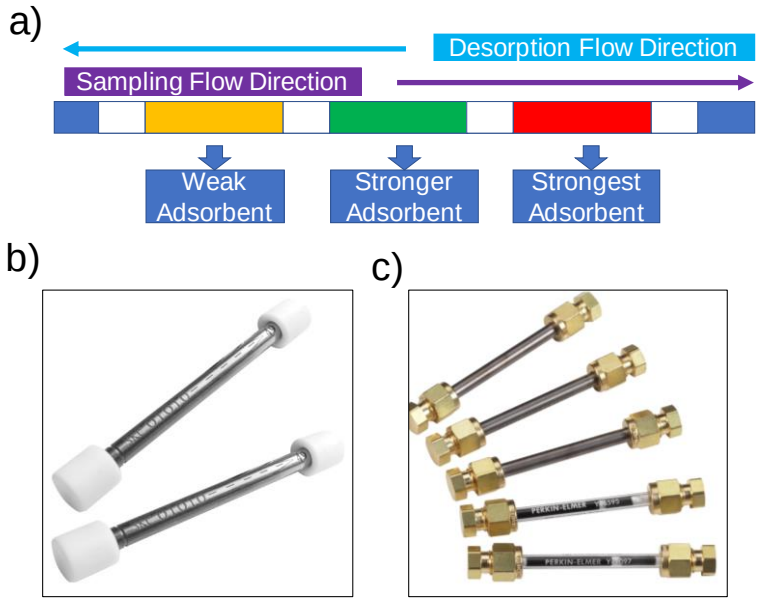

Figure 1.4. a) the diagram of a representative adsorbent tube with multiple adsorbents in the bed; b) a multi-adsorbent sorbent tube with graphitized carbon black 1(10 m^2/mg), graphitized carbon black 2 (100 m^2/mg) and Carbosieve S-III (975 m^2/mg) from SKC in ref. 30; c) the stainless steel Tenax tube from Perkin Elmer in ref 31.

As discussed above, the adsorption process is highly related to the enthalpy governed by intermolecular interactions. The carbon-based adsorbents preferentially trap non-polar or relative moderately polar compound but poorly capture polar compounds. Thus, tuning the surface chemistry of the adsorbent materials can selectively collect a certain kind of the compounds, for

example, polar compounds. The surface chemistry of adsorbent can be modified by engineering a polarity-varied coating material on the adsorbent surface. This coating material requires thermal stability (no decomposition at high temperature, e.g. >250°C, the typical VOC thermal desorption temperature), negligible vapor pressure (no mass loss at room temperature), and versatile solvent interaction (selectivity). Room temperature ionic liquids (RTILs) have been shown many great properties as the above requirements. These properties have been proved when employed as the gas chromatography stationary phase.[32-34] In Chapter 5 of this work, a trigonal-tripyramidal room-temperature ionic liquid (RTIL) was explored as a surface modifier on graphitized carbons in the adsorbent tube for selectively sampling polar VOCs.

Table 1.3. Adsorbent materials, their thermal characteristic and VOC analytes for each adsorbent

Adsorbent	Surface area, m^2/g	Max.temp.°C	Composition	VOC analytes	Ref.
Porous organic polymers					
Tenax TA	~35	350	Poly (2,6-diphenyl-p-phenylene oxide)	C7-C26, aromatic compounds, and nonpolar VOC	40
Porapak N	300	20–190	Polyvinylpyrrolidone	Acetylene, aliphatic, ydrocarbons	41
Chromosorb 106	750	180	Polystyrene	C5-C12 hydro-carbons, oxygenated VOCs	
Porapak Q	550		ethylvinylbenzene and divinylbenzene copolymer	oxygenated VOCs	41
Graphitized carbon blacks					
Carpopack/Carbotrap F	5	>300	Graphitized carbon, whose specific surface depends on the degree of graphitization	> C20	42
Carpopack/Carbotrap C	10	>300		C12-C20	
Carpopack/Carbotrap Y	24	>300		C12-C20	
Carpopack/Carbotrap B	100	>300		C5-C12	
Carpopack/Carbotrap X	240	>300		C3-C9	
Carpopack Z	220	>300		C3-C9	
Carbograph 1 and 2	100	>400		C5-C12, /C12-C20	42
Molecular sieves					
Spherocarb	1200	>400	Formed during the pyrolysis of organic polymers, e.g., polyvinyl chloride	Very volatile organic compounds, methanol, acetone C3C5	42,43
Unicarb	>1000	>400			
Carbosieve S-III and G	800	400			
Carboxen	Most > 485	>330			
Activated carbon	>1000	400	Formed by the low-temperature oxidation of	Aliphatic and aromatics hydrocarbons, e.g., C2-C4	44
Zeolite	vary	~250	$Na_6[AI_6Si_{30}O_{72}]_{24}H_2O$	broad polar/nonpolar, even CH_4	45

1.3.1.3 Aqueous VOC Sampling Collections

The detection of VOCs in the aqueous phase is challenging due to the incompatibility of water with the GC based analytical system. Water vapor could capture the polar active sites on the adsorbents reducing the sample capacity[35] and causing the damage of the polymer-based stationary phase in the column which would result in the alternation of retention properties and column bleedings.[36] Water vapor can also extinguish the universal flame ionization detection (FID) and diminish the sensitivity of electronic capture detector (ECD) was also reported.[37,38] Reducing or removing water during sampling is thus critical for aqueous VOC collection and analysis. Three types of techniques, gas-liquid partitioning, gas-solid partitioning, and membrane aided extraction have been developed to overcome the water vapor problems.

Static and dynamic portioning of VOC between gas and liquid phase is used in the headspace (Figure 1.6a) and purge and trap (Figure 1.6b) sampling techniques, respectively. For both techniques, the VOC molecules are transferred from the aqueous phase to the gas phase driven by the chemical potential differences. In the static headspace sampling method, the maximum the concentration of the vapor in the headspace is determined by the partition coefficient (see Eq. 1.5) of that compound between gas and aqueous phase under certain constant temperature. Thus, the typical limit of detection is at ppm ranges.[39,40] For the dynamic headspace sampling like purge and trap, the vapors in the headspace are continuously purged into the adsorbent bed in the flow downstream. With this dynamic flow, the partition equilibrium of VOC between phases is hardly established and thus the VOCs continuously move to the gas phase. In such a way, the sensitivity of dynamic headspace sampling is 10-100 times higher than the static one.[41] Although gas-liquid methods are easy to set up, it suffers the poor reproducibility, low sensitivity, large sample volume

or long sampling time and water vapor problem. Compared to direct partitioning methods, membrane extraction approaches provide much higher (10^3-10^6 ×) sensitivity.[42]

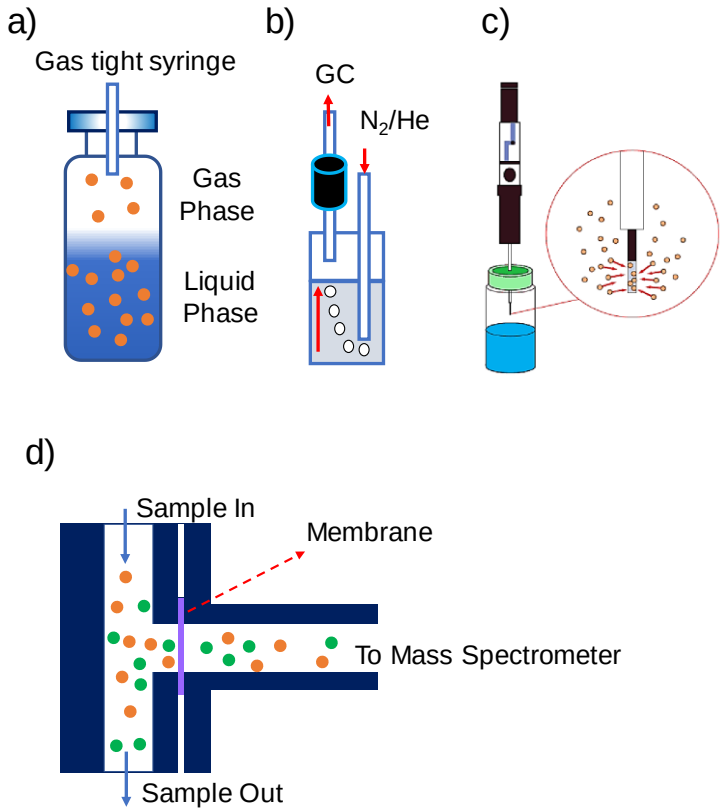

Figure 1.5. a) static headspace sampling where VOCs partitions between gas phase and liquid phase in the vial; b) purge and trap setup where VOCs in the liquid is continuously purged by N_2 or He and the vapors are trapped in the downstream adsorbent tube and then thermally injected into GC; c) static headspace solid phase microextraction with the fiber suspended in the headspace to adsorb vapors; In other application, the fiber can be immersed in the liquid for higher extraction; d) membrane inlet mass spectrometry (MIMS), VOCs in liquid or gas are extracted to the ionization chamber of the MS by a thin membrane, usually PDMS.

The solid phase microextraction(SPME) is one of the widely used gas-solid partitioning techniques.[43,44] SPME typically is engaged with the silica fiber coated with sorbent coating, for example, polydimethylsiloxane, divinylbenzene, carboxen, polyacrylate, and polyethylene glycol.[44] The fiber is inserted into the headspace or directly into the aqueous solution to extract the VOCs. The system is then left to stabilize or equilibrate in a period of time, usually, from minutes

to hours.[43] The sample afterward is thermally injected into the GC instrument or other analyzers. SPME is broadly applied in the aqueous VOC analysis practices because of its virtue of high sensitivity, short extraction time, and solvent-free operation.[45] However, SPME has some shortcomings including low sensitivity of the membrane polarity incompatible compounds, sample loss, and limited choice of fiber coatings.[46]

The membrane aided extraction is commonly seen membrane inlet mass spectrometry (MIMS) technique.[47-49] Figure 1.6d shows the block diagram of the generic MIMS system for VOC analysis (only the extraction part is shown in details). VOCs in the liquid or gas sample diffuse into and permeate through the membrane and then evaporate into the gas phase. Those VOCs then are ionized and analyzed by MS. The major of the advantage of MIMS is the little or no sample pretreatment but the membrane is very selective to the VOCs. Normally, the hydrophobic membrane (e.g. PDMS) is used to exact VOCs while removing the water vapor problem. In this fashion, MIMS has low detection limits (ng/L in water) for nonpolar compounds, whereas relatively high detection limits (high µg/L in water) for polar compounds.[50] Additionally, limited by the evaporation step, MIMS is not applicable to the compounds with a boiling point <200 °C.[50]

1.3.2. VOC Analysis By GC

1.3.2.1. GC Fundamentals

Invented by A.T. James and A.J.P. Martin in 1952,[51] Gas chromatography (GC) is well developed along the way. The modern GC is one of the common techniques to quantitively analyze VOCs. It separates the VOCs in the complex mixture into individual component based on different retention strengths (e.g. partition coefficients) of the VOCs on the stationary phase when they travel along the column with the carrier gas.

Figure 1.7 shows a block diagram of a typical GC system comprising of the three key analytical components, external carrier gas, and data acquisition system. The sample is introduced into a liner by the injector or autosampler, then immediately and completely or partially passed into the column with a carrier gas (e.g, N_2, He, H_2). In the column, the mixture of VOCs is separated by different chemical partitioning (or different partition coefficient *K*) with the stationary phase which is usually a ~µm thin layer polymer. The larger *K* the compound has, the slower it migrates in the column. This different migration rates leading a separation in the column. A detector in downstream of the column captures the chemical migration time and peak information (e.g. peak width, peak height, and peak area) which are acquired by the computer for chemical identifications and quantifications.

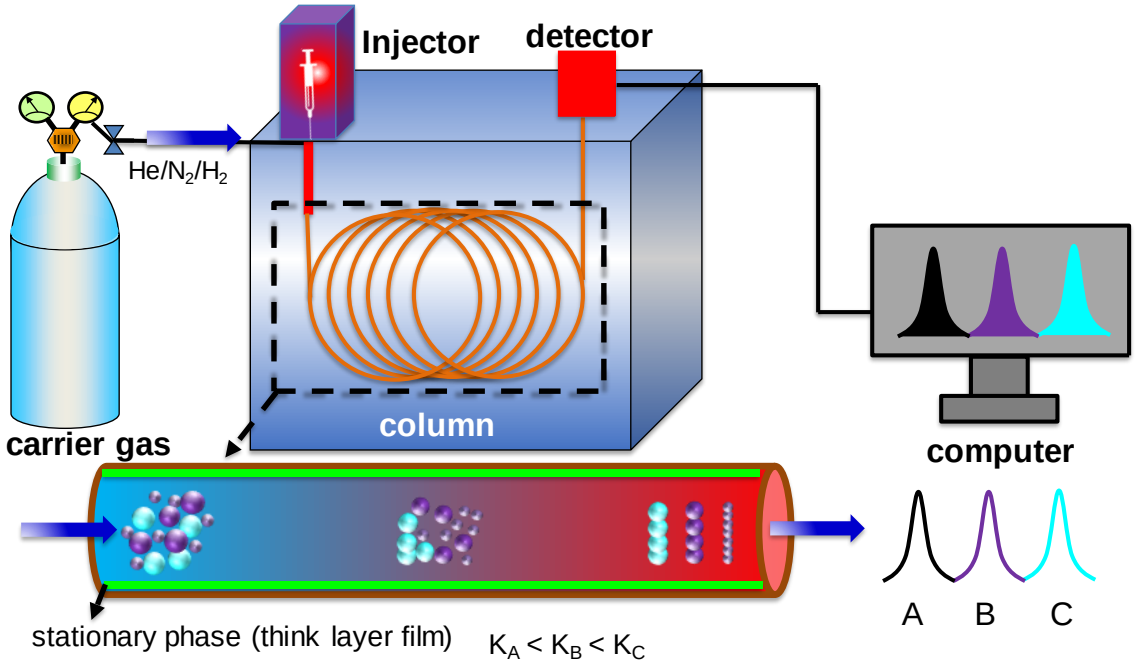

Figure 1.6. The diagram schemes a generic GC system with all essential components for a complete chemical analysis cycle. The red color represents the hot parts in the system and the light blue (cold) and red (hot) along the column means a temperature program.

1.3.2.2. GC Injectors

GC injections comprise injection devices and injection methods. Here the focus is given to the injection devices or the injectors which are encountered in the most common GC system. Depending on the phase of VOC, concentration, volatility, and polarity, an appropriate injector or injector combination should be chosen for accurate and precise VOC injection. In general, the injectors can be categorized as a thermal desorption (TD) sampler/injector, valve-based loop injector, and split/splitless (S/SL) injector. To a real practice, one or multiple injectors are used to complete a good quality injection.

The TD sample/injector is designed for use with adsorbent tubes. The adsorbent tubes are placed in the TD sampler and heated under the flow. During the TD, a carrier gas is usually flushed through the adsorbent to facilitate this TD process and more importantly passes the desorbed vapors into the column the vapors into a separation-detection unit or sometimes just a detection unit. Such TD devices include adsorbent tube and fiber coated needle in SPME which has been covered in Section of 1.3.2.1. TD sampler/injector is particularly useful for low concentration VOC analysis since it traps VOCs from a large sample volume on a relatively small volume of adsorbent leading to several magnitudes of preconcentration. However, the injection volume is highly limited by the heating rate. Slow heating usually results in a broad injection bandwidth and causes the chromatographic resolution sacrifice. So, the TD is always used with a focuser which narrowly focuses injection plugs by rapid thermal desorption. For airborne VOC injection, the loop injector is commonly used. This injector encompasses a fix volume loop (10-5000 µL) where the sample resides in temporarily and a valve system is used to direct the gas flow. A common loop injection system is shown in Figure 1.7 and includes a two-position, six-port valve. The entire assembly can be enclosed in a heated unit to reduce the wall-adsorption of low volatility analytes. When

collecting sampling, the valve is positioned in configuration A as Figure 1.8a. The sample is drawn through the loop usually by a pump under a constant flow rate. After a short period of time, the valve is thrown to the other configuration B as Figure 1.8b. The sample fully loaded in the loop is swept by the carrier gas to a GC column for separation or sometimes to a detector directly for analysis. But for the low volatility compounds, the extra work is needed to heat the fluidic pathway between the sample and the 6-port heating unit to avoid the wall-adsorption during the sample collection and injection processes.

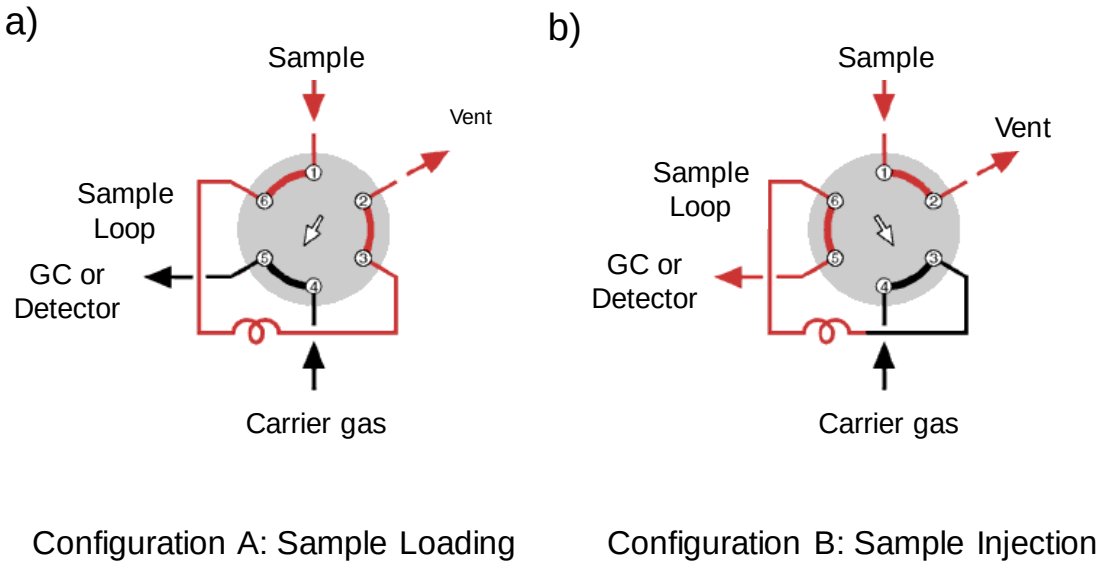

Figure 1.7. A two-position, 6-port valve directed loop injection with a) sample loaded into the fixed volume loop in position A and b) sample injected into GC in position B.

The S/SL injector is the most common injector in the modern GC system. The splitless and split modes of injections are demonstrated in Figure 1.9a and 1.9b, respectively. The liquid sample is introduced into the liner by a syringe in the autosampler or hand (manual injection). The sample is vaporized immediately at 250 °C-300 °C in the liner. In the splitless mode, the valve on the split vent line is closed and the carrier gas passes all the sample to the column; while in the split mode, the valve on the split vent line is open and a portion of the sample is vented from the split vent port

and only the small fraction of the sample is passed to the column. Depending on the split ratio (i.e. vent flow rate/column flow rate), the fractions of the sample to the column can be controlled and determined. The split ratio is usually established by adjusting the flow resistance among column line (determined by the column dimensions), septum purge line and the split vent line. An example of 50 mL /min total flow rate distribution in each line is shown in Figure 1.9a and 1.9b for splitless and split injection, respectively. It is worth noting that under the split injection mode, the reduced mass on the column leads to narrower peaks and thus better chromatographic resolved peaks; however, the loss of the mass results in lower sensitivity because of smaller peak areas and peak heights. This tradeoff has to be balanced when designing or optimizing an analysis method.

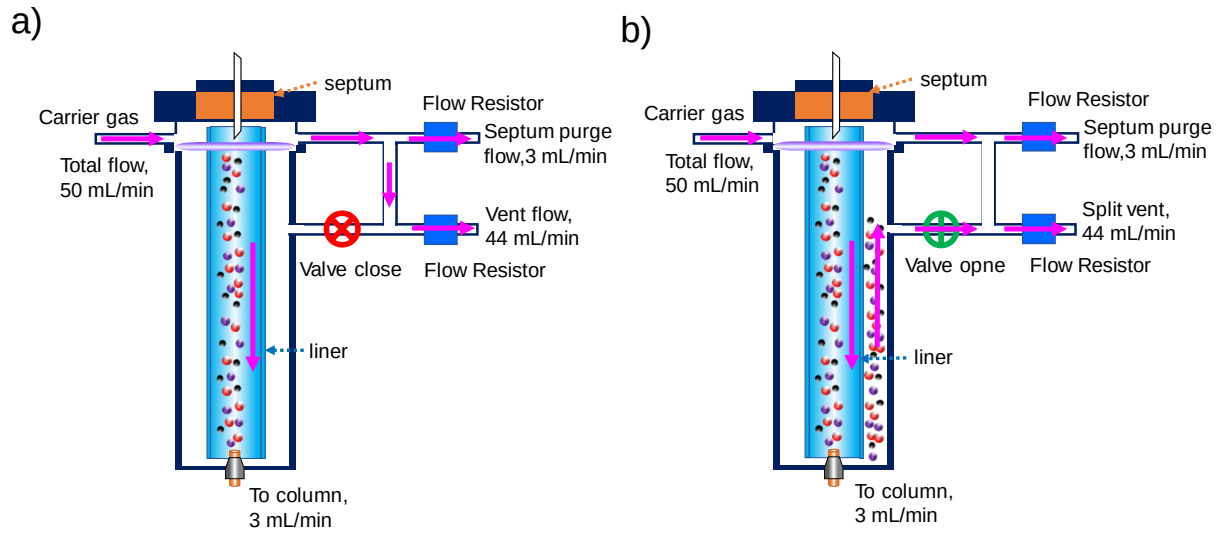

Figure 1.8. The diagrams of a) splitless injection and b) split injection in the split/splitless injector. Pink arrows are flow directions in the injector.

1.3.2.3. GC Columns

GC column is responsible for the entire separation tasks in a GC instrument. Basically, there are two types of the GC column, open tubular and packed. When the stationary phase is a solid adsorbent, the separation process is called gas-solid chromatograph (GSC) and most of the

packed columns are GSC. When the stationary is liquid, the process is termed as gas-liquid chromatography (GLC) and most of the open tubular column is GLC. It is noted that some packed columns are GLC and some open tubular column are GSC. In general, GSC has a very constrained application in the research laboratory and is rarely used due to severe peak tailing and semipermanent retention of polar compounds within the column.[52] Packed GSC and open tubular GSC like porous layer open tubular columns (PLOT) and support coated open tubular columns (SCOT) are not relevant to this work and thus not reviewed in this work. The following discussion focuses on so-called walled coated open tubular columns (WCOT) in the aspects of the stationary phases, column chromatographic performance metrics, and column selection principles.

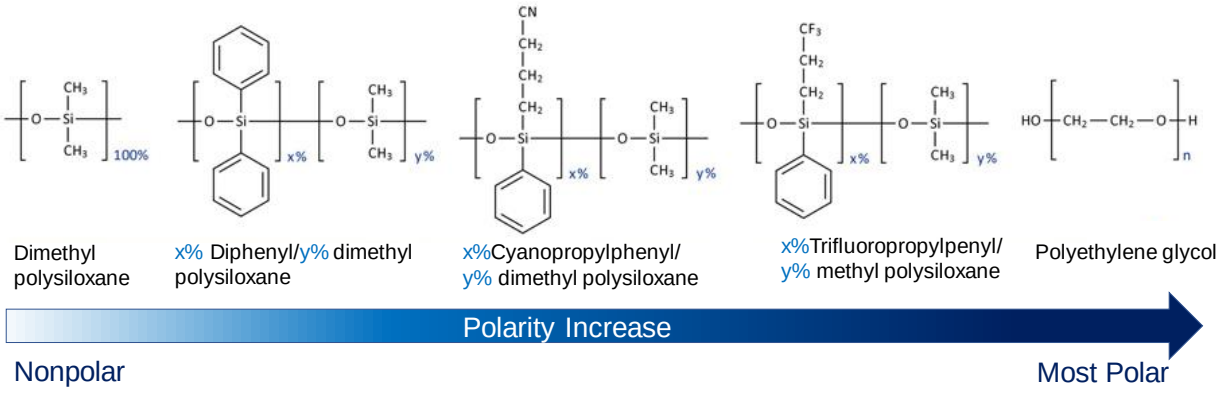

Figure 1.9. Chemical structures of common stationary phase polymers. The polarity of the polymer is increasing from left to right and x% and y% is the percentage of the polarity-different chains of the polymer.

The most common stationary phase in GC is the siloxane-based polymer. These polymers are thermally stable at high temperature (usually >350°C.[72] The polarity is tuned by substituting the methyl connected to the backbone comprised of the phenyl, cyanopropyl, trifluorpropyl and a combination of them. Figure 1.10 shows the basic chemical structure of these stationary phases including the most polar polymer stationary phase polyethylene glycol (PEG). The principle of selecting the stationary phase among those polarity varied polymers will be discussed after the

chromatographic performance metrics part. The method of deposition of these polymers on the inner wall of the capillary tubing will also be discussed.

There are two ways to coat the column with the stationary phase, static and dynamic methods. In both methods, the stationary phase and a crosslinker, for example, dicumyl peroxide, are dissolved in the organic solvents like pentane and dichloromethane. The coating solution is then either pushed or pulled through the column. For the dynamic coating process, a plug of the solvent containing the stationary phase is placed at the beginning of the column and then is pushed through the column. A film is left behind on the column wall as the solvents partially evaporate at the meniscus of the plug when the plug is pushed through the column channel. The film thickness and uniformity depend on the concentration, surface extension and viscosity of the solution, the velocity and constancy of the velocity of plug the moving, and the temperature.[53] In practice, 5% (w/w) of the stationary phase in the solvent produce a film thickness of about 0.5 mm but the uniformity of the film throughout the column is usually poorly controlled.[53,54]

The static coating is a more complicated process that typically results in more uniform films with known thickness. The process begins by filling the column completely with a solution of the stationary phase. One end of the column is then sealed while the vacuum is applied to the other to cause the solvent portion of the coating solution to evaporate and leaving a uniform coating on the capillary wall. The thickness of which can be calculated on the basis of the column internal surface area and concentration of the coating solution. After deposition, the stationary phase will be cross-linked at ~180°C with the N_2 in the column for ~ 1 hour. Usually, hexamethyldisilazane (HMDS) treatment is used to remove the PDMS stationary phase surface hydroxyl groups after cross-linked.

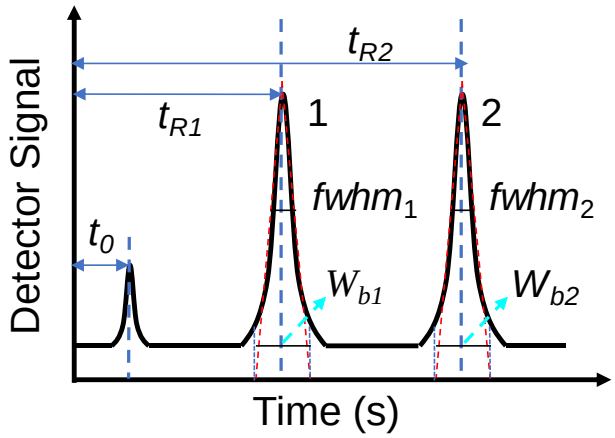

Figure 1.10. A simulated GC chromatogram. The retention time for unretented compound, compound 1, and compound 2 are t0, tR1, and tR2, respectively. Baseline line peak width (Wb) and full width at half maximum (fwhm) are used for the peak sharpness evaluation and resolution calculation.

A good quality coated column provides the basis of a good chemical separation and detection, but the development and optimization of the separation method is the key to realize good chromatogram. There are some chromatographic metrics to be considered when designing the GC analysis method. Among all these metrics, resolution (R_s) is the key parameter used to guide the GC septation method development. The R_s is a quantitative measurement of how well two adjacent elution peaks are differentiated in a chromatogram. It is defined as the difference in retention times (t_R) between the two peaks, divided by the combined widths of the elution peaks. Figure 1.11 shows a simulated GC chromatogram and t_R, baseline peak width (w_b), and full half width at half maximum (*fwhm*) information for two adjust peaks with a peak for unretented compound at the very beginning. The formulation of R_s is shown in Eq. 1.9. The goal a GC separation method development is to make the R_s as large as possible for all adjust peaks in the chromatogram while keeping the analysis speed tradeoff balanced. Because, in practice, sharp symmetrical peaks require certain long retention on the column to get baseline resolved (i.e. R_s=1.5); in the meanwhile, too long retention times broaden the peaks consequently reducing the

R_s. To better understand this separation process, the plate theory[55], van Deemter rate theory,[56] and Golay equation[56] are discussed below.

Plate theory divides the column into a series of consecutive segments called theoretical plates. For each plate, an equilibrium between the amount of solute in the stationary and mobile phase is assumed. A separation process a number of discrete equilibriums in each plate when the solute moves through the column. For a given column, the smaller of the height of the theoretical plate, the more plates the column has. Consequently, more distribution steps can be performed resulting in better separation results. In a certain column length (L), the number of theoretical plates N and height equivalent to a theoretical plate, *HETP* or H and R_s are derived from the chromatogram using t_R, w_b) and *fwhm*:

$$N=\left(\frac{t_R}{w_b}\right)^2 \qquad \text{(Eq. 1.6)}$$

$$N=5.545\left(\frac{t_R}{fwhm}\right)^2 \qquad \text{(Eq. 1.7)}$$

$$H=\frac{L}{N} \qquad \text{(Eq. 1.8)}$$

$$R_s=\frac{t_{R2}-t_{R1}}{\frac{1}{2}(w_{b1}+w_{b2})}=1.18\left(\frac{t_{R2}-t_{R1}}{fwhm_1+fwhm_2}\right)^2 \qquad \text{(Eq. 1.9)}$$

Since t_R implicitly includes the mobile phase holding-up time (t_0)which is not contributing to the separation, the adjust retention time ($t_R^{'}$), effective plate number (N_{eff}) and the effective plate height (H_{eff})are also usually calculated by:

$$t_R^{'}=t_R-t_0 \qquad \text{(Eq. 1.10)}$$

$$N_{eff}=5.545\left(\frac{t_R^{'}}{fwhm}\right)^2 \qquad \text{(Eq. 1.11)}$$

$$H_{eff}=\frac{L}{N_{eff}} \qquad \text{(Eq. 1.12)}$$

A disadvantage of this plate theory is the simplifications made to develop the model. Most of all, chromatography is a dynamic process and a complete equilibrium is never reached. The plate number under nonequilibrium conditions is smaller than the theoretical number under the equilibrium condition.[56] Another disadvantage of the plate theory is that it does not explain peak band broadening in the separation, although it delivers *N* to evaluate the efficiency of a column.

The peak band broadening can be explained by the rate theory by van Deemter.[56,57] The van Deemter equation describes the relationship of the height of a theoretical plate (*H*) and the average linear velocity ($\bar{u}$) of the mobile phase. In condensed form is expressed as follows:

$$H=A+\frac{B}{\bar{u}}+C\bar{u} \qquad \text{(Eq. 1.13)}$$

where *A* refers to the band broadening by Eddy diffusion; *B* represents band broadening by longitudinal diffusion; *C* designates the band broadening from the solute mass transfer delay to the stationary. Since *A* terms the Eddy diffusion process which only exists in the packed column, and thus Golay redeveloped the equation without A term but a new *D* term for extra-column band broadening in Eq. 1.14.

$$H=\frac{B}{\bar{u}}+(C_s+C_m)\bar{u}+D\bar{u}^2 \qquad \text{(Eq. 1.14)}$$

where the new terms C_s and C_m describes the mass transfer delay because of the diffusion int the stationary phase and mobile phase, respectively. It is worth noted that the C_m is not included in the van Deemter equation and *D* is related to the extracolumn banding broadening from injection and detection. *B*, C_s, C_m, and *D* are defined as:

$$B=2D_m f_1 f_2 \qquad \text{(Eq. 1.15)}$$

$$C_s=\frac{2kd_f^2}{3(1+k)^2 D_s} \qquad \text{(Eq. 1.16)}$$

$$C_m=\frac{(1+6k+11k^2)d_c^2 f_1}{96(1+k)^2 D_m f_2} \qquad \text{(Eq. 1.17)}$$

$$D=\frac{t_0^2}{l(k+1)^2} \qquad \text{(Eq. 1.18)}$$

where k is the retention factor which is defined as the $k=(t_R-t_0)/t_0$; D_m is the analyte diffusion coefficient in the mobile phase in the unit of cm^2/s; D_s is the analyte diffusion coefficient in the stationary phase in the unit of cm^2/s; d_f is the thickness of the stationary phase; f_1 and f_2 are Martin-James gas compression coefficient and Golay-Gidding gas compression coefficient, respectively; l is the column length; d_c is the column diameter. For a better separation, a smaller H is preferred. Figure 1.12 are Golay plots that decribes the minimum H_{min} of a column can reach at the optimal linear velocity ($\bar{u}$) with three common carrier gases, N_2, He, and H_2. As the plots indicate, the H_{min} characterized by different carrier gas are very close to each other, although the optimal ($\bar{u}_{opt}$) are very different (this can be explained by $H_{min}=2\sqrt{B\cdot(C_s+C_m)}$ and $\bar{u}=\sqrt{\frac{B}{C_s+C_m}}$). When the $\bar{u} > \bar{u}_{opt}$, the H increases much faster for N_2 than He and H_2. For a given separation, the $\bar{u}$ should be close to $\bar{u}_{opt}$ as much as possible for a small H and extra-column band broadening (the D term) should be also kept to a minimum. if $\bar{u} > 30$ cm/s, the choice of carrier gas should be given in the order of H_2, He and N_2 for better chromatographic performance. For the safety issue, in some circumstances, He is preferred to H_2, although He is much more expensive.

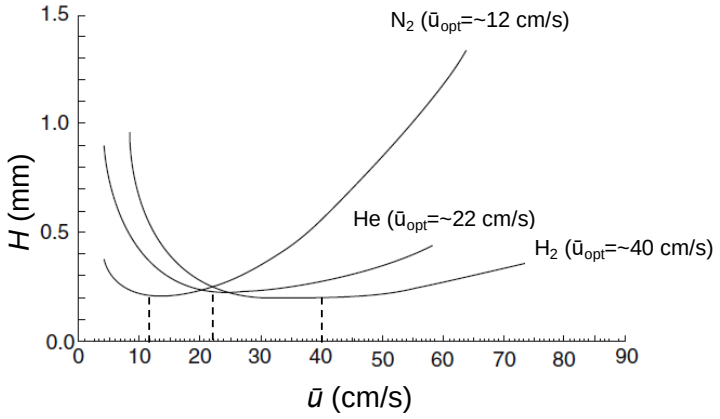

Figure 1.11. The Golay plots for the three common carrier gas, N_2, He and H_2 and their respective optimal linear velocities.

There are two more parameters to characterize the column performance, the Trennzahl number (T_z) and peak capacity (n_c). T_z describes the number of peaks that can be separated between two consecutive n-alkanes with carbon from z and z+1 with sufficient resolution (R_s=1.177) [76]

$$T_z = \frac{t_{R(z+1)} - t_{Rz}}{fwhm_z + fwhm_{z+1}} \qquad \text{(Eq. 1.19)}$$

where, $t_{R(z)}$ is the retention time of the n-alkane with z carbon atoms; $t_{R(z+1)}$ is the retention time of the n-alkane with z + 1 carbon atoms; $fwhh_z$ is the peak width at half height of the n-alkane with z carbon atoms; $fwhh_{z+1}$ is peak width at half height of the n-alkane with z + 1 carbon atoms. Since T_z depends on the n-alkanes used, they should always be specified when discussing T_z. Another better descriptor is peak capacity (n_c) which is defined as the maximum number of peaks that can be separated on a given column with a defined resolution in a retention time window(e.g., starting from the first peak (hold-up time) up to the last peak (retention time of the last peak)). n_c can be calculated by

$$n_c = 1 + \frac{\sqrt{N}}{4R_s} In\ (\frac{t_{R,max}}{t_0}) \qquad \text{(Eq. 1.20)}$$

Where $t_{R,max}$, retention time of the last peak. Both T_z and n_c are theoretical values. The T_z and n_c of a chromatogram from the experiment usually smaller because of the peak distortion, like peak fronting or peak tailing. In a chromatogram from testing, n_c is hardly to be reached. Giddings demonstrated that peak shapes were affected if the number of solutes exceeds 37% of the peak capacity.[58]

All above theory is helping to understand the separation process and guide the method development for the separation. The goal of a separation method development is usually generating a chromatogram with all $R_s \geqslant 1.5$ in time as little as possible. The method related GC column is the critical part of a complete GC method.

Selecting an appropriate column is the first step toward developing a separation method. The most common resolution equation is used to guide the selection process. For any adjacentst peaks, peak 1 (smaller t_R) and peak 2 (larger t_R), the resolution of the two peaks:

$$R_s = \frac{\sqrt{N}}{4}\left(\frac{\alpha\text{-}1}{\alpha}\right)\left(\frac{k_2}{k_2+1}\right) \qquad \text{(Eq. 1.21)}$$

where α is the separation factor, which is equal to k_2/k_1. k_1 *and* k_2 are the retention factors for peak 1 and peak 2 (see. Figure 1.10), respectively. When choosing the column, the polarity of the analytes and stationary phase and α should be considered first. The stationary phase with similar polarity with the analytes is the right one. Since α describes the retention differences of the two compounds on a stationary phase, it, in other words, represents the "selectivity" of a stationary phase for these two compounds. Sometimes, a few stationary phases can be roughly picked after study polarity of the individual analytes in a complex mixture and the stationary phase. α usually requires more and further explorations to nail down the best stationary phase.

Table 1.4. Kovat's retention indices (Ix) of representatives for GC stationary phases can be used to approximate selectivity from ref.59.

Stationary Phase	Benzene	Butanol	Pentanone	Nitropropane
100% Dimethyl polysiloxane	651	651	667	705
5% Diphenyl/95% dimethyl polysiloxane	667	667	689	743
20% Diphenyl/80% dimethyl polysiloxane	711	704	740	820
6% Cyanopropylphenyl/94% dimethyl polysiloxane	689	729	739	816
35% Diphenyl/65% dimethyl polysiloxane	746	733	773	867
Trifluoropropylmethyl polysiloxane	738	758	884	980
Phenyl methyl polysiloxane	778	769	813	921
14% Cyanopropylphenyl/86% dimethyl polysiloxane	721	778	784	881
65% Diphenyl/35% dimethyl polysiloxane	794	779	825	938
50% Cyanopropylmethyl/50% phenylmethyl polysiloxane	847	937	958	958
Polyethylene glycol	963	1,158	998	1,230

In real practice, before running any experiments to collect *k* data, Kovat's retention index for polarity representative compounds on common polarity varied stationary phases provide very useful insight to guide the selection and decision-making process. The Kovat's retention index (I)[60] solely depends on the column temperature and the type of stationary phase, but are independent of column length, phase ratio, carrier gas type, and linear velocity and is defined as

$$I_x=100\ (z+(\frac{log t_x^{'}-log t_z^{'}}{log t_{z+1}^{'}-log t_z^{'}}) \qquad \text{(Eq. 1.22)}$$

where I_x is the Kovat's retention index of the analyte x; z is number of carbon atoms of the n-alkane eluting right before the analyte; $t_x^{'}$ is the adjusted retention time of analyte; $t_z^{'}$ is the adjusted retention time of the n-alkane with z number of carbons eluting right before the analyte ; $t_{z+1}^{'}$is the adjusted retention time of the n-alkanes with $z+1$ number of carbons. Table 1.4 summaries the I values for 4 representatives on a broad polarity stationary phases. Those 4 compounds represent a broad functionality and polarity with aromatic rings, hydroxyl, carbonyl, and lone pair in the structure. The table is a very useful tool for comparing stationary phase selectivity and deciding which is most appropriate for a specific analysis. For example, polyethylene glycol has better selectivity than 100% dimethyl polysiloxane to the benzene and butanol. If the separation involved with aromatic compounds and alcohol with closed carbon numbers in the molecules, a polyethylene glycol stationary phase should be chosen.

After proper stationary phase selection, the retention factor *k* needs to be optimized. In general, certain *k* (usually 2-10) is essential for a good quality separation and symmetric peaks. If it's too large or too small, the peaks will be broadened leading to resolution lose; if it's too small, little retentions results in coelution problems. There are four *k* related factors needs to be considered: film thickness, inner diameter (ID) of the column, phase ratio, and temperature.

Stationary film thickness (d_f) universally affects the sample loading capacity and the retention of the analytes. The thicker of the stationary phase film, the larger *k* and better separation is achieved because the compounds spend more time in the stationary phase. But if analyzing low volatility compounds, a thin film stationary phase should be used to avoid too much band broadening. Sometimes, a higher temperature can be used to drive the low volatility compound elution which also could cause the column bleed. Generally speaking, the thin film stationary (0.1 µm -0.5 µm) is used for low volatility compounds with a medium and high molecular weight to speed up the separation rate while a good *k* is maintained. In comparison, a thick film stationary phase (0.5 µm -10 µm) is recommended for high volatility compounds with a small molecular weight. It should be noted that the film thickness also affects the sample loading capacity. For high concentration sample analysis, a thicker stationary phase should be used to avoid the column overloading or front problems and vice versa.

Although column ID is not as critical as film thickness, an appropriate ID column should be used whenever possible to produce a good *k*. Basically, a smaller ID generates a larger *k* because higher chance and longer time of the analyte spending a longer time in the stationary phase. Thus, the small ID (150 µm-180 µm) column is suited for high volatility compounds and fast GC analysis for good separation performance; for large ID (0.53 µm) column, it is most useful for low volatility compounds; the intermediate ID (0.25 µm-0.35 µm) column is used for a complex mixture with from low to high volatility compounds. If a good separation has been achieved on a larger ID column and a faster analysis is desired, this can often be accomplished by reducing the ID of the column without sacrificing, and sometimes even improving, separation efficiency.

More importantly, the column ID and d_f have to be optimized together to generate a good quality chromatogram. The phase ratio (β) is the parameter expressing the ratio of column ID and

d_f of the stationary phase. When narrowing or enlarging column ID is necessary to adjust column efficiency or the sample capacity, the film thickness must be changed accordingly as well to maintain a good β for chromatographic performance. When translating a method and keeping a similar compound elution pattern, β is the parameter reserved among methods.

Developing a temperature program is the most important part of separation method development. Isothermal separations are occasionally used, but the temperature program is desired for complex mixture GC analysis. An optimized temperature program is highly depended on the analytes and column. Thus, the temperature program has to be developed case by case. Although the program varies from one analysis to another, there are three critical parameters for optimization: initial temperature (T_i), ramp rate (R_r)and final temperature (T_f). The initial oven temperature T_i is usually set up at room temperature or 20 °C lower than most of the sample in the mixture with a hold time (t_h) of ~30 s. The purpose of doing this initial low temperature is to provide the on-column focusing near the head of the column. With the negative temperature difference when sample transfer from the injector to the column, the relatively low volatility compounds (boiling point $\leqslant T_i$ +20°C) could be reconcentrated and thus form a narrower band width and ~30 s is the right time period (not too long for broadening or too short leaving reconcentration uncompleted) that for this reconcentration process.[59,61] This on-column focusing is demonstrated in Figure 1.13.

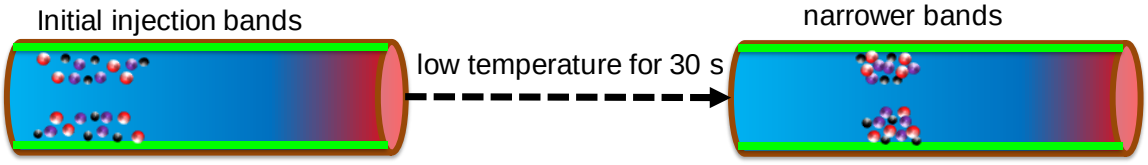

Figure 1.12. On-column focusing process at the range near the cold head of the column. Light blue represents a low temperature. The hot-injection band from the injector is reconcentrated under a sharp negative temperature program. Only compounds that benefit from the on-column focusing is shown.

Adjusting the R_r has the most pronounced effect on for the separation performance in the middle range of the chromatogram. The optimized R_r is equal to the 10°C per holding-up time,[6182]

$$R_{r,opt} = \frac{10\ ^{\circ}\mathrm{C}}{t_m} \qquad \text{(Eq. 1.23)}$$

T_f of a temperature program is usually setup up 10-20°C (T_0) higher than the elution temperature of the last or final analyte (T_l),[61] where

$$T_l = T_i + RT_{opt} \cdot (t_f - t_h) \qquad \text{(Eq. 1.24)}$$

$$T_f = T_l + T_0 \qquad \text{(Eq. 1.25)}$$

1.3.3. GC Detectors

If the column is the heart of a GC system, the detector is the brain. A good GC detector represents the elution profile faithfully and provides quantitative analysis. Many GC detectors have been developed and used in the commercial GC systems.

Table 1.5. common detectors in commercial GC systems with summary of properties, strength and weakness for each detector.[62]

detector	M/C[a]	S/U[b]	detection principal	detected species	D/N[c]	LOD[d]	strength	weakness
FID	M	U	flame ionization	hydrocarbons	D	100s pg	sensitive, universal, cheap	H_2 supplied required; les sensitive to hgeteros
TCD	C	U	conductivity difference between analytes and career gas	compound itsefl	N	ng/mL	nondestructive; and response to all species	not that sensitive;; requires H_2 or He
PID	C	S	ionization by UV irradiation	ions of photons dissociated compounds	N	pg/s	sensitive, fast response, no consumable	only compounds with ionization engery lower than the energy of the photons produced by the PID lamp
ECD	C	S	electrons capture in electronegative groups	halides, nitrates, nitriles, peroxides, anhydrides, organometallics	N	sub-pg/mL	super sensitive, no consumable	radioactive resource, not universal
NPD	M	S	ionization by thermal energy	nitrogen/phosphorus	D	10s pg	highly sensitive and selective	not sensitive to compounds without nitrogen/phosphorus
FPD	M	S	excited sulphur and excited hydrogen phosphorous oxide	sulfur/phosphorus	Y	100s pg	highly sensitive and selective	not sensitivity for compounds without sulfur/phosphorus
CLD	C	S	photons produced from the compound reaction with O_3	sulfur/nitrogen	Y	pg/s	highly sensitive and selective	only response to compounds with sulfur/nitrogen
MS	M	S,U	ionization; m/z separation	ionized compounds/fragments	Y	sub-pg	extremely sensitive; mass/structure information	expensive, higher power and high vacuum requirement

[a] M=mass detector, C=concentration detector; [b] S=selective, U=universal; [c] D=destructive, N=nondestructive

These detectors include flame ionization (FID), thermal conductivity (TCD), photoionization (PID), electron capture (ECD), nitrogen phosphorous (NPD) and flame photometric types (FPD), chemiluminescence (CLD), and mass spectrometer (MS). These detectors can be generally classified according to quite different criteria that are useful for different purposes. Any detector can be classified as universal or selective based on whether its response is selective or not. Another general classification is, destructive vs. nondestructive. The third instructive classification is based on whether the signal depends on the concentration of detection species in the detector or on the "mass flow". Actually, this classification is related to the first and second ones, since, with few exceptions, mass flow detectors are destructive and concentration detectors are nondestructive. Some of the unique properties, strengths, and weakness which is summarized in Table 1.5. For details of each detector, for example, physical structure, detection mechanisms are beyond the scope of this work and thus will not be discussed here.

1.4. μGC

1.4.1. μGC introduction

Benchtop GC instrument is not suitable for off-site laboratory VOC analysis because they are large, heavy, and require high voltage power for operation. Additionally, samples collected out in the field are subjected to lose, contamination, degradation, and/or decomposition during storage or transport. Pushed by the increasing demands of the *on-site* and *real-time* or *near-real-time* analysis of the complex VOC mixture, the efforts to develop portable or hand-held gas analyzer have been made.[63-69] Among these technologies, GC-based technology seems to be very promising for onsite repaid analysis. With the goal of developing small footprint, low power dissipation, and high capability GC and relying on Micro-Electro-Mechanical Systems(MEMS) technology,

significant amounts of the work have been devoted to developing Si-microfabricated GC microsystem (μGC) over the past 40 years in either component level or system level.

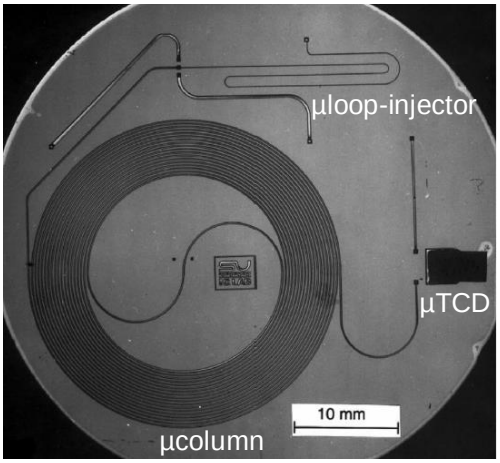

Figure 1.13. First μGC with an on-chip microfabricated loop injector, a 1.5 m × 20 μm × 30 μm spiral column, and a μthermal conductivity detector (μTCD). The figure and details of μGC is from ref. 91.

μGC was first introduced by of Terry et al. at Stanford University in 1979.[70] That first μGC in Figure 1.14 has a loop injector, a 1.5 m separation column, and a micro-thermal conductivity detector (μTCD) all integrated on a single 2-inch Si wafer. Twenty years after the first μGC work, Kolesar and Reston reported the second μGC with 10 μL sample loop, 0.9 m long rectangular channel shape (300 μm width and 10 μm height) capillary column, and a dual detector (chemiresistor and TCD).[71] Following on those pioneer works, numerous examples of microelectromechanical (MEMS) μGC components and systems have been reported, primarily from current and/or former researchers from: the University of Michigan's Center for Wireless Integrated MicroSystems (e.g. Dr. Kensall Wise, Dr. Richard Sacks, Dr. Edward Zellers, Dr. Yogesh Gianchandani, Dr. Katuso Kurabayashi, Dr. Sherman Fan, Dr. Masoud Agah -now at Virginia Tech University),[72-85] Sandia National Laboratories (SNL) (e.g. Dr. Gregory Frye-Mason, Dr. Ronald Manginell, Dr. Patrick Lewis),[85,86] the University of Catania Institute for

Microelectronics and Microsystems (e.g. Dr. Stefano Zampolli, Dr. Ivan Elmi),[87] the University of Illinois at Urbana-Champaign (e.g. Dr. Richard Masel and Dr. Mark Shannon) [88,89] and the Louisiana Tech University (e.g. Dr. Edward Overton, Dr. Adarsh Radadia)[88-90], Each of these groups has taken somewhat different approaches in optimizing individual components, to exploring novel fabrication and design features, and to full system integration. The term "μGC" is reserved to describe a portable analytical system having microfabricated versions of all three key components: sampler/injector, column, and detector. Some of the portable GC or μGC prototypes are shown in Figure 1.15 and reviews of the microanalytical components and the complete microsystem can be found in references 113-116.

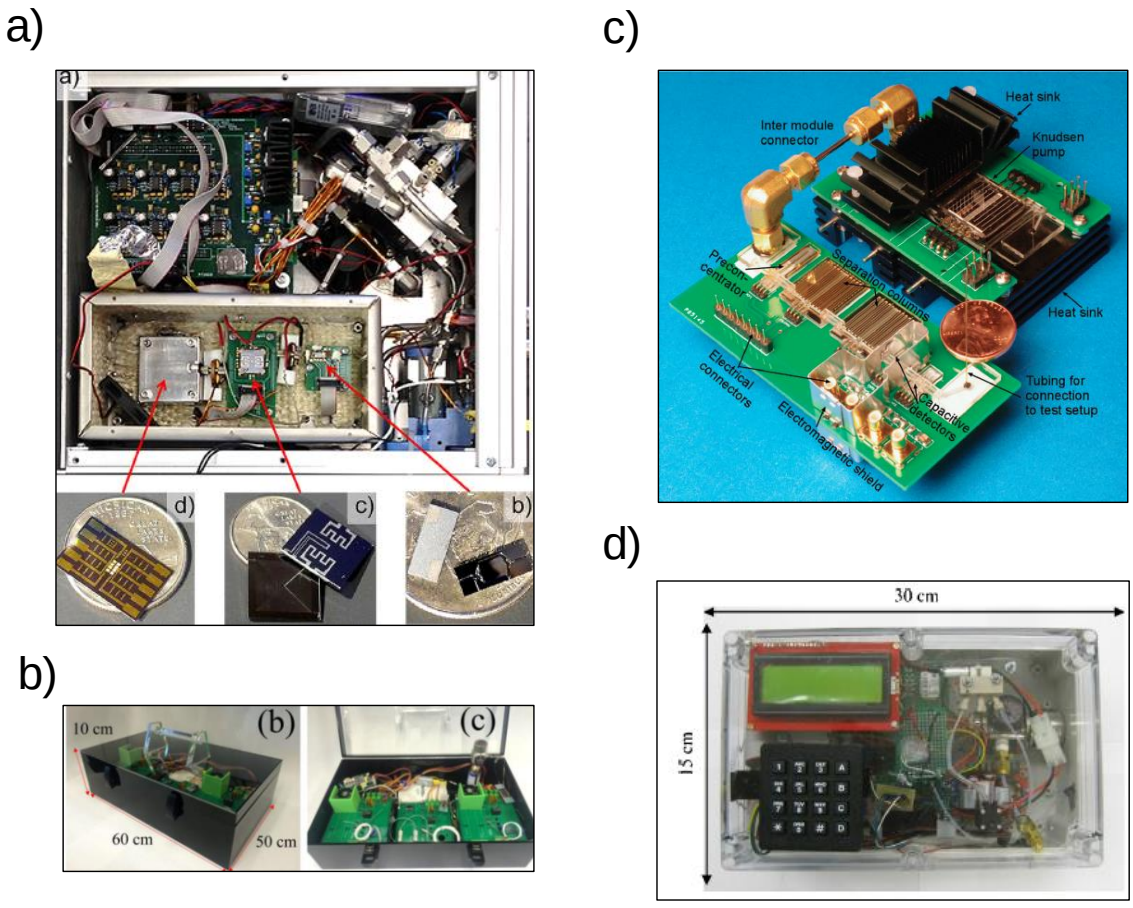

Figure 1.14. μGC prototypes a) Zellers' group INTREPID in Ref. 79; b) Fan's group 2D GC (microfabricated injector and detector but not for the column) in Ref. 81; c) iGC 3 from Gianchandani group in Ref. 80; d) Agah group Zebra GC in ref. 82.

Commercialization of the µGC has been pursued by several companies. Traditionally, there are some well developed and marketed portable GC products. The notable products are Agilent's 490 Micro GC based on Stanford µGC, Defiant's FROG-5000 based on SNL µGC,[65] INFICON's MicroGC Fusion® also based on Stanford µGC.[64] Recently years, the µGC products markets are also developing in oil and gas, pharmaceutical, homeland security, environmental and industrial process control business sectors. Those emerging products either commercially available or still under development. have been reported byAPIX Analytics,[91] Zebra Analyticx,[92] Nanova Environmental,[93] Omniscent.[94]

1.4.2. µGC Samplers/Injectors

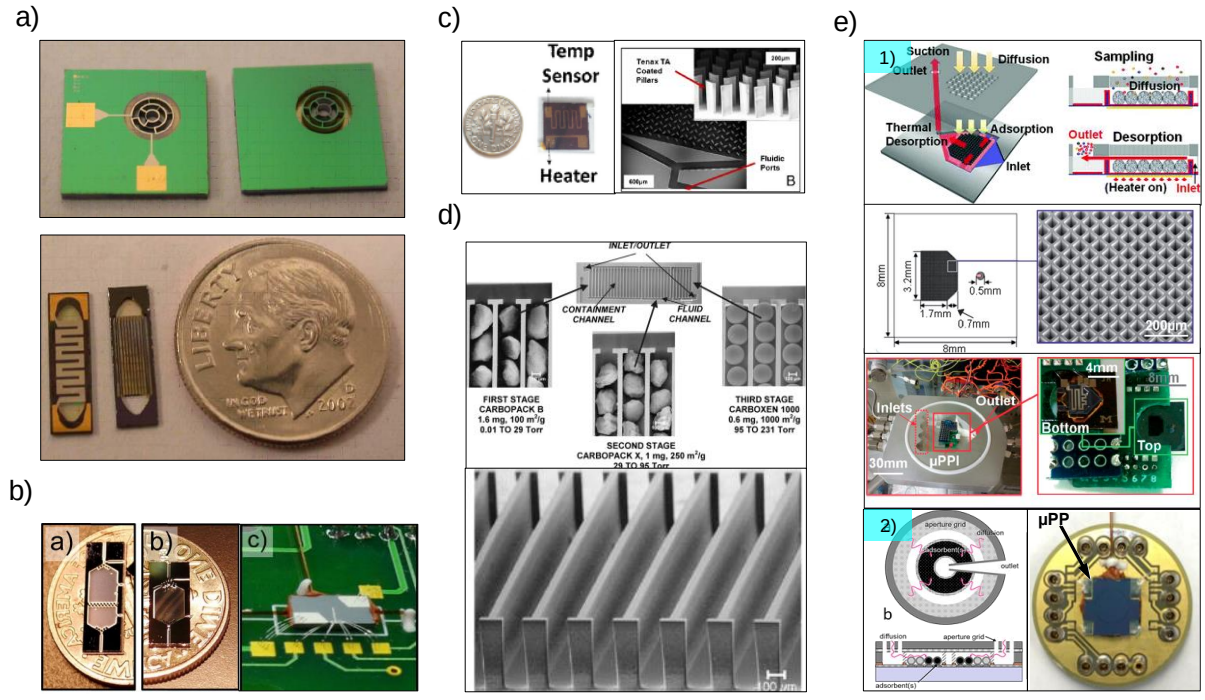

Figure 1.15. µPCF works from a) Sandia National Laboratory in Ref. 86; b) Zellers group one and dual beds devices in Ref. 101; c) Agah group with embedded microposts and Tenax adsorbent in Ref. 82; d) Zellers group three-bed device with Carbopack B, X and Carboxen 1000 in the microchannels in Ref. 100; passive sampler e1) Zellers and Kurabayashi groups with Carbopack X in the device in Ref. 102; e2) Zellers and Potkay groups with Carpoack B and Caropack X in a passive micro preconcentrator in Ref. 102a.

There are two mainstream microfabricated sampler/injectors: micro valve-loop injector (used an on-chip small sample loop and off-chip solenoid valve. This type of the injectors was also presented in other following work [84,95-99] More often, the adsorbent based µPCF has been used in the µGC system. Figure 1.16 shows the noteworthy µPCFs which are unique either in device design, materials, or collection method. µPCF has two major advantages over µVLIs: 1) significantly improved the system sensitivity by ~1000s times; 2) reduced the water vapor by using nonpolar adsorbents.

A µPCF usually contains one or more cavities to house the adsorbent materials; a resistive heater deposited on one side of the Si-chip for thermal desorption; and 2 or 3 fluidic ports for sample collection and split/splitless injection. The first µPCF (Zellers coined the term of µPCF) was introduced by SNL in 2000.[85] The device incorporated a surfactant templated sol-gel adsorbent deposited on a micro-hotplate. The preconcentration factor of 100-500 for dimethyl methyl phosphonate (DMMP) was achieved. SNL advanced the work further on µPCF (see Figure 1.14a) in their µChemLab work.[86] Zellers group at the University of Michigan designed and developed serval types of µPCF. Those devices include ones in Figure 1.14b and d which are active µPCF with one (packed with Carbopack X),[100] two (packed with Carbopack B and X),[101] and three(packed with Carbopack B, X and Carboxen 1000) adsorbent beds,[100]and the passive µPCF[102] in Figure 1.14e1 in which airborne vapors are captured by passive diffusion into the adsorbent Carbopack X through >1500 parallel diffusion channels, each 54 ×54 × 200 mm. The passive µPCF has shown a 9.1 mL/min sampling flow rate for ~1 ppm toluene and collected ~1 µg in 30 min. The passive micro preconcentrator (µPP) has a sampling grid of 237 47×47×180 µm (L×W×H) apertures located at the periphery of the top surface of µPP; two concentric annular

adsorbent cavities filled with ~800 µg of Carbopack B (surface area: 100 m^2/g, outer) and 700 µg Carbopack X (surface area: 240 m^2/g, inner); it achieved nearly constant, zero-power (diffusional) sampling rates for up to 24 hr (at ~1 mg/m^3) and over a 2,500-fold concentration range (for 15-min samples). Agah group at Virginia Institute of Technology developed the µPCF with high-aspect-ratio microposts embedded inside of the chamber to increase the surface area where the adsorbent material Tenax TA was coated.[82]

1.4.3. µColumns

The miniaturization of a GC column can be by MEMS technology. A microfabricated separation column (µSC) typical have a microchannel etched in the Si substrate. The channel is typically hermetically sealed by a glass wafer through an anodic bonding process in which the Si and glass are treated with the high temperature (300-600°C) and an external electron field (200-2000 V) is applied. [103] A resistive heater on the back side and temperature sensor are usually patterned on the back side of the Si wafer. Polymeric stationary phase (for example, OV-1) can be applied by a dynamic or static coating method.

µSCs have some advantages over conventional capillary columns. Some of the advantages include small size because of the tightly packed channels, lower power dissipation because of smaller thermal mass, better and heat control from on-chip heater than oven heating, and much higher heating ramp rate for fast analysis. There are some drawbacks as well, such as, pooling effect at the sharp corner of the channels, non-uniform film thickness, that could lead to peak band broadening; one side heating resulting in a temperature gradient; racetrack effect in a tight column; and length limitation

Conventional GC columns are usually made of circular fused silica capillary, while most of the µSC have rectangular channels on the Si chip because the wet etching process hardly

produces circular geometry channels. Some research reported the circular channel of the μSC produced by drying etching.[104] The cross-sections of the channels of the μSCs can have trapezoidal,[134] square, [135] semi-circular[136] shapes.

Reported channel layouts are also varied and include square spiral (Figure 1.17a),[105-113 137-144, 150] circular spiral (Figure 1.17b),[114] serpentine (Figure 1.17e)[90,112], wavy (Figure 1.17d),[115,146] Radadia et al. compared the separation performance of three popular μSC layouts, serpentine, circular spiral, and square spiral designs using fix length 3-meters longμSCs with (100 × 100 μm)square cross-section .[88] The results show the gas permeability and unretained solute, methane, band broadening are similar among these three geometries. For a slightly retained iso-octane, the serpentine μSC has ~70% higher plate numbers than the circular-spiral and square-spiral μSC for both of which the plate numbers are similar. The authors attribute the enhanced plate numbers to favorable hydrodynamic flow as well as a thinner and more homogeneous stationary-phase coating in a serpentine configuration.

Some other efforts have been made to develop the μSC in past years: exploring new materials for fabrications, for instance, using metals (e.g. nickel, steel, and titanium)[116,117] and polymeric material (e.g. parylene (poly(p-xylylene))[118] designing new heater and zone-heating strategy;[113] patterning microchannels (e.g. multi-capillary, semi-packed);[119] investigating new stationary phase (e.g. RTIL, MOF);[120,121] advancing multi-dimensional μGC.[33]

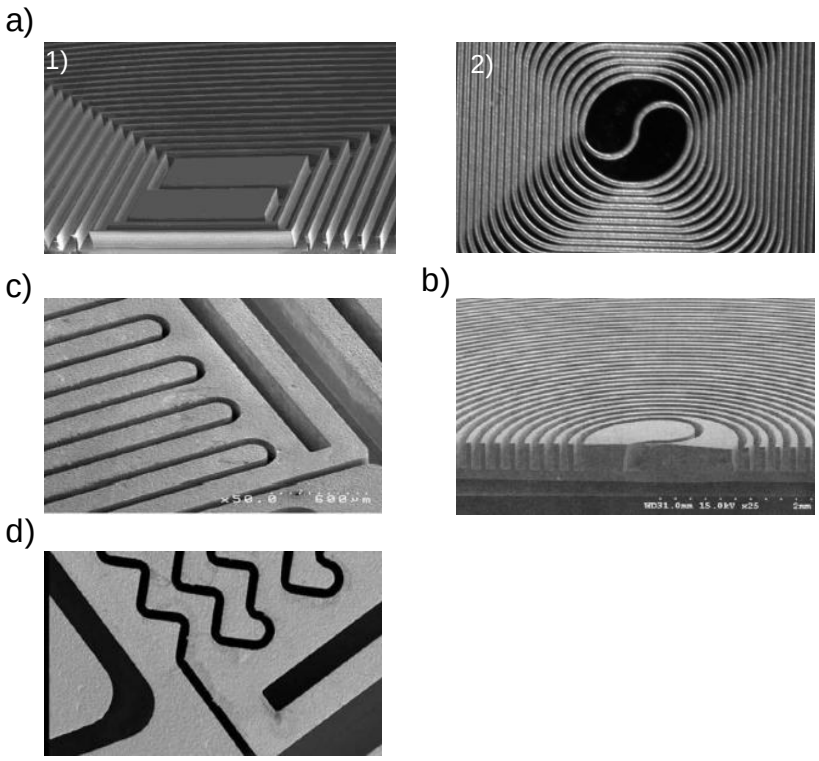

Figure 1.16. The layout of the channel over the chip a) square spiral, figure 1a is from ref. [110] and figure 1b is from ref 113; b) circular spiral in ref. 114; c) serpentine in ref. 90; d) wavy in ref. 115.

1.4.4. µGC Detectors

Many detectors which are used in the conventional bench scale GC have been attempted to be miniaturized. Some of them have been explored in µGC systems. µTCD is the one employed in the first µGC.[70] The signal of the µTCD is generated based on the conductivity decrease when the analyte presents in the carrier gas. Similar µTCDs were developed by other researchers.[82,98,122,123] µTCD is very sensitive with a sub-ppm detection limit and has been used in commercial Agilent 490 Micro GC,[124] but it suffers from baseline drifts because of the thermal temperature program in the µSC. The universal FID has also been miniaturized.[125-129] Because of the requirements of the external supply of the hydrogen and air, µFID is less competitive. More recently, the µPID has drawn great attention from the µGC community. µPID is developed along

in two avenues. One aspect is reducing the ionization chamber (typical conventional PID has a 40-200 µL chamber) by MEMS technology to improve ionization efficiency. Sun et al. recently developed a µPID reaching a ~5 ppb LOD in a 10 µL ionization chamber.[130] The µPID developed by Zhu et al. at the University of Michigan reached a pg LOD in a 1.3 µL chamber which was ~200 times lower than the commercial PIDs.[163] The other aspect is of developing the higher ionization lamp photon energy (commercial UV lamp photons energy upper limit is 8.4-11.7 eV). The Agah group developed a helium discharge photoionization detector on the Si chip with a 10 pg of octane[83,131] and Fan group developed miniaturized a helium dielectric barrier discharge PID with a detection limit of a few picograms.[132] both µPID extends the ionization energy up-limit above 11.8 eV.

There are more types of microfabricated detectors developed for µGC systems. Those sensors include reversibly-sorptive interfaces such as surface acoustic wave (SAW) devices,[133] thickness shear mode resonators (TSMR),[134] microcantilevers[135,136] chemiresistors.[75,137-140] SAW and TSMR (also commonly referred to as a quartz crystal microbalance, QCM) devices measure changes in the resonant frequency of piezoelectric material as mass goes in/out of the interface film which is typically a polymer, though, ionic liquids[138] and thiolate-protected gold nanoparticles have been used with success. Stress-induced responses to mass deposition on the suspended beam structure of microcantilever devices also were used for µGC detections. [141,142]

Most of Zellers' group work has used multi-monolayer-protected gold nanoparticles (MPNs) coated on interdigitated electrodes (IDEs) on a glass substrate as µGC detectors.[add references] These have been configured as µchemiresistor array (µCR) arrays for chemical identification and quantification. These µCR arrays are quite versatile for VOC determinations. Figure 1.18a shows the generic structure of the MPN. Each MPN has a 3-4 nm gold core with

functionalized thiolate ligand, R. Each kind of MPN has a unique thiolate functionality with one or more functional groups in the ligand. After coating those MPNs onto the IDEs, a voltage is applied and a tunneling current is established through the MPN files and the baseline resistance (R_b) is measured. Once the VOC molecules are reversibly partitioning into MPN film, the film swells and the average distance (δ) between MPNs increases $\Delta\delta$. The dielectric constant of the film can also change. These changes lead to changes in the baseline resistance to $R_b+\Delta R$. When the VOC molecules spontaneously desorb from the film, the baseline is regenerated.

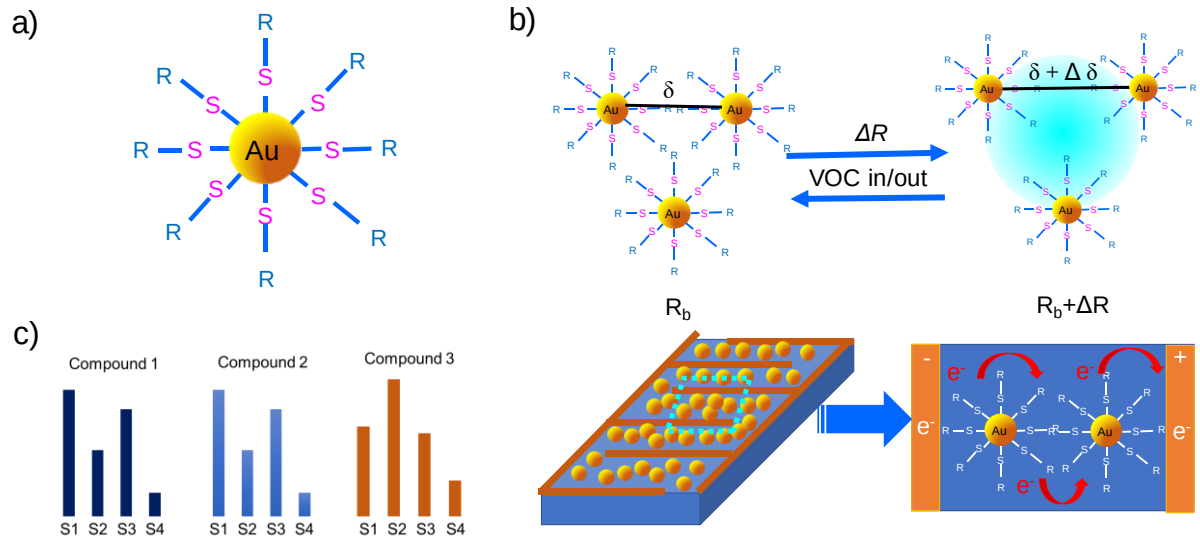

Figure 1.17. a) Diagram of an MPN, where, R is the thiolate ligand moiety; b) the detection mechanism of an MPN-coated μCR array of this study; c) hypothetical normalized response patterns of 3 VOCs obtained from a 4-element μCR array.

This MPN film and VOC molecule interactions between an IDE is shown in Figure 1.18b. For the same VOC compound, different functionalized MPNs response differently. For different VOC compounds (assume the same concentration), the ΔR and $\Delta\delta$ will be different from the same MPN because of the different intermolecular interactions between the VOCs and that MPNs. By coating 4-5 different functionalized MPNs on a set of IDEs, the μCR array generates a unique

response pattern to each VOC. An example of patterns for three VOCs from a 4-functionalized MPN coated μCR array is showed in Figure 1.18c.

The exclusive advantage of this μCR array is that it not only provides quantification but also facilitates the chemical identifications based on the unique response patterns. For compounds with very different structures, if they fully or partially coelute from the μSC. The response patterns can be used to discriminate them. The Zellers group has developed and applied serval multi-variate statistical methods for pattern recognition using microsensor array data. To differentiate components of binary and ternary mixtures, extended disjoint principal component regression (EDPCR) [143-146] and multivariate curve resolution analysis, like evolving factor analysis (EFA) and alternating least squares (ALS)[147] were used.

1.5. Modeling for VOC adsorption on the adsorbent

1.5.1. Gas-Solid Adsorption Theory

Table 1.6. The difference comparison between the chemisorption and the physisorption from ref 158.

physisorption	**chemisorption**
Occurs only at the temperature below the boiling point of the adsorbate	Can occur at most of the temperatures
Heat of adsorption is less than 40 KJ/mol	Heat of adsorption can be more than 200 KJ/mol
The adsorbed amount increases with vapor pressure of adsorbate decrease	Pressure is insignificant
No appreciable activation energy is required	Appreciable activation energy is involved
Can occur multilayer adsorption	Only the monolayer adsorption

The adsorption is brought about when the adsorbent interacts with the molecules in the fluid phase. There are two kinds of adsorptions based on the types of forces involved. They are physisorption and chemisorption. The intermolecular forces and valence forces are involved in chemisorption and physisorption, respectively. The major differences between these two types of

adsorption are summarized in Table 1.6. The physisorption adsorption is directly related to this study and further discussed here.

The adsorption isotherm describes the relationship between the amount adsorbed by a unit mass of solid and the equilibrium pressure at a known temperature in physisorption. The adsorption isotherms recorded in the literature for many different gas-solid systems have various characteristic shapes. These shapes provide critical information in pore size, surface area, and porosity of an adsorbent. There are nine types of adsorption isotherms by extended IUPAC classification.[159] They are shown in Figure 1.18.

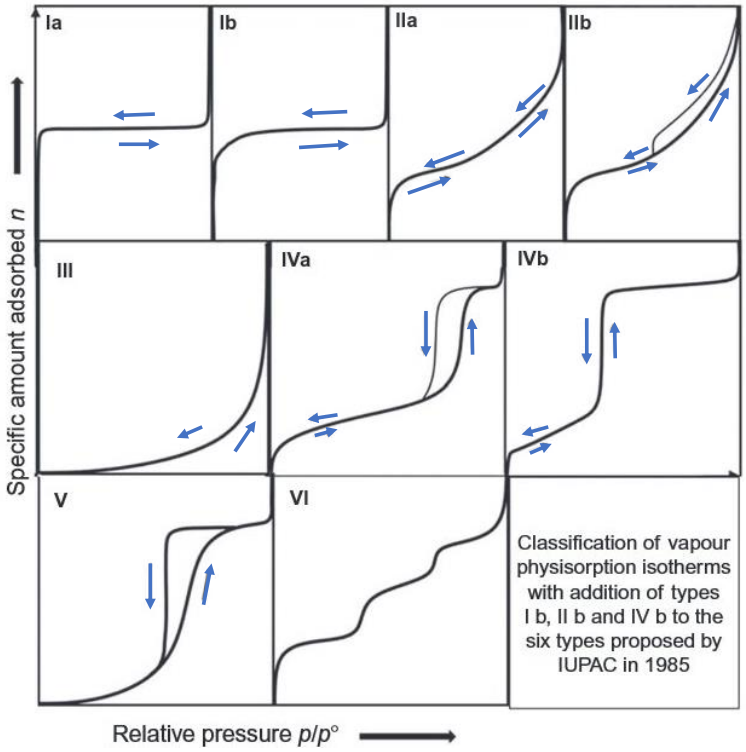

Figure 1.18. Classification of adsorption isotherms combining proposals from IUPAC. The figure is taken from ref. 159.

Type I(a) and I(b) corresponds to the filling of narrow micropores and wider micropores, respectively. With all Type I isotherms, the adsorption is limited by the available micropore volume of the adsorbents.

In type II adsorption isotherms, if the knee of the isotherm is sharp, the uptake at Point B- the beginning of the middle quasi-linear section- is usually considered to represent the completion of the monomolecular layer (the monolayer) and the beginning of the formation of the multimolecular layer (the multilayer). The ordinate of Point B gives an estimation of the amount of adsorbate required to cover the unit mass of solid surface with a complete monolayer. A number of powders or aggregates (e.g. clays, pigments, cement) give Type II isotherms. The narrow hysteresis loop is the result of inter-particle capillary condensation.

Type III isotherms indicate weak adsorbent-adsorbate interactions on a non-porous or macroporous adsorbent because there is no point B in the entire range of relative pressure.

Type IV(a) isotherms is much more common than Type IV(b) isotherms. For the hysteresis loop: the lower branch (adsorption) is obtained because of the progressive gas uptake and the upper branch (desorption) is obtained due to the progressive withdrawal. This phenomenon is usually associated with the filling and emptying the mesopores by the capillary condensation.

Type V isotherms also represents the weak interactions between the adsorbent and the adsorbate. Different from Type III, Type V isotherms is usually observed on a microporous or a mesoporous adsorbent. Here again, the hysteresis loop is from the gas filling and emptying the microspores and mesopores.

Type VI isotherms describes the layer-by-layer adsorption. The type of isotherms is usually observed on a highly uniform surface.

1.5.2. The Wheeler Model

The modified Wheeler Model has been used to guide the design and assess the performance of packed-bed preconcentrators and micropreconcentrators.[160-162] It relates several device design and operating parameters to the volume of vapor-laden air that can be drawn through an adsorbent bed, $V_{b\text{-}x}$, prior to observing a given fractional breakthrough (x) of an initial challenge concentration under continuous exposure conditions:

$$V_{b\text{-}x} = \frac{W_e W_b}{C_0}\left[1 - \frac{1}{k_v \tau}\ln\left(\frac{C_0}{C_x}\right)\right] = \frac{W_e W_b}{C_0} - \frac{W_e \rho Q}{C_0 k_v}\ln\left(\frac{C_0}{C_x}\right) \qquad \text{(Eq. 1.26)}$$

$$t_{b\text{-}x} = \frac{\rho W_e}{C_0}\left[\tau - \frac{1}{k_v}\ln\left(\frac{C_0}{C_x}\right)\right] = \frac{W_e W_b}{C_0 Q} - \frac{\rho W_e}{C_0 k_v}\ln\left(\frac{C_0}{C_x}\right) \qquad \text{(Eq. 1.27)}$$

Where $V_{b\text{-}x}$ is the breakthrough volume in liters, $t_{b\text{-}x}$ is in breakthrough in min, W_e is the adsorption capacity (g adsorbate/g adsorbent), W_b is the adsorbent bed mass (g), $\tau = W_b/(\rho Q)$ is the bed residence time (min), ρ is the adsorbent bed density (g/cm^3), Q is the volumetric flow rate (cm^3/min), k_v is the kinetic rate constant (min^{-1}), C_0 is the inlet concentration (g/cm^3), and C_x is the outlet concentration (g/cm^3). Typically, a 10% fraction breakthrough is accepted as the criteria for an exhaustive vapor trapping; ergo, the key performance parameters $t_{b\text{-}10}$ and $V_{b\text{-}10}$ are used in practical.

Estimates of the true (i.e., thermodynamic) W_e (i.e., $W_{e\text{-}th}$) can be obtained from theoretical adsorption isotherm models or from experimental measurements of equilibrium vapor uptake as a function of concentration. Estimates of the so-called kinetic W_e ($W_{e\text{-}k}$) can be obtained via Eq. (1.27) by measuring $t_{b\text{-}x}$ for a series of devices with different W_b values at a fixed Q or for a single device with fixed W_b tested over a range of Q values; plotting $t_{b\text{-}x}$ vs. either τ or W_b yields a line the slope of which is proportional to $W_{e\text{-}k}$.

1.5.3. Linear Solvation Energy Relationship

The interactions between vapors and sorbent materials can be quantified using the partition coefficient, K, which is the ratio of vapor concentration in the sorbent phase, C_s, to that in the gas phase, C_g, at the equilibrium: $K = C_s/C_g$. For adsorbents, C_s would be expressed as the ratio of vapor mass to adsorbent mass (rather than volume) and can be considered equivalent to W_e in Eq. 1.26 and Eq. 1.27 at least at very low concentrations where a quasi-linear isotherm (i.e., constant K) is typically assumed.

Linear solvation energy relationships (LSER), such as those developed by Abraham et al. are generally considered as the most comprehensive approach to modeling partitioning phenomena.[163,164] Its latest evolved equation is

$$log\ K = c + eE + sS + aA + bB + lL \qquad (\text{Eq. } 1.28)$$

where K is the partition coefficient of the solute (i.e. vapor) and solvent (i.e. adsorbent) at the equilibrium. The capital letters on the right side of the equation are solute descriptors: E, excess molar refraction; S, polarizability/dipolarity parameter; A, solute hydrogen bond acidity; B, solute hydrogen bond basicity; L, the log of the gas-hexadecane partition coefficient. It is important to note and understand that some of these descriptors have overlaps between them in accounting for the various interaction. The lower-case letters are coefficients that characterizes interactions between solute and solvent. e is for interactions of π electrons or lone-pair electrons; a represents hydrogen bonding basicity; b illustrates hydrogen bonding acidity; l interprets the dispersion forces and cavity formation. c is a regression constant comprising all other interactions that was not captured by the other terms in the equation and might be related to combinational entropy, free-volume effects, and interactional enthalpy.

Each production term in the LSER equation quantitatively describes one kind of the intermolecular interactions that contributes to the partitioning phenomenon between the solute and the solvent. For instance, *aA* quantifies the H-bonding interactions between H-donating solute and H-accepting solvent, and *bB* also computes the H-bonding interactions but in the opposite relationship with *aA*. The rest terms of *eE*, *sS*, and *lL* represent the interactions of π and lone electrons interactions, dipole-dipole and dipole-induced dipole interactions, cavity formation and dispersion interactions, respectively. It is important to note and understand that *eE*, *sS*, *lL* have overlaps among them in accounting for the various interactions.

1.6. Research Significance

This dissertation entails several projects which are independently conducted yet interrelated towards the development of μGC and its related technologies. The μVE in Chapter 2 expanded the μGC capability for airborne VOC analysis to the aqueous VOC determinations. The μVE-μGC is the first ever such microsystem for aqueous VOC determinations. The RTIL in Chapter 5 is capable of selectively enhancing the polar VOC adsorption and rejecting nonpolar VOCs. Both Chapter 2 and Chapter 5 improved VOC sampling techniques by developing a new microdevice and implementing new adsorbent materials, respectively. These techniques are directly related to μGC sampling technique development. The work in Chapter 3 and Chapter 4 is developing the state-the-art of the μGC instrument prototypes including the first ever belt-mountable μGC. The system design, operation, and characterization would provide insights and references for future μGC development to the whole μGC community.

1.7. Reference

(1) EPA. "Rule 102 Definitions." from https://www3.epa.gov/region02/air/sip/Amendments_Aug_29_2012.pdf.February, 2019.

(2) EPA. "Air Quality: Revision to the Regulatory Definition of Volatile Organic Compounds-Exclusion of 1,1,2,2-Tetrafluoro-1-(2,2,2-trifluoroethoxy) Ethane (HFE-347pcf2)." from https://www.federalregister.gov/documents/2016/08/01/2016-17790/air-quality-revision-to-the-regulatory-definition-of-volatile-organic-compounds-exclusion-of.

(3) European Parliament and of the Council. "Directive 2004/42/CE of the European Parliament and of the Council of 21 April 2004 on the limitation of emissions of volatile organic compounds due to the use of organic solvents in certain paints and varnishes and vehicle refinishing products and amend." Directive 1999/13/EC. from https://eur-lex.europa.eu/legal-content/EN/TXT/?uri=celex%3A32004L0042.

(4) EPA. "Technical Overview of Volatile Organic Compounds." from https://www.epa.gov/indoor-air-quality-iaq/technical-overview-volatile-organic-compounds.

(5)WHO. "Indoor air quality: organic pollutants." from www.euro.who.int/__data/assets/pdf_file/0009/128169/e94535.pdf.accessed February, 2019.

(6) Chin, J.-Y.; Godwin, C.; Parker, E.; Robins, T.; Lewis, T.; Harbin, P.; Batterman, S., *24*, 403–415.

(7) Park, M.-K.; Park, H.-J.; Lim, S.-J.; Um, T.-Y.; Park, M.-K.; Son, B.-S. *Journal of Odor and Indoor Environment* 2015, *14* 33–40.

(8) ACGIH. *Threshold Limit Values for Chemical Substances and Physical Agents & Biological Exposure Indices* 2018.

(9) OSHA. "OSHA Annotated Table Z-1." from https://www.osha.gov/dsg/annotated-pels/tablez-1.html.accessed March 2019.

(10)NOISH. "NIOSH Manual of Analytical Methods." from http://www.cdc.gov/niosh/docs/2003-154/.

(11) OH. "Sampling and Analytical Methods." from https://www.osha.gov/dts/sltc/methods/.

(12) EPA. "Volatile Organic Compounds Emissions." from https://www.epa.gov/report-environment/outdoor-air-quality.

(13) Risticevic, S.; Niri, V. H.; Vuckovic, D.; Pawliszyn, J. *Analytical and Bioanalytical Chemistry* 2008, *393* 781–795.

(14) EPA. "National Primary Drinking Water Regulations." from https://www.epa.gov/ground-water-and-drinking-water/national-primary-drinking-water-regulations#Organic.

(15) Matsumura, K.; Opiekun, M.; Oka, H.; Vachani, A.; Albelda, S. M.; Yamazaki, K.; Beauchamp, G. K. *PLoS One* 2010, *5*.

(16) Potkay, J. A.; Magnetta, M.; Vinson, A.; Cmolik, B. *Lab on a Chip* 2011, *11* 2901.

(17) Quality, E. C. A. I. A. from http://www.inive.org/medias/ECA/ECA_Report19.pdf.1997.

(18) D. L. Rose, M. P. S., Methods of analysis by the U.S. Geological Survey National Water Qualit Laboratory -- Determination of volatile organic compounds in water by purge and trap capillary gas chromatography/mass spectrometry; U.S. Geological Survey Denver, Colorado, 1995.

(19) V. Safarovaa, S. S., E. Djazhenkob, G. Teplovaa, G. Shajdulinaa and F. Kudashevab. *Journal of Chromatography B* 2004, *800* 325-330.

(20) S. K. Golfinopoulos, T. D. L., A. D. Nikolaou. *Chemosphere* 2001, *45*, 275-284.

(21) K. F. Pratt, J. P. *Analytical Chemistry* 2002, *64*, 2107-2110.

(22) EPA. "Choosing an Adsorption System for VOC." from https://www3.epa.gov/ttncatc1/cica/other6_e.html.

(23) Health, N. I. f. O. S. a. "NIOSH Method 3704." from https://www.cdc.gov/niosh/docs/2003-154/pdfs/3704.pdf.

(24) Zhang, X.; Gao, B.; Creamer, A. E.; Cao, C.; Li, Y. 2017, *338*, 102–123.

(25) Li, M. S.; Wu, S. C.; Shih, Y. H. *Journal of Hazardous Materials* 2016, *315*, 35–41.

(26) Gallego, E.; Roca, F.; Perales, J.; Guardino, X. *Talanta* 2010, *81*, 916–924.

(27) Vellingiri, K.; Szulejko, J. E.; Kumar, P.; Kwon, E. E.; Kim, K.-H.; Deep, A.; Boukhvalov, D. W.; Brown, R. J. C., Metal organic frameworks as sorption media for volatile and semi-volatile organic compounds at ambient conditions; Scientific Reports 2016.

(28) Luebbers, M. T.; Wu, T.; Shen, L.; Masel, R. I. *Langmuir* 2010, *26*, 11319–11329.

(29) Giddings, J. C. *Unified separation science*; John Wiley & Sons: New York, 1991.

(30) SKC. "Adsorbent Tube Product Catalog." from https://www.skcinc.com/catalog/index.php?cPath=200000000_201000000_201000050_201000051.

(31) PerkinElmer. "ATD ST STL TUBE W/TENAX TA PK/10-N9307005." from http://www.perkinelmer.com/product/atd-st-stl-tube-w-tenax-ta-pk-10-n9307005.

(32) Payagala, T.; Zhang, Y.; Wanigasekara, E.; Huang, K.; Breitbach, Z. S.; Sharma, P. S.; Sidisky, L. M.; Armstrong, D. W. *Anal. Chem.* 2009, *81*, 160–173.

(33) Collin, W. R.; Bondy, A.; Dibyadeep, P.; Kurabayashi, K.; Zellers, E. T. *Anal. Chem.* 2015, *87*, 1630–1637.

(34) Regmi, B. P.; Chan, R.; Atta, A.; Agah, M. *J. Chromatogra A.* 2018, *1566*, 124-134.

(35) Foley, N. J.; Thomas, K. M.; Forshaw, P. L.; Stanton, D.; Norman, P. R. *Langmuir* 1997, *13*, 2083–2089.

(36) Technologies, A. "“How Wet Can You Get?” Water Injections in Capillary GC." from https://www.agilent.com/cs/library/eseminars/Public/water injections.pdf.

(37) Grob, K.; Habich, A. *J. High Resolut. Chromatogr.* 1983, *6*, 11–15.

(38) Bernier, U. R.; Bray, C. L.; Yost, R. A. *J. Microcolumn Sep.* 2000, *12*, 226–235.

(39) Portari, G. V.; Marchini, J. S.; Jordão, A. A. 2007, *39*, 42–45.

(40) Tipler, A. "An Introduction to Headspace Sampling in Gas Chromatography." from http://www.perkinelmer.com/PDFs/downloads/GDE_Intro_to_Headspace.pdf.

(41) Poole, C. F. *Gas chromatography*; Elsevier: Oxford, 2012.

(42) Demeestere, K.; Dewulf, J.; DeWitte, B.; Van Langenhove, H. *J. Chromatogr. A* 2007, *1153*, 130–144.

(43) Pawliszyn, J. *Solid Phase Microextraction; Theory and Practice*; Wiley-VCH: New York, 1997.

(44) Eyes-Garcés, N.; Gionfriddo, E.; Gómez-Ríos, G. A.; Alam, M. N.; Boyacı, E.; Bojko, B.; Singh, V.; Grandy, J.; Pawliszyn, J. *Anal. Chem.* 2017, *90*, 302–360.

(45) Zhang, Z. Y.; Yang, M. J.; Pawliszyn, J. *Anal. Chem.* 1994, *66*, 844A–853A.

(46) Spietelun, A.; Pilarczyk, M.; Kloskowski, A.; Namieśnik, J. *Chemical Society Reviews* 2010, *39*, 4524.

(47) Hoch, G.; Kok, B. *Archives of Biochemistry and Biophysics* 1963, *101*, 160–170.

(48) Lauritsen, F. R.; Kotiaho, T. *Reviews in Analytical Chemistry* 1996, *15*.

(49) Krogh, E. T.; Gill, C. G. *Journal of Mass Spectrometry* 2014, *49*, ii-ii.

(50) Kotiaho, T.; Lauritsen, F. R. *Sampling and Sample Preparation for Field and Laboratory Comprehensive Analytical Chemistry* 2002, 531–557.

(51) Dewulf, J.; Langenhove, H. V.; Wittmann, G. *TrAC Trends in Analytical Chemistry* 2002, *21*, 637–646.

(52) Rahman, M. A. M.; Abd, E.; Choi, J.; Shin, H.; Shin, S. C.; J., S. *Analytical Separation Science* 2015, 823–834.

(53) Poole, C. F. *The essence of chromatography*; Elsevier: Amsterdam, 2010.

(54) Purcaro, G., Raymond P., Scott W. *Analytical and Bioanalytical Chemistry* 2018, *410*, 6689–6690.

(55) James, A. T.; Martin, A. J. P.; Smith, G. H. *Biochemical Journal* 1952, *52*, 238–242.

(56) Dettmer-Wilde, K. *Springer* 2014.

(57) Deemter, J. V.; Zuiderweg, F.; Klinkenberg, A. *Chemical Engineering Science* 1956, *5*, 271–289.

(58) Davis, J. M.; Giddings, J. C. *Analytical Chemistry* 1983, *55*, 418–424.

(59) Science, G. "Sample introduction in capillary gas chromatography." from https://www.glsciences.eu/optic/gc-injections-manual.pdf.

(60) *Analytical Chemistry* 1964, *36*, 31A-41A.

(61) Watson, D. W. "LCGC: The Secrets of Successful Temperature Programming." from http://www.chromatographyonline.com/secrets-successful-temperature-programming.

(62) "The Power of Gas Chromatography." from https://blog.sepscience.com/gaschromatography/gc-solutions-4-the-power-of-gc-detectors.

(63) Technology, S. "Accusense Chemical Recognition System ". from http://www.seertechnology.com/accusense.2017.

(64) INFICON. "Micro GC Fusion Gas Analyzer." from http://products.inficon.com/en-us/nav-products/Product/Detail/Micro-GC-Fusion-Gas-Analyzer?pathProducts%2FpgChemicalDetection.

(65) Technologies, D. "Hand Held Gas Chromatography." from www.defiant-tech.com.

(66) Technology, E. S. "zNose® Portfolio ". from http://www.estcal.com/products.

(67) Technologies, G. "Portable DX4040 FTIR Gas Analyzer." from http://www.gasmet.com/products/portable-gas-analyzers/dx4040.

(68) INFICON. "HAPSITE® ER Chemical Identification System." from http://products.inficon.com/en-us/Product/Detail/HAPSITE-ERIdentification-System?path=Products%2Fpg-ChemicalDetection.

(69) FLIR. "Griffin G510." from http://www.flir.com/G510/.

(70) Terry, S. C.; Jerman, J. H.; Angell, J. B. *IEEE Trans. Electron. Devices* 1979, *26*, 1880–1886.

(71) Kolesar, E. S.; Reston, R. R. *IEEE Trans. Compon. Packag. Manuf. Technol.* 1998, *21*, 324–328.

(72) S. Reidy, G. L., J. Reece, R. Sacks,. *Anal. Chem.* 2006, *78*, 2623-2630.

(73) J. Lu, J. W., R. D. Sacks, E. T. Zellers. *Anal. Chem.* 2003, *75*, 1400-1409.

(74) C-J. Lu, W. H. S., W. C. Tian, M.C. Oborny, J.M. Nichols, M. Agah, J.A. Potkay, H.K.L. Chan, J. Driscoll, R.D. Sacks, K.D. Wise, S. W. Pang, E.T. Zellers. *Lab on Chip* 2005, *5*, 1123-1131.

(75) Q. Zhong, W. S., E. T. Zellers. *Analyst* 2009, *134*, 283-293.

(76) S. K. Kim, H. C., E. T Zellers. *Anal. Chem.* 2011, *83*, 7198-7206.

(77) S. K. Kim, D. R. B., H. Chang, J. Bryant-Genevier, and E. T. Zellers. *Env. Sci. and Tech.* 2012, *46*, 6065-6072.

(78) W. R. Collin, G. S., L. K. Wright, H. Chang, N. Nuñovero, E. T. Zellers. *Anal. Chem.* 2013, *86*, 655-663.

(79) W. Collin, A. B., D. Paul, K. Kurabayashi, E. T. Zellers. *Anal. Chem.* 2015, *87*, 1630-1637,.

(80) Qin, Y.; Gianchandani, Y. B. 2016, *2*, 15049.

(81) Lee, J.; Zhou, M.; Zhu, H.; Nidetz, R.; Kurabayashi, K.; Fan, X. *Anal. Chem.* 2016, *88*, 10266−10274.

(82) Garg, A.; Akbar, M.; Vejerano, E.; Narayanan, S.; Nazhandali, L.; Marr, L. C.; Agah, M. *Sens. Actuators, B* 2015, *212*, 145−154.

(83) Akbar, M.; Shakeel, H.; Agah, M. *Lab on Chip* 2015, *15*, 1748–1758.

(84) Akbar, M.; Restaino, M.; Agah, M. 2015, *1*.

(85) G. Frye-Mason, R. K., P. Lewis, E. Heller, R. Manginell, D. Adkins, G. Dulleck, D. Martinez, D. Sasaki, C. Mowry, C. Matzke, L. Anderson,. In *Proc. Micro Total Analysis Systems Workshop*: Enschede, Netherlands, 2000, pp 229-232.

(86) P.R. Lewis, R. P. M., D.R. Adkins, R.J. Kottenstette, D.R. Wheeler, S.S. Sokolowski, D.E. Trudell, J.E. Bymes, M. Okandan, J.M. Bauer, R.G. Manley, G.C. Frye-Mason,. *IEEE Sensors J.* 2006, *6*, 784-795.

(87) S. Zampolli, I. E., F. Mancarella, P. Betti, E. Dalcanale, G. C. Cardinali, M. Severi,. *Sens. Actuator, B Chemical.*, *141*, 322-328.

(88) A.D. Radadia, R. D. M., R.I. Masel, M.A. Shannon. *Anal. Chem.* 2009, *81*, 3471–3477.

(89) D. Radadia, A. S.-K., R. I. Masel, M. A. Shannon,. *Sens. Actuators, B Chemical* 2010, *150*, 456-464.

(90) A. Bhushan, D. Y., D. Trudell, E. B. Overton, J. Goettert. *Microsyst. Technol.* 2007, *13*, 361-368.

(91) APIX Analytics, P. from https://www.apixanalytics.com/.

(92) Zebra Analytix, I., Technolgy. from https://zebraanalytix.com/technology/

(93) Nanova Environmental Inc. "Products." from https://www.nanovaenv.com/.

(94) Inc., O. "Homepage." from https://omniscent.com/.

(95) Bruns, M. W. *Erdol Kohle Erdgas Petrochemie* 1994, 80–84.

(96) Cagliero, C.; Galli, S.; Galli, M.; Elmi, I.; Belluce, M.; Zampolli, S.; Sgorbini, B.; Rubiolo, P.; Bicchi, C. . *J. Chromatogr. A.* 2016, *1429*, 329–339.

(97) Lehmann, U.; Krusemark, O.; Muller, J.; Vogel, A.; Binz, D. *In Proceeding of the Micro TAS.* 2000, 167–170.

(98) Dziuban, J. A.; Mroz, J.; Szczygielska, M.; Ma»achowski, M.; Gorecka- Drzazga, A.; Walczak, R.; Bua, W.; Zalewski, D.; Nieradko, L.; Lysko, J.; Koszur, J.; Kowalski, P. *Sens. Actuators B.* 2004, *115*, 318–330.

(99) Nachef, K.; Marty, F.; Donzier, E.; Bourlon, B.; Danaie, K.; Bourouina, T. *J. Microelectromech. Chem.* 2012, *21*, 730–738.

(100) Tian, W.-C.; Chan, H.; Lu, C.-J.; Pang, S.; Zellers, E. T. *Journal of Microelectromechanical Systems* 2005, *14*, 498–507.

(101) Bryant-Genevier, J.; Zellers, E. T. *Journal of Chromatography A* 2015, *1422*, 299–309.

(102) Seo, J. H.; Kim, S. K.; Zellers, E. T.; Kurabayashi, K. *Lab on a Chip* 2012, *12*, 717.

(103) Cui, Z. *Springer* 2015, 68−73.

(104) C.M. Yu, M. L., J.C. Koo, P. Stratton, T. DeLima, E. Behmeyer,. In *Proceedings of the ASME Micro-Electro-Mechanical Systems*: Anaheim CA, 1998, pp 481–486.

(105) S. Ali, M. A.-K., L.T. Taylor, M. Agah. *Sens. Actuators B: Chem.* 2009, *141*, 309–315.

(106) M. Agah, J. A. P., J.A. Driscoll, R.D. Sacks, M. Kaviany, K.D. Wise. In *Proceedings of the Transducers'03, USA, June 8–12*, 2003.

(107) Potkay, J., et al. *Microelectromechanical Systems* 2007, *16.5*, 1071-1079.

(108) M. Agah, J. P., A. Elstro, G. Lambertus, R. Sacks, K.D. Wise. In *Tech. Digest, North American Solid-State Sensors, Actuators, and Microsystems Workshop*: Hilton Head, SC, USA, June 6.

(109) M. Agah, J. A. P., G.R. Lambertus, R.D. Sacks, K.D. Wise. *IEEE J. Microelectromech. Syst.* 2005, *14*, 1039–1050.

(110) J.A. Potkay, G. R. L., R.D. Sacks, K.D. Wise. *J. Microelectromech. Syst.* 2007, *16*, 1071–1079.

(111) Shakeel, H., and Masoud Agah. *Microelectromechanical Systems* 2013, *22.1*, 62-70.

(112) Shakeel, H., et al. *Sensors and Actuators B: Chemical* 2015, *216*, 349-357.

(113) Z.J. Lin, N. N., J.Q. Wang, R. Nidetz, S. Buggaveeti, K. Kurabayashi, E.T. Zellers. *Sens. Actuators B-Chem.* 2018, *254*, 561–572.

(114) H.S. Noh, P. J. H., G.C. Frye-Mason. *J. Microelectromech. Syst.* 2002, *11*, 718–725.

(115) H. Yuan, X. S. D., H.L. Tai, Y. Li, X.L. Zhao, P.F. Guo, X. Yang, Y.J. Su, Z.S. Xiong, M. Xu,. *Sens. Actuators B-Chem.* 2017, *239*, 304–310.

(116) U.S. Patent 7,273,517, September 25, 2007.

(117) Iwaya, T.; Akao, S.; Sakamoto, T.; Tsuji, T.; Nakaso, N.; Yamanaka, K. *Jpn. J. Appl. Phys.* 2012, *51*, 07GC24.

(118) Noh, H.-S.; Hesketh, P. J.; Frye-Mason, G. C. *J. Microelectromech. Syst.* 2002, *11*, 718−725.

(119) Zareian-Jahromi, M. A.; Ashraf-Khorassani, M.; Taylor, L. T.; Agah, M. *J. Microelectromech. Syst.* 2009, *18*, 28−37.

(120) Regmi, B. P.; Chan, R.; Atta, A.; Agah, M. *J. Chromatogr. A* 2018, *1566*, 124.

(121) Read, D.; Sillerud, C. H. In *Sandia Report SAND2016-0706*; Sandia National Laboratories (SNLNM): Albuquerque, NM, 2016.

(122) Cruz, D.; Chang, J.; Showalter, S.; Gelbard, F.; Manginell, R.; Blain, M. *Sens. Actuators, B* 2007, *121*, 414−422.

(123) Kaanta, B. C.; Chen, H.; Zhang, X. *J. Micromech. Microeng.* 2010, *20*, 055016.

(124) Technologies, A. "490 Micro GC System." from https://www.agilent.com/en/products/gas-chromatography/gc-systems/490-micro-gc-system.

(125) Zimmermann, S.; Wischhusen, S.; Müller, J. *Sens. Actuators, B* 2000, *63*, 159−166.

(126) Hayward, T. C.; Thurbide, K. B. *J. Chromatogr. A* 2008, *1200*, 2−7.

(127) J. Kim, B. Bae, J. Hammonds, T. Kang, M. A. Shannon, *Sens. Actuators, B* 2012, *168*, 111−117.

(128) J, Wang , C, Duan, Y. Guan *Talanta.* 2010, *82*, 1022-1026.

(129) X. Zhu, Z. Ning, Y. Zhang, J. Liu. *Review of Scientific Instruments 87* 2016, 044102.

(130) Sun, J. Guan, F. Cui, D. Chen, X. Zhang, L. Chen, J. *Sens. Actuators, B* 2013, *188*, 513−518.

(131) Narayanan, S.; Rice, G.; Agah, M. *Sens. Actuators, B* 2015, *206*, 190−197.

(132) H Zhu,. M. Zhou, Lee, J. R. Nidetz, K. Kurabayashi, X. Fan, *Anal. Chem.* 2016, *88*, 8780−8786.

(133) P. J. Chapman, F. V., P. Dutta, P. G. Datskos, G. L. Devault, and M. J. Sepaniak. *Anal. Chem.* 2007, *79*, 364–370.

(134) M. Li, E. M., H. X. Tang, S. J. Aldridge, H. C. McCaig, J. J. Whiting, R. J. Simonson, N. S. Lewis, and M. L. Roukes. *Nano Lett.* 2010, *10*, 3899–3903.

(135) L. Han, X. S., W. Wu, F. L. Kirk, J. Luo, L. Wang, D. Mott, L. Cousineau, S. I. I. Lim, S. Lu, C. J. Zhong. *Sens. Actuators B Chem.* 2005, *106*, 431–441.

(136) Y. Joseph, A. P., X. Chen, J. Michl, T. Vossmeyer, and A. Yasuda. *J. Phys. Chem. C* 2007, *111*, 12855–12859.

(137) E. Dovgolevsky, U. T., and H. Haick. *Small* 2009, *5*, 1158–1161.

(138) Rehman, A., et al. *Analytical chemistry* 2011, *83.20*, 7823-7833.

(139) Liu, J., et al. *Analytical chemistry* 2010, *82.11*, 4370-4375.

(140) K. Scholten,, X.Fan, and Edward T. Zellers. *Applied physics letters* 2011, *99.14*, 141108.

(141) Scholten, K., et al. *Nanoscale* 2015, *7.20*, 9282-9289.

(142) Collin, W. R., et al. *Analyst* 2015.

(143) C. Jin, P. K., A. Hierlemann, E. T. Zellers. *Anal. Chem.* 2008, *80*, 227-236.

(144) J. Park, W. A. G., E. T. Zellers. *Anal. Chem.* 1999, *71*, 3877-3886.

(145) M. D. Hsieh, E. T. Zellers. *Anal. Chem.* 2004, *76*, 1885-1895.

(146) M. D. Hsieh, E. T. Zellers. *J. Occup. Environ. Hyg.* 2004, *1*, 149-160.

(147) J Bryant-Genevier, K. S., SK Kim, ET Zellers. *Sensors and Actuators B: Chemical*, *202*, 167-176.

(148) S. M. Rappaport, L. L. K. 2008.

(149) S. O. Hansson,; Oxford University Press: New York, 1999.

(150) J. S. Ignatio, W. H. B.; AIHA Press: Fairfield, VA, 2006.

(151) S. A. Roach, S. M. R. *Am. J. Ind. Med.* 1990, 727-753.

(152) G. D. Nielsen, L. H., P. Wolkoff. *Indoor Air* 1997, *7*, 17-32.

(153) C. Wild, *J. of Epid.* 2012, *41*, 24-32.

(154) S. Rappaport,*J. Expos. Sci. Environ. Epid.* 2011, *21*, 5-9.

(155) E. Hubal, *Tox. Sci.* 2009, *111*, 226-232.

(156) J. A. Potkay,*Biomedical Microdevices* 2007, *10*, 379–392.

(157) J. A. Potkay, *Lab Chip* 2014, *14*, 4122–4138.

(158) JAAN's Science Class, Differences between physisorption and chemisorption, http://jscienceclass.blogspot.com/2012/06/physisorption-and-chemisorption.html (accessed May 23, 2019)

(159) F. Rouquerol, J. Rouquerol, K. Sing. Adsorption by Powders and Porous Solids, 2nd edition, Elsevier, 2014.

(160) C.J. Lu, E.T. Zellers, *Anal. Chem*, 2001, *73*, 3449–3457.

(161) W.C. Tian, S.W. Pang, C.J. Lu, E.T. Zellers, *J. Microelectromech. S.* 2003, *12*, 264-272.

(162) S.T. Sukaew, E. T. Zellers, *Sens. Actuators B Chem.* 2013, *183*, 163-171.

(163) M. H. Abraham, A. Ibrahim, A. M. Zissimos, *J. Chromatogr. A* 2004, *1037* (1−2), 29−47.

(164) M. H. Abraham, W. E. Acree, *Sep Sci Technol.* 2013 *48*, 884-897.

Chapter 2 Bio-Inspired Microfabricated Vapor Extractor for On-Site Determinations of Aqueous Volatile Organic Compounds by Microfabricated Gas Chromatography

Adapted with permission from J.Wang et al., "Micro vapor extractor for on-site determinations of volatile organic compounds in water and biofluids," 19th International Conference on Solid-State Sensors, Actuators and Microsystems (TRANSDUCERS), pp.668-67, 18-22 June 2017, Kaohsiung, Taiwan, Copyright: 2017 IEEE.

2.1. Introduction

Volatile organic compounds (VOCs) are ubiquitous. Long-term exposure to VOCs can cause adverse health effects. The American Conference of Governmental Industrial Hygienists (ACGIH) has established exposure guidelines for individual VOCs in air and biological fluids to protect workers[1] and the US Environmental Protection Agency (EPA) has developed limits for VOCs in drinking water to protect the public.[2]

On-site analysis of VOC levels in liquid media facilitates assessments of water pollution, biomonitoring of exposures to toxic chemicals, and disease diagnosis. Traditionally, VOC extraction from aqueous media has entailed purge-and-trap, headspace sampling, or solid-phase microextraction (SPME) followed by analysis by GC with flame ionization detector (FID) or a mass spectrometer (MS).[3] Such approaches are not well suited for on-site analysis because of low extraction efficiencies, poor precision, or because the analysis system is too cumbersome.

Microscale gas chromatographic analysis systems (μGC) may represent a way to perform on-site analyses of aqueous VOCs more effectively due to their small size and portability, but an improved front-end extraction device is needed to transfer samples from the liquid phase to the gas phase in a manner that is compatible with μGC operation. A novel micro-purge extractor (μPE) device was reported recently,[4] but it suffered some shortcomings, such as non-quantitative extraction, low efficiency, long purge times, and large sample volumes.

The mcirofabricated vapor extractor (μVE) described here was modeled after microchannel artificial lung technology.[5] It has a sanwhich structure which liquid channels on one substrate and gas channel on ther substrate. A thin layer PDMS membrane in the between. By operating at the micro scale, diffusion distances are reduced, and surface-to-volume ratios are increased, thereby resulting in faster and more efficient VOC extraction. Further, the hydrophobic PDMS membrane employed minimizes the transfer of water vapor which can degrade separations and/or interfere with detection in GC systems.

Our group and others have developed several μGC prototypes over the past decade or so.[6-14] The prototype μGC used in this study was described in Chapter 3.[12] It includes the following core set of discrete Si-microfabricated devices: a dual-cavity micro-preconcentrator/focuser (μsampler) chip that quantitatively captures and injects VOCs in split/splitless mode; tandem μcolumn chips with PDMS wall coatings capable of temperature-programmed separations; and a detector chip consisting of an integrated array of four μchemiresistors (μCR) coated with different thiolate-monolayer protected gold nanoparticle (MPN) interface films that quantifies analyte masses and differentiates the analytes by virtue of the response patterns generated.

Here we describe first results from the μVE chip for VOC extraction from water and synthetic urine using a commercial GC-FID and the μGC described above. For μVE design and evaluation, we adapted a membrane-based diffusion model originally developed for in microchannel based artificial lungs.[15] Modeling, described in detail below, indicated that detectable quantities of typical VOCs could be extracted by the μVE from sub-mL sample volumes containing sub-ppm concentrations in a matter of seconds. Modeling was conducted to explore the μVE demensions and operating conditions with mutpile VOCs inludeing polar, intermediate polar and nonpoarl compounds. After summarizing the key design features, fabrication steps, and test

methods employed, we present results of tests aimed at optimizing the liquid and gas flow rates. We then show an analysis of 4 VOCs in spiked synthetic urine with the hybrid integrated μVE-μGC system. The hybrid μVE-μGC microsystem is the first such micro system to date and will permit rapid field/clinical analyses of water contaminants and urinary biomarkers of exposure and disease.

2.2. μVE Modeling

The μVE was inspired by artificial lung technology developed by Potkay.[5] The referenced artificial lung technology exhibits micron-scale liquid blood flow channels separated from gas flow channels by a 15 μm thick PDMS membrane. Driven by a partial pressure gradient, O_2 diffuses from the gas stream, through the membrane, and into the blood enriching it. For CO_2, the process is reversed but analogous. The described artificial lung achieved unpresented gas exchange efficiency through minimized, micron-scale diffusion distances and large surface-area-to-volume ratios for gas exchange.

Potkay also developed a simple, closed-form, mathematical model for gas exchange in microchannel artificial lungs to understand and describe O_2 and CO_2 exchange.[15] The partial pressure of O_2 in the blood along with the microchannel was modeled as:

$$PO2\ (x) = PO2_G + (PO2_0 - PO2_G)\, e^{\frac{x}{L_{O2}}} \qquad \text{(Eq. 2.1)}$$

$$L_{O2} = v \bullet H \bullet S_{B,O2} \bullet R_{D,O2} \qquad \text{(Eq. 2.2)}$$

$$R_{D,\,O2} = \frac{\delta_M}{P_{M,\,O2}} + \frac{\delta_B}{S_{B,O2} \bullet D_{B,O2}} \qquad \text{(Eq. 2.3)}$$

where, $PO2(x)$ is the partial pressure of oxygen a distance x from the beginning of the artificial channel, $PO2_G$ is the partial pressure of oxygen on the gas side of the device, $PO2_0$ is the partial pressure of oxygen at x=0, L_{O2} is the "critical length" for oxygen diffusion in the device, ν is the

average blood flow velocity in the artificial channels, H is the artificial capillary height, $S_{B,O2}$ is total effective solubility of oxygen, $R_{D,O2}$ is the total resistances to oxygen diffusion, δ_M is the membrane thickness, δ_B is the thickness of the blood side fluidic boundary layer, $P_{M,O2}$ is the permeability of the membrane to oxygen and $D_{B,CO2}$ is the total effective diffusivities.

In Potkay's artificial lung model, oxygen diffuses from the gas stream through the membrane and into the blood stream due to a partial pressure gradient. The μVE uses a structure similar to the artificial lung to extracts aqueous VOCs in a liquid phase through a membrane and into the gas phase. Concentration of the VOC is large in the liquid phase and small in the gas phase and this transport is driven by a concentration gradient (via diffusion). Thus, a model similar to Potkay's artificial lung model can be developed as follows. This model serves to understand the operation and trade-offs inherent in the microchannel device and is given by the following equations:

$$C_x = C_g + (C_i - C_g) e^{\frac{x}{L}} \qquad \text{(Eq. 2.4)}$$

$$L = v \bullet H \bullet S_W \bullet R_D \qquad \text{(Eq. 2.5)}$$

$$R_D = \frac{\delta_M}{P_M} + \frac{\delta_W}{S_W \bullet D_W} \qquad \text{(Eq. 2.6)}$$

Figure 2.1 is the conceptual diagram of μVE . Figure 2.1a shows the size view of channels in μVE and Figure 2.1b shows the concentration profie in the gas and liquid channels during extraction. For given VOC, C_x is the concentration of that VOC at a distance x from inlet port of the liquid channel, C_g is the VOC concentration in the gas channel, C_i is VOC concentration at liquid inlet port (i.e. x=0), L is the "critical length" for VOC diffusion in the device, V is the average liquid flow velocity in the liquid channel, H is the liquid channel height, S_W is the water solubility, R_D is the diffusion resistances, δ_M is the membrane thickness, δ_W is the boundary layer thickness on the

liquid channel, δ_M is the VOC permeability of the membrane and D_W is the VOC water diffusion coefficient.

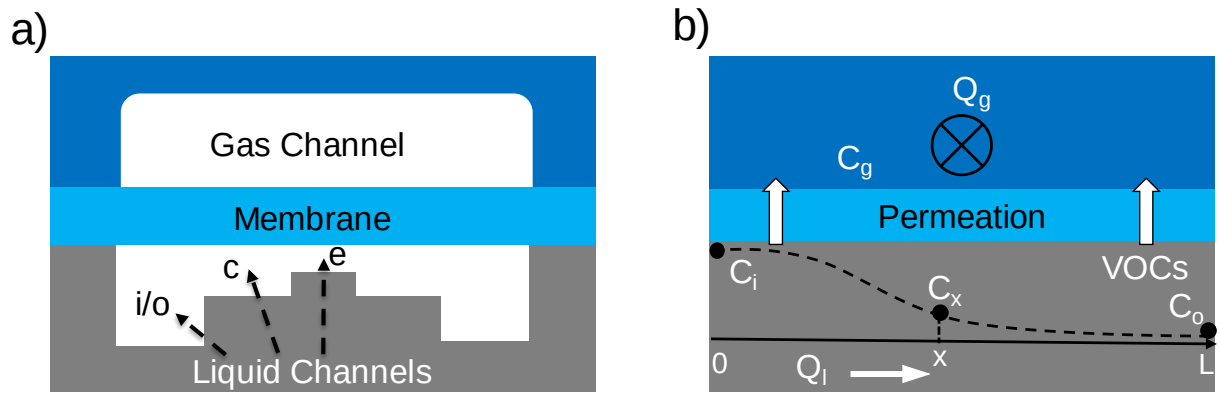

Figure 0.1. Side view concept diagram of the μVE with gas channels in the upper glass substrate and liquid channels in bottom Si separated by a thin PDMS diffusion membrane. The three liquid channels are: inlet/outlet channels (i/o), conduction channels (c), and extraction channels (e). b) The extraction process between liquid and gas channels and the conceptional VOC concentration profile along with the liquid channel.

Several parameters have been chosen to evaluate the performance of μVE regarding to the critical design parameters that describe the extraction performance of the device. These interesting parameter, the steady state extraction efficiency (*SSEE*), steady state permeation rate (*SSPR*), and time to steady state (*TTSS*).

$$SSEE=\frac{C_i-C_o}{C_i}\times 100\% \qquad \text{(Eq. 2.7)}$$

$$SSPR=C_i \bullet Q_l \bullet SSEE \qquad \text{(Eq. 2.8)}$$

Where, C_o is the VOC concentration at the outlet port of the liquid channel. Also,

$$Q_l=v \bullet w \bullet h \qquad \text{(Eq. 2.9)}$$

$$P_W=S_W \bullet D_W \qquad \text{(Eq. 2.10)}$$

$$A = w \bullet l \quad \text{(Eq. 2.11)}$$

$$K_{MW} = \frac{S_M}{S_W} \quad \text{(Eq. 2.12)}$$

Where Q is the liquid flow rate, W is the liquid channel width, P_W is the permeability of VOC in water, A is the total extraction area. K_{MW} is the VOC partition coefficient between membrane and water, S_M is the solubility in the membrane. By combing the equation 4-12, we had

$$SSEE = (1 - e^{-\frac{A}{Q_l \bullet (\frac{\delta_M}{D_M \bullet K_{MW}} + \frac{H}{2 \bullet D_W})}}) \times 100\% \quad \text{(Eq. 2. 13)}$$

$$SSPR = C_i \cdot Q_l \cdot (1 - e^{-\frac{A}{Q_l \bullet (\frac{\delta_M}{D_M \bullet K_{MW}} + \frac{H}{2 \bullet D_W})}}) \times 100\% \quad \text{(Eq. 2. 14)}$$

Four assumptions were also made for SSEE and SSPR modeling equations:

1. C_g=0. The VOC concentration in the gas stream is ~0 relative to the VOC in the liquid because of the fast sweep of the extracted vapor on the gas side.
2. . The fluidic boundary layer on the liquid side is the half of the channel height, which was previously proven as a reasonable approximation.[15]
3. VOC diffusion is unidirectional and only occurs from the liquid channels through the membrane and into the gas channel. There is no lateral diffusion in the membrane;
4. The VOC concentration in liquid only varies along the length of the liquid channels, not along with the liquid channel height or width.

The other parameter, time to steady state (TTSS) were also modelled by

$$TTSS = t_0 + 3 \cdot \frac{(H) \cdot K_{pw} \cdot \delta_m}{2 \cdot D_w} \quad \text{(Eq. 2.15)}$$

where t_0 is the time to fill the µVE liquid channels (µVE liquid channel volume divided by liquid flow rate) and the second component is the time for VOC diffusion through the liquid boundary layer and the membrane. It was discussed by Pawliszyn in this modeling equation which quantifies the time the VOCs diffuse from the liquid to the fiber of SPEM.[16]

2.2. Experimental

2.2.1. Materials

Toluene, 2-hexanone, n-butyl acetate, trichloroethylene and tetrachloroethylene were purchased from Sigma-Aldrich (St. Louis, MO) or Acros/Fisher (Pittsburgh, PA) in >99% purity. Water (HPLC grade) was obtained from Fisher (Pittsburgh, PA) and synthetic urine was from Ricca Chemical (Arlington, TX). Si and borofloat glass wafers were purchased from University Wafer.

2.2.3. µVE Fabrication

Figure 2.2 summarizes the process of the µVE fabrication and assembly. It has three main steps: 1) liquid and gas flow channel etching in silicon and glass substrates, respectively; 2) membrane formation; and 3) membrane and substrate bonding. There are three types of interconnected liquid microchannels etched in the lower Si substrate via a sequence of deep-reactive-ion etches: a) inlet/outlet (320 µm deep, 540 µm wide); b) conduction (50 µm deep, 80 µm wide); and, c) extraction channels (17 µm deep, 10 µm wide). The inlet/outlet and conduction channels are used to efficiently route (i.e. with a small pressure drop) the fluid to the extraction channels where the majority of vapor extraction occurs (due to the small diffusion distances). The etch masks used for the liquid microchannels in the Si substrate were photoresist (inlet/outlet channels), sputtered Cr (conduction channels), and SiO_2 (extraction channels). The upper

Borofloat 33 glass substrate was etched with HF using an LPCVD amorphous-Si mask to form the gas microchannel (320 µm deep, 640 µm wide). To form the thin diffusion membrane, liquid PDMS (Sylgard 184) was spun onto a thin and flexible, silanized PMMA substrate and cured. The membrane thickness was controlled by the spin speed. The exposed face of the membrane was irreversibly bonded to the Si (with formed liquid microchannels) after pre-exposing both the membrane and Si surfaces to an O_2 plasma (100 W, 40 s) and then merely pressing them together. The PMMA carrier was discarded and the plasma activation process was repeated to bond the other side of the membrane to the glass substrate. Devices were then diced, and fused-silica capillaries epoxied (Hysol 1C, Rocky Hill, CT) into the inlet/outlet ports for interconnection to other components. At every stage, metrology and microscopy was used to confirm patency and dimensions.

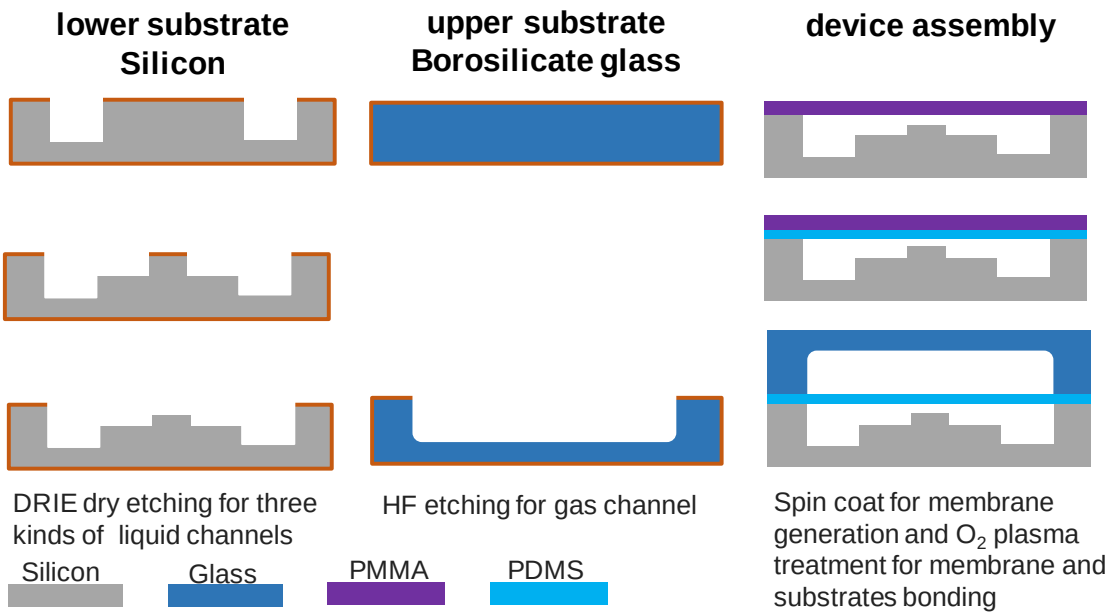

Figure 0.2. the the procedure of the µVE substrate fabrication, membrane generation and and the substrates assemble.

2.2.4. µVE operating condition optimization and performance characterization

Operating conditions for the µVE were optimized by interfacing to a gas chromatography-flame ionization detector (GC-FID) (Agilent 6890, Santa Clara, CA) equipped d with a 6-port valve with a 250 µL of sample loop (Figure A2.3). Aqueous samples were introduced to the µVE by a syringe pump (Fusion 100, Chemyx Inc, Stafford, TX) with a 25 mL of the gas-tight syringe. A female Luer adapters (Part No. ZLA-1, Valco Instruments Co. Inc, Houston, TX) was chosen to connect the syring pump with 12 inch of 1/16'' stainless steel tubing and reduced unit (Part No. ZU1T, Valco Instruments Co. Inc, Houston, TX was used to connect the 1/16'' tubing and glass capillary (I.D. 250 µm; O.D. 360 µm; Restek, Bellefonte, PA). A press-tight union was used to connect to the capillary emanating from the inlet port of µVE. A flask was placed at the other end to collect the liquid waste from the µVE. The µVE chip was placed in a metal enclosure which could be optionally heated with a resistive heater pad (Omega, Stamford, CT) and type K thermal couple (Omega, Norwalk, CT) to control and maintain a desired constant temperature in the range of 26 to 60 °C depending on the test. A thermal couple was placed inside the metal enclosure approximately 1 mm above to the µVE chip. The N_2 was chosen as the purge gas and N_2 flow rate was controlled through the second inlet of the GC-FID system. During µVE testing, N_2 gas flow from the outlet of the µVE was directed to a sampling loop via a 6-port valve. The sampling loop was then injected into GC-FID equipped with a 6-m PDMS coated commercial capillary column. The GC-FID was pre-calibrated with standards of each analyte in CS_2. The completed testing setup is shown in Figure 2.3.

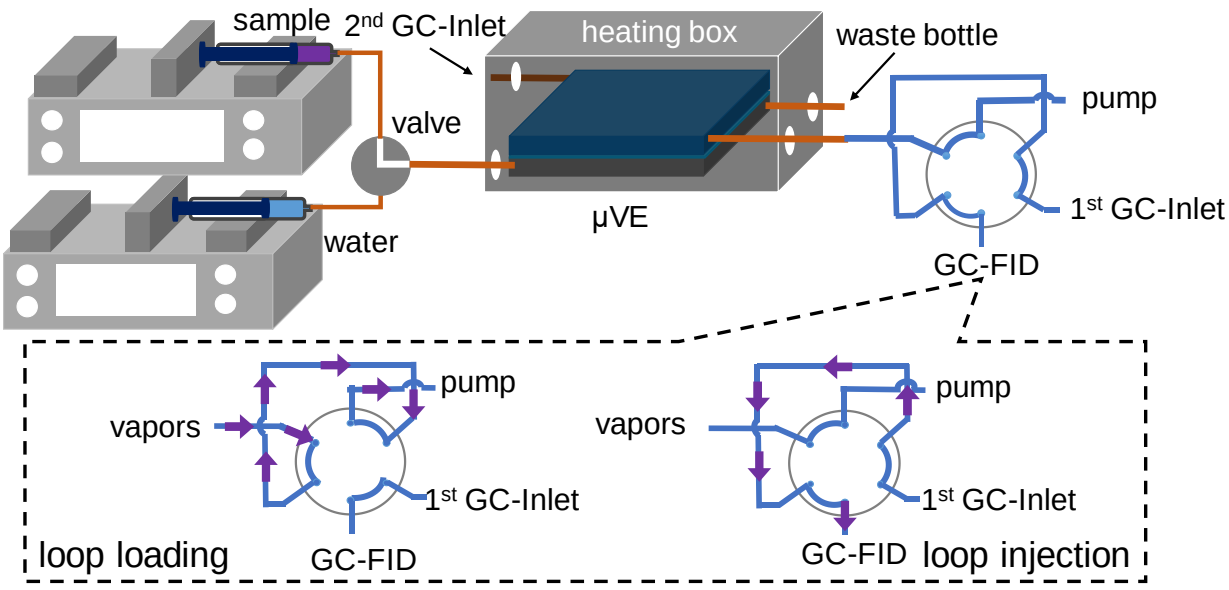

Figure 0.3. µVE operation condition optimization system with loop injection and GC-FID analysis.

2.2.5. General Operation of the µVE-µGC Microsystem

The µGC was used for testing was discribed in Chapter 3. It features a dual stage µpreconcentrator/focuser (µPCF) packed with 2.0 mg of Carbopack B (100 m^2/g) and 2.3 mg Carbopack X (240 m^2/g) to trap and thermally inject VOCs collected from µVE. 2 tandem 3-m PDMS wall coated µcolumns were used for mixture separations and VOCs are detected by a µchemiresistor array (µCR array) coated with differently functionalized monolayer-protected-nanoparticle (MPN) films were used for detection. The MPNs derived from the following thiols: n-octanethiol (C8), 6-phenoxyhexane- 1-thiol (OPH), isooctyl-3-mercapto-propionate (EOE), and methyl-6-mercaptohexanoate (HME). TEG was purchased from Nanoprobes, Inc. (Yaphank, NY, USA). The remaining MPNs were synthesized in house by known methods.[17,18] The prototype was controlled by a custom LabVIEW program on a laptop.

In the µVE-µGC microsystem. The output capillary from the µVE was connected to the inlet port of the µGC. During the sampling phase, a liquid pump delivered the liquid sample into

the liquid channel of the µVE at a fixed rate. Extracted vapors were transferred to the µPCF by the µGC mini pump at 5 mL/min. After transfer into µPCF, the pump was stopped, a mini valve (Model LHLA1221111H, Lee Company, Westbrook, CT) was thrown to the other end and the helium in the onboard canister was directed into the µPCF and µcolumns for VOC thermal injection and separation, respectively, at 3 mL/min. The µCR array at the output of µcolumn quantifies and identifies VOCs.

2.3. Results and Discussion

2.3.1. µVE Design and Fabrication

Table 0.1. Biological exposure indices (BEIs) in biological fluids and their vapor pressure values from ref. 19

Compound	BEI Information	Vapor Pressure (mm Hg) @ 25°C
acetone	25 mg/L in urine	230
n-hexane	0.4 mg/L of 2,5-hexanedione in urine	2,5-hexanedione: 1.6
methyl isobutyl ketone	1 mg/L in urine	19.9
methyl ethyl ketone	2 mg/ in urine	90.6
styrene	40 µg/L in blood	6.4
trichloroethylene	0.5 mg/L of trichloroethanol in blood	trichloroethylene:69; trichloroethanol: 1@ 20 °C
trichloroethylene	----- (SQ in blood)	69
tetrachloroethylene	0.5 mg/L in blood	18.5
tetrahydrofuran	2 mg/L in urine	162
toluene	0.02 mg/L in blood and 0.03 mg/L in urine	28.4

Some of the biological exposure indices (BEIs) in Table 2.1 were used to determine the key parameters and to guide the design of the μVE. A SSEE value of 90% was used as the minimum value to be able to perform (semi-)quantitative analyses in order to guide design choices. The mathematical model developed in Equations 2.4-2.15 above was used to investigate trade-offs in the design space using a subset compound in Table 2.1. Steady state extraction efficiency (SSEE) was calculated and plotted as a function of various design parameters including extraction channel area, extraction channel height, liquid flow rate, and liquid flow rate. Initial values for membrane thickness (δ_M = 15 μm) and extraction channel height (H = 10 μm) were taken from the previous artificial lung design from which this work was inspired (and which proved to be extremely efficient at extraction).5 As is apparent in Figure 2.4a, A large SSEE is desirable to ensure the ability to perform quantitative or semi-quantitative analyses. In Figure 2.4b and 2.4c , SSEE decreases with increasing liquid channel height and with increasing liquid flow rate.

Figure 2.4d shows the SSEE of polar acetone and nonpolar benzene calculated using Eq. 2.14 based on 1.6 cm2 of surface area and 15 μm of membrane thickness. For both acetone and benzene, device dimensions such as A and H, operating liquid flow rate Q_l affect *SSEE* in the similar fashion but SSEE of nonpolar benzene is universally larger than that of acetone. This is because VOC polarity had a great impact on the μVE extraction performance. In general, nonpolar compounds readily are absorbed into and diffuse through nonpolar PDMS. Thus, for these compounds, their performance is limited by their ability to diffuse through water. This was support by the modeling results is in Figure 2.5 , nonpolar compounds (for example, KPW >100 in Figure 2.5b) had a much higher SSEE than polar compounds (Kpw < 3 in Figure 2.5a). Additionally, A nonpolar compound with large water diffusivity (solid line, Figure 2.5) can achieve large extraction rates. However, a nonpolar compound with small water diffusion (dash line, Figure 2.5)

is limited in its extraction performance. For polar compounds, the opposite is generally true. Polar compounds do not readily absorb or diffuse into the PDMS membrane. Thus, the extraction performance of polar compounds is limited by their diffusivity in PDMS.

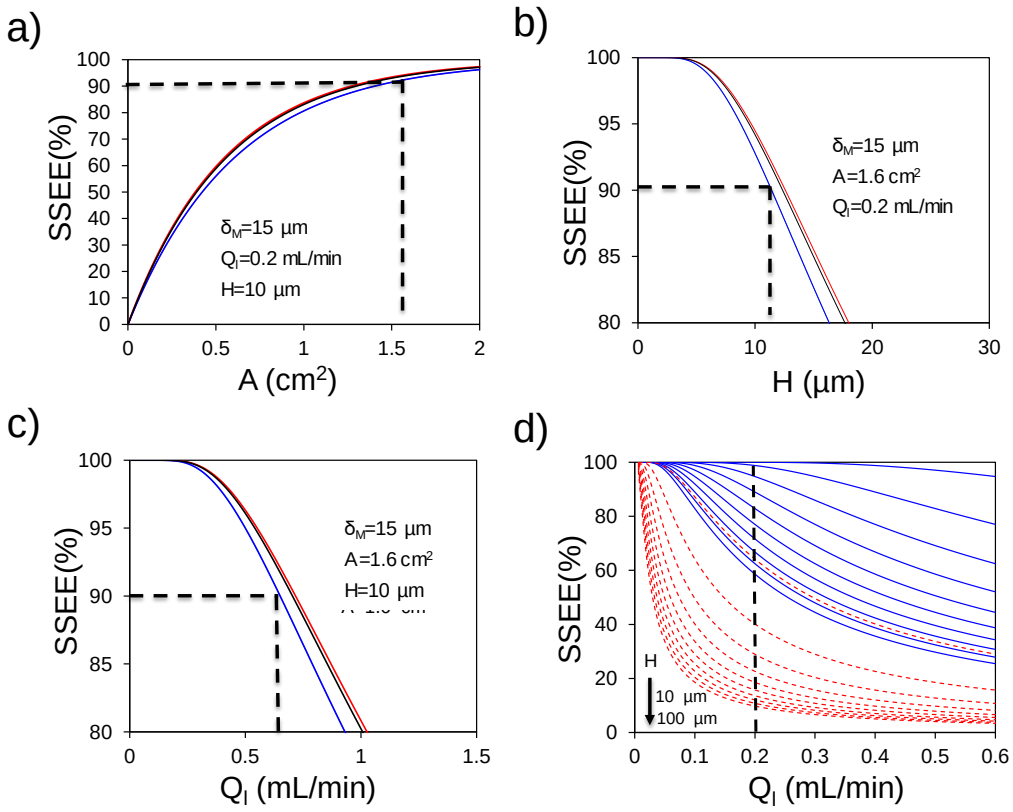

Figure 0.4. The modeled SSEE of benzene (blue solid line), toluene (red solid line) and p-xylene (black solid line) under the parameter of a) extraction surface area, A; b) liquid channel height, H, and c) liquid flow rate, Ql; the minimum of 90% of SSEE is used to select individual parameters for device fabrication and d) shows modeled SSEE of nonpolar benzene (solid blue line) and polar acetone (red dash line) under different liquid flow rate with A=1.6cm², H=15 µm.

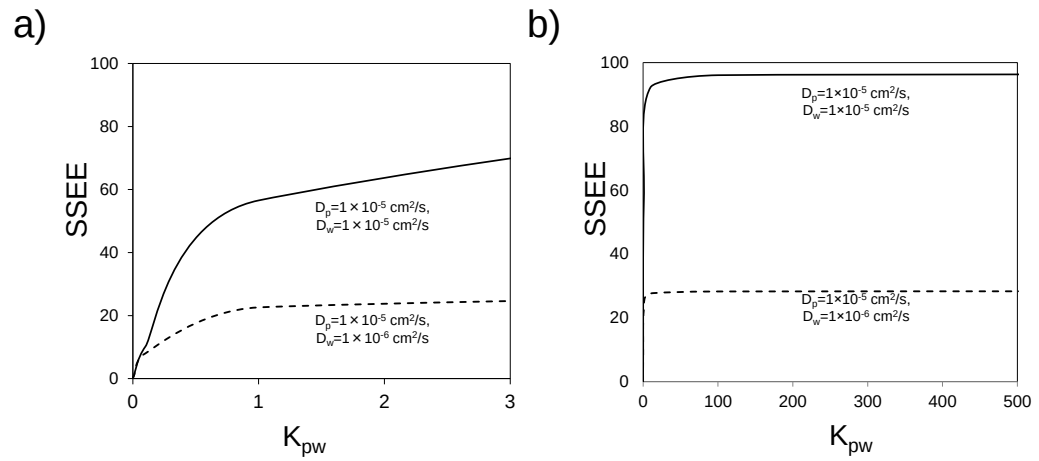

Figure 0.5. a) Polar compounds with K_{MW} <3, SSEE <80%; b) nonpolar compounds with K_{MW}>100, Dw affect SSEE significantly, and SSEE >90% for chemical with Dw at ~10^{-5} cm^2/s.

Using methanol (K_{MW}=*0.03*, D_W=*1.6×10^{-5} cm^2/s*, *DM*=1.9×10-5 cm2/s) as the exreme polar represntative, its theoretical extraction was analyzed as shown in Figure 2.6. It's apparent that the extraction performance of polar compounds can be increased by either using very thin membranes, for example, 0.15 µm, (see Figure 2.6a) or by using large extraction areas larger than 4 cm^2 (Figure 2.6b). However, using very thin membranes may compromise the robustness of the membrane. In fact, the artificial lungs on which this work is based used PDMS membranes with thicknesses greater than 15 µm to avoid issues with membrane rupture under pressure. In addition, large areas will increase the require device area on a silicon area, thereby increasing cost and fabrication time (through less devices per wafer).

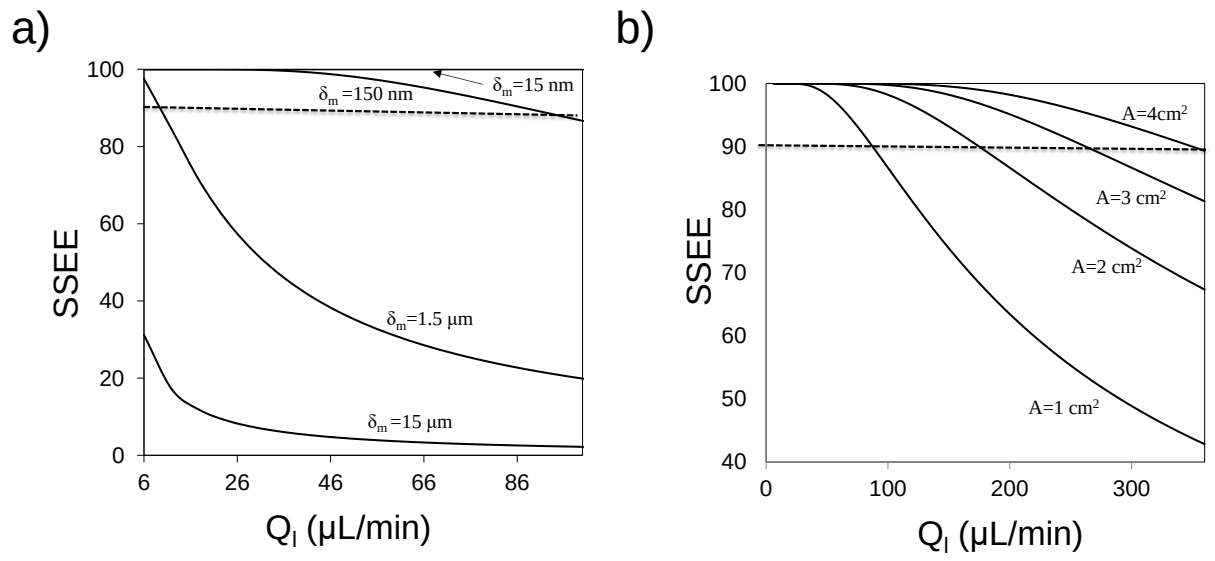

Figure 0.6.Theoretical µVE SSEE for polar compounds (Kpw < 3). a) 150 nm membrane with all other parameters kept the same as modeling or A>4 cm2 is needed for SSEE>90% with no changes of all other parameters.

Table 2.2 summarsied the modeled values of the key variables that determine the performance of the µVE after combing the modeling results in Figure 2.4 and many others in Appendix 1 (Table A1.2) and practical consideration. 90% SSEE was used to as the benchmark value defining a good extraction performance. Higher SSEE requries a smaller Q_1 which results in longer analysis time and a lower permeation rate. The larger of *A* surface area will produce a better extraction efficiency but it become impractical for the fabrication on a 4'' silicon wafer. A thinner PDMS membrane would also enhance the SSEE but it has to be mechanically strong enough to avoid the burst. The finally fabricated devices physical parameters were summarized in Table A1.1 (Appendix 1). Previous experience on artificial lung has been taken as the starting point of the µVE design. To determine the liquid channel height, 1.6 cm2 and 15 µm PDMS membrane have been borrowed from artificial lung design.[5] The modeling results in was used to help determined the liquid channel and membrane thickness. All channels were etched as previously designed

except extraction channels which was over-etched resulting in a depth of 17 µm instead of 10 µm. The 15, 30, and 100 µm thick membranes were generated, but the 15 µm devices were damaged during assembly. The final devices were used for testing is either 30 µm or 100 µm with the total extraction surface of 1.4 cm^2. The extraction area is is close to the model value of 1.6 cm^2.

Table 0.2. Determined target parameters for µVE fabrication and the optimized liquid flow rate.

Variables	Determined Values
Extraction Area (A)	1 cm^2
Flow Rate (Q_l)	0.36 mL/min
Channel Height (H)	10 µm
PDMS Thickness (δ_M)	15 µm

Figure 2.5a shows the picture of two fabricated substrates: Si substrates etched with liquid channels, and glass substrate etched one gas channel. Figure 2.5b was the picture of the fully assembled µVE and Figure 2.5cand d are SEM images of channels and PDMS membranes.

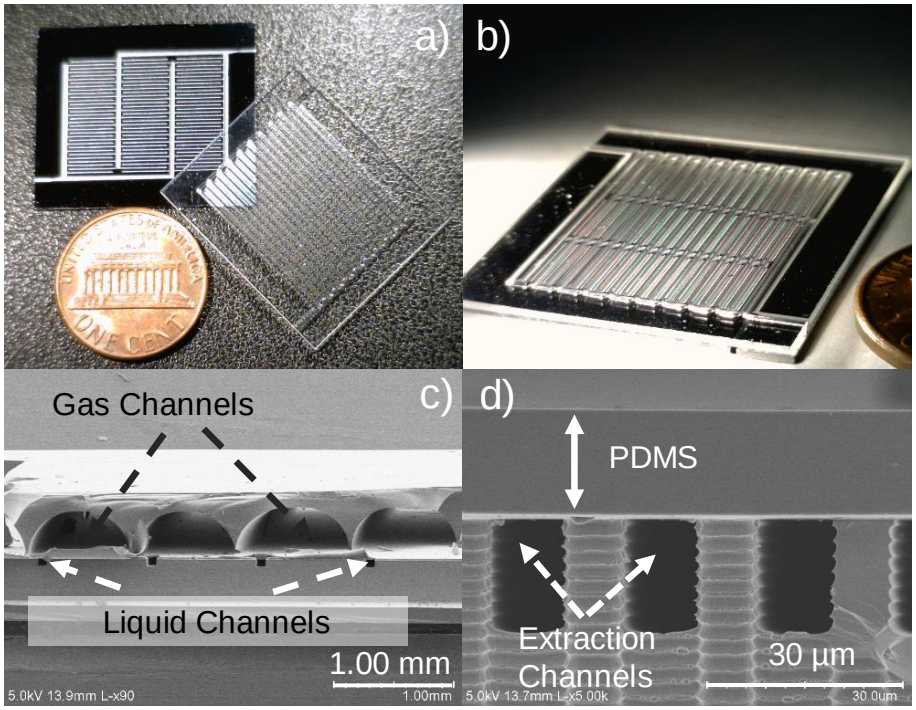

Figure 0.7 a) fabricated substrates with tched channels; b) fully assembled µVE; SEM of c) gas channels (320 µm (h), 640 µm (w)); d) extraction channels (17 µm (h), 10 µm (w) and PDMS membrane (15 µm).

2.3.2. Chemical Targets

Table 2.3are the subset of VOCs from Table 2.1 that were used in this study with additional relevant physical parameters. VOCs in Table 2.3 spans a range of polarity (water solubility) and volatility, and their modeled SSEE were aslo reported.

Table 0.3.Target VOCs and their BEIs and relevant physical parameters.

Compounds	BEI (ppm)	p_v (torr)[b]	S_w (mg/L)[c]	D_w (cm^2/s)[d]	D_p (cm^2/s)[e]	K_{pw}[f]	SSEE (%)
methyl ethyl ketone	2 (urine)	90.0	2.2×10^{5}	9.8×10^{-6}	7.6×10^{-6}	0.79	66
tetrachloroethylene	0.5 (blood)	18.5	2.06×10^{2}	8.2×10^{-6}	1.1×10^{-6}	1862	91
toluene	0.03 (urine)	28.4	5.26×10^{2}	8.6×10^{-6}	1.2×10^{-6}	189	90
trichloroethylene	---- (blood)[a]	69	1.28×10^{3}	9.1×10^{-6}	1.4×10^{-6}	174	91

[a]TCE BEI is confirmatoiry only (no specific value). [b] p_v, ref. 19, 20; [c] S_w, ref. 21; [d]D_w, ref.22,23, [e]K_{pw}: ref. 24, 25. All physical parameters are at 25 °C.

2.3.4. µVE Operating Condition Optimization with GC-FID System

2.3.4.1. Gas Flow Rate Optimzation

Figure 2.8 showed the gas flow rate effect on SSPR. The gas flow rate was first investigated by varying gas flow rate from 2-10 mL/min while keep the liquid flow rate at the constant 0.36 mL/min as the modeling suggested. Both devices with 30 µm and 100 µm thick membrane were evaluated. Figure 2.8 shows their SSPR of toluene (5 ppm) under N_2 gas flow rate (Q_g) from 2-10 mL/min. The SSPR for TOL increased from 2-4 mL/min with the increase of the gas flow rate and reached the plateau at flow rate >4 mL/min. 2 mL/min for thinner membrane device was not tested by the suggestion of the inefficient purge for the thicker membrane at this low flow rate. For both device, the steady state could be reached by a >4 mL/min N_2 flow. Thus, 6 mL/min of gas flow was chosen for the subsequence testing.

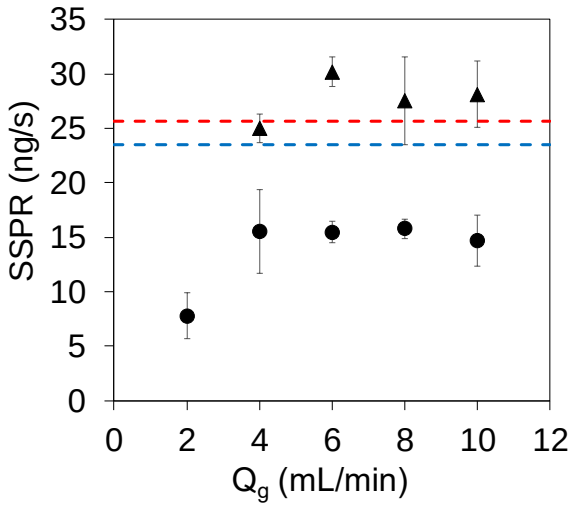

Figure 0.8. SSE SSPR of toluene (5ppm) increased with the gas flow rates from 30 µm to 10 µm. liquid flow rate is 0.36 mL/min and the temperature was 23°C.

The average SSPR of TOL were 28.6 ng/s and 15.4 ng/s, respectively, for 15 µm and 100 µm membrane device. The modeled SSPRs were highlighted with the dash lines with the red one for 30 µm membrane and the blue one for 100 µm membrane. As the figure shows, SSPR from 30 µm membrane is 11.5% higher than the modeled value, 25.7 ng/s, while SSPR from 100 µm membrane device was 34.6% lower than the modeled number 2.36 ng/s.

2.3.4.2 Liquid Flow Rate Optimzation

Figure 2.9 a and b showed The effect of liquid flow rate on TTSS and SSPR was evaluated at 23 ºC, respectively. For TOL, TTSS did not vary significantly with flow rate whereas for the polar BAC and 2-HEX, TTSS values decreased at higher liquid flow rates. In the 0.1-0.4 mL/min range, SSPR increased with flow rate up to 0.3 mL/min and then reached a plateau for all three VOCs. As mentioned above, we speculate that the SSPR is dictated primarily by solubility in the PDMS membrane. As the liquid flow rate increases, the amount of VOC supplied to the chip increases. At some flow rate, the VOC delivery rate exceeds the permeation rate. Above that flow rate (~0.3mL/min), SSPR reaches a constant value.

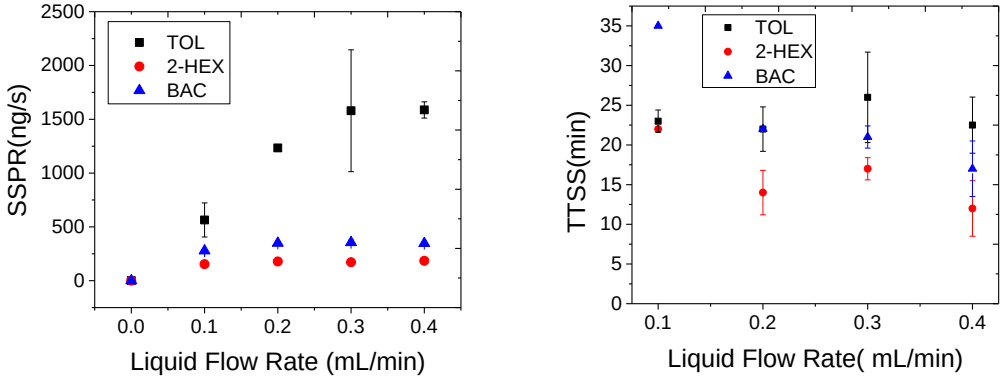

Figure 0.9. Liquid flow effect on a) SSPR and b) TTSS of 3 VOCs from 0.1-0.4 mL/min. Gas flow rate was kept at the constant 4 mL/min for the tests.

2.3.4.3. Temperature Effect

Figures 2.10a and b show the effects of temperature on µVE performance in terms of TTSS and steady state permeation rate (SSPR), respectively. For all three VOCs, TTSS decreased and SSPR increased with increasing temperature. At room temperature (23 ºC), TTSS values decreased in the order TOL > BAC > 2-HEX. The TTSS values and the differences in TTSS among the VOCs decreased with increasing temperature, converging at 5 min at 60 °C. Values of SSPR also decreased in the order TOL > BAC > 2-HEX. The SSPRs of BAC and 2-HEX did not increase significantly beyond 50 ºC while the SSPR of TOL continued to increase up to 60 °C.

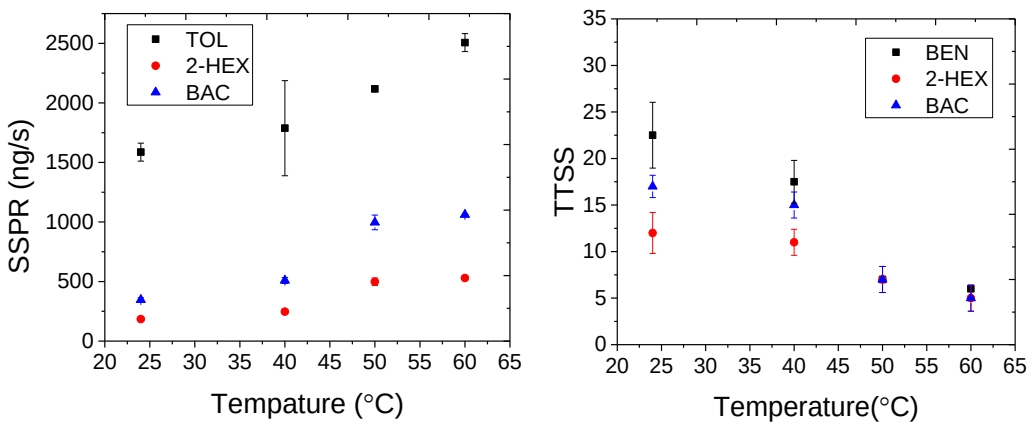

Figure 0.10. Temperature effect on a) SSPR and b) TTSS of the TOL, 2-Hex and BAC.

Figure 2.11 shows GC-FID measurements of the extraction profiles of a solution of toluene (TOL), 2-hexanone (2-HEX), and butyl acetate (BAC) in water (50 ppm each) collected from a µVE with a 30 µm PDMS membrane at 50 °C. These VOCs span a range of polarities (polarity index: 2.4 for TOL; 4.0 for BAC; 4.5 for 2-HEX),[25,26] vapor pressures (pv in kPa at 25ºC TOL, 3.78; BAC, 1.53; 2-HEX, 1.46),[27] and PDMS:water partition coefficient (K_{pw}: TOL, 174; BAC, 46; 2-HEX, 7).[17d] The liquid flow rate was 0.4 mL/min and the N_2 collection flow rate was 6 mL/min. As shown, the time to steady state (TTSS) was ~5-7 min for all VOCs, which is faster than reported for VOCs extracted with SPME (0.25 to 5 hr)[28] and the previously cited µPE technology (≥ 21 min).[4]

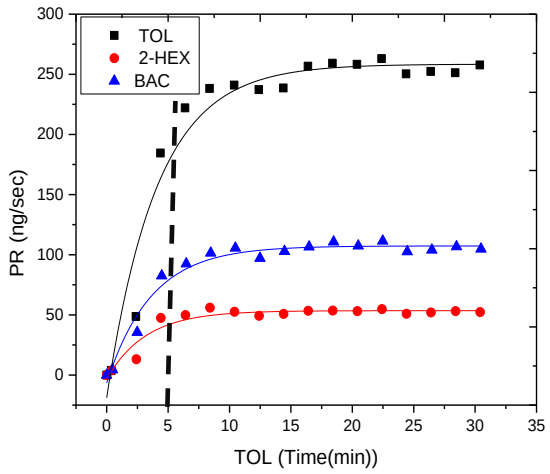

Figure 0.11. µVE performance under the optimal operatiing conditions for TOL, 2-HEX and BAC. 50 ppm of each spiked in water. Q_l=0.4 mL/min, Q_g=4 mL/min. T=50 °C.

2.3.5. Hybrid µGC-µVE System Performance

Figure 2.12a show the block diagram for the hybrid µGC-µVE system and Figure 2.12b is the µGC is used in this study. A single test was performed with the system using a µVE device with a 100-m thick PDMS membrane. A sample of synthetic urine was spiked with a mixture of 4 VOCs that can be found in the urine after inhalation exposure.[1] This spiked solution was then passed through the µVE at ambient temperature and 0.2 mL/min (N_2 = 6 mL/min). For this preliminary test, the effluent from the µVE was allowed to pass without being sampled for the first 2.5 min (due to concerns of overloading the µsampler). Then the GC pump was then activated and a sample collected for 60-sec and analyzed. The experiment was terminated prior to SSPR being reached for any of the VOCs. Thus, these results represent preliminary findings.

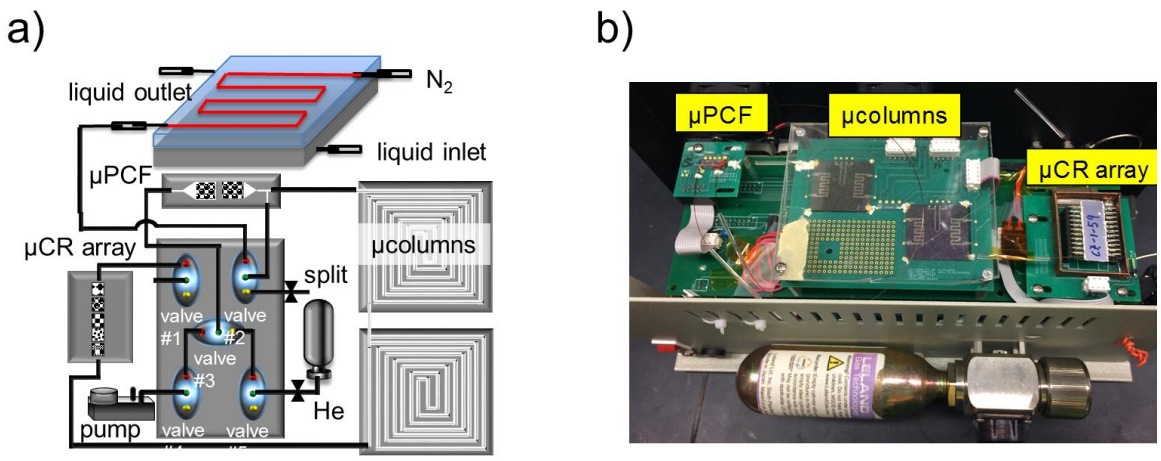

Figure 0.12. block diagram of μVE-μGC test system with the photography of the μGC prototype and its key analytical components.

Figure 2.13 shows representative μGC chromatograms from 4 of the sensors in the array and the downstream reference FID. The temperature-programmed μGC separation required ~80 sec with all peaks well resolved. Some tailing was observed in peaks from the sensors with polar MPN lile OPH-coated sensor. The total extraction time was 3.5 min and used 700 μL of the liquid sample. The limits of detections of the 4 VOCs on all 4 sensors were summarized in Table 2.4. For nonpolar TOL, its LODs on all sensors were well below its MCL. For intermediate polar compound TCE, its LODs on nonpolar sensors were closed to its BEI but LODs on polar HEM and OPH were larger than its BEI. For polar MEK, its LODs were higher its BEI on all sensors.

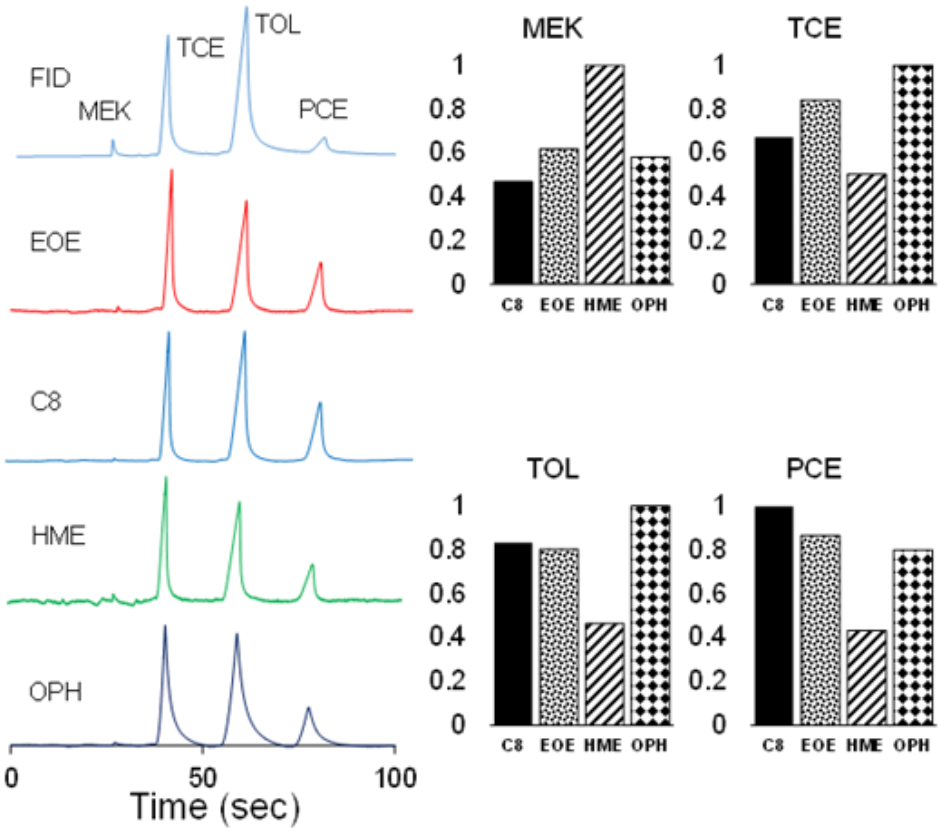

Figure 0.13.(left) Chromatograms from the 5-CR array and downstream FID reference of biomarkers in urine measured with the μVE-μGC system; and (right) relative response patterns from the μCR array. MEK, 2-butanone; TCE, trichloroethylene; PCE, perchloroethylene. μColumn temperature program: 30 s at 28 ºC, then 10 ºC/min to 50 ºC.

Table 0.4. the limites of detection of 4 VOCs by the hydrid μGC-μVE.

VOC	LODs [a] (ppm)				MCL or BEIs (ppm)
	C8	EOE	HME	OPH	
MEK	12	6.6	11	13	2.0 (BEI)
TCE	0.48	0.46	1.3	0.66	0.5 (BEI)
TOL	0.28	0.34	0.70	0.42	1.0 (MCL)
PCE	1.2	1.4	4.8	2.2	--

[a]LOD is estimated by 3σ/sensitivity, where σ is the standard deviation of the baseline noise for each sensor. Noise levels were determined as the standard deviation of the baseline of each sensor. The values of σ, in units of $(\Delta R/R_b) \times 10^6$ were as follows: 147 (C8), 167 (EOE), 284 (HME), and 169 (HME).

Although good chromatographic resolution was achieved for this simple VOC mixture, the use of sensor array response patterns can enhance the reliability of analyte determinations that would otherwise be based on retention time alone. The VOC response patterns were derived from the corresponding sensitivities (peak area/injected mass) and normalized by dividing by that of the most sensitive sensor in the array for that VOC. As shown in Figure 2.13 (right), patterns were significantly different, and the relative sensitivities were in accordance with expected affinities, as in previous reports.[6-12]

2.4. Conclusions

We have designed, microfabricated, and characterized a μVE for VOC extraction from water and biofluids. The effects of operating conditions on the performance of the μVE were characterized. The hybrid μVE-μGC system was demonstrated using synthetic urine spiked with 4 VOCs. Combining response patterns from the μCR array with chromatographic retention times was shown to enhance the reliability of VOC determinations. Although these preliminary results are promising, further work is needed to assess the impact of VOC properties, PDMS membrane thickness, and device operating conditions on performance. With decreases in LODs and sample volumes, the μVE-μGC microsystem should be suitable for on-site analyses of a wide range of VOCs in water and biofluids in the environmental, workplace, and clinical settings.

Despite this promising performance, the μVE performance was less than optimal particularly the time required to reach a steady state extraction rate. This larger than expected time constant increases analysis time and the required sample volume. Through a thorough design review, improvements have been identified to reduce the time constant. They are 1) improved liquid-side fluidic design. The current design has areas of low or stagnant flow in the largest liquid flow channels. These areas of stagnant flow increase device filling time and result in “dead

volume", both of which increase the time required to reach steady state. The liquid side could be redesigned to increase flow uniformity throughout and thereby improve analysis time; 2) improved membrane bonding. In the current devices, the bonding of the membrane to the liquid side die was imperfect. Under liquid flow, it was observed that small areas of the membrane became detached from the liquid side. This detachment occurred over some of the extraction channels, thereby effectively increasing the channel height in these areas. This increase in channel height increases resistance to diffusion, which in turn increases the time constant of the system. Bonding will be improved in future devices; 3) decreased membrane thickness. The original design targets called for a 15 µm membrane and µVE devices with 15, 30, and 100 µm membranes were fabricated. 15 µm-membrane devices were damaged during assembly and initial testing. 30 µm-membrane devices were damaged during the testing process. Most of the results presented in this report are thus for 100 □m-membrane devices. Increased membrane thickness will increase resistance to diffusion and thus increase the time to steady state. Membrane thickness will be reduced in future designs. When these improvements are implemented, it is expected that the required extraction time and sample volume will be decreased by approximately an order of magnitude each.

2.5. References

1. ACGIH, Threshold Limit Values for Chemical Substances and Physical Agents & Biological Exposure Indices for 2016, ACGIH, Cincinnati, OH, 2016.
2. EPA National Primary Drinking Water Regulations, available via http://www.epa.gov/ground-water-anddrinking-water/table-regulated-drinking-watercontaminants#Organic (access by May, 2019).
3. A. Astier, "Chromatographic determination of volatile solvents and their metabolites in urine for monitoring occupational exposure", J Chrom. A, vol. 643, pp. 389- 98, 1993.
4. M. Akbar, S. Narayanan, M. Restaino, M. Agah, "A purge and trap integrated μGC platform for chemical identification in aqueous samples", Analyst, vol. 139, pp. 3384-92, 2014.
5. J. Potkay, M. Magnetta, A. Vinson, B. Cmolik, "Bioinspired, efficient, artificial lung employing air as the ventilating gas," Lab Chip, vol.11, pp. 2901-9, 2011.
6. C-J. Lu, W.H. Steinecker, W-C. Tian, M.C. Oborny, J.M. Nichols, M. Agah, J.A. Potkay, H.K.L. Chan, J. Driscoll, R.D. Sacks, K.D. Wise, S. W. Pang, E.T. Zellers, "First-generation hybrid MEMS gas chromatograph", Lab Chip, vol. 5, pp. 1123-31, 2005.
7. Q. Zhong, W. Steinecker, E. T. Zellers, "Characterization of a High-Performance Portable GC with a Chemiresistor Array Detector," Analyst, vol. 134, pp. 283-293, 2009.
8. S. K. Kim, D. R. Burris, H. Chang, J. Bryant-Genevier, and E. T. Zellers, "Microfabricated gas chromatograph for on-site determinations of trichloroethylene in indoor air arising from vapor intrusion, part 1: field evaluation", Env. Sci. and Tech., vol. 46, pp. 6065- 6072, 2012.
9. S. K. Kim, D. Burris, J. Bryant-Genevier, K. Gorder, E. Dettenmaier, E. T. Zellers, "Microfabricated gas chromatograph for on-site determinations of trichloroethylene in indoor air arising from vapor intrusion, part 2: spatial/temporal monitoring,", Env. Sci. and Tech., vol. 46, pp. 6073-6080, 2012.
10. W. R. Collin, G. Serrano, L. K. Wright, H. Chang, N. Nuñovero, E. T. Zellers, "Microfabricated gas chromatograph for rapid, trace-level determinations of gas phase explosive marker compounds," Anal. Chem., vol. 86, pp. 655-663, 2014.
11. W. Collin, , K. Scholten, D. Paul, K. Kurabayashi, X. Fan, E. T. Zellers, "μGC × μGC microsystem with resistive and optical detection," Proc. Transducers '15, 6/21-25/2015, Anchorage, AK, pp. 949-952.
12. Wang, J.; Bryant-Genevier, J.; Nunovero, N.; Zhang, C.; Kraay, B.; Zhan, C.; Scholten, K.; Nidetz, R.; Buggaveeti, S.; Zellers, E.T. Compact Prototype Microfabricated Gas Chromatographic Analyzer for Autonomous Determinations of VOC Mixtures at Typical Workplace Concentrations. Microsyst. Nanoeng. 2018, 4, 17101.
13. A. Garg, M. Akbar, E. Vejerano, S. Narayanan, L. Nazhandali, L. C. Marr, M. Agah, "Zebra GC: A mini gas chromatography system for trace-level determination of hazardous air pollutants," Sens. and Actuators B: Chem, vol. 212, pp. 145–154, 2015

14. J. Lee, M. Zhou, H. Zhu, R. Nidetz, K. Kurabayashi, X. Fan, “Fully Automated Portable Comprehensive 2- Dimensional Gas Chromatography Device,” Anal. Chem. vol 88, pp. 10266-10274, 2016.

15. J. Potkay, "A simple, closed-form, mathematical model for gas exchange in μchannel artificial lungs”, Biomed. Microdev, vol. 15, pp. 397-406, 2013.

16. J.Pawliszyn, Handbook of Solid Phase Microextraction, Elsevier: Waltham, MA, 2012.

17. M. P. Rowe, K. E. Plass, K. Kim, C. Kurdak, E. T. Zellers, A. J. Matzger, “Single-phase synthesis of functionalized gold nanoparticles functionalized gold nanoparticles”, Chem. Mater. Vol. 16, pp. 3513-3517, 2004.

18. Jian RS, Huang RX, Lu CJ. A micro GC detector array based on chemiresistors employing various surface functionalized monolayer-protected gold nanoparticles. *Talanta* 2008; 88: 160–167.

19. U.S. National Library of Medicine, "NIH TOXNET Databases," [Online]. Available: http://toxnet.nlm.nih.gov/newtoxnet/hsdb.htm. [Accessed May 2019].

20. Sigma Aldrich, "Sigma Aldrich," [Online]. Available: http://www.sigmaaldrich.com/united-states.html. [Accessed May 2019].

21. GSI Environmental, "GSI Chemical Properties Database," [Online]. Available: http://www.gsi-net.com/en/publications/gsi-chemical-database/. [Accessed May 2019].

22. Environmental Protection Agency, "Chemical Specific Parameters," [Online]. Available: http://www.epa.gov/superfund/health/conmedia/soil/pdfs/part_5.pdf. [Accessed 10 09 2015].

23. K. Chao, Y. Lu and H. Yang, "Prediction of partition coefficients of organic compounds between SPME/PDMS and aqueous solution," *Int J Mol Sci*, vol. 15, pp. 2585-2595, 2014.

24. H. Golmohammadi and Z. Dashtbozorgi, "Prediction of water-to-polydimethylsiloxane partition coefficient for some organic compounds using QSPR approaches," *J Struct Chem,* vol. 51, no. 5, pp. 833-884, 2010.

25. Polarity Index, available via http://macro.lsu.edu/howto/solvents/Polarity%20inde x.htm (acess by May, 2019);

26. Properties of Solvents on Various Sorbents, available via http://www.sanderkok.com/techniques/hplc/eluotropi c_series_extended.html (acess by March 2017);

27. TOXNET Toxicology Data Network, available via https://toxnet.nlm.nih.gov/cgibin/sis/htmlgen?HSDB(acess by March 2017); (d) H.Golmohammadi, Z. Dashtbozorgi, “Predication of water-to-PDMS partition coefficient for some organic compounds using QSPR approaches”, J. Struct. Chem. Vol 51, pp. 833-846, 2010.

28. J. Langenfeld, S. Hawthorne, D. Miller, “Quantitative analysis of fuel-related hydrocarbons in surface water and wastewater samples by SPME”, Anal. Chem. vol. 68, pp. 144-55, 1996.

Chapter 3 Compact Prototype Microfabricated Gas Chromatographic Analyzer for VOC Mixtures at Typical Workplace Concentrations

Adapted with permission from J.Wang et al., "Compact prototype microfabricated gas chromatographic analyzer for autonomous determinations of VOC mixtures at typical workplace concentrations," Microsystems & Nanoengineering, 4, 2018, 17101, Copyright: Microsystems & Nanoengineering, Springer Nature.

3.1. Introduction

Gas chromatographic instrumentation constructed using Si-microfabricated analytical components (μGC) may afford the means to quantitatively measure individual worker exposures to multiple specific volatile organic compounds (VOC) in near-real time. Such multi-VOC measurements are currently only possible with portable GCs[1-4] and transportable FTIR[5] and GC-MS[6,7] instruments, which are too large and expensive for routine evaluations of personal exposures. Although significant advances have been reported recently in the design and development of individual μGC components for preconcentration,[8-11] separation,[12-20] and detection[21-25] and systems that combine one or more such microdevices with conventional GC components,[26-29] surprisingly few reports have appeared on integrated and/or packaged μGC systems in which the core analytical components were microfabricated.[30-36]

Members of our group have reported on a number of μGC and μGC×μGC components and systems in recent years.[37-50] We have also developed automated prototype instruments containing μGC systems for measuring low- to sub-ppb concentrations of trichloroethylene (TCE) in vapor-intrusion impacted homes,[51-52] and markers of explosives for transportation security.[53,54] Features common to these prototype instruments include a partially selective high-volume sampler of conventional design, a micromachined preconcentrator-focuser (μPCF) for focusing and injection, one or more μcolumns for temperature-programmed separations, and arrays of μchemiresistors

(μCR) with thiolate-monolayer protected gold nanoparticle (MPN) interface films for multichannel detection and recognition of eluting VOCs.

Our current efforts are directed toward creating a μGC that we have termed a Personal Exposure Monitoring Microsystem (PEMM), which is being designed as a belt-mountable instrument for measuring worker exposures to numerous target VOCs simultaneously. Toward that end, we created a first-generation (Gen-1) bench-top PEMM-1 prototype that is AC powered and laptop controlled for the purpose of gathering experience and data to inform the design, assembly, and operating conditions of the wearable Gen-2 PEMM (i.e., PEMM-2).

The core microanalytical system in the PEMM-1 comprises a redesigned dual-bed μPCF with a new heater design, a dual-μcolumn separation stage, and a redesigned μCR array. These are combined with ancillary non-microfabricated fluidic components, interface circuitry, and data acquisition and control software, as described below. The μPCF and μCR array devices of the PEMM-1 unit are the same as those incorporated into the PEMM-2 design, and neither has been presented previously. The separation module differs from the monolithic PEMM-2 μcolumn,[55] and a dual-μcolumn ensemble of similar length has been used in our recent study of μGC×μGC separations,[45] but it has not yet been incorporated into a complete microsystem. Other unique aspects of the PEMM-1 design are the use of a pre-trap, split-flow injection, and He carrier gas. Our focus on VOCs at relatively high (i.e., ~parts per million, ppm) concentrations is also new and obviates the need for high-volume samplers.

The instrument is intended to provide generalized VOC measurements in industrial workplaces, with a capability for quantitatively analyzing up to ~20 VOCs per measurement at a rate of ~6-8 measurements per hour. For practical reasons, we focused on VOCs falling within a moderate volatility window defined by their vapor pressures, p_v. For quantification, it was

assumed that concentrations would fall in the high parts-per-billion (ppb) to high ppm range, which is the most relevant range for workplace exposure monitoring.[56] Following the presentation of component-level test results intended to confirm critical performance capabilities, we present a comprehensive series of system-level test results intended to demonstrate reliable mixture-component determinations and autonomous operation. The implications of the results for the design and operation of the PEMM-2 are then assessed.

3.2. Materials and Methods

3.2.1. Materials

Most test compounds and reagents were purchased from Sigma-Aldrich/Fluka (Milwaukee, WI) or Acros/Fisher (Pittsburgh, PA) in >95% (most >99%) purity and were used as received. MPNs used as μCR interface films had core diameters in the range of 3.5-5 nm and were derived from the following thiols: n-octanethiol (C8), 6-phenoxyhexane-1-thiol (OPH), isooctyl-3-mercaptopropionate (EOE), methyl-6-mercaptohexanoate (HME) and 1-mercapto-(triethylene glycol) methyl ether (TEG). TEG was purchased from Nanoprobes, Inc. (Yaphank, NY). The remaining MPNs were synthesized in house by known methods.[57,58] The graphitized carbon adsorbents Carbopack X (C-X, 240 m^2/g), Carbopack B (C-B, 100 m^2/g), Carbopack C (C-C, 10 m^2/g), and Carbopack F (C-F, 5 m^2/g) were all 60/80 mesh and were obtained from Supelco (Bellefonte, PA). The C-X and C-B were sieved such that only the fractions with nominal diameters between 212 and 250 μm were used. Polydimethylsiloxane (PDMS) was purchased from Ohio Valley Specialty Chemicals (OV-1, Marietta, OH). Pressurized gas canisters (95 mL, 4.0 cm o.d. × 13 cm) of He (purity >99.5%; 2500 PSI) and a custom regulator were obtained from Leland (South Plainfield, NJ).

A block diagram of the analytical subsystem of the PEMM-1 prototype is presented in Figure 3.1.

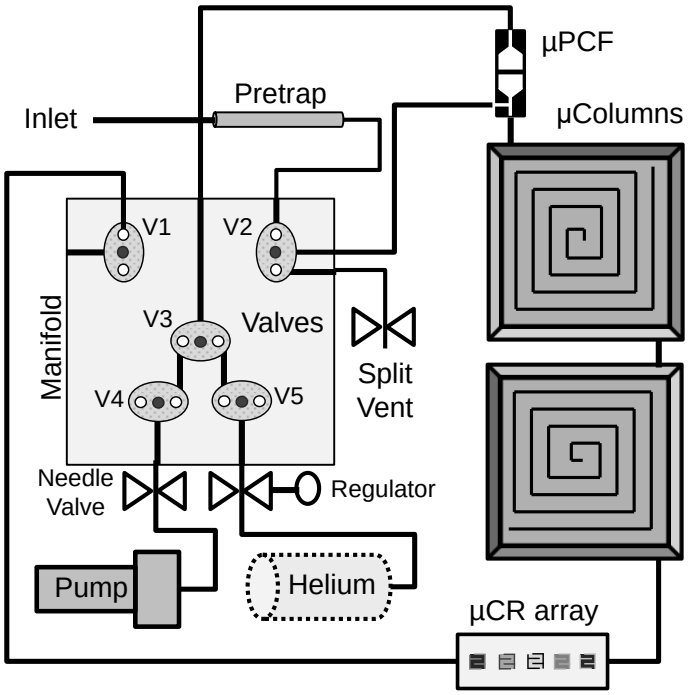

Figure 3. 1 Layout diagram of fluidic and analytical components of the PEMM-1 prototype µGC.

3.2.2. Pre-trap

Two configurations of pre-traps for precluding low-volatility interferences from entering the system were explored. The first, referred to as pre-trap A, consisted of a thin-walled stainless-steel tube (1.58 mm i.d.) packed with up to 5.4 mg of either C-F or C-C and retained with glass wool. The second consisted of short sections cut from commercial capillary columns, 250 µm or 530 µm i.d., with stationary phases of PDMS (Rtx-1; pre-trap B1) or polymethylphenylsiloxane (Rtx-20; 80:20 methyl:phenyl; pre-trap B2), respectively (Restek, Bellefonte, PA). The effects of several relevant variables on the breakthrough volumes of representative test compounds were evaluated.

3.2.3. µPCF

The µPCF chip, shown in Figure 3.2a, has dimensions of 13.6×4.1 mm and was fabricated from Si using deep-reactive-ion etching (DRIE). Each cavity is 380 µm deep, has a volume of ~4.7 µL, and is separated from the adjacent cavity by a row of 150-µm-diameter pillars spaced 150 µm from one another. Filling ports were etched into the sidewalls of each cavity for adsorbent loading. Fluidic ports were etched to snugly accommodate a 250-µm i.d. (380-µm o.d.) fused silica capillary affixed with a flexible, high-temperature silicone adhesive (Duraseal 1531, Cotronics, Brooklyn, N.Y.). The fluidic inlet channel features a tee junction to permit sample loading through one branch and back-flushed injection through the other. A 200-µm thick Pyrex plate was anodically bonded to the top surface at wafer level to seal the cavities and channels. A Ti/Pt resistive heater and resistive temperature device (RTD) were patterned onto the backside of the Si after growing a thin oxide layer for electrical isolation (Figure 3.2a). SolidWorks (R2014, Dassault Systems, Waltham, MA) and COMSOL Multiphysics (R4.2, Burlington, MA) packages were used for heater design and simulations, respectively, to minimize expected temperature gradients across the cavities.

Using mild suction, the front cavity (i.e., during sampling) was loaded with 2.0 mg of C-B and the rear cavity was loaded with 2.3 mg of C-X, as determined gravimetrically to ±0.1 mg. Filling ports were subsequently sealed with Duraseal. The device was inverted, mounted on a custom printed circuit board (PCB) using epoxy (Hysol 1C, Rocky Hill, CT), and wire-bonded to the PCB bonding pads for electrical connections.

The injection bandwidth was characterized using a bench-scale GC-FID (7890 Agilent, Santa Clara, CA) with the µPCF connected across two ports of a 6-port valve. Test atmospheres containing selected VOCs in N_2 were generated in Flex-foil® inert gas sample bags (Supelco). A

suction pump (model UMP015, KNF Neuberger, Trenton, N.J.) was used to draw a sample from the bag through the µPCF to load 50-100 ng of analyte, after which the valve was switched, and He from the GC injection port was backflushed through the µPCF while it was heated. An initial fast (uncontrolled) ramp of 400 °C/sec was used to heat from 30 to 100 °C, followed by a pulse-width modulated (PWM) ramp of 150 °C/sec to 225 °C, which was maintained for 40 sec, as subsequently applied for the injection step with the prototype. Passive cooling to 30 °C required ~90 sec. Injected samples were passed to an FID via a section of capillary maintained at 100 °C.

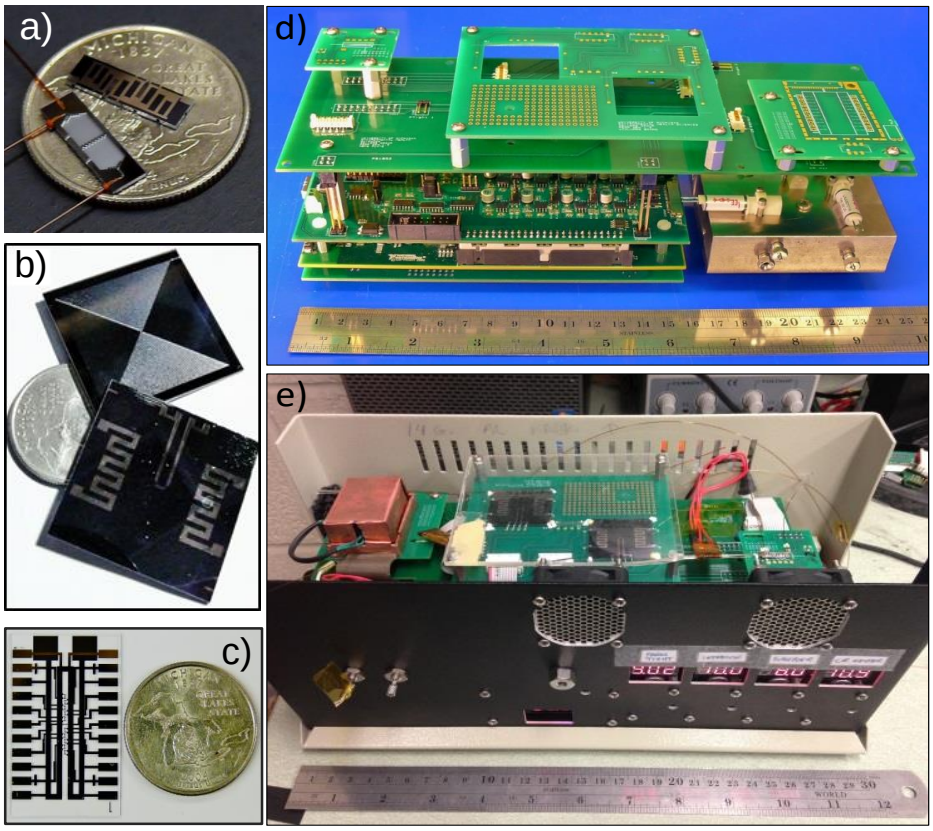

Figure 3. 2 Photographs of a) the front and back side of an unloaded µPCF fitted with capillaries (U.S. quarter for scale); b) the front and back side of a µcolumn (U.S. quarter for scale); c) the µCR array with backside heater and RTD (U.S. quarter for scale); d) assembled PCBs (sans fluidic components) and valve manifold; and e) the fully assembled PEMM-1 prototype with lid removed.

3.2.4. µColumns

Each of the two µcolumn chips (Figure 3.2b; 3.1×3.1 cm) contains a single DRIE channel (240 µm (h)×150 µm (w); 3.1 m long) that spirals in to the center and back out to the edge of the chip in a square pattern with chamfered corners.[45] A 500 µm thick Pyrex cap was anodically bonded to the top face to seal the fluidic channel at wafer scale. A pair of heaters and an RTD were patterned from Ti/Pt onto the backside. Deactivated capillaries (250 µm i.d.) inserted into the inlet and outlet ports of each µcolumn were sealed with Duraseal.

A previously described static method was used to deposit and crosslink the PDMS stationary phase on the inner walls of the channels to a nominal thickness of 0.20 µm.[14,40] After coating, the inlet and outlet capillaries were replaced with fresh uncoated (deactivated) capillaries sealed to the chip with Hysol. The capillaries emanating from the outlet of the first µcolumn and the inlet of the second µcolumn were cut to ~5 mm, inserted into opposite ends of a short (i.e., ~1.2 cm) Pyrex/Si conduit interconnect with a Ti/Pt meander-line heater patterned on the Pyrex, and sealed (Hysol). The assembly was inverted, affixed with Hysol to a custom PCB with rectangular cutouts below the µcolumns, and wire-bonded.

3.2.5. µCR Array

The µCR array chip (33×20×0.5 mm; Figure 3.2c) has a set of 5 primary and 5 back-up Au (300 nm)/Cr (30 nm) interdigital electrodes (IDE) in a single row, with a Au/Cr RTD at the center that was deposited and patterned via a standard lift-off process onto a Pyrex substrate. Each µCR contains 27 pairs of IDEs 5 µm wide, spaced 4 µm apart, and overlapping by 210 µm. A meander-line Ti/Pt heater was patterned on the backside. Header pins were bent to 90^0 and low-temperature soldered to each of the 22 IDE bonding pads. Cables were soldered to the heater bonding pads. A Si lid (33×10×0.5 mm) was also fabricated with a linear, recessed DRIE channel,

150 µm deep × 350 µm wide, running lengthwise down the center to align directly above the sensors in the array. The linearity of the interconnection with external capillaries was an improvement over previous µCR array configurations.[47,51] The array was plugged into a socket on a carrier PCB, and the entire assembly was covered with a grounded Cu Faraday cage.

MPNs were dissolved in suitable solvents (toluene for C8, OPH, and TEG; chloroform for EOE, dichloromethane for HME) at concentrations of ~5 mg/mL. Each sensor was coated with a film of one type of MPN by drop casting from a 1-µL syringe to create multilayer films with baseline resistances between 100 kΩ and 10 MΩ, depending on the MPN and the film thickness. The film thicknesses were not uniform and were not measured but were roughly estimated to be on the order of 200-500 nm on average on the basis of previous work.[59]

After coating, 0.3×2.5 cm strips of 50-µm thick double-sided adhesive tape (VHB tape, 3M, St Paul, MN) were mounted along both sides of the array, the Si lid was pressed down onto the tape, and a narrow bead of Hysol was applied along the outer seam. Short segments of deactivated inlet/outlet capillary (250 µm i.d.) were sealed to the fluidic ports (Hysol) for connection to other devices via press-tight unions. Although the integrated heater on the µCR array could be used to control temperature via a constant voltage bias, it was eventually found to be unnecessary (*vide infra*).

3.2.6. System Integration and Prototype Assembly

Two custom PCBs were designed, fabricated (Advanced Circuits, Aurora, CO), populated, and checked for proper performance. One PCB was dedicated to the microsystem components and the other to the mini-pump, mini-valves, and fans. Individual carrier PCBs for each microsystem device were mounted on stand-offs to the baseplate board. For more details, please refer to the Appendix 2, Section A2.2.

Figures 3.2d and 3.2e show the arrangement of the PCBs and fluidic components prior to final assembly and the fully assembled PEMM-1 prototype, respectively. The PEMM-1 measures 15.2 (h) × 30.5 (w) × 14 (d) cm and weighs 3.18 kg. The rear-panel-mounted He canister and regulator increase the net depth by 3.8 cm and the weight by 0.34 kg. In Figure 3.2d, the three carrier PCBs are shown (sans microcomponents) mounted on stand-offs to a single base-plate PCB. Beneath this PCB, arranged in order, are the microsystem control PCB, DAQ board, and fluidic-control PCB. The custom stainless-steel valve manifold accepts zero-dead-volume fittings for capillary interconnects and five face-mounted, 3-way, latching solenoid valves (Model LHLA1221111H, Lee Co., Westbrook CT). A wall-mounted diaphragm mini-pump (NMP-09M, KNF Micro AG, Reiden, Switzerland) collected the air samples. Two miniature needle valves (Beswick, Greenland, NH) were mounted to the front panel (Figure 3.2e) for manual adjustment of the sampling flow rate and injection split-flow ratio.

Sections of stainless-steel tubing (750 μm i.d.) and fused silica capillary (250 μm i.d.) were used for fluidic interconnections. For the latter, press-tight unions (Supelco) were used, with a subset wrapped in polyimide-embedded resistive film heaters (Omega, Stamford, CT) held at ~80 °C. Voltage regulators for the pump and solenoid valves were mounted to the inside of the front panel. Small axial fans were used for cooling. The 24-V DC power was supplied through an AC-to-DC converter connected to wall power. For most initial testing, a separate compressed gas cylinder of He was connected through the bench-scale GC for pressure regulation and subsequently to the fitting on the prototype used later to connect the on-board He canister regulator. The head pressures necessary to achieve a flow rate of 3 mL/min through the analytical system (both splitless and with a 2:1 split) were 18 and 23 psi, respectively.

3.2.7. System Control, Data Acquisition and Processing

The instrument was operated from a laptop computer running a custom LabVIEW (Ver. 14.0, National Instr., Austin, TX) program. Operating parameter settings and control functions were entered through a graphical user interface (GUI) for either manual operation of each run or multiple continuous runs. Independent proportional-integral-derivative (PID) feedback loops were designed to control heating rates and temperatures via solid-state relays and PWM of the generated signals. Although not critical for this prototype, power efficiency was considered in the design of the components. The power and energy per analysis are provided in the Appendix 2, Section A2.2.

Raw chromatogram traces were stored as text files and analyzed using OriginPro (Ver. 9.1, OriginLab, Northampton, MA). Calibration curve regression models and response patterns were generated in Excel. Monte Carlo simulations coupled with extended disjoint principal components regression (MC-EDPCR) analyses were implemented in Visual Basic via custom programs.[43]

3.3. Results and Discussion

3.3.1. System Design and Operation Specifications

By design, air samples are drawn by the mini-pump through the inlet, and low volatility interfering VOCs are retained by the wall-coated-capillary pre-trap (Figure 3.1). The air sample then passes through the µPCF, where target VOCs are quantitatively captured in one of the two adsorbent beds. After turning off the pump and switching the valves to start the flow of He through the microsystem, the µPCF is rapidly heated to thermally desorb the captured VOCs for passage to the µcolumns in a narrow band. Temperature-programmed separation of the VOC mixture components is performed, with detection provided by the transient changes in the resistance of the MPN-coated µCRs in the array as VOCs reversibly sorb into the MPN films to different extents,

giving rise to a response pattern. The flow is then redirected to backflush the pre-trap and the fore-line to purge any residual VOCs, and the μcolumns are allowed to cool in preparation for the next cycle.

Several performance criteria were used to rationalize the design, integration, and operation of the instrument components.[39] The primary constraint placed on the target VOCs was that they fall within a p_v range of ~0.03 to 13 kPa. Less volatile compounds would tend to adhere to surfaces in the (unheated) fluidic pathways, and more volatile compounds would be difficult to trap, separate, and detect because these functions rely on partitioning phenomena. Where possible, target VOCs were chosen that also had assigned Threshold Limit Values (TLV®),[56] which serve as reference values for specifying the ranges of concentrations to be encountered. To assess the selectivity of the pre-trap and μPCF, we included several potentially interfering compounds outside of the designated p_v range. For the target VOCs, a set of 17 common workplace VOCs was selected with the understanding that actual workplace exposures might involve greater or fewer VOCs in practice. Table 3.3.1 lists the set of 24 target and interfering VOCs selected, together with p_v values and assigned TLVs.

Results from previous studies were considered in the selection of the μPCF adsorbents, the μcolumn stationary phase and total length, the number of sensors and nature of MPN coatings for the μCR array, and the 5- and 10-mL air sample volumes used at the outset.[39,40,47,50,58,60] For the latter, we assumed a working limit of detection (LOD) of ~5 ng for the μCR sensors.[47,50,58,60] A 40-fold concentration range limit was imposed, indexed to the TLV Time-Weighted Average (TLV-TWA, 8-hr average) for each VOC. That is, it was assumed that 0.1×TLV was a suitable LOD-level concentration to measure and that 4×TLV was a suitable maximum quantification limit for any given measurement. Several target compounds also have an assigned Short-Term

Exposure Limit TLV (i.e., TLV-STEL), which is a 15-min average limit set to protect against acute health effects, and is usually within 4× the TLV-TWA (see Table 3.3.1). The challenge of specifying a fixed sample volume for mixtures of VOCs with widely different TLV values is discussed in the Appendix 2, Section A2.3.

3.3.2. Pre-trap

Our working goal was to pre-trap compounds with p_v values similar to or lower than that of n-tridecane (C_{13}, p_v = 0.0075 kPa) while allowing compounds with p_v values similar to or greater than that of C_{12} (p_v = 0.027 kPa) to pass through with negligible retention. Compounds of intermediate volatility would be partially retained, as a practical concession. Additionally, the pre-trap had to be regenerable via backflushing without heating.

Details of the tests performed and results obtained are given in the Appendix 2 (Section A2.4). Initial tests using packed tubes containing ~mg quantities of either C-F or C-C (i.e., pre-trap A) challenged with n-alkanes C_{11} to C_{13} at ~200 ppm failed to yield acceptable results. In subsequent tests with capillary-column pre-traps, B1 and B2 gave similar results, the best of which were obtained with segments 6.5 cm in length. Representative results from pre-trap B2 are shown in Figure A2 (Appendix 2), which produced a 10% breakthrough volume of 5 mL for C_{13} but a 90% breakthrough volume of only 1.2 mL for C_{11}. The breakthrough volume of C_{12} was ~2.6 mL. For a sample of 5-10 mL, this pre-trap was considered to offer an acceptable tradeoff in performance. Backflushing/cleaning of the pre-trap required ~2× the sample volume.

Table 3.1. List of 24 test compounds with corresponding vapor pressures (pv), TLVs, and limits of detection (LODs) for the PEMM-1 prototype (10-mL air sample; 2:1 split injection).

No.[a]	Compound	Acronym	p_v[b] (kPa)	TLV[c] (ppm)	LOD[d] (ppm)				
					EOE	C8	OPH	TEG	HME
1	methanol	MOH	16.9	200/250	nde	nd	nd	nd	nd
2	n-pentane	C5	68.5	1000	nd	nd	nd	nd	nd
3	diethyl ether	DEE	71.7	-- f	nd	nd	nd	nd	nd
4	acetone	ACE	30.8	250/500	nd	nd	nd	nd	nd
5	dichloromethane	DCM	58.0	50	nd	nd	nd	nd	nd
6	2-butanone	MEK	12.1	200/300	nd	nd	nd	nd	nd
7	ethyl acetate	EAC	12.4	400	nd	nd	nd	nd	nd
8	benzene	BEN	12.6	0.5/2.5	0.89	1.0	3.0	1.8	2.8
9	trichloroethylene	TCE	9.2	10/25	0.56	1.1	4.1	1.0	10
10	n-heptane	C_7	6.13	400/500	1.2	1.7	10	8.1	15
11	4-methyl-2-pentanone	MIBK	2.65	20/75	1.3	2.4	3.7	2.1	4.2
12	toluene	TOL	3.78	20/--	0.69	0.80	2.6	1.7	2.7
13	2-hexanone	MBK	1.46	5/10	1.9	5.4	5.8	3.0	7.4
14	butyl acetate	BAC	1.53	50/150	0.69	0.88	1.3	1.1	2.3
15	ethylbenzene	ETB	1.27	20/--	0.48	0.55	1.8	1.5	2.1
16	m-xylene	XYL	1.01	100/150	0.42	0.48	1.3	1.2	1.9
17	3-heptanone	EBK	0.187	50/75	0.35	0.51	0.71	0.71	1.4
18	n-propylbenzene	PPB	0.456	--f	0.43	0.51	2.1	1.9	2.0
19	1,2,4-trimethylbenzene	TMB	0.270	25/--	0.34	0.38	1.7	1.7	1.7
20	n-decane	C_{10}	0.191	--f	0.25	0.39	2.4	2.5	3.3
21	nitrobenzene	NBZ	0.033	1/--	0.23	0.66	0.29	0.44	0.34
22	n-undecane	C11	0.055	-- f	0.61	1.1	4.9	9.4	7.1
23	1,2,4-trichlorobenzene	TCB	0.039	5(C)	0.10	0.12	0.21	0.25	0.44
24	n-dodecane	C_{12}	0.027	--f	4.6	6.2	35	28	26

[a] Peak assignments for chromatograms in Figure 3.4. [b] At 25 °C (ref. 63). [c] Ref. 56; 8-hr TLV-TWA is listed first; if a TLV-STEL is assigned to a compound, then it is listed second; for TCB, the C designation indicates that the TLV is a ceiling limit. [d] Lowest detectable air concentration calculated assuming a 10-mL air sample with 2:1 split injection; for splitless injections, LOD would be 2.5-3× lower than shown; acronyms for the MPNs are defined in the text. [e] Not determined (interference). [f] No assigned TLV value.

3.3.3. µPCF Characterization

The dynamic adsorption capacities and desorption efficiencies for representative VOCs were determined previously using the predecessor to the current µPCF device, which had the same fluidic layout.[39] A sampling rate of 5 or 10 mL/min made no difference in capacity. Because the same mass of C-B and a greater mass of C-X were used in the new µPCF, the capacities were not re-confirmed.

Since a new heater design was used in the current μPCF, a limited set of tests of the injection band width was conducted at an analytical-path flow rate of 3 mL/min for both splitless injections and injections with a 2:1 split ratio (vent:analysis). Benzene, toluene, and C_{12} (~5 ppm each) were tested to span the range of target-VOC p_v values. The values of full width at half maximum (*fwhm*) of the FID peaks measured with splitless injection were 0.94, 1.0, and 1.4 sec, respectively, and the asymmetry factors were 1.1, 1.7 and 2.3, respectively. Desorption efficiencies were >99%. With a 2:1 split (i.e., desorption, 9 mL/min; analysis, 3 mL/min), the *fwhm* values decreased to 0.59, 0.79, and 0.85 sec, respectively, and the asymmetry factors for toluene and C_{12} decreased by approximately 10% (see Figure A3, Appendix 2, Section A2.5). These *fwhm* values are somewhat smaller than those observed with the previous μPCF,[39] attesting to the improved heater of the new device.

The sharp injections for benzene and toluene are more important for achieving good chromatographic resolution because C_{12} and compounds of similar volatility benefit from on-column focusing. Thus, in those cases where separation of earlier eluting compounds is more important than sensitivity, split injection is advantageous.[39,50]

3.3.4. μColumn Characterization

Helium was chosen as the carrier gas because of its superior chromatographic performance relative to scrubbed ambient air at typical operating flow rates.[61] The 2.4 g of He in each canister is projected to allow 228 analyses, corresponding to 30 hr of continuous operation at 8 min (and 63 mL of He) per cycle. Tests of the separation efficiency of the dual μcolumn ensemble with n-octane yielded optimal average volumetric flow rates of 0.17 and 0.56 mL/min for N_2 and He, respectively (Figure A4, Appendix 2, Section A2.6) and a maximum plate count N of ~4,300 plates/m. At our operating flow rate of 3 mL/min (i.e., >> the optimal flow rate), the values of N

were 150 and 570 plates/m for N_2 and He, respectively, which justifies the use of He as the carrier gas.

Tests of the μcolumn capacity indicated that the *fwhm* values of the peaks from several test compounds started to increase significantly and resolution started to degrade significantly at injected masses > 8 μg (see Figure A5, Appendix 2, Section A2.6). For an air sample of 10 mL, 8 μg corresponds to an air concentration of 800 mg/m^3, which is > 2×TLV for most, but not all, compounds with assigned TLVs (see Table 3.1 and ref. 56). For reference, toluene has a TLV of 20 ppm, or 75 mg/m^3, whereas heptane has a TLV of 400 ppm, or 1600 mg/m^3. Thus, the capacity of the μcolumns, while sufficient for the vast majority of VOCs of interest, might be exceeded for VOCs with high TLVs at concentrations > TLV, with a resulting slight decrease in chromatographic resolution. In such cases, a modest injection split could be used.

3.3.5. PEMM-1 Temperature Control, Sample Throughput, and Humidity Effects

The assembled PEMM-1 prototype was first run through a series of 22 discrete sampling and analytical cycles over a 3-hr period using blanks of N_2: 1-min sample (10 mL/min), splitless injection and 4-min separation (3 mL/min) using a typical μcolumn temperature program, with a 3-min cool-down period. See Figure A6, Appendix 2, Section A2.7 for typical temperature profiles. The internal (i.e., baseplate) temperature rose by only ~3 °C during μcolumn heating and returned to baseline during cool down. The run-to-run variability in the temperature ramps of the μcolumns was <3% (RSD). The μCR array temperature varied randomly by <1.7% (range <0.4 °C) around its average of 30 °C within a run, *without active heating*, and showed no net drift. Tests of the two press-tight union heaters showed no effect on eluting peak widths with the upstream heater and significant effects with the downstream heater only for C_{11} and C_{12}, where the *fwhm*

values were 12 and 21% larger, respectively, without heating. Therefore, the upstream press-tight heater was not used.

A limited test of humidity effects was run on a mixture of benzene and toluene, assuming that the only effect might be overlap of the water vapor peak with peaks from early-eluting compounds.[41] Comparison of a dry test atmosphere with one at 60% relative humidity showed that water vapor eluted as small broad peaks ~20 sec before benzene with no significant changes in the magnitudes of the benzene (or toluene) peaks from any sensor. Consistent with the MPN polarities, the ratios of water peak magnitudes were 1:1:2.3:4.6:3.7 for C8, EOE, OPH, TEG, and HME. Rejection of most atmospheric water vapor is attributable to the use of hydrophobic μPCF adsorbents.

PEMM-1 Calibrations and LODs. Prior to generating the calibration curves, the throughput of a 10-VOC mixture was determined by bypassing the μCR array and connecting the output of the second μcolumn to an FID via a heated transfer line. A 10-mL sample of the mixture (100 ppm each in a Flex-foil bag) was sampled and analyzed in triplicate with and without the pre-trap installed. The results were also compared with those obtained from the bench scale GC-FID for samples drawn from the same test atmosphere but with sample-loop injection.

For benzene through C_{12}, a <3% reduction in average peak area was observed with the pre-trap installed. For C_{13}, a 72% reduction in peak area was noted with the pre-trap, indicating substantial retention of this low-volatility interference per the design of the pre-trap. However, the results from the reference GC-FID indicated that some loss of C_{13} to surface adsorption in the flow path is also involved (see Figure A7, Appendix 2, Section A2.8 for details).

Calibrations were performed using a 2:1 split-flow injection setting over a 40-fold range of sample mass (i.e., from 0.1 to 4× TLV-TWA) on two subsets of compounds, i.e., those with

TLVs of 0.5 to 20 ppm and those with TLVs of 25 to 400 ppm. Samples of 10 and 20 mL were drawn from each of three test atmospheres in bags to span the injection masses corresponding to these concentration ranges. The analysis proceeded as described above using the same temperature program as in all subsequent testing, and all compounds within a subset were fully resolved chromatographically.

Peak shapes differed significantly among VOCs and sensors, and tailing (i.e., peak asymmetry) generally increased with elution time. The peaks for 2-hexanone (MBK, compound 13 in Table 3.3.1), which had a mid-range retention time t_R of 63 sec, are shown in Figure 3.3 in order of increasing asymmetry. Sensors coated with HME, EOE, and C8 showed much less tailing than did TEG and OPH, and asymmetry factors ranged from 1.4 to 4.3. Data collected from one of the back-up sensors ruled out location along the flow path as a contributing factor to peak broadening. The trends with VOC elution time indicate that vapor sorption and desorption rates in/out of the MPN films contribute to both peak broadening and tailing, which is consistent with previous reports.[47,51,53]

Plotting of peak height versus sample mass yielded straight lines with linear regression R^2 values ≥0.99 (forced-zero y-intercept) for most VOC-sensor pairs and >0.98 for all pairs. Calibration curves for each compound on all 4 μCR sensors are presented in Figure A8 (Appendix 2), and the slope sensitivities and R^2 values are compiled in Table A2 (Appendix 2, Section A2.9). As shown, the EOE sensor exhibited the highest sensitivity for most VOCs due apparently to its amphiphilicity and the accessibility and flexibility of the thiolate monolayers, which could enhance the rates of sorption and desorption of VOCs in the MPN film.[62] The non-polar C8-coated sensor showed high sensitivity for aromatic and aliphatic hydrocarbons, as expected. Among the more polar VOCs, the TEG-coated sensor was more sensitive than the OPH- and HME-coated sensors,

particularly for ketones and butyl acetate. The generally low sensitivity exhibited by the OPH sensor can be attributed to the greater thickness of the MPN film compared with the others, since previous work with this material as a sensor coating resulted in peak widths similar to those with C8 and HME coatings.[47] This would reduce VOC sorption-desorption rates and thus promote shorter, tailing peaks (see Figures 3 and 4).

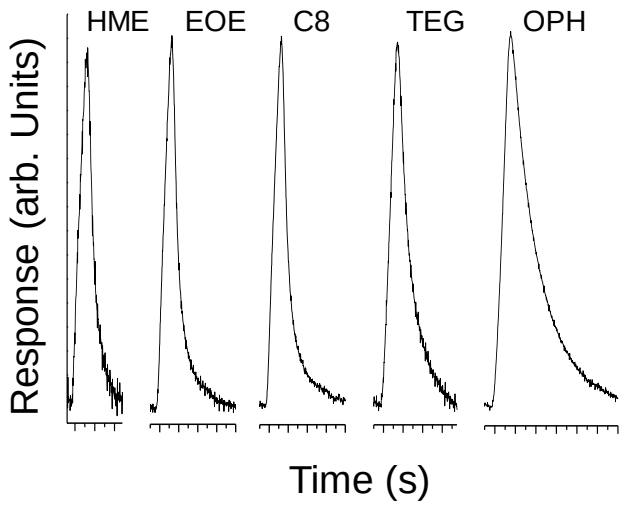

Figure 3.3. Range of peak shapes among the μCR sensors in the array for the representative compound 2-hexanone (MBK, compound 13 in Table 3.3.1, tR = 67 s) from calibration test series. From left to right, the sensor and corresponding peak asymmetry factor (at 10% of peak max.) are listed as follows: HME, 1.4; EOE, 1.7; C8, 1.8; TEG, 2.3; and OPH, 4.3. Each small tick mark on the x-axis is 1 sec. Peaks have been scaled vertically to have similar heights such that the y-axis units are arbitrary.

The limits of detection were estimated from the slopes of the regression models (peak height vs. injected mass) of each sensor from the equation 3σ/slope, where σ is the RMS baseline noise level from each sensor, and these values are compiled in Table A3, Appendix 2, Section A2.9. Because a 2:1 split injection was used, for the purpose of deriving LODs in terms of air concentrations for a given sample volume, it was necessary to divide the slope by a factor of 3 to account for the loss of 2/3 of the captured mass. Assuming a 10-mL air sample, the LODs range

from 0.1 ppm for TCB with the EOE sensor to 36 ppm for C_{12} with the OPH sensor (Table 3.3.1). The LODs for a given VOC generally differ by < 5-fold among the sensors in the array, with the notable exceptions of the alkanes, for which the range is higher due to low sensitivity from the polar sensor films.

Importantly, our decision to use 2:1 split injections gave priority to chromatographic resolution over sensitivity and resulted in a loss in sensitivity of ~3-fold (somewhat less for early-eluting compounds that benefit from peak compression at the higher desorption flow rate[39]). Thus, for splitless injections, the sensitivity should increase ~2.5-3-fold, and the LODs should decrease proportionally from the values listed in Table 3.3.1. Assuming that splitless injections are used and further assuming that detectable signals from only 4 of 5 sensors are required for vapor recognition (OPH sensor omitted, *vide infra*),[42,43] all compounds could be detected and recognized well below their TLV-STEL values, all but benzene could be detected and recognized well below their TLV-TWA values, and all but benzene, MIBK, and MBK could be detected and recognized at or below 0.1×TLV.

3.3.6. PEMM-1 Response Stability and Autonomous Operation

Table 3.2 presents the RSDs around the average values of peak area obtained for 9 selected compounds from the C8- and OPH-coated MPN sensors each day for 7 consecutive days on the basis of 4 analyses per day (note: RSD values for peak heights were very similar to those for peak area with the exceptions of those of the last three compounds for the OPH-coated sensor, where the peak height variability was consistently a few % higher, undoubtedly due to the broadness of the peaks). The RSD values for the other sensors fell within the ranges spanned by these two sensors, with a few exceptions for the TEG-coated sensor. For the C8 sensor, the intra-day RSDs ranged from 1.0 to 8.0% among the VOCs, and the OPH sensor RSDs were generally higher and

ranged from 0.8 to 9.9%. Later-eluting compounds generally gave higher values, but no trend over time was noted in any case. The greater variability observed for the OPH (and TEG) sensors is consistent with responses that are more highly dependent on sorption/desorption rates and are therefore more sensitive to small flow rate fluctuations. The corresponding RSDs for t_R values, which are presented in Table A2.4 (Appendix 2, Section A2.10), were <1.2% for all compounds except for the earliest eluting C_7 (RSD <3.6%). Also shown in Table 3.2 are the inter-day RSD values calculated from the 7 daily average peak area values. For reference, the RSD values are given for the peak areas from separate analyses of the same test atmosphere performed with a bench-scale GC-FID (loop injection, 1 sample per day). As shown, the PEMM-1 peak area measurements showed excellent stability/reproducibility, with RSD values consistently higher than but comparable to those from the GC-FID for all compounds (i.e., 2.7-9.6% and 1.3-7.5%, respectively). The values of t_R and *fwhm* were similarly stable (see Table A2.5, Appendix 2, Section A2.10).

Table 3. 2. Medium-term stability of PEMM-1 analyses as indicated by the relative standard deviation (RSD) of the average peak area from the least (C8) and most (OPH) variable sensors for a subset mixture of 9 VOCs analyzed 4 times per day for 7 days.[a]

		RSD (%) of Peak Area[b]								
Cmpd	μCR	Intra-day (n = 4)							Inter-day (n = 7)	
		1	2	3	4	5	6	7	PEMM-1	GC-FID
C_7	C8	1.6	2.1	2.4	2.4	2.4	1.1	1.6	3.9	1.9
	OPH	4.1	3.1	4.7	7.3	6.6	3.4	3.0	4.1	
BAC	C8	1.3	2.4	2.1	1.5	3.7	2.9	2.0	2.9	1.3
	OPH	0.8	2.0	1.2	1.4	1.4	2.6	1.5	4.1	
XYL	C8	2.4	3.1	1.8	3.6	4.4	3.0	1.0	2.7	2.2
	OPH	2.2	3.5	3.6	5.0	2.1	4.0	2.8	5.7	
EBK	C8	2.4	4.1	3.5	3.5	3.5	4.2	4.7	4.9	4.6
	OPH	2.3	3.2	1.9	2.4	1.6	3.0	3.5	5.0	
PPB	C8	2.7	3.2	3.4	1.9	4.8	3.2	2.0	5.2	4.3
	OPH	3.0	5.9	4.1	5.1	5.7	7.9	4.0	6.9	
TMB	C8	2.7	3.0	2.8	3.3	2.4	5.9	2.3	6.8	5.3
	OPH	6.3	6.6	9.8	5.4	7.3	7.3	5.1	9.9	
C_{10}	C8	2.3	1.3	1.6	3.7	4.2	4.8	4.4	5.3	4.4
	OPH	6.2	2.3	1.7	5.0	2.0	7.5	6.6	5.7	
C_{11}	C8	4.5	4.2	5.8	3.6	4.5	5.8	3.8	9.0	6.0
	OPH	8.5	9.8	8.5	8.5	5.1	6.2	6.7	11	
C_{12}	C8	4.6	7.4	8.0	4.2	5.8	7.0	5.4	9.6	7.5
	OPH	9.1	7.8	9.9	9.7	6.3	7.6	9.3	13	

[a] *Intra-day RSD is based on 4 samples of the same static test atmosphere containing 9 VOCs at 2×TLV concentrations (see Table 3.3.1) analyzed approximately every other hour over a single day; inter-day RSD is based on the daily average peak areas.* [b]*PEMM-1 analytical conditions: 10-mL air sample, 2:1 split injection (3 mL/min analytical path flow rate), and the same temperature program as used in calibrations; reference GC-FID data (1 sample per day) were obtained from the same test atmosphere using 100-μL loop injections.*

The PEMM-1 prototype was then operated continuously and autonomously for 8 hr on each of two consecutive days (i.e., 8 min/cycle, 60 cycles/day). For this series, the 6-VOC mixture was analyzed in triplicate at the outset, 54 blank analyses were performed, and the same mixture

was re-analyzed in triplicate at the end of the day. As shown in Table A2.6, Appendix 2, Section A2.10, the t_R values and sensitivities were notably stable, decreasing only slightly over the course of each day, which we attribute to small increases in flow rate and/or baseline temperature. More specifically, t_R values decreased by <1.6%, and peak heights and peak areas decreased by ≤9.8 % (typically <6%) over the course of 8 hr. Although the average values of these variables were lower on the second day than on the first, differences were again small and sufficiently stable for any practical application.

3.3.7. PEMM-1 24 VOC Analysis with Vapor Recognition

Figure 3.4 shows a set of 24-VOC chromatograms generated from the reference GC-FID (Figure 3.4a) and the five μCR sensors of the PEMM-1 prototype (Figure 3.4b) for a test atmosphere containing a mixture of these compounds at ~100 ppm each (500 ppm for acetone). The separation required only 3 min with PEMM-1. Although the retention order was the same, the specific retention times differed between the reference GC-FID and PEMM-1 traces due to differences in linear velocities. The lower overall resolution for the PEMM-1 traces relative to the GC-FID can be attributed to a combination of lower μcolumn separation efficiency and longer sensor response times. Consistent with Figure 3.3, the C8, EOE, and HME sensors gave relatively sharp peaks. Values of *fwhm* were <2.7 sec in all cases and ≤1.5 sec for the early-eluting target compounds 8-13. With the TEG and OPH sensors, the peaks were broader and more asymmetric, and *fwhm* values were 4.0 sec for C_{12} and <2.5 for compounds 8-13.

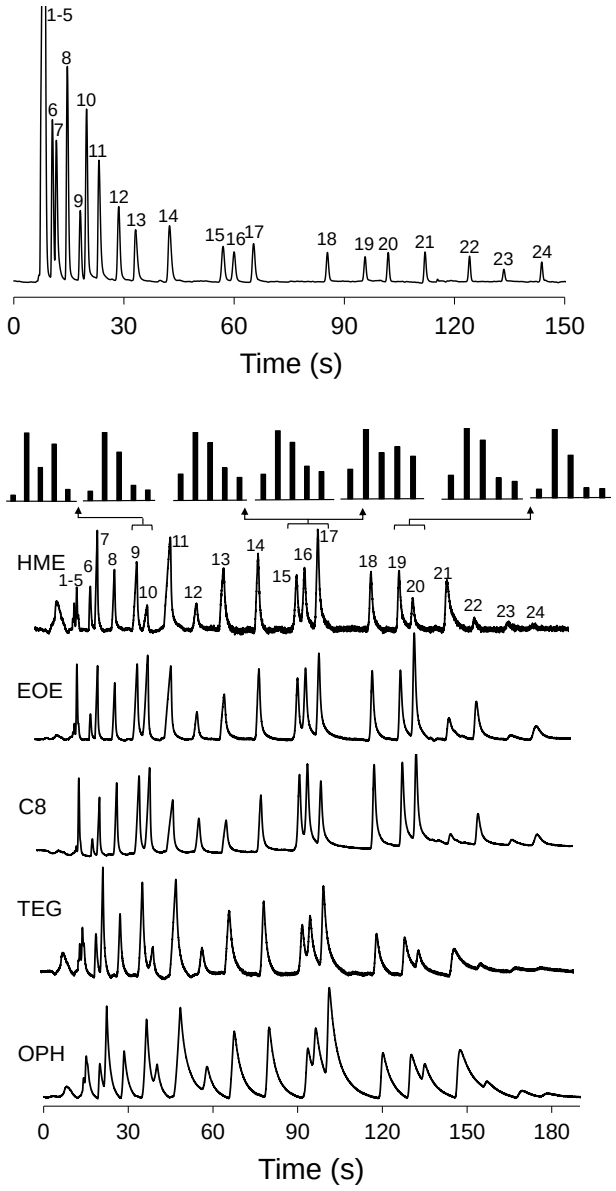

Figure 3.4. a) Reference GC-FID chromatogram of the 24-VOC mixture. Conditions: 6-m capillary column (PDMS); He carrier gas; 50 μL loop injection; and each vapor at ~100 ppm except for acetone (500 ppm) in a Flex-foil bag in N2. b) Corresponding PEMM-1 chromatograms from the 5 μCR sensors. Conditions: 1-min sample at 5 mL/min; 60 sec desorption at 225 °C; 2:1 split injection (3 mL/min for analysis); He carrier gas; μcolumns at 28 °C for 0.5 min, followed by 10 °C/min to 33 °C then 50 °C/min to 125 °C, then hold; and μCR array at 30 °C. See Table 3.3.1 for peak assignments and text for sensor acronym definitions. Normalized response patterns (pk. ht.) shown for 7 vapors (order, l-to-r: HME/EOE/C8/TEG/OPH).

The first (broad) peak in each PEMM-1 trace was water vapor presumably present at trace levels in the liquid samples from which the test atmosphere was generated. Peaks 1-7, most of which co-elute, were from the interferences, which were well resolved from the first target compound of benzene (peak 8). The separation of the 17 target mixture components with the PEMM-1 was excellent with the EOE, C8, and HME sensors (R_s >1.5), somewhat less good with TEG, and rather poor with the OPH sensor. The observed increases in peak width with increasing elution time were expected and were also observed in the GC-FID trace. Notwithstanding the OPH sensor, the excessive tailing of which renders it of less value as a detector, the speed and resolution obtained were quite good. Taken together with the peak capacities, which ranged from 80-103 among the sensors for a 4-min separation based on MBK, and the peak production rates, which ranged from 20-25/min (also based on MBK), the chromatographic performance of the PEMM-1 exceeds that of other reported GC prototypes employing microfabricated separation components.[28,29,31-36,50-53]

The normalized response pattern for each compound was obtained by dividing the calibrated slope (i.e., sensitivity) from each sensor by the slope from the sensor that gave the highest sensitivity in the μCR array for that compound. The patterns for all compounds are presented in Figure A2. 9, Appendix 2, Section A2.11, and those for the four partially co-eluting target VOC pairs in Figure 3.4b are shown above the set of chromatograms. The ability to differentiate individual VOCs was assessed via Monte Carlo (MC) simulations coupled with extended disjoint principal components regression (EDPCR) classification models, as summarized in the Appendix 2, Section A2.11. This technique yields statistical estimates of single-vapor recognition rates (RR, %) based on the actual response variabilities and calibrated sensitivities.[41-43]

The resulting confusion matrix for all 17 target compounds obtained using the responses from all 5 sensors in the array (Table A2.7, Appendix 2 Section A2.11) shows that 8 of the 17 targets could be recognized with <10% error based on their response patterns alone if they were chromatographically resolved from other compounds. Even for the other 9 compounds with lower RR values, the use of t_R values together with the response patterns could lead to unequivocal confirmation of their identities by reference to a calibration library. Removing the OPH sensor and re-running the MC-EDPCR analysis with the remaining 4 sensors resulted in relatively little change in RR values for most VOCs (with certain exceptions; see Tables A2.7 and A2.8, Appendix 2 Section A2.11) and no net loss in the effective vapor recognition capability. Regardless of the number of sensors used, it was not possible to differentiate m-xylene (XYL) from ethylbenzene (ETB) at a high rate based on their response patterns. The n-alkanes were also difficult to differentiate, as were 3-heptanone (EBK) and butyl acetate (BAC). Fortunately, homologous n-alkanes are always well resolved chromatographically, as were EBK and BAC (due to large differences in p_v values).

For those pairs of peaks that were not fully resolved with all sensors (i.e., those for which patterns were included in Figure 3.4b), MC-EDPCR analyses were run on each binary mixture to assess the capability for local discrimination. To simplify the analysis, the peaks from each pair were assumed to completely overlap. The RR values were ≥95% for TCE+C7, TMB+C10, and XYL+EBK. Only the XYL+ETB pair (RR = 77%) could not be effectively differentiated from its individual component compounds. This exceptional case notwithstanding, it is clear that this feature of the PEMM-1 prototype significantly enhances its analytical power.

3.4. Conclusions

We have demonstrated that the PEMM-1 prototype μGC described in this work is capable of direct, autonomous, multi-VOC determinations at concentrations relevant to workplace applications. The speed, reliability, selectivity, limits of detection, dynamic ranges, low operating power, and types of VOCs amenable to accurate detection and recognition render the PEMM-1 an effective new addition to the repertoire of quantitative exposure assessment tools available to occupational health scientists. Reconciling the tradeoffs among VOC mixture pre-selection, pre-concentration, separation, and recognition/detection functions was central to realizing effective system-level performance. Collectively, the operational features and performance characteristics of the PEMM-1 prototype demonstrated in this study exceed those demonstrated with other prototype μGCs reported to date.[28,29,31-36,50-53] Future work on optimizing sensor coating strategies should yield improvements in peak shapes and reductions in LODs. The results obtained from this study have been used to inform the design of a battery-powered, wearable prototype (PEMM-2), from which promising preliminary data to have recently been generated. The results from that effort will be the subject of a forthcoming article.

3.5. References

1. SEER Technology. *Accusense® Chemical Recognition System. Salt Lake City:* SEER Technology, 2017. Available at: http://www.seertechnology.com/accusense (accessed June, 2017)
2. INFICON. *Micro GC Fusion® Gas Analyzer*. *Basel:* INFICON, 2017. Available . at: http://products.inficon.com/en-us/nav-products/Product/Detail/Micro-GC-Fusion-Gas-Analyzer?path=Products%2Fpg-ChemicalDetection (accessed July, 2017)
3. Defiant Technologies. *Hand Held Gas Chromatography. Albuquerque:* Defiant Technologies, 2017. Available at: www.defiant-tech.com (accessed July, 2017).
4. Electronic Sensor Technology. *zNose® Portfolio*. *Newbury Park:* Electronic Sensor Technology, 2009, Available at: http://www.estcal.com/products (accessed July, 2017).
5. Gasmet Technologies. *Portable DX4040 FTIR Gas Analyzer*. *Helsinki:* Gasmet 2017. Available at: http://www.gasmet.com/products/portable-gas-analyzers/dx4040 (accessed April, 2017).
6. INFICON. *HAPSITE® ER Chemical Identification System. East Syracuse:* INFICON, 2017. Available at: http://products.inficon.com/en-us/Product/Detail/HAPSITE-ER-Identification-System?path=Products%2Fpg-ChemicalDetection (accessed April, 2017).
7. FLIR, *Griffin G510, Wilsonville:* FLIR Systems, 2017. available at http://www.flir.com/G510/ (accessed June, 2017)
8. Voiculescu I, McGill RA, Zaghloul ME, *et al.* Micropreconcentrator for enhanced trace detection of explosives and chemical agents. *IEEE Sens. J.* 2006; 6: 1094-1104.
9. Manginell RP, Adkins DR, Moorman MW, *et al.* Mass sensitive microfabricated chemical preconcentrator. *J. Microelectromech. Syst.* 2008; 17: 1396-1407.
10. Wong MY, Cheng WR, Liu MH, *et al.* A preconcentrator chip employing μ-SPME array coated with in-situ synthesized carbon adsorbent film for VOCs analysis. *Talanta* 2012; 101: 307-313.
11. Camara EH, Breuil P, Briand D, *et al.* A micro gas preconcentrator with improved performance for pollution monitoring and explosives detection. *Analyt. Chim. Acta* 2011; 688: 175-182.
12. Lambertus G, Elstro A, Sensenig K, *et al.* Design, fabrication and microfabricated columns evaluation of for gas chromatography. *Anal. Chem.* 2004; 76: 2629-2637.
13. Bhushan A, Yemane D, Trudell D, *et al.* Fabrication of micro-gas chromatograph columns for fast chromatography. *Microsyst. Technol.* 2007; 13: 361-368.
14. Reidy S, Lambertus G, Reece J, Sacks R. High-performance, static-coated silicon microfabricated columns for gas chromatography. *Anal. Chem* 2006; 78: 2623-2630.
15. Stadermann M, McBrady AD, Dick B, *et al.* Ultrafast gas chromatography on single-wall carbon nanotube stationary phases in microfabricated channels. *Anal. Chem.* 2006; 78: 5639-5644.

16. Potkay JA, Lambertus GR, Sacks RD, Wise KD. A low power pressure and temperature-programmable micro gas chromatography column. *J. Microelectromech. Syst.* 2006; 16: 1071–1079.

17. Radadia D, Salehi-Khojin A, Masel RI, Shannon MA. The effect of microcolumn geometry on the performance of micro-gas chromatography columns for chip scale gas analyzers. *Sens. Actuators, B Chemical* 2010; 150: 456-464.

18. Shakeel H, Agah M. High density semipacked separation columns with optimized atomic layer deposited phases. *Sensors and Actuators B: Chem.* 2017; 242: 215-223.

19. Chen BX, Huang TY, Jian RS, *et al.* A multidimensional micro gas chromatograph employing a parallel separation multi-column chip and stop-flow μGC× μGCs configuration. *Lab Chip* 2013; 13: 1333-1341.

20. Gaddes D, Westland J, Dorman FL, Tadigadapa S. Improved micromachined column design and fluidic interconnects for programmed high-temperature gas chromatography separations, *J. Chrom. A* 2014; 1249: 96-104.

21. Archibald R, Datskos P, Devault G, *et al.* Independent component analysis of nanomechanical responses of cantilever arrays. *P. Analytica Chimica Acta* 2007; 584: 101-105.

22. Li M, Myers E, Tang HX, *et al.* Nanoelectromechanical resonator arrays for ultrafast, gas-phase chromatographic chemical analysis. *Nano Lett.* 2010; 10: 3899-3903.

23. Chen FY, Chang WC, Jian RS, Lu CJ. Novel gas chromatographic detector utilizing the localized surface plasmon resonance of a gold nanoparticle mono layer inside a glass capillary. *Analytical Chemistry* 2014; 28: 5257-2564.

24. Zhu HB, Nidetz R, Zhou ML, *et al.* Flow-through microfluidic photoionization detectors for rapid and highly sensitive vapor detection. *Lab Chip* 2015; 15: 3021-3029.

25. Jian RS, Huang RX, Lu CJ. A micro GC detector array based on chemiresistors employing various surface functionalized monolayer-protected gold nanoparticles. *Talanta* 2012; 88: 160-167.

26. Akbar M, Shakeel H, Agah M. GC-on-chip: integrated column and photoionization detector. *Lab Chip* 2015; 15: 1748-1758.

27. Liu J, Seo JH, Li YB, *et al.* Smart multi-channel two-dimensional micro-gas chromatography for rapid workplace hazardous volatile organic compounds measurement. *Lab Chip* 2013; 13: 818-825.

28. Lee J, Zhou M, Zhu H, *et al.* Fully automated portable comprehensive 2-Dimensional gas chromatography device. *Anal. Chem.* 2016; 88: 10266-10274.

29. Dziuban JA, Mroz J, Szczygielska M, *et al.* Portable gas chromatograph with integrated components. *Sens. Actuators A: Physical* 2004; 115: 318-330.

30. Manginell RP, Bauer JM, Moorman MW, *et al.* A Monolithically-integrated μGC chemical sensor system. *Sensors* 2011; 11: 6517-6532.

31. Qin YT., Gianchandani YB. A fully electronic microfabricated gas chromatography with complementary capactitive detectors for indoor pollutants, *Microsystems and Nanoengineering* 2016; 2: 15049.

32. Akbar M, Restaino M, Agah M. Chip-scale gas chromatography: from injection through detection. *Microsystems and Nanoengineering* 2015; 1, 15039.

33. Lewis PR, Manginell RP, Adkins DR. *et al.* Recent advancements in the gas-phase μChem Lab. *IEEE Sensors J*. 2006; 6: 784-795.

34. Zampolli S, Elmi I, Mancarella F, *et al.* Real-time monitoring of sub-ppb concentrations of aromatic volatiles with a MEMS-enabled miniaturized gas-chromatograph. *Sens. Actuator, B Chemical*. 2009; 141: 322-328.

35. Garg A, Akbar M, Vejerano E. *et al.* Zebra GC: A mini gas chromatography system for trace-level determination of hazardous pollutants. *Sens. Actuator, B: Chemical* 2015; 212: 145-154.

36. Tzeng TH, Kuo CY, Wang SY, et al. A portable micro gas chromatography system for lung cancer associated volatile organic compound detection. *IEEE J. Solid-State Circuit* 2016; 51: 259-272.

37. Tian WC, Pang S, Lu CJ, *et al.* Microfabricated preconcentrator-focuser for a microscale gas chromatograph. *J. Microelectromech. Syst.* 2003 12: 264-272.

38. Sukaew T. Zellers ET. Evaluating the dynamic retention capacities of microfabricated vapor preconcentrators as a function of flow rate. *Sens. Actuators B: Chemical* 2013; 183:163-171.

39. Bryant-Genevier J, Zellers ET. Toward a microfabricated preconcentrator-focuser for a wearable micro-scale gas chromatograph. *J. Chrom. A.* 2015; 1422: 299-309.

40. Serrano G, Reidy S, Zellers ET. Assessing the reliability of wall-coated microfabricated gas chromatographic separation columns. *Sensors and Actuators: B Chemical* 2009; 141: 217-226.

41. Zhong Q, Steinecker W, Zellers ET. Characterization of a high-performance portable GC with a chemiresistor array detector. *Analyst* 2009; 134: 283-293.

42. Hsieh MD, Zellers ET. Limits of recognition for simple vapor mixtures determined with a microsensor array. *Anal. Chem.* 2004; 76: 1885-1895.

43. Jin C, Kurzawski P, Hierlemann A, *et al.* Evaluation of multitransducer arrays for the determination of organic vapor mixtures. *Anal. Chem.* 2008; 80: 227-236.

44. Kim SJ, Serrano G, Wise KD, *et al.* Evaluation of a microfabricated thermal modulator for comprehensive two-dimensional gas chromatography. *Anal. Chem.* 2011; 83:5556–5562.

45. Collin WR, Bondy A, Paul D, *et al.* μGC × μGC: comprehensive two-dimensional gas chromatographic separations with microfabricated components. *Anal. Chem.*2015; 87:1630-1637.

46. Scholten K., Collin WR, Fan X, *et al.* Nanoparticle-coated micro-optofluidic ring resonator as a detector for microscale gas chromatographic vapor analysis. *Nanoscale* 2015; 7: 9282-9289.

47. Wright L, Zellers ET, A nanoparticle-coated chemiresistor array as a microscale gas chromatograph detector for explosive marker compounds: flow rate and temperature effects. *Analyst* 2013; 138: 6860-6868.

48. Collin WR, Nunovero N, Paul D, *et al.* Comprehensive two-dimensional gas chromatographic separations with a temperature programmed microfabricated thermal modulator. *J. Chrom. A* 2016*;* 1444: 114-122.

49. Collin WR, Scholten KW, Fan X, *et al.* Polymer-coated micro-optofluidic ring resonator detector for a comprehensive two-dimensional gas chromatographic microsystem: μGC × μGC– μOFRR. *Analyst* 2016; **141**: 261-269.

50. Lu CJ, Steinecker WH, Tian WC, *et al.* First-generation hybrid MEMS gas chromatograph. *Lab Chip* 2005; 5:1123-1131. 51.

51. Kim, K.S. et al. Microfabricated gas chromatography for the selective determination of trichloroethylene vapor at sub-parts-per-billion concentration in complex mixtures, Anal.Chem, 2011; 83: 7198-7206.

52. Kim SK, Burris DR, Chang H, *et al.* Microfabricated gas chromatograph for on-site determinations of trichloroethylene in indoor air arising from vapor intrusion, part 1: field evaluation. *Env. Sci. and Tech*. 2012; 46: 6065-6072.

53. Collin WR, Serrano G, Wright LK, *et al.* Microfabricated gas chromatograph for rapid, trace-level determinations of gas phase explosive marker compounds, *Anal. Chem.* 2014; 86: 655-663.

54. Wright LK and Zellers ET, A nanoparticle-coated chemiresistor array as a microscale gas chromatograph detector for explosive marker compounds: flow rate and temperature effects. *Analyst* 2013; 138: 6860-6868.

55. Lin Z, Nuñovero N, Wang J, *et al.* A zone-heated gas chromatographic microcolumn: energy efficiency. *Sens. Actuator B: Chemical*. 2018; **254:** 561-572.

56. ACGIH, Threshold Limit Values® for Chemical Substances and Physical Agents & Biological Exposure Indices. 2016 ed. Cincinnati: ACGIH, 2016.

57. Rowe MP, Plass KE, Kim K, *et al.* Single-phase synthesis of functionalized gold nanoparticles. *Chem. Mater*. 2004; 16: 3513-3517.

58. Jian RS, Huang RX, Lu CJ. A micro GC detector array based on chemiresistors employing various surface functionalized monolayer-protected gold nanoparticles, *Talanta* 2008; 88:160-167.

59. Bohrer FI, Covington E, Kurdak C, *et al.* Characterization of dense arrays of chemiresistor vapor sensors with sub-micron features and patterned nanoparticle interface layers. *Anal. Chem.* 2011; 83:3687-3695.

60. NIH U.S. National Library of Medicine. *TOXNET Databases: Hazardous Substances Data Bank (HSDB)*. Bethesda: U.S. National Library of Medicine, 2017. Available at: https://toxnet.nlm.nih.gov/newtoxnet/hsdb.htm (accessed April, 2017).

61. Bryant-Genevier J. Scholten K, Kim SK, *et al.* Multivariate curve resolution of co-eluting vapors from a gas chromatograph with microsensor array detector. *Sens. Actuator B: Chemical* 2014; 202: 167-176.

62. Grob RL, Barry EF, *Modern practice of gas chromatography*. 4th ed. Hoboken: Wiley Interscience, 2004: 114-115.

63. Krasteva N, Besnard I, Guse B, et al. Self-assembled gold nanoparticle/dendrimer composite films for vapor sensing applications, *Nano Lett.*2002; 2: 551-555.

Chapter 4 Belt-Mounted Micro Gas Chromatograph Prototype for Determining Personal Exposures to VOC Mixture Components

Adapted with permission from J.Wang et al., "Belt-Mounted Micro Gas Chromatograph Prototype for Determining Personal Exposures to VOC Mixture Components," Analytical Chemsitry, 91, 2019, 74747-4754, Copyright: Analytical Chemistry, ACS.

4.1. Introduction

Volatile organic compounds (VOCs) are ubiquitous, and most are toxic to humans at sufficiently high concentrations. Health effects can range from mild narcosis and respiratory tract irritation to dysfunction and disease in various organs and systems, including cancer.[1,2] The effects of exposure to mixtures of VOCs are not well understood.[2,3] Exposure to VOCs is often higher in industrial workplaces due to the volumes of chemicals used, the nature of activities performed, and the proximity of workers to the sources of emission.[4] The collection of so-called *personal* measurements of worker exposures to toxic chemicals, ideally from the breathing zone, is mandated by regulations issued by the Occupational Safety and Health Administration (OSHA)[5] and guidelines issued by the National Institute for Occupational Safety and Health (NIOSH)[6] and the American Conference of Governmental Industrial Hygienists (ACGIH).[7]

For VOC mixtures, this typically entails collecting air samples with a passive or active adsorbent-containing sampling devices clipped to the lapel of a worker for several hours, followed by subsequent laboratory analysis.[8] Obtaining measurements over shorter time intervals (i.e., ~

minutes) could help identify high excursions, which may have health implications.[2,9] This is difficult because quantitative measurements of the individual components of VOC mixtures in near-real time are only possible with field-portable/-transportable instruments employing gas chromatography with single-channel or mass spectrometric detectors (GC, GC-MS)[10-12] or Fourier-Transform Infrared Spectrophotometry (FTIR),[13] which are generally too large and expensive for routine or personal VOC exposure monitoring. Smaller, highly sensitive GC-based instruments have become available more recently but appear to be limited by the nature and number of compounds that can be determined in a single analysis. [14,15]

GC instruments made with Si-microfabricated components (μGC) offer the enticing possibility of measuring worker exposures to multiple specific VOCs in near-real time. Essentially, a μGC system suitable for analyzing airborne VOCs requires three (micro-) analytical components: a collector/concentrator, which also functions as an injector, for sample capture and introduction; a chromatographic column for separation; and a sensor or sensor array for detection. Selected publications concerned with these components of possible μGC systems are listed in the Appendix 3. Of course, additional means for transferring samples through the system and controlling system functions are also required to create a functional instrument. Surprisingly few reports have appeared on functional systems or prototypes containing all three essential μGC components,[16-25] and a wearable μGC suitable for routine measurement of personal multi-VOC exposures has not yet been realized.

Building on prior work from our group,[19, 23-28] we recently mounted an effort to develop μGC-based technology for which we coined the general term Personal Exposure Monitoring Microsystem (PEMM). The 1st-generation PEMM (PEMM-1) was a compact benchtop prototype,[25] built as a test bed for exploring design and operating features ultimately intended for

incorporation into a 2nd-generation prototype (PEMM-2). PEMM-1 employs a hybrid-integrated μGC analytical subsystem consisting of a dual-adsorbent micropreconcentrator-focuser (μPCF), tandem separation microcolumns (μSC), and an array of microchemiresistor (μCR) sensors coated with differently functionalized monolayer protected nanoparticle (MPN) films for recognition and quantification of eluting VOCs. The PEMM-1 prototype provided reliable, autonomous operation over ≥8 hr, with low- or sub-parts-per-million (ppm) limits of detection (LOD) for targeted VOCs. However, it was AC powered and tethered to a laptop computer for system control and data acquisition (i.e., not configured for personal exposure monitoring).

Here we report on the 2nd generation PEMM prototype (PEMM-2), which is one-third the size of its predecessor PEMM-1, battery powered, and equipped with on-board microcontrol hardware and software. This belt mountable, fully packaged prototype is designed to simultaneously measure ~10-20 VOCs 6-10 times per hour and to store the data for subsequent assessment. The μPCF and μCR array devices in PEMM-2 are of the same design as those developed for PEMM-1, but a more power-efficient, monolithic μSC replaces the PEMM-1 dual-μSC module.[25,28] Additional innovative features of the PEMM-2 (some also developed/validated via PEMM-1) include: a pre-trap comprising a short wall-coated capillary for excluding intractable low-volatility interferences; a split-flow injector for increasing chromatographic resolution of early eluting VOCs; a stream-lined fluidic layout; improved circuitry for sensor signal amplification and conditioning; on-board microcontrol of system functions and data acquisition; and a companion Raspberry Pi® module for wireless communication. These and other improvements (discussed below) have resulted in lower LODs, more complex mixture analyses, enhanced vapour recognition, and lower operating power in the PEMM-2. Preliminary results of our PEMM-2 development effort have been described in two conference proceedings papers.[29,30]

4.2. Experimental Section

4.2.1. Materials

The VOCs used for characterizing performance were as follows: benzene (BEN), trichloroethylene (TCE), n-heptane (C_7), 4-methyl-2-pentanone (MIBK), toluene (TOL), 2-hexanone (MBK), butyl acetate (BAC), ethylbenzene (ETB), m-xylene (XYL), 3-heptanone (EBK), n-nonane (C_9), α-pinene (PIN), cumene (CUM), n-propylbenzene (NPB), 1,2,4-trimethylbenzene (TMB), n-decane (C_{10}), d-limonene (LIM), nitrobenzene (NBZ), n-undecane (C_{11}), trichlorobenzene (TCB), and n-dodecane (C_{12}). These were purchased from Sigma-Aldrich/Fluka (Milwaulkee, WI) or Acros/Fisher (Pittsburgh, PA) in > 95% purity (most >99% pure) and used as received. The graphitized carbon adsorbents Carbopack B (C-B, 100 m^2/g) and Carbopack X (C-X, 240 m^2/g) (Supelco, Bellefonte, PA) were manually sieved (212-250 µm) prior to loading into the µPCF. PDMS (OV-1) was obtained from Ohio Valley Specialty Co. (Marietta, OH). MPNs (~ 4 nm Au core diameter) derived from the following thiols were used as µCR interface films: isooctyl-3-mercaptopropionate (EOE), n-octanethiol (C8), methyl-6-mercaptohexanoate (HME), 6-phenoxyhexane-1-thiol (OPH), and 1-mercapto-(triethylene glycol) methyl ether (TEG). TEG was purchased from Nanoprobes (3-5 nm core, Yaphank, NY). Other MPNs were from existing stocks synthesized by reported methods.[31,32] He gas canisters (>99.5%; 2500 PSI, 95 mL, 4.0 cm o.d. × 13 cm) and associated pressure regulator (Model 50047, NR24) were obtained from Leland (South Plainfield, NJ).

4.2.2. Microsystem Layout and Components

Figure 4.1a shows a block diagram of the core microsystem of the PEMM-2 prototype. Figures 1b-d show photographs of the three microfabricated analytical components: µPCF, µSC, and µCR array, respectively. Figure 4.1e shows the assembled PEMM-2 with the cover removed

to reveal the layout of the key components, fluidic manifold, and He canister. Detailed descriptions of the fabrication, mounting, packing/coating, and fluidic interconnections of the μPCF, μSC, and μCR array devices have been published previously (consult references 25 and 28) and therefore only salient features are recapitulated here.

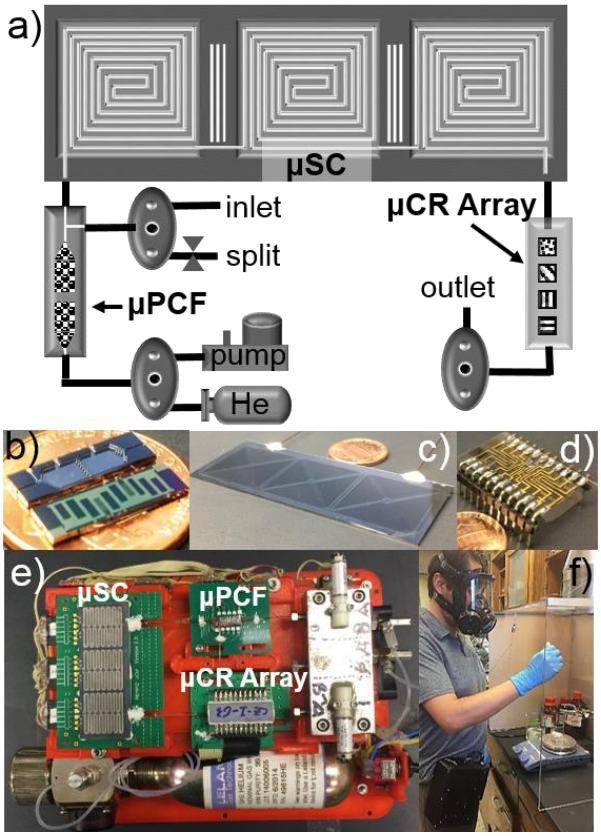

Figure 4.1. a) PEMM-2 fluidic layout diagram; b) micro preconcentrator/focuser (μPCF); c) micro separation column (μSC); d) micro chemiresistor array (μCR array); e) fully assembled PEMM-2 with lid removed; and f) belt-mounted PEMM-2 during set-up for mock field tests.

The cavities and fluidic channels of the μPCF and μSC were formed in separate Si substrates by deep-reactive-ion-etching (DRIE) and sealed with an anodically-bonded Pyrex cap. For the μCR array the substrate was Pyrex and the cap was Si with a central channel formed by DRIE. Fluidic ports of all devices accepted 250 μm i.d. fused silica capillaries affixed with a flexible, high-temperature silicone adhesive (Duraseal 1531, Cotronics, Brooklyn, N.Y.) or a rigid

epoxy (Hysol 1C, Henkel Corp., Rocky Hill, CT). Thin-film Ti/Pt resistive heaters and resistance temperature detectors (RTD) were patterned on the backsides of the devices.

The μPCF chip (Figure 4.1b, 1.4 × 4.1 cm footprint) has two ~4.7 μL cavities flanked by rows of pillars to retain the adsorbent materials (2.0 mg C-B, 2.3 mg C-X, determined gravimetrically), which were loaded by gentle suction through side-ports subsequently sealed with Duraseal. The tee junction in the fluidic inlet channel allows vapor-sample loading through one branch (via sampling pump) and back-flushed injection (via He carrier gas) through the other. The device was inverted, mounted, and wire-bonded to a custom printed circuit board (PCB).

The μSC chip (Figure 4.1c, 7.1 × 2.7 cm footprint) has a channel (6-m long, 250 × 140 μm cross section) divided into three 2-m-long spiral segments. A 0.2 μm thick wall coating of PDMS was deposited statically and cross-linked thermally by a known method.[33] The chip has through-wafer (DRIE) slots between each segment and around its periphery for thermal isolation.[29] Three independent backside meander-line heaters were designed to minimize temperature gradients and power dissipation. The chip was inverted, mounted, and wire-bonded to a PCB. Note that this μSC has a smaller footprint, fewer interconnections, and lower power consumption than the dual-μSC module used in the PEMM-1 prototype. Results of efficiency testing are presented in the SI.

The μCR array chip (Figure 4.1d, 3.3 × 2.0 × 0.05 cm) has 10 sets of adjacent Au/Cr (300/30nm) interdigital electrodes (IDEs), with a central Au/Cr RTD. Each μCR contains 27 electrode pairs, 5 μm wide with 4 μm gaps, and a 210-μm overlap. The Si lid has a 150 (d) × 350 μm (w) channel down the center (above the linear array of IDEs). MPNs were drop-cast from solution to create (non-uniform) multilayer films with baseline resistances of 0.1 to 10 MΩ. Films of selected MPNs were cast on the IDEs, but only four μCRs were used per analysis because of imposed limitations on data acquisition channels in the prototype. The lid was sealed to the

substrate with 0.05 cm thick strips of double-sided tape (VHB, 3M, St. Paul, MN) and an outer bead of Hysol. Right-angle metal pins were soldered to the bonding pads and plugged into a socket mounted on a custom PCB.

4.2.3. Prototype Assembly

A 3-D printed plastic platform supports each microsystem component on its respective PCB, elevated to a common plane on stand-off bolts. The μPCF and μCR-array PCB stand-offs fit into slide mounts for facilitating fluidic connections. The machined stainless-steel flow manifold (Figure 4.1e) has ports machined to accept the three gasket-sealed, 3-way latching solenoid valves (Model LHLA1221111H, Lee Co., Westbrook, CT). The capillaries emanating from the μPCF and μCR array connect to the appropriate manifold ports with zero-dead-volume fittings (Valco, Houston, TX) and to the μSC with press-tight connectors (Supelco). The pre-trap consists of a 6.5-cm segment of PDMS-coated capillary column,[25] and is mounted to the inlet port of the prototype with a threaded fitting. A set of four mini-fans installed above the microsystem components (not shown) provides cooling between cycles. A diaphragm mini-pump (NMP-09M, KNF, Reiden, Switzerland) is bolted beneath the manifold. Miniature needle valves (Beswick, Greenland, NH) mounted upstream of the mini-pump and downstream of the μPCF permit manual adjustment of the sampling flow rate and injection split-flow ratio, respectively. The He canister is secured to the floor of the enclosure, and a separate rechargeable battery pack wired to the unit provides primary operating power (the μCR sensors were powered by a 3 V Li-ion coin cell). Four PCBs stacked under the microsystem platform contain the microcontrollers and other electronic components for running the prototype autonomously from a customized set of downloaded parameters. Please refer to the SI for a description.

System Control and Data Acquisition. A Raspberry Pi (RP) mini-computer module (12 × 8 × 2.5 cm, Raspberry Pi Foundation, Cambridge, UK) with wireless capability was mounted to the side of the PEMM-2 with Velcro. The RP stored acquired data, and served as an interface between the embedded microcontrollers and a remote laptop computer connected to the same local network. A custom web graphical user interface allowed communication with the laptop for adjusting controls and monitoring the μCR array output during testing. The PEMM-2 hardware supports autonomous operation; however, data retrieval, setpoint and timing adjustments, and real-time updates require the RP.

Prior to any set of experiments, the operating parameters of the instrument, including RTD calibration factors, μPCF and μSC temperature programs, μCR reference resistance matching, and timing of the modes of operation within a run were entered in an Excel macro, converted to a machine-readable configuration file, and uploaded to the PEMM-2 system memory via a USB link. Additional details are in the SI.

4.2.4. Sample Preparation and Calibration

Test atmospheres of the VOCs were generated in 10-L Flex-foil® gas sample bags (Supelco) by injecting the appropriate volume of each liquid and diluting with 8 L of N_2. Concentrations were approximately 0.1×, 0.5×, and 2× the respective ACGIH 8-hr Threshold Limit Value® (TLV-TWA) for each vapor (see Table 4.1). By collecting (triplicate) samples of 5 mL and 10 mL (at 5 mL/min) with the PEMM-2, a 40-fold concentration range was spanned for each VOC. For verification, parallel samples drawn through a 250-μL sample loop (via 6-port valve) were injected to the inlet of a bench scale GC-FID (7890B, Agilent Technol., Santa Clara, CA) equipped with a short commercial (PDMS-coated) capillary column for separation and analysis. The concentrations (injected masses) were confirmed by reference to calibration standards prepared

from mixtures in CS_2 and analyzed by GC-FID. For stability tests, replicate analyses were conducted over different time periods.

4.2.5. Mock Field Test Set-up

Mock field tests were conducted by use of a custom, benchtop enclosure made of Plexiglass (61 × 60 × 43 cm, w×h×d) with an open front panel and a variable-speed, ceiling-mounted exhaust fan that vented to a lab hood. For the tests reported below, liquid TCE, MIBK, BAC, XYL, and C_{10} were mixed in a 250-mL beaker. Small aliquots of the mixture were transferred by pipette to a second beaker on a hotplate-stirrer at different times and temperatures to induce vapor concentration fluctuations. The research team member wore a properly fit-tested air-purifying respirator, and the VOC concentrations measured at the face of the chamber were maintained below their respective 8-hr TLV-TWA and 15-min TLV Short-Term Exposure Limit (TLV-STEL) levels.[7]

The PEMM-2 (with RP) was clipped to the belt of the researcher on the right hip and the battery pack was placed in the left-front pocket. A deactivated capillary extension to the pre-trap allowed collection of samples near the breathing zone. For reference, parallel samples were drawn through a co-located capillary connected to a 6-port valve with a 250-μL sample loop mounted on a nearby bench-scale GC-FID.

4.2.6. Data Management and Processing

Raw chromatogram traces (i.e., μCR signals) could be stored in the PEMM-2, but for testing were instead transferred to the RP and then wirelessly to a laptop computer for display, storage, conversion of voltage readings to normalized resistance readings, and subsequent processing (see SI). Chromatograms were analyzed using OriginPro (Ver. 9.1, OriginLab, Northampton, MA). Regression models, calibration curves, response patterns, and other data plots

were generated in Microsoft Excel. Principal components analyses (PCA) were conducted in R (Ver. 3.4.0, R Foundation, Vienna, Austria). Monte Carlo (MC) simulations were implemented in Visual Basic. See SI for MC-PCA procedures.

4.3. Results And Discussion

4.3.1. Basic Operation

The assembled PEMM-2 measures 20×15×9 cm, and weighs 2.1 kg (sans battery pack). Thus, it is 66% smaller and 40% lighter than PEMM-1.[25] The selections of μPCF adsorbent materials, μSC stationary phase, and MPNs in the μCR were based on prior development work.[25,27,34] A standard operating cycle entails of the following steps: sample collection; injection; separation; multi-sensor detection/recognition; and re-initialization. First, the pump draws a pre-programmed volume of air in through the pre-trap and μPCF. The pump is then turned off, valves are switched, and He gas is passed through the microsystem at 2-3 ml/min. Rapid heating of the μPCF to 225 °C desorbs the VOCs captured on the C-X or C-B adsorbents, which are then carried into the μSC in a sharp bolus with the option for split or splitless injection. After a temperature-programmed separation, eluting VOCs are detected by the resistance changes of the μCR sensors as the VOCs reversibly partition into the different MPN coating films, giving rise to a response pattern. While the μPCF and μSC are cooling, the He flow is then directed back through the pre-trap to flush any retained compounds.

As with PEMM-1,[25,27] the target VOCs for which quantitative analysis would be possible were restricted to those with vapor pressures, p_v, in the range 0.03 kPa < p_v < 13 kPa because lower volatility compounds would tend to adhere to all unheated surfaces in the flow path and higher volatility compounds would not be completely trapped by the adsorbents in the μPCF. Furthermore, compounds with higher p_v values would be difficult to separate on the short μSC,

and they would also be detected with lower sensitivity on the sorption-dependent μCR sensors. This concession acknowledges the inherent limitations of our system architecture and materials, as well as considerations of prototype size and power requirements. But, it also minimizes the capture of water vapor by excluding a higher surface adsorbent (e.g., a carbon molecular sieve[35]).

Table 4.1. Set of nine VOCs, pv values, TLV values, and measured LODs.

Peak[a]	Cmpd	p_v[b] (kPa)	TLV[c] (ppm)	LOD (ppb)[d]			
				C8	EOE	HME	TEG
1	BEN	12.6	0.5/2.5	150	140	600	550
2	C_7	6.13	400/500	180	110	170	300
3	TOL	3.78	20/--	110	100	460	430
4	MBK	1.55	5/10	89	60	58	170
5	BAC	1.53	50/150	65	49	90	230
6	XYL	1.01	100/150	92	78	330	330
7	EBK	0.533	50/75	100	50	58	220
8	NPB	0.456	--[e]	51	68	88	100
9	TMB	0.270	25/--	33	43	63	66

[a] peak assignments for the chromatograms in Fig. 2; [b] at 25 °C; [c] 8-hr TLV-TWA is listed first and 15-min TLV-STEL is listed second (if assigned) (ref. 7); [d] lowest detectable air concentration derived from mass-based LOD assuming a 5-mL air sample volume; acronyms are defined in the Experimental Section; [e] no assigned TLV.

The nine VOCs in Table 4.1 were selected for the initial test mixture because their p_v values fall well within the stipulated range, they collectively represent several different functional group classes, they were easily separable, and most had assigned TLV values. It was assumed that 0.1×TLV to 4×TLV represented a reasonable concentration range for which accurate quantification would be required.[27] For subsequent tests focused on vapor recognition, a set of 21 common workplace VOCs was selected that extended the range of compound p_v values to the limits designated above.

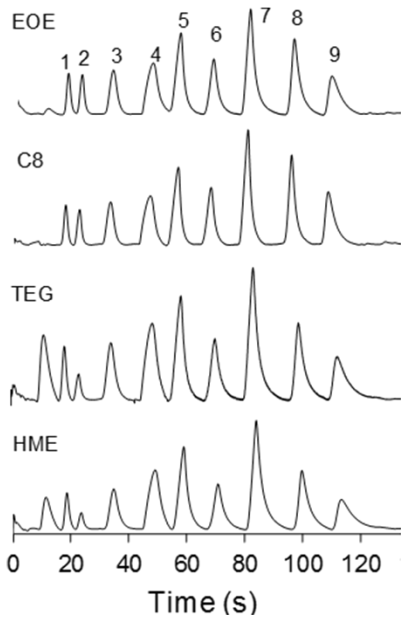

Figure 4.2. 9-VOC chromatograms (voltage readings) from PEMM-2. Conditions: ~100 ppm of each vapor; 2.5 mL sample, 5 mL/min; splitless injection at 2 mL/min He carrier gas; µPCF, 225 °C for 40 s; µSC temp. program, 30 °C for 35 s, then 40 °C/min to 105 °C; µCR array, 30 °C. Peaks: 1, BEN; 2, C7; 3, TOL; 4, MBK; 5, BAC; 6, XYL; 7, EBK; 8, NPB; 9, TMB.

4.3.2. Calibration and LODs

A simple temperature program was established to permit baseline separation of the peaks corresponding to the selected set of nine VOCs in < 120 sec. Representative chromatograms from each of the four MPN-coated sensors in the µCR array are shown in Figure 4.2. As shown, peaks were generally symmetric but tailing occurred, particularly from the sensors coated with the more polar TEG and HME MPNs. Asymmetry factors were < 1.2 in most cases and < 2.8 in all cases. Values of retention time (t_R), full width at half maximum (*fwhm*), and resolution, R_s, under these conditions are listed in Table A-1 (Appendix 3). The peak eluting before BEN (i.e., peak 1) is attributed to trace levels of water vapor in the N_2 used to create the test atmosphere.

For calibration, average peak area, *A* ($\Delta R/R_b \times s$), and peak height, *H* ($\Delta R/R_b$), were separately plotted versus injected mass. Linear regression with a forced-zero y-intercept ($R^2 > 0.99$ in all cases) yielded sensitivity values from the slopes of the lines (see Figure A-2 and Table A-2,

Appendix 3). Response patterns for all nine VOCs are presented as bar charts in Figure S-3. Although patterns could be analyzed, we have elected to address the matter of vapor recognition using the more complex 21-VOC mixture data presented below.

LODs, estimated from the regression models (*H* vs. injected mass) and typical baseline noise values of each sensor, are compiled in Table A-2 (Appendix 3) . These mass-based LODs ranged from 1.2 ng (i.e., TMB with the C8 sensor) to 9.5 ng (i.e., BEN with the HME sensor). In terms of air concentrations (Table 4.1), LODs ranged from 33 ppb (TMB, C8) to 600 ppb (BEN, HME) assuming a 5-mL air sample. The LODs for a given VOC differ by ≤ 5-fold among the sensors in the array, whereas LODs for a given sensor differ by ≤ 10-fold among all VOCs.

All compounds could be detected by all sensors at << 0.1×TLV-TWA concentration levels except BEN, for which the LODs with HME and TEG sensors were somewhat higher than this threshold. This is due to the low TLV-TWA for benzene (i.e., 0.5 ppm), and to its high p_v value and low polarity, both of which limit partitioning into these polar MPN films. If the sample volume were increased to 10 mL, then the LODs would be < 0.1×TLV-TWA for all vapor-sensor pairs. Of course, all LODs are << 0.1 ×TLV-STEL with the default 5 mL sample volume. These LODs are lower than those obtained with the PEMM-1 prototype for VOCs common to both studies,[25] owing apparently to the sharper peaks obtained by use of the new, monolithic μSC and more streamlined fluidic pathways in PEMM-2.

4.3.3. Stability of Responses and Response Patterns

Values of *A*, *H*, and t_R of the nine VOCs were compiled and the relative standard deviations (RSD) around the different average values were used for assessment of short-term (i.e., 30-min), intra-day (i.e., 8-hr), and inter-day (i.e., 5-day) stability of responses for samples collected from

the same test atmosphere. Detailed results are presented in Figure S-4 and Table A-2 for the (representative) EOE sensor.

In summary, the short-term stability was excellent for all three measured parameters over 30 min (n = 6 consecutive 5-min measurements): all RSD values were < 2.5% and most were < 2.0%. Intraday stability (n = 6 time-separated measurements over 8 hr on each of 5 days) was also very high, with RSD values ≤ 5.0% in all cases and < 2.0% in most cases. The interday stability (n = 5 daily average measurements over 5 days) was lower for all three parameters, with RSD values as high as 7.7% for *A* and ~6% for *H* and t_R. Notably, the reference GC-FID responses (n = 5 individual measurements over 5 days; loop injections) gave interday RSDs for *A* and *H* comparable to those for the PEMM-2, suggesting that a portion of the variation may be attributable to small changes in ambient temperature or pressure causing changes in the absolute concentrations of the VOCs in the bag.

The interday stability of the response patterns was investigated by use of MC-PCA. The response vector (from peak areas) obtained from the sum of the responses of the four μCR sensors for each vapor on day 1 was used as the reference point, and the 95% confidence interval (CI_{95}) around that pattern was established for each VOC by use of MC simulations that assumed an average random error of 5% for each sensor in the array. Response vectors from measurements collected on subsequent days were then evaluated relative to this CI_{95}. Of the 36 data points (i.e., 4 days × 9 VOCs) only three fell (barely) outside of their respective CI_{95} (see Figure S-4b).

4.3.4. 21-VOC Mixture

For the analysis of the more complex 21-VOC mixture, a new μCR array was installed wherein OPH was substituted for TEG due to a persistent baseline resistance drift in the previous TEG sensor output. After optimizing the separation conditions, the influence of split-flow injection

was evaluated and then the utility of combining a retention-time window approach to parsing the chromatogram with chemometric analysis of array responses for vapor recognition was explored.

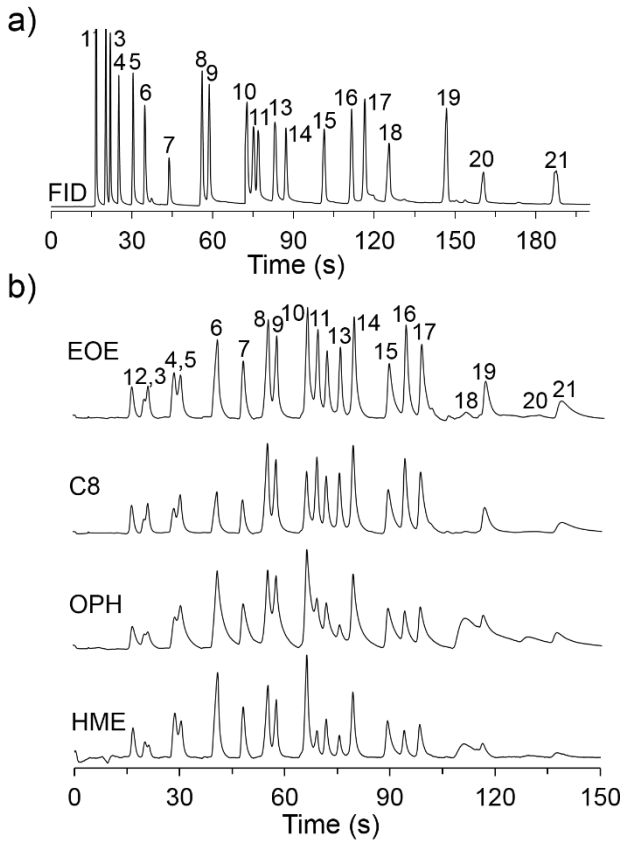

Figure 4.3. 21-VOC chromatograms a) from GC-FID, 250 µL loop injection, temp. program: 30 °C for 36 s, then 50 °C/min to 115 °C, hold; b) from the four µCR-array sensors in PEMM-2 (baseline corrected), sample at 5 mL/min for 1 min; 2:1 split injection with 3 mL/min He flow through µSC; µPCF, 225 °C for 40 s; µSC temp. program: 30 °C for 50 s, then 50 °C/min to 125 °C, hold. Peaks: 1, BEN; 2, TCE; 3, C7; 4, MIBK; 5, TOL; 6, MBK; 7, BAC; 8, ETB; 9, XYL; 10, EBK; 11, C9; 12, PIN; 13, CUM; 14, NPB; 15, TMB; 16, C10; 17, LIM; 18, NBZ; 19, C11; 20, TCB; 21, C12. Test atmosphere: ~100 ppm of each VOC except NBZ (~50 ppm) and TCB (~10 ppm).

Figure 4.3 shows the set of 21-VOC chromatograms obtained from the four µCRs in the array along with the reference GC-FID separation performed under similar conditions. The p_v range spanned by the analytes is 430 fold: from ~13 kPa (BEN) down to 0.03 kPa (C_{12}). Retention times were assigned during preliminary tests with subsets of compounds. A 1-min sample was collected at 5 mL/min, the µPCF was heated and backflushed at 9 mL/min with a 2:1 injection

split ratio so that the flow through the μSC was 3 mL/min. The temperature-programmed separation required about 150 s.

Several features of the chromatograms (Figure 4.3b) are noteworthy. First, the peak shapes from three of the four sensors are quite symmetric, the exception being the OPH sensor, which shows significant tailing that degrades the quality of the separation. This MPN was found later to have exhibited partial agglomeration in the vial in which it was stored, which could account for the apparently slower responses to vapor sorption/desorption. This notwithstanding, the overall separation quality is quite good, with near-baseline separation achieved for most analytes. Exceptions include the full or partial binary co-elutions of peaks 2/3, 4/5, 8/9, and 10/11. Although broader peaks are expected for later eluting compounds, and the finite dead volume of the CR array headspace may be a minor factor, it is clear from a comparison with the GC-FID trace (Figure 4.3a) that the VOC-MPN sorption/desorption rates contribute significantly to peak broadening and some loss in resolution for the late eluters (e.g., peaks 18-21).[26]

For fully or partially co-eluting peak pairs, the array response patterns may help to resolve the identities of the compounds in the pair. To explore this, we chose the four binary co-elutions cited above (Figure 4.3) and applied MC-PCA to the composite responses. Figures 4a-d shows PC score plots for these compound pairs for which R_s ranged from 0.4-1.3. The elliptical region plotted for each compound is the projected CI_{95} around its response vector derived from MC-PCA, again, assuming 5% random variation in each sensor response. Also included is the projected CI_{95} of the 1:1 mixture of each pair (dashed lines).

As shown, for three of the four pairs, the vector for one member is well separated from that of the other member and from the mixture (i.e., no overlap of CI_{95}) indicating that compounds in these pairs could be differentiated even if their peaks fully overlapped. The exceptional pair is

ETB and XYL (Figure 4.4c), which cannot be resolved chemometrically because they are isomers and their partitioning behavior will be nearly identical for all sensors. Thus, only a composite measure of their exposure concentrations could be obtained.

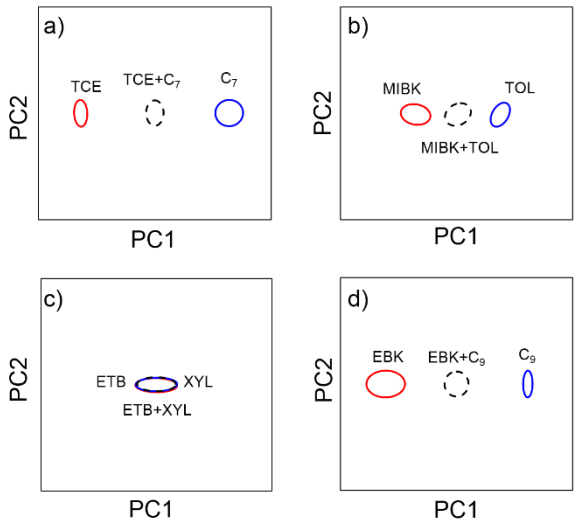

Figure 4.4. Principal components score plots derived from μCR array response patterns for the four pairs of compounds with fully or partially co-eluting peaks in Figure 4.3. Ellipses correspond to the projected CI95 around the calibrated pattern (vector) for each vapor (solid line) at 1:1 mixture (dashed line).

The use of a modest 2:1 injection split resulted in significant improvements in chromatographic resolution, albeit at the expense of sensitivity -- 2/3 of the sample mass is vented.[27] Figures 5a and b compare the chromatograms for the 21-VOC mixture with and without the split, respectively, based on the EOE sensor output. The split injection did not change t_R for any compounds, but the *fwhm* values decreased by as much as 40%. The effect is much more prominent for the early eluting compounds. For example, the *fwhm* of BEN (peak 1) decreased by 40% (from 1.7 s to 1.0 s) and that for MBK (peak 6) decreased by 20% (i.e., from 2.0 s to 1.6 s) with the split. Additional peak narrowing is observed to a progressively lesser extent out to NPB (peak 14, 6%) beyond which there is little or no impact.

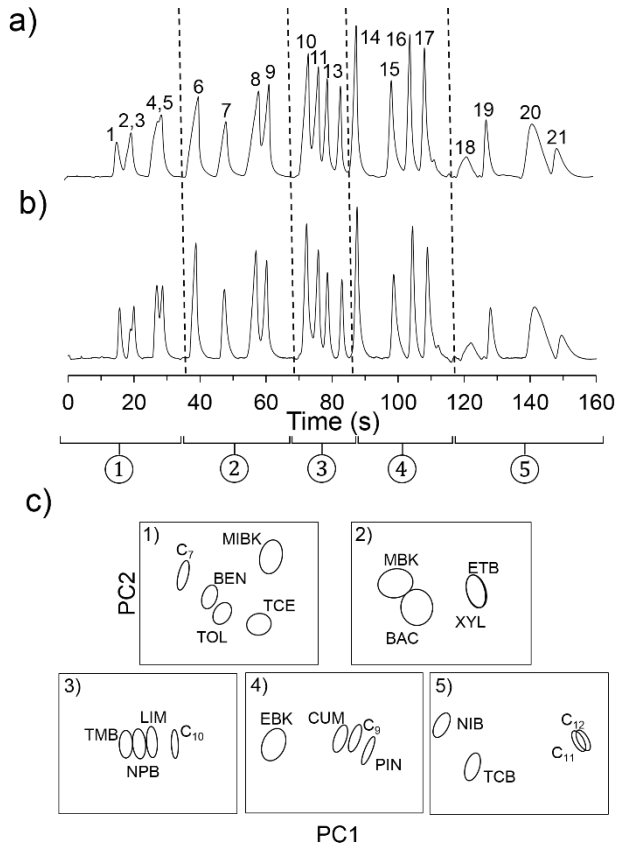

Figure 4.5. 21-VOC chromatograms from the EOE sensor in PEMM-2 with a) splitless and b) 2:1 split injection. Conditions: same as in Figure 4.3 except the µSC maximum temperature was 110 °C. c) PC score plots for compounds falling within retention-time windows defined by the dashed lines in a), where the elliptical region for each VOC represents the CI95 around its pattern (vector).

Accordingly, the resolution of adjacent peaks in the first part of the chromatogram is enhanced. So, R_s for ETB (peak 8) and XYL (peak 9) increased 63%, from 0.8 to 1.3, with the split, but R_s for TMB (peak 15) and C_{10} (peak 16) remained at 2.1 despite the split. This is consistent with expectations that compounds with lower vapor pressures (i.e., below ~ 0.5 kPa) will exhibit on-column focusing with an initial column temperature of 30 °C, such that there is little or no benefit from a sharper injection. In contrast, more volatile compounds do not spontaneously focus and their resolution is strongly dependent on the injection bandwidth.

Returning now to the entire set of four chromatograms from PEMM-2 for the 21-VOC mixture, we first performed an MC-PCA on the data set without regard for chromatographic separations. The PC score plot in Figure S-5 shows that the patterns for some compounds are well separated (i.e., differentiable as individual VOCs) while many are not. Recognizing all components of this mixture on the basis of array response patterns alone is not possible.

The approach we took to incorporating retention-time information into the analysis entailed dividing the chromatogram into retention-time windows containing subsets of compounds, and then performing vapor recognition analyses on each subset sequentially.[16] For illustration, we arbitrarily chose to divide the chromatogram into five windows, each containing 4-5 compounds, as indicated by the dashed lines in Figures 5a and b. MC-PCA was then conducted within each window.

Results are shown graphically in Figure 4.5c. For the first window (Figure 4.5c-1, compounds 1-5), the pattern separation is excellent indicating that the identities of the compounds could be confirmed as long as all peaks are resolved chromatographically. Certain binary co-elutions could be tolerated, as shown above for the case of BEN and C_7, but additional testing would be needed to assess which other co-eluting pair patterns could be separated (note: in general, ternary co-elutions cannot be resolved on the basis of their array response patterns[36]). For the second window (Figure 4.5c-2), MBK and BAC are sufficiently separated from each other and from ETB and XYL for effective vapor recognition. Per above, however, ETB and XYL could not be differentiated. For the third and fourth windows (Figure 4.5c-3,4), once again all VOC patterns are well resolved. For the last window (Figure 4.5c-5), not surprisingly, C_{10} and C_{11} patterns overlap. Fortunately, adjacent members of homologous series such as these are always well resolved chromatographically. Thus, despite being in the same window, their peaks are well

separated (Figure 4.5a) and they are thereby differentiable. Note that constraining the pattern library to only those VOCs within the designated window greatly facilitates recognition via response patterns. Single-channel detectors lack the capability to confirm compound identities.

4.3.5. Mock Field Test.

PEMM-2 conditions were adjusted so that the mixture of five VOCs could be sampled and analyzed every 5 min. Figure 4.6 shows representative 60-min exposure profiles for one of the VOCs (i.e., TCE) from the PEMM-2 and reference GC-FID for the individual wearing the PEMM-2 while he was engaged in solvent transfer activities. The inset in Figure 4.6 shows a representative set of chromatograms. Profiles for all five VOCs are presented in Figure A-6 (Appendix 3).

The ranges of concentrations spanned from 9- to 40-fold among the five VOCs, but remained below TLV values. In general, the PEMM-2 and GC-FID concentrations agreed quite closely, and the spatial and temporal variability in the actual VOC concentrations could account for differences observed at a given point in time. The error bars bracketing the GC-FID measurements correspond to RSD values ranging 6-76% (most from 10-30%), indicating occasionally large concentration fluctuations between sequential 30-s samples. Concentration estimates from the PEMM-2 sensors at a given point in time varied by ≤ 13% (RSD) and response patterns were also quite stable, with ~85% of the 60 vectors falling within the CI_{95} and no errors in assigned identities (see Figure S-6f).

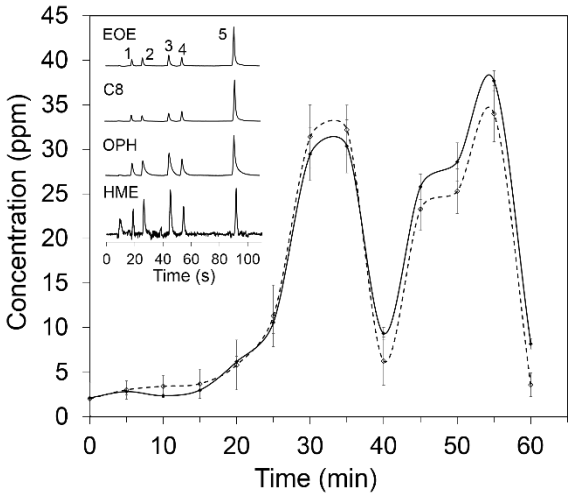

Figure 4.6. Representative exposure-time profiles for one of the five VOCs (i.e., TCE) over 60 min of continuous, unattended operation of PEMM-2 (solid line) while worn on the belt of one of the research team members, along with the reference measurements by GC-FID (dashed line). Two GC-FID samples were analyzed during each 1-min sampling period of PEMM-2. Each data point is the avg. of either four sensors from PEMM-2 or two analyses from the GC-FID. Error bars depict standard deviations. Inset shows representative PEMM-2 chromatograms (at t = 50 min). Peaks: 1, TCE; 2, MIBK; 3, BAC; 4, XYL; and 5, C10. Activities are described in the caption of Figure A-6 in Appendix 4.

4.3.6. Power/Energy

The average power consumption for a typical cycle (i.e., 1 min sample, 2.5 min analysis, and 2.5 min for cooling/reset) is only 5.8 W, which is 68% of that for the PEMM-1 prototype (see Table A-4, Appendix 3). The energy per 6-min cycle is only 2.1 kJ and is dominated by the electronics. Thus, a battery with a capacity of < 50 W-hr should permit operation for at least 8 hr.

4.4. Conclusions

We conclude that the PEMM-2 prototype, employing a core analytical subsystem made entirely from Si-glass microfabricated components, is well-suited for measuring near-real-time worker (personal) exposures to the components of moderately complex multi-VOC mixtures at concentrations encountered in industrial environments. The capability for recognizing and quantifying VOC mixture components embodied in the PEMM-2 is not available in current wearable monitoring instrumentation and has not been reported in the literature. MPN film quality

and stability could be improved with greater care in synthesis, storage, and film deposition. Further reductions in size and weight could be achieved readily by incorporating a smaller (custom) He canister and regulator, and a smaller and lighter valve manifold. Reductions in power should be possible by implementing sequential heating of the μSC segments.[28] On-going work is focused on demonstrating unattended (battery) operation for 8 hr and testing in actual workplaces.

4.5. References

1. Department of Energy National Laboratory. Indoor Air Quality Scientific Findings Resource Bank: Volatile Organic Compounds. https://iaqscience.lbl.gov/voc-summary (accessed November 2018)
2. American Conference of Governmental Industrial Hygienists, Documentation of the TLVs and BEIs, 7th ed,; ACGIH: Cincinnati, OH, 2001, with annual supplements through 2018.
3. Bruckner, J.; Anand, S.; Warre, D. In *Casarett and Doull's Toxicology: The Basic Science of Poisons*; Klaassen, C.D. Ed.; McGraw-Hill: New York, 2013; pp 1031-1132.
4. Harper, M.; Weis, C.; Pleil, J.D.; Blount, B.C.; Miller, A.; Hoover, M.D.; Jahn, S. Commentary on the Contributions and Future Role of Occupational Exposure Science in a Vision and Strategy for the Discipline of Exposure Science. *J. Expo. Sci. Environ. Epidemiol.* **2015,** *25*, 381–387.
5. Occupational Safety and Health Administration, Permissible Exposure Limits, Annotated Tables. https://www.osha.gov/dsg/annotated-pels/tablez-1.html (accessed November 2018).
6. National Institute for Occupational Safety and Health. Pocket Guide to Chemical Hazards. https://www.cdc.gov/niosh/docs/2005-149/pdfs/2005-149.pdf (accessed November 2018).
7. American Conference of Governmental Industrial Hygienists, TLVs for Chemical Substances and Physical Agents & BEIs; ACGIH: Cincinnati, OH, 2018.
8. National Institute for Occupational Safety and Health. Manual of Analytical Methods; https://www.cdc.gov/niosh/nmam/pdfs/ NMAM_5thEd_EBook.pdf (accessed November 2018).
9. Shen, D.D. In *Casarett and Doull's Toxicology: The Basic Science of Poisons*; Klaassen, C.D. Ed.; McGraw-Hill: New York, 2013; pp. 367-390.
10. INFICON. HAPSITE®ER Chemical Identification System. https://products.inficon.com/ en-us/nav-products/product/detail/hapsite-er-identification-system/ (accessed June 2018).
11. INFICON. Micro GC Fusion® Gas Analyzer. https://products.inficon.com/en-us/nav-products/product/detail/micro-gc-fusion-gas-analyzer/ (accessed June 2018).
12. Electronic Sensor Technology. zNose® Portfolio. http://www.estcal.com/products (accessed August 2018).
13. Gasmet Technologies. Portable DX4040 FTIR Gas Analyzer. http://www.gasmet.com/ products/portable-gas-analyzers/dx4040 (accessed April 2018).
14. Defiant Technologies. TOCAM and Frog 5000 Portable GCs. http://www.defiant-tech.com (accessed November 2018).
15. Bentekk. X-PID. https://www.bentekk.com/en/x-pid/ (accessed August 2018).
16. Lu, C.J.; Steinecker, W.H.; Tian, W.C.; Oborny, M.C.; Nichols, J.M.; Agah, M.; Potkay, J.A.; Chan, H.K.; Driscoll, J.; Sacks, R.D.; Wise, K.D.; Pang, S.W.; Zellers, E.T. First-Generation Hybrid MEMS Gas Chromatograph**.** *Lab Chip* **2005**, 5,1123-1131.

17. Qin, Y.; Gianchandani, Y.B. A Fully Electronic Microfabricated Gas Chromatograph with Complementary Capacitive Detectors for Indoor Pollutants. *Microsyst. Nanoeng.* **2016**, *2*, 15049.

18. Garg, A.; Akbar, M.; Vejerano, E.; Narayanan, S.; Nazhandali, L.; Marr, L.C.; Agah, M. Zebra GC: a Mini Gas Chromatography System for Trace-Level Determination of Hazardous Pollutants. *Sens. Actuators, B* **2015**, *212*,145–154.

19. Collin, W.R.; Bondy, A.; Paul, D.; Kurabayashi, K.; Zellers, E.T. μGC × μGC: Comprehensive Two-Dimensional Gas Chromatographic Separations with Microfabricated Components**.** *Anal. Chem.* **2015**, *87*, 1630-1637.

20. Manginell, R.P.; Bauer, J.M.; Moorman, M.W.; Sanchez, L.J.; Anderson, J.M.; Whiting, J.J.; Porter, D.A.; Copic, D.; Achyuthan, K.E. A Monolithically-Integrated μGC Chemical Sensor System**.** *Sensors* **2011**, *11*, 6517-6532.

21. Lewis, P.; Manginell, P.; Adkins, D.R.; Kottenstette, R.; Wheeler, D.; Sokolowski, S.S.; Trudell, D.E.; Byrnes, J.E.; Okandan, M.; Bauer, J.M.; Manley, R.; Frye-Mason, C. Recent Advancements in the Gas-Phase Micro-ChemLab**.** *IEEE Sens. J.* **2006**, *6*, 784-795.

22. Zampolli, S.; Elmi, I.; Mancarella, F.; Betti, P.; Dalcanale, E.; Cardinali, G.C.; Severi, M. Real-Time Monitoring of Sub-ppb Concentrations of Aromatic Volatiles with a MEMS-Enabled Miniaturized Gas-Chromatograph. *Sens. Actuators, B* **2009**,141, 322-328.

23. Kim, K.S.; Chang, H.; Zellers, E.T. Microfabricated Gas Chromatograph for the Selective Determination of Trichloroethylene Vapor at Sub-Parts-Per-Billion Concentrations in Complex Mixtures. *Anal. Chem.* **2011**, *83*, 7198-7206.

24. Collin, W.R.; Serrano, G.; Wright, L.K.; Chang, H.; Nuñovero, N.; Zellers, E.T. Microfabricated Gas Chromatograph for Rapid, Trace-Level Determinations of Gas-Phase Explosive Marker Compounds. *Anal. Chem.* **2014**, *86*, 655-663.

25. Wang, J.; Bryant-Genevier, J.; Nunovero, N.; Zhang, C.; Kraay, B.; Zhan, C.; Scholten, K.; Nidetz, R.; Buggaveeti, S.; Zellers, E.T. Compact Prototype Microfabricated Gas Chromatographic Analyzer for Autonomous Determinations of VOC Mixtures at Typical Workplace Concentrations. *Microsyst. Nanoeng.* **2018**, *4*, 17101.

26. Wright, L. K.; Zellers, E. T. A Nanoparticle-Coated Chemiresistor Array as a Microscale Gas Chromatograph Detector for Explosive Marker Compounds: Flow Rate and Temperature Effects. *Analyst* **2013**, *138*, 6860-6868.

27. Bryant-Genevier, J.; Zellers, E. T. Toward a Microfabricated Preconcentrator-Focuser for a Wearable Micro-Scale Gas Chromatograph. *J. Chrom. A* **2015**, *1422*, 299-309.

28. Lin, Z.; Nuñovero, N.; Wang.J.; Nidetz R.; Buggaveeti, S.; Kurabayashi, K.; Zellers, E.T. A Zone-Heated Gas Chromatographic Microcolumn: Energy Efficiency. *Sens. Actuators, B* **2018**, *254*, 561-572.

29. Wang, J.; Nuñovero, N.; Lin, Z.; Nidetz, R.; Buggaveeti, S.; Zhan, C.; Kurabayashi, K.; Steinecker W.H.; Zellers, E.T. A Wearable MEMS Gas Chromatograph for Multi-Vapor Determinations. *Procedia Eng*. **2016**, *168*, 1398-1401.

30. Wang, J.; Nuñovero, N.; Zhan, C.; Nidetz, R.; Steinecker W.H.; Zellers, E.T. Microscale Gas Chromatography with Microsensor Array Detection: Challenges and Prospects. *Proceedings* **2017**, 1, 633.

31. Rowe, M.P.; Plass, K.E.; Kim, K. Kurdak, C.; Zellers, E.T.; Matzger, A.J. Single-Phase Synthesis of Functionalized Gold Nanoparticles. *Chem. Mater.* **2004**, *16*, 3513-3517.

32. Jian, R.S.; Huang, R.; Lu, C.J. A Micro GC Detector Array Based on Chemiresistors Employing Various Surface Functionalized Monolayer-Protected Gold Nanoparticles. *Talanta* **2012**, *88*, 160–167.

33. Reidy, S.; Lambertus, G.; Reece, J.; Sacks, R. High-Performance, Static-Coated Silicon Microfabricated Columns for Gas Chromatography. *Anal. Chem.* **2006**, *78*, 2623-2630.

34. Serrano, G.; Reidy, S.; Zellers, E. T. Assessing the Reliability of Wall-Coated Microfabricated Gas Chromatographic Separation Columns *Sens. Actuators, B* **2009**, *141*, 217-226.

35. Brown, J.; Shirey, B. *A Tool for Selecting an Adsorbent for Thermal Desorption Applications*; T402025; Supelco: Bellefonte, PA, 2001.

36. Jin, C.; Zellers, E. T. Limits of Recognition for Binary and Ternary Vapor Mixtures Determined with Multi-transducer Arrays. *Anal. Chem*. **2008**, *80*, 7283-7293.

Chapter 5 Room-Temperature-Ionic-Liquid Coated Graphitized Carbons for Selective Preconcentration of Polar Vapors

5.1. Introduction

Adsorbent-based sampling for airborne volatile and semi-volatile organic compounds (S/VOC) has been practiced for decades.[1,2] The availability of synthetic, high-surface-area, granular materials amenable to thermal desorption of capture S/VOCs has facilitated air sampling with conventional adsorbent-packed tubes followed by laboratory analysis.[3-5] It has also facilitated preconcentration with adsorbent-packed devices of various configurations used as integral or auxiliary components of current field-portable gas chromatographic (GC) instruments[6-10] and reported prototypes employing GC microsystems (μGC),[11-18] which can provide on-site analysis. Preconcentration of S/VOCs is typically required prior to separation and detection in order to achieve detection limits low enough for effective monitoring of indoor or ambient air quality,[19-21] analysis of breath constituents,[22] or detection of trace levels of explosives or chemical warfare agents.[11,23]

Key physical properties of adsorbents that govern their capacity and desorption efficiency include their composition, specific surface area, pore size and structure, physical form (i.e., granules, thin films, or composites with polymers), and surface functionality. Those derived from carbon-based materials are the most common,[3-5] and are generally relatively non-polar, which reduces their affinity for atmospheric water vapor, but also for polar S/VOCs. [24]

We are pursuing the development of a novel microscale collector-injector (μCOIN) device for μGC systems in which a passive μpreconcentrator is integrated with a progressively heated μinjector.[25] The former serves as a collector and the latter as means for achieving sharp injections, which are important for μGC systems with inherently short separation columns. In both μCOIN devices the default adsorbents employed are graphitized carbons that rely on direct thermal desorption via integrated heating elements for sample transfer. For certain application scenarios of interest, it would be desirable to preferentially retain polar compounds, such as organophosphorus compounds comprising nerve agents or their precursors.[26] Reports on adsorbents used for nerve-agent model compounds can be found.[27-29] Yet, with the notable exception of work from Sandia National Laboratories,[11,30] the nature and extent of selectivity of such materials, if any, have not been characterized.

Given our successful implementation of μpreconcentrators packed with the commercial graphitized carbons, Carbopack X (C-X) and Carbopack B (C-B), in portable and wearable instruments containing μGC systems,[17,18] we chose to use these as our baseline adsorbents. To increase the affinity of these high-surface area adsorbents for polar S/VOCs in general and organophosphorus compounds specifically, we pursued a simple approach of coating them with a thin layer of a room-temperature ionic liquid (RTIL).

RTILs have been used extensively as GC stationary phases[31] and also as modifiers of conventional adsorbents for solid-phase microextraction (SPME) of analytes directly from aqueous solutions or from the headspaces above such solutions.[32-34] Of interest to us was a class of trigonal tripyramidal RTILs developed by the Armstrong group.[35,36] One, in particular, tri(tripropypphosphoniumhexanamido) triethylaminebis(trifluoromethylsulfonyl) imide, showed high viscosity, low volatility, a wide liquidus temperature range, and stability at high

temperatures.[36] As a GC or (μ)GC × (μ)GC stationary phase, it retained non-polar compounds weakly and showed interesting retention selectivity patterns among polar compounds.[37-39] In addition, in analyses of the water content of fuel samples, the retention of water vapor was moderate and reversible, with no tailing or other indications of excessive affinity.[39a]

Although it is commercially available as a stationary phase in pre-coated capillary columns (ILB-76, Supelco), the freestanding RTIL is not available commercially. The retention selectivity of this RTIL has been independently studies in the context of linear solvation energy relationships (LSER) by several investigators, and LSER solvation coefficients derived for this material were generally consistent among them.[36-38]

In this paper, we explore the use of RTIL-coated graphitized carbons as adsorbents for ultimate use in one or both of the devices comprising our μCOIN for μGC systems. Toward that end we performed conventional packed-tube breakthrough tests of Carbopack B and Carbopack X, with and without ~monolayer RTIL coatings, when challenged with ppm-range vapor concentrations of several polar and non-polar compounds. Results were then evaluated in the context of LSER models to explore the degree to which such models might predict performance. Following a discussion of relevant models and the methodology employed, we present results of materials characterizations, breakthrough tests, and modeling. The implications of the results for application of the RTIL-coated carbons in our μCOIN or other preconcentration devices are assessed.

5.2. Models

5.2.1. Wheeler Model

The modified Wheeler Model has been used to guide the design and assess the performance of packed-bed (μ)preconcentrators.[40-43] It relates several device design and operating parameters to the volume of vapor-laden air that can be drawn through an adsorbent bed, $V_{b\text{-}x}$, prior to observing a given fractional breakthrough (x) of an initial challenge concentration under continuous exposure conditions:

$$V_{b-x} = \frac{W_e W_b}{C_o}\left[1 - \frac{1}{k_v \tau}\ln\left(\frac{C_o}{C_x}\right)\right] = \frac{W_e W_b}{C_o} - \frac{W_e \rho Q}{C_o k_v}\ln\left(\frac{C_o}{C_x}\right) \qquad (5.1)$$

where $V_{b\text{-}x}$ is in liters, W_e is the dynamic adsorption capacity (g adsorbate/g adsorbent), W_b is the adsorbent bed mass (g), $\tau = W_b/(\rho Q)$ is the bed residence time (min), ρ is the adsorbent bed density (g/cm^3), Q is the volumetric flow rate (cm^3/min), k_v is the kinetic rate constant (min^{-1}), C_o is the inlet concentration (g/cm^3), and C_x is the outlet concentration (g/cm^3) corresponding to the chosen fraction x.

As shown, $V_{b\text{-}x}$ is proportional to W_e/C_o. Although W_e increases with C_o the rate of its increase is a steadily decreasing function of C_o, consistent with a classic Type I (or II) isotherm, [44] and at a monolayer coverage of the adsorbent it no longer increases with C_o. Accordingly, $V_{b\text{-}x}$ will decrease with increasing C_o. Multiplying $V_{b\text{-}x}$ by C_o to obtain the corresponding breakthrough mass, $M_{b\text{-}x}$ (in μg), yields a variable that is directly proportional to W_e and that compensates, if only approximately, for the concentration dependence of W_e. Although k_v is a potential mitigating factor in the correlation of $M_{b\text{-}x}$ with W_e, it is primarily a function of linear velocity through the

bed.[43] By maintaining a constant flow rate for all tests and by further using ratios of $M_{b\text{-}x}$ values for a given vapor for the modeling described below, this factor should not be important.

5.2.2. LSER Model

The interactions between vapors and sorbent materials can be quantified using the partition coefficient, *K*, which is the ratio of vapor concentration in the sorbent phase, C_s, to that in the gas phase, C_g, at the equilibrium: $K = C_s/C_g$. For adsorbents, C_s would be expressed as the ratio of vapor mass to adsorbent mass (rather than volume) and can be considered equivalent to W_e in Eq. 1, at least at very low (i.e., "infinitely dilute") concentrations where a linear isotherm is assumed and K is constant.

LSERs are generally considered the most comprehensive approach to modeling partitioning phenomena.[45-50] The current form of the LSER model as applied to vapor-phase solutes interacting with a sorbent phase expresses K as a function of several variables:[49]

$$log\ K = c + eE + sS + aA + bB + lL \qquad (5.2)$$

The capital letters on the right side of the equation are solute descriptors: *E*, excess molar refraction; *S*, polarizability/dipolarity parameter; *A*, solute hydrogen bond acidity; *B*, solute hydrogen bond basicity; *L*, the log of the vapor-hexadecane partition coefficient. The lower-case letters are coefficients that characterize the sorbent with respect to its ability to interact with solutes via the same types of interactions portrayed in the model. Thus, *e* is for interactions of π electrons or lone-pair electrons; s is for dipole-dipole interactions, *a* represents hydrogen bonding basicity; *b* represents hydrogen bonding acidity; and *l* formally combines the interaction by dispersion with an entropic cavity formation contribution. The *c* term is a regression constant comprising all other

interactions not captured by the other terms in the equation, which may be specific to the measurement system employed. The products of the paired terms in Eq. 5.2 quantify the importance of each of the intermolecular interactions to partitioning.

Lenca and Poole,[37] among others,[36,38] employed LSER models to rationalize the retention patterns among various compounds separated on a GC column having the RTIL used in this study as the wall-coated stationary phase. They generated the solvation coefficients for the RTIL on the basis of a large number of GC experiments, and they compared their values to those from the other groups that also generated such values. On the basis of their analyses of the values, we have adopted their values of *e, s, a, b,* and *l* following corrections for temperature (see below and A4.5.1 in Appendix 4). It should be noted, however, that pre-treatment of the capillary wall with salt is needed to promote adhesion and achieve a uniform film of this RTIL on the wall of capillary columns,[36,39] and the effect of this factor on derived LSER coefficients is not known and was not considered in any study.

Although the LSER model represented by Eq. 5.2, has been applied to vapor sorption onto porous solids, the rigor of such efforts is questionable because there are no explicit provisions in the model for particle size, specific surface area, or porosity (size or volume) as they affect adsorption equilibria. Furthermore, assumptions of isotropic vapor-sorbent interactions inherent in Eq. 5.2, will not occur on solid surfaces, and the entropic cavity-formation contribution to the value of "l" would not apply to fixed pores within solids.[51] Nonetheless, LSER coefficients for granular adsorbents of various types have been established, and used to good effect in correlating partitioning, typically in liquid-liquid extraction or separation studies.[46-48,52-54]

Since we could not find published LSER coefficients for C-B, we considered three surrogate materials for which LSER coefficients were derived empirically from sorption

studies.[52,54, 55] We have adopted values reported for Carbotrap,[52] which is a graphitized carbon similar to C-B in composition and specific surface area.

Values of the corresponding LSER solute (vapor) descriptors *E*, *S*, *A*, *B*, and *L* for the vapors tested in this study were obtained from published literature[45,55, 56] with the exception of two of the organophosphonates. However, for the latter it was possible to derive values by extrapolation from homologues for which values were known (see below and A4.5.2 Appendix 4).[56]

5.2.3 Relating *K* to *We*

The LSER model is a thermodynamic model that relates solubility interactions to infinite-dilution K values. The Wheeler Model combines kinetic and thermodynamic variables to describe breakthrough, and values of W_e that can be derived from the Wheeler Model under dynamic conditions are typically fractionally lower than those obtained by static uptake experiments.[43] Furthermore, W_e is concentration-dependent and, as stated above, has a non-linear relationship with concentration, whereas *K* is assumed to be constant over some low concentration range. For breakthrough testing, we are using finite concentrations. Thus, the relationship between *K* and W_e is not direct.

Despite these mitigating factors, we have proceeded under the assumption that $K \approx W_e/C_o$, and thus that *K* values derived from LSER models would have a correlation with breakthrough via $M_{b\text{-}x}$. In recognition of the fact that we have have not tested the RTIL alone, and have applied ~ a monolayer of RTIL onto the C-B, such that the pore structure of the C-B is still a critical factor affecting vapor adsorption, we have used the ratios of (log) *K* values for the RTIL-coated C-B and the uncoated C-B as the independent variables, and the ratios of V_{b10} values for the test compounds as the dependent variables.

5.3 Experimental Methods

5.3.1 Materials

Reagents for RTIL synthesis included trimethylamine, 6-bromohexanoylchloride, tripropylphosphine, lithium trifluoromethanesulfonimide (Sigma-Aldrich, St. Louis, MO) and tris(2-aminoethyl)amine (Alfa Aesar, Haverhill, MA), which were obtained in ≥97% purity and used as received. Chemicals used for breakthrough testing are listed in Table 5.1 and were obtained from Fisher Chemical (Waltham, MA) in > 93% purity (most of >99%). The graphitized-carbon adsorbents, Carbopack B (C-B, 100 m^2/g) and Carbopack X (C-X, 240 m^2/g) were obtained from Supelco (Bellefonte, PA) and were manually sieved to isolate granules in the nominal size range of 212-250 μm (C-X) or 180-212 μm (C-B) and pretreated at 200°C in N_2 gas for 30 min prior to use (note: the size difference was inadvertent).

Tri(tripropylphosphoniumhexanamido)trimethylamine-bis(trifluoromethylsulfonyl) imide, RTIL), was synthesized according to a known procedure,[35,39] and the product was characterized by ^1H NMR, thermogravimetric analysis (TGA, Pyris 1, Perkin Elmer, Waltham, MA) and elemental analysis (Atlantic Microlab, Norcross, GA). Details of the synthesis and characterization are given in the section of A4.1 (Appendix 4). All analytical results were consistent with the expected product.

5.3.2 Coating of Adsorbents with RTIL

A sample of 3.24 ± 0.03mg of the RTIL was dissolved in 2 mL of dichloromethane and diluted to 20 mL with m-xylene in a scintillation vial. To this solution, 20 mg of C-B was added with gentle swirling. This mass ratio of RTIL to C-B corresponds to that required to achieve a monolayer of the RTIL on the adsorbent surface assuming ideal coverage (see A4.2.2, Appendix

4). For C-X, a similar solution of 7.78 mg of the RTIL was combined with 20 mg of C-X to achieve the same nominal monolayer coverage. In both cases, the vial was capped and allowed to stand for 2 hr at room temperature. The solvent was removed by rotary-evaporator and the vial with was then placed in a vacuum oven at 100 °C overnight.

5.3.3 Characterization of Adsorbents

The specific surface area and the distribution of pore volume with pore size were determined for C-B and the RTIL-coated C-B (RTIL/C-B) from N_2 adsorption-desorption isotherms measured with a gas sorption analyzer (NOVA4200E, Quantachrome Instruments, Boynton Beach, FL). Samples of ~150 mg were analyzed at 77 K using high purity N_2 (99.999%, Cryogenic Gases, Pittsfield Township, MI). Specific surface areas were calculated using the Brunauer−Emmett−Teller (BET) method in the relative pressure range (p/p_o) of 0.08−0.34 using NOVAwin software (Quantachrome). The pore size/volume distributions were calculated from the adsorption branch based on nonlocal density functional theory (NLDFT) using the Barret Joiner Halenda model.

5.3.4 Adsorbent Tube Assembly

Adsorbent-packed tubes were constructed from Inconel tubing (5 cm long, 1.59 mm O.D, 1.35 mm ID). The adsorbents were introduced into the tubes by gentle suction and were positioned and retained by plugs of stainless steel mesh and silanized glass wool inserted before and after adsorbent loading. The loaded mass of RTIL-CB and C-B were 2.64 mg and 2.50 mg, respectively. Loaded masses of RTIL/C-X and C-X were 2.61 and 2.54 mg, respectively. The ~5% difference

in coated and uncoated masses was considered small enough to ignore in comparisons of breakthrough volumes. A thin sleeve of polyimide (Microlumen, Tampa, FL) was wrapped around the tube and a fine-wire type thermocouple K (OMEGA Engineering, INC., Norwalk, CT) was held snugly against the tube with second polyimide sleeve. A section of fine-gauge, insulated, varnished Cu wire, used to resistively heat the adsorbent bed, was then coiled tightly around adsorbent bed assembly and wrapped with another layer of polyimide to create a heated length that extended beyond the adsorbent bed length. Following a given breakthrough test, the tube was heated by applying a dc voltage sufficient to raise the temperature to 250 °C while passing N_2 through the tube to purge the desorbed vapor(s).

5.3.5 Breakthrough Testing

A diagram of the breakthrough test set-up is shown in Figure A4.3 (Appendix 4). Test atmospheres were generated by injecting the liquid chemical into a 10-L Flexfoil gas sampling bag (Supelco). The vapor concentration was confirmed with a bench scale GC with flame-ionization detector (GC-FID, Model 7890A, Agilent Technologies, Palo Alto, CA), previously calibrated with auto-injected samples of CS_2 solutions of the target chemical, by use of sample-loop injections of samples taken from the well-mixed bag contents.

Breakthrough was monitored while drawing the atmosphere through the adsorbent tube at 5 mL/min using a vacuum pump (UN86KTDC, KNF Neuberger, Trenton, NJ) and periodically (every 1-3 min) directing an aliquot of the outlet stream into the GC column (6 m long, 320 µm i.d., 0.25 µm thick Rtx-1 stationary phase, Restek) via a six-port valve equipped with a 250 µL gas sampling loop. That is, the sample was continuously drawn through the loop by a pump under a fixed flow rate and, periodically, the valve was switched and the sample was injected into GC-FID for analysis. The flow rate did not change with the position of the valve. Note that the bed

residence time at this flow rate is ~80 msec which is long enough for the V_{b10} value to be fairly stable to small changes in flow rate.[43]

A needle valve placed upstream from the pump was adjusted to achieve the desired flow rate, which was measured upstream from the adsorbent tube with a bubble buret meter. A differential pressure gauge was connected by a tee-fitting between the adsorbent tube and 6-port valve to monitor for possible constrictions or leaks between experiments. All tests were performed at ambient temperature, which varied from 25 to 27 ºC.

Monitoring the peaks from the FID downstream from the adsorbent tube over time allowed construction of a breakthrough curve (C_x/C_o vs. sample volume). By convention we used the volume, V_{b10}, corresponding to when the downstream concentration reached 10% of the challenge concentration (i.e., C_x/C_o = 0.10) as the primary performance metric. FID peak areas were integrated using OriginPro (Ver. 9.1, OriginLab, Northampton, MA, USA) and breakthrough curves were plotted in Microsoft Excel (Office 365, Microsoft Cooperation, Redmond, WA).

5.4. Results and Discussion

5.4.1. Material Characterization

Figure 5.1a shows the structure of the RTIL. H^1 NMR and elemental analysis confirmed the structure and purity of the material, and were consistent with previous reports.[35,39] TGA results indicated 1% and 5% mass losses at 283 °C and 351 °C, respectively, within 6 and 19 °C of those reported previously (see A4.3 in Appendix 4).

The N_2 adsorption isotherms presented in Figure 5.2a show that both C-B and RTIL/C-B exhibit classical Type II isotherms with small hysteresis loops. The BET surface area of C-B, 97.8 m^2/g, is just 2% lower than that reported by the manufacturer. The specific surface area of RTIL/C-B, 52.2 m^2/g, is 47% lower than the uncoated C-B. The consistently smaller N_2 uptake volume of

RTIL-CB is in accordance with the results in Figure 5.2a, which shows the distributions of pore volume with pore size from 1.5-30 nm for both C-B and RTIL/C-B. As shown, the basic pore structure is retained after coating but the pore volume is reduced at all diameters, implying a fairly uniform RTIL coverage. The slightly greater fractional reduction at ~4 nm and loss of volume below 3.2 nm is consistent with pore filling or blocking by the RTIL. The summary in Table 5.2 shows that the average pore size did not change, and that the decrease in average pore volume (39%) was somewhat less than the decrease in surface area.

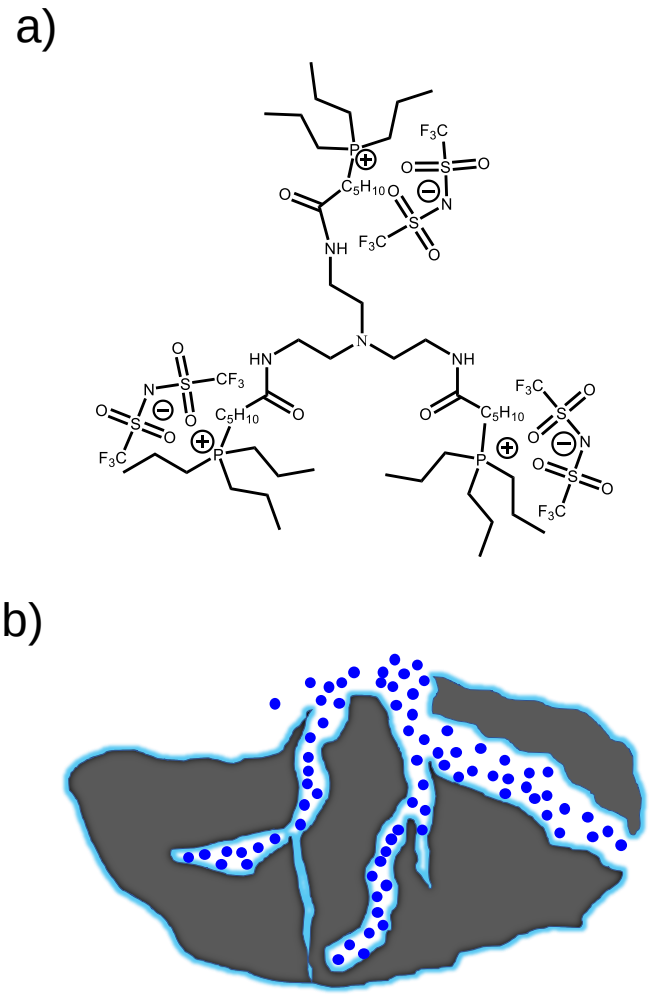

Figure 5.1. a) Structure of RTIL; b) conceptual diagram of vapor interactions with the RTIL-coated graphitized carbons (i.e. C-B or C-X) with a range of pore sizes.

Figure 5.2b shows the distributions of pore volume with pore size from 1.5-30 nm for both C-B and RTIL/C-B, and indicates that the basic pore structure is retained after coating but that the overall pore volume is lower. The apparently greater reduction in pore volume at ~4 nm and loss of pore volume below ~3.2 nm is consistent with pore filling or blocking by the RTIL in the smallest pore is size range. The fairly consistent reduction in pore volume with size over the range of larger pores implies a relatively uniform coating of the RTIL.

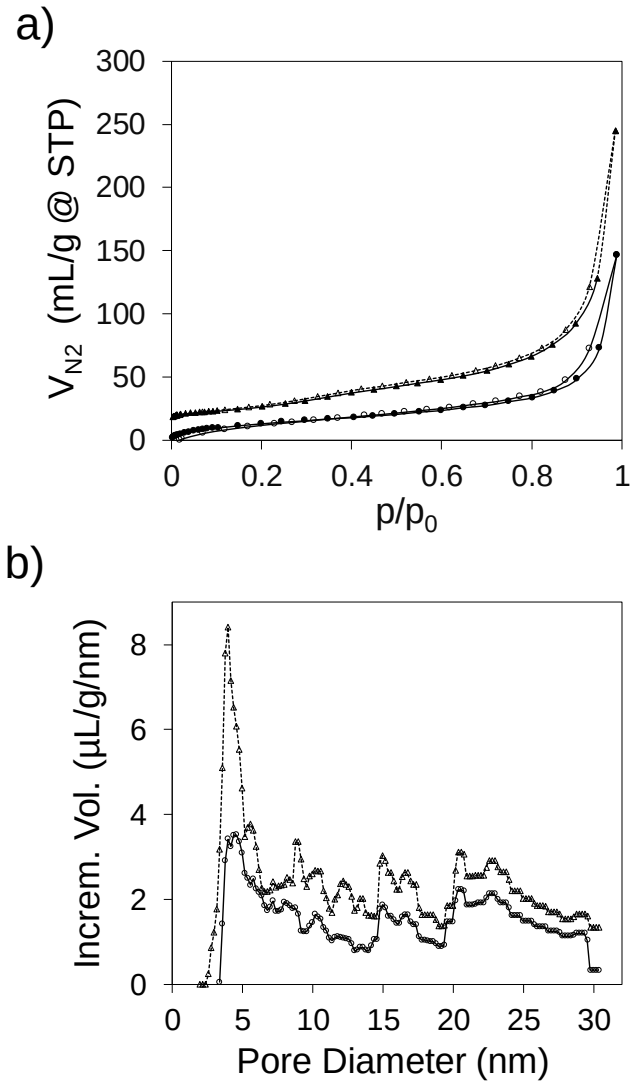

Figure 5.2. a) N_2 isotherm adsorption (solid symbols) and desorption (open symbols) isotherms of C-B (triangles, dashed line) and RTIL/C-B (circles, solid line); b) pore volume distributions of C-B (triangles, dashed line) and RTIL/C-B (circles, solid line).

The N_2 adsorption isotherms presented in Figure 2b show that both C-B and RTIL/C-B exhibit classical Type II isotherms with small hysteresis loops. The consistently smaller N_2 uptake volume of RTIL-CB is in accordance with the results in Figure 2b. The average pore size, average pore volume and surface area of CB and RTIL-CB are summarized in Table 5.2. The BET surface area of C-B, 97.8 m^2/g, is just 2% lower than that reported by the manufacturer. The specific surface area of RTIL/C-B, 52.2 m^2/g, is 47% lower than the uncoated C-B.

5.4.2. Breakthrough Test Results

A preliminary series of breakthrough tests was run as a function of flow rate for DMMP from 4.3 to 7.0 mL/min with both C-B and RTIL/C-B. The V_{b10} was a non-linear function of flow rate (refer to Eq. 5.1) and it decreased by a significant degree for both materials over this range. This indicated that fairly tight control of the flow rate was needed. Although flow rates did vary among some experiments they were held within 0.5 mL/min for all pairs of tests for a given chemical between the two adsorbents. For quality control, tests with XYL and DMMP were repeated several times over the course of this 15-month study. Results indicated no significant changes in V_{b10} over this time period, which involved frequent cycling from ambient temperature to 250 °C. This documents that the RTIL is stable.

The representative set of breakthrough curves shown in Figure 5.3 for challenges of 57 mg/m^3 of m-xylene (XYL) and 133 mg/m^3 of dimethylmethylphosphonate (DMMP) at 5 mL/min for both adsorbents illustrate the selectivity of the RTIL/C-B. As shown, all curves gave the characteristic S shape with steep central regions indicative of a well formed concentration profile within the bed. The V_{b10} values for XYL were 210 mL with C-B and 8.0 mL with RTIL/C-B,

which is a reduction of 26-fold (-96%). In stark contrast, the V_{b10} values for DMMP were 29 mL with C-B and 75 mL with RTIL/C-B, which is an increase of 2.6-fold (158%). Clearly, the effect of the RTIL on capacity is significant with respect to both enhancement for the polar DMMP and rejection of the relatively non-polar XYL.

Table 5.1. Compounds, vapor pressures, test concentrations, breakthrough volumes and ratios, modelled log K values, and breakthrough masses.

Acronym[a]	p_v (kPa)[b]	Conc. (mg/m^3)[c]	V_{b-10} (mL)		R_{Vb-10}[d]	logK[e]		M_{b-10} (µg)	
			No RTIL	RTIL		C-B, C-X	RTIL	No RTIL	RTIL
C-B									
DMMP	0.13	130	29	75	2.6	9.41	6.57	3.9	10
DEMP	0.056	55	210	520	2.5	11.7	6.93	11	29
DIMP	0.045	54	290	750	2.5	13.8	7.27	16	41
TETP	0.051	62	220	550	2.6	12.1	6.34	14	34
DMPI	0.16	100	15	35	2.5	6.94	4.56	1.5	3.5
NBZ	0.03	110	220	500	2.3	10.8	5.42	24	54
XYL	1.1	57	210	8.0	0.04	9.25	3.72	12	0.46
C_9	0.60	55	350	33	0.09	8.86	2.44	20	1.8
C_{10}	0.19	100	290	20	0.07	11.3	3.12	28	2.0
C_{11}	0.055	52	625	50	0.08	12.5	3.44	23	1.2
CEOH	0.93	60	~5	~5	--	6.34	4.34	--	--
CHNO	0.57	110	~5	~5	--	9.14	4.66	--	--
C-X									
CEOH	0.96	110	5.0	7.0	1.4	6.34	4.34	0.55	0.77
BTOH	0.93	110	12	15	1.3	6.27	3.70	1.33	1.67
CHNO	0.57	110	32	65	2.1	9.14	4.66	3.50	7.22
DMMP	0.13	130	84	210	2.5	9.41	6.57	11.2	27.9

[a.] *CEOH, 2-chloroethanol; BTOH, 1-butanol; CHNO, cyclohexanone; DMMP, dimethyl methylphosphonate; DEMP, diethyl methylphosphonate; DIMP, diisopropyl methylphosphonate; TETP, triethylphosphate; DMPI, dimethylphosphite; NBZ, nitrobenzene; XYL, m-xylene; C_9, n-nonane; C_{10}, n-decane; C11, n-undecane)*

[b.] *Vapor pressure at 25°C from https://toxnet.nlm.nih.gov/cgi-bin/sis/htmlgen?HSDB.*

[c.] *Challenge concentration (C_o)*

[d.] *Breakthrough volume ratio: V_{b-10} [RTIL/C-B])/V_{b-10}[C-B or C-X]) from LSER modeling.*

Table 5.2. Physical properties of C-B and RTIL/C-B.

Adsorbent	avg. pore diam.[a] (nm)	avg. pore vol.[b] (cm^3/g)	surface area[c] (m^2/g)

C-B	~4	0.18	97.8
RTIL/C-B	~4	0.11	52.2

[a] *Calculated using the density functional theory (DFT);* [b] *The total pore volume is based on the sum of the mesopore and macropore volumes from the BJH model;* [c] *Calculated using the multipoint Brunauer−Emmett− Teller (BET) method.*

As shown in Table 5.1, the trends in V_{b10} values for XYL and DMMP depicted in Figure 5.3 are reproduced consistently among the additional five polar compounds and three non-polar compounds tested with C-B and RTIL/C-B. Note that the range of vapor pressures spanned by the polar vapors is similar to that spanned by the non-polar vapors. For the organophosphorus compounds, the ratio of V_{b10} values was remarkably consistent at 2.3-2.6 in favor of the RTIL/C-B adsorbent. Even for nitrobenzene the ratio was 2.3. For the n-alkanes, nonane, decane, and undecane, as for XYL, the RTIL coating led to a dramatic reduction in capacity, with V_{b10} ratios ranging from 0.09 to 0.04, corresponding to 11-26-fold rejections of these non-polar compounds with the RTIL/C-B. Note that the range of vapor pressures spanned by the polar vapors is comparable to that spanned by the non-polar vapors.

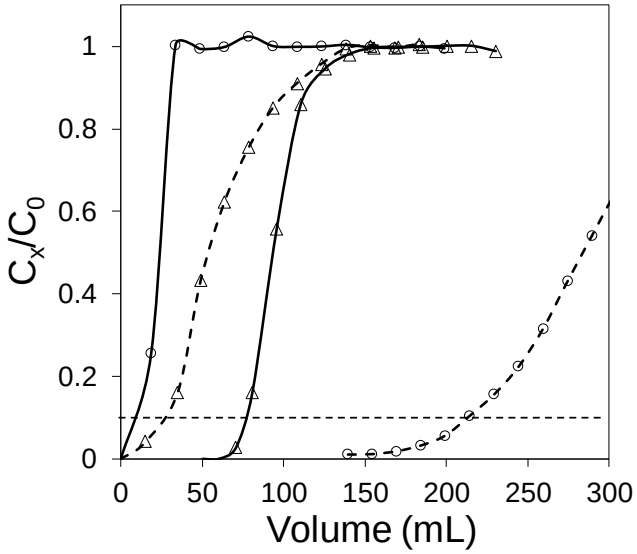

Figure 5.3. Representative breakthrough curves of DMMP (133 mg/m3, triangle) and XYL (57 mg/m3, circle) at 5 mL/min sampling flow rate and 26°C temperature. Individual compound was tested on C-B (solid lines) and RTIL/C-B (dash lines) separately.

Also shown in Table 5.1 are data for 2-chloroethanol (CEOH) and cyclohexanone (CHNO), for which V_{b10} values were < 5 mL for C-B and RTIL/C-B; too small to allow for reliable comparisons. Therefore, these were tested with the higher surface area C-X and RTIL/C-X. 1-butanol (BTOH) was also tested and DMMP was re-tested with this adsorbent pair as well.

As shown in Table 5.1, the V_{b10} ratios for these polar compounds were all > 1, and for DMMP the ratio was the same as that for the lower-surface-area adsorbent pair. The latter further demonstrates that the RTIL is dictating the relative affinities for the S/VOCs regardless of the surface area or pore structure of the adsorbent. The selectivity appears to be general, since the capacities for all polar compounds were enhanced with the RTIL. In terms of rejection, although the test set was limited, the effect also appears to be general, as it is evident in both aliphatic and aromatic hydrocarbons.

Another way to assess the selectivity of the RTIL/C-B is to compare M_{b10} values of polar and non-polar vapors of similarly volatility. For example, DEMP, DIMP, and TETP have vapor pressures similar to that of C_{11}. The ratios of M_{b10} values among these compounds range from to 24 to 34 in favor of the polar compounds. Interestingly, comparing DMPI and DMMP to C_{10}, all of which have similar, higher vapor pressures, the ratios are only 1.8 and 5, respectively. Thus, the selectivity varies inversely with volatility, consistent with less partitioning into the sorbent (i.e., smaller values of M_{b10}).

5.4.3. Humidity and Co-Vapor Effects

To test the potential effect of background humidity on the capacity of the RTIL/C-B, challenge tests with DMMP (110 mg/m^3) were repeated using two test atmospheres differing only in the humidity of the dilution matrix: one was dry N_2 and the other was N_2 to which sufficient water was added to achieve 70% relative humidity. As shown in Figure 5.4, the DMMP breakthrough curves were superimposable and the V_{b10} value was 75 mL in both cases. This indicates that water vapor does not mitigate the interaction of DMMP with the RTIL. It seems reasonable to extrapolate from this finding that it would not change the capacity for other organophosphorus compound either.

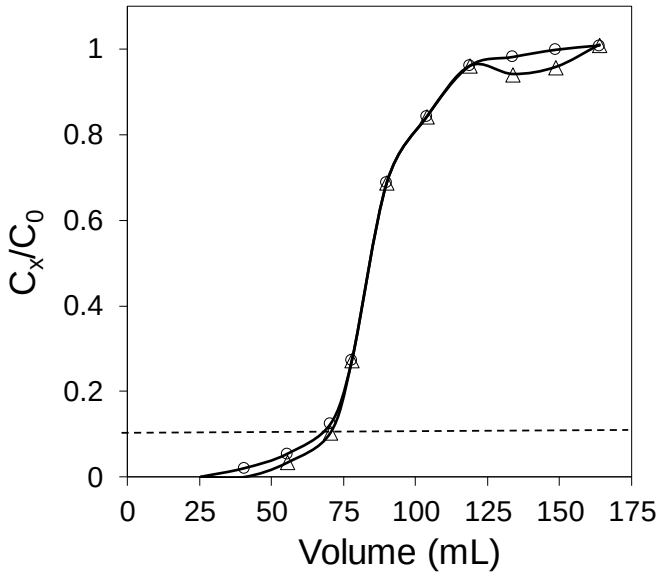

Figure 5.4. Effect of humidity on the capacity of the C-B and DID YOU ALSO TEST C-B? RTIL/C-B. Plots DMMP (~110 mg/m3) breakthrough curves in dry N_2 (circle, solid line) and N_2 with 70%RH (triangles, dashed line). Testing was conducted under 5 mL/min sampling flow rate and 26°C temperature.

Table 5.3 shows V_{b10} values for DMMP and XYL tested individually and then as a binary mixture at concentrations of 133 mg/m^3 and 14 mg/m^3, respectively. The individual V_{b10} values

are consistent with those in Table 5.1, with the values for DMMP being identical to those in Table 6.1 and those for XYL being much larger due to the lower concentration employed in these tests. For the mixture, V_{b10} for XYL did not change, while for DMMP it increased by 6 mL with both adsorbents. This corresponds to only ~1 min in breakthrough time. Thus, there is no competitive loss of either compound due to the presence of the other.

Table 5.3. DMMP and XYL breakthrough volume (Vb10) from individual and mixture testing

	V_{b10} (mL)			
	C-B		RTIL/C-B	
	individual	mixture	individual	mixture
XYL [a]	330	330	12	12
DMMP [b]	29	35	75	81

[a] *XYL,14 mg/m^3;* [b] *DMMP,133 mg/m^3* .

5.4.4. Modeling of Capacity

Prior to exploring the LSER-based modeling, we determined if vapor pressure alone could account for the trends in capacity we observed for C-B and for RTIL/C-B. Here again, we used values of M_{b10} rather than V_{b10} (see see Table 5.1). As shown in Figure 5a, for adsorption onto the uncoated C-B, plotting the M_{b10} values versus p_v^{-1} yielded a straight line for the polar compounds ($R^2 = 0.99$) and a separate non-linear, but monotonic, curve for the hydrocarbons. Of course, all of the M_{b10} values for the nonpolar compounds are larger than those of the polar compounds of similar vapor pressure for this nonpolar adsorbent. Thus, within the broad groups we have defined, vapor pressure provides an excellent means of predicting relative capacity. As shown in Figure 5b, for the RTIL/C-B, plotting the M_{b10} values versus p_v^{-1} also showed a strong linear dependence of capacity on vapor pressure among the polar compounds ($R^2 = 0.99$) but for the non-polar compounds there is no apparent dependence at all.

As discussed first by Payagala, et al.[36] the structure of this RTIL (Figure 5.1) is such that multiple solvation interactions might be possible with vapors partitioning into this RTIL thin film. These include ionic (the core cation and ligand anion), hydrogen-bond donation (via the amide hydrogen), hydrogen-bond acceptance (via the amide oxygen), π interactions (via the double bonds), dipole interactions via several moieties, and dispersion interactions, which are universal. Thus, it is well-suited for LSER modeling which can ostensibly identify those interactions having more or less importance in the net partitioning with different vapor phase compounds.

The values of the solvation coefficients *e*, *s*, *a*, *b*, and *l* for the RTIL reported by Lenca and Pooler were corrected for temperature by extrapolation of their values collected at elevated temperature to 26 °C, as described in the A4.5.1 in Appendix 4. The temperature-corrected values are listed in Table A4.3 (Appendix 4). The published values for Carbotrap, which we used as a surrogate for C-B, are also listed in Table A4.21 (Appendix 4). It is interesting to note that Carbotrap solvation coefficient values are all zero except for the *l* term. This implies an "ideal" surface with no functionality, which is consistent with the composition of all graphitized carbons[3], though at odds with reports by some researchers on other comparable graphitized carbon materials, where finite values for *s*, and *e* were found.[53,54]

Although LSER solute descriptors have been determined for numerous small organic molecules,[45] those for two of our test compounds, diethylmethylphosphonate (DEMP) and diisopropylmethylphosphonate (DIMP) have not yet been reported. Based on Abraham and Acree's work[56] we modelled descriptors for DEMP and DIMP by extrapolation from those reported for dimethylmethylphosphonate (DMMP) and related organophosphorus compound parameters. The approach taken to calculating values of DEMP and DIMP is given in the A4.5.2

(Appendix 4). To our best knowledge, this is the first report of LSER descriptors for DEMP and DIMP.

The products of the LSER solvation coefficients and descriptors for the RTIL and the targets vapors used in this study are listed in Table A4.4 (Appendix 4). Also listed are the corresponding "lL" products for the Carbotrap. From these, we calculated modeled *log K* values of our test vapors for C-B and for the RTIL using the respective versions of Eq. 5.2 with the regression constant *c* omitted. These are reported as *log* K_c and *log* K_{RTIL}, respectively, in Table 5.1. Note the importance of the dipolarity term (*sS*) and dispersion term (*lL*) among the variables, as well as the smaller but significant values of the *bB* term, which reflects the hydrogen bond acidity of the RTIL and basicity of the vapors (Table A4.4, Appendix 4). Note also that the *log* K_{RTIL} values are orders of magnitude lower than the corresponding *log* K_C values, as expected because the carbon is a high surface area material which interacts with vapors to a much greater extent than the liquid RTIL.

The dependence of M_{b10} on *log* K_C and *log* K_{RTIL} for the uncoated C-B and RTIL/C-B, respectively, are presented in Figure 6a and b, respectively. Not surprisingly, the former is very similar to Figure 5a because the only non-zero term in the LSER model for C-B is the dispersion term, which is highly correlated with solute size and, therefore, volatility. The only curious difference is that NBZ has shifted to the left and is now grouped with the hydrocarbons instead of the organophosphorus compounds as in Figure 5a. This can be explained by the relatively small value of L for NBZ, which is smaller than that for C11 despite NBZ having a lower vapor pressure. The correlation of M_{b10} for the RTIL/C-B with *log* K_{RTIL} is not particularly strong; while the hydrocarbons with lower *log* K_{RTIL} values also have smaller M_{b10} values, the dependence of M_{b10} on K for the polar compounds is not as strong as hoped.

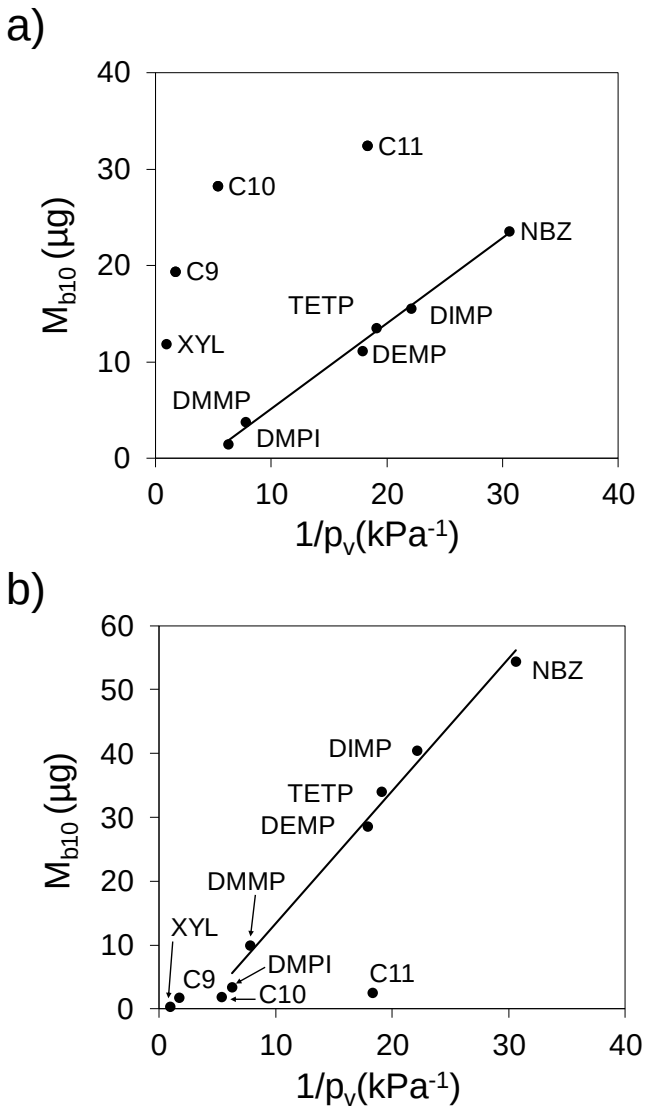

Figure 5.5. Plots of M_{b-10} versus $1/p_v$ of the test compounds for a) C-B and b) RTIL/C-B. Lines are the least-squares fit from linear regression for the 6 polar vapors (R^2>0.99 for both plots).

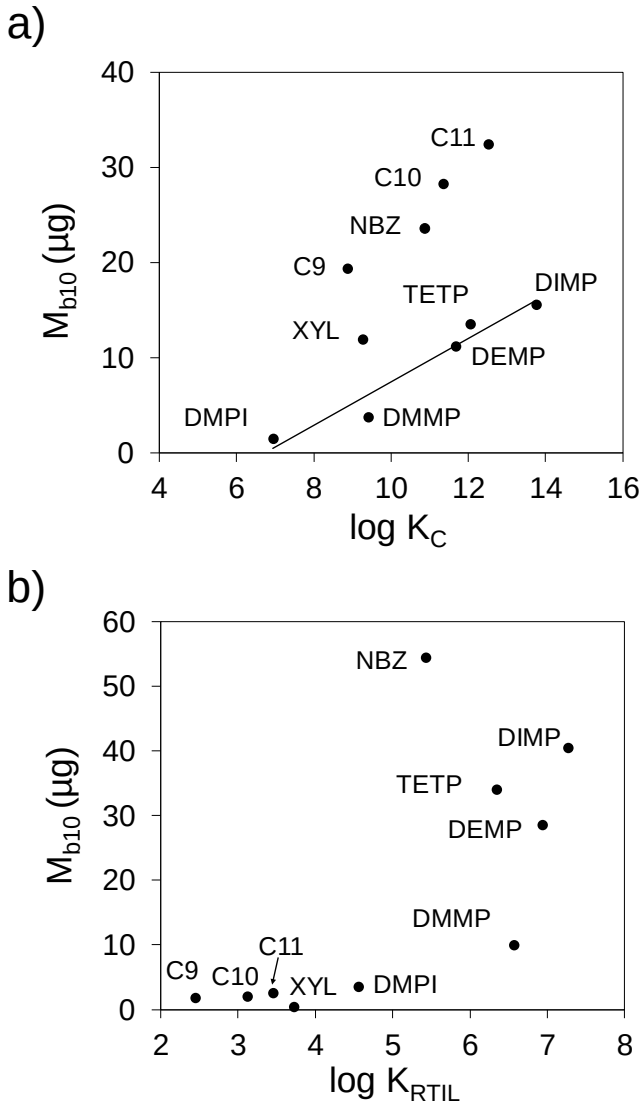

Figure 5.6. Plots of $M_{b\text{-}10}$ versus predictor of log K for a) C-B; b) RTIL/C-B. R^2>0.95 for regression in a

Finally, we tested the correlation of the ratio of *log K* values to the ratio of V_{b10} values (equivalent to ratio of M_{b10} values). The plot is shown in Figure 5.7. Although the clusters are apparent, one would expect to see a more positive correlation. Instead, for some of the mid-range ratios, for the same ratio value the ratio of breakthrough volumes is large for polar compounds. Thus, it appears that LSER modeling has limited value for this system.

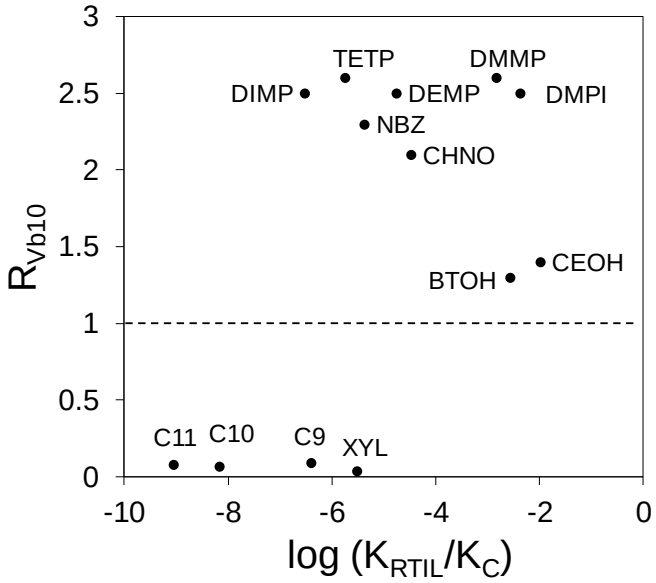

Figure 5.7. Plot of the ratio of breakthrough volumes RTIL/C-B:C-B to the ratio of log KRTIL/log KC.

5.5. Conclusions and Outlook

We conclude that the trigonal-tripyramidal RTIL used here serves as a highly effective surface modifier for Carbopack B and Carbopack X with respect to imparting selectivity for polar S/VOCs and against non-polar S/VOCs of similar volatility. Despite reducing the accessible surface area and pore volume, the capacity for polar vapors was enhanced significantly by applying ~monolayer quantities of the RTIL, and capacity ratios of polar-to-nonpolar vapors of similar vapor pressures ranged from 1.5 to 34. Breakthrough volumes for the 2.5-mg RTIL/C-B adsorbent bed tested ranged from 35 to 750 min for organophosphorus compounds with vapor pressures in the range of 0.045 to 0.13 kPa at concentrations of 50-130 mg/m^3. Neither humidity nor the presence of competing vapors affected the performance of the coated adsorbent, which was also stable for > 15 months of frequent vapor exposure and thermal cycling to 250 °C. Among the members of each sub-group of polar or non-polar compounds the trends in breakthrough volumes (masses) were strongly correlated with vapor pressure. Attempts to reconcile the trends further

using linear-solvation-energy relationship models were not highly successful. Nonetheless, it appears that RTIL-coating of carbon adsorbents can be used to impart a high degree of selective trapping of polar vapors, which could be useful in a new series of microfabricated preconcentration devices currently under development.

5.6. References

1. L.D. White, D.G. Taylor, P.A. Mauer, R.E. Kupel, A convenient optimized method for the analysis of selected solvent vapors in the industrial atmosphere, Am. Ind. Hyg. Assoc. J. 31 (1970) 225–232.
2. J. Namiesnik, Preconcentration of gaseous organic pollutants in the atmosphere, Talanta. 35 (1988) 567–587.
3. K. Dettmer, W. Engewald, Adsorbent materials commonly used in air analysis for adsorptive enrichment and thermal desorption of volatile organic compounds, Analytical Bioanalytical Chem. 373 (2002) 490–500.
4. M. Harper, Sorbent trapping of volatile organic compounds from air, J. Chromatogr. A. 885 (2000) 129–151.
5. SKC, Sorbent Tubes for Thermal Desorption, SKC, Inc - https://www.skcinc.com/catalog/index.php?cPath=200000000_201000000_201000100&osCsid=9678dcc5a4da19d4176ba71b8440b94a (accessed on May 23, 2019).
6. .Znose® , Electronic Sensor Technology, Inc. https://www.estcal.com/products. (accessed on May 23, 2019).
7. HAPSITE ER, Inficon, Available at http://products.inficon.com/en-us/nav-products
8. FROG-5000™, Defiant Technologies, http://www.defiant-tech.com/frog-5000-portable-gas-chromatograph.php (accessed on May 23, 2019).
9. Torion T-9 Portable GC/MS, PerkinElmer Inc. https://www.perkinelmer.com/lab-solutions/resources/docs/PRD_Torion-T-9-GCMS_012311B_01.pdf (accessed on May 23, 2019).
10. Apix Analytics. http://www.apixanalytics.com/chrompix/ (accessed on May 23, 2019).
11. P.R. Lewis, R. P. M., D.R. Adkins, R.J. Kottenstette, D.R. Wheeler, S.S. Sokolowski, D.E. Trudell, J.E. Bymes, M. Okandan, J.M. Bauer, R.G. Manley, G.C. Frye-Mason,. IEEE Sensors J. 2006, 6, 784-795.
12. C.-J. Lu, J. Whiting, R.D. Sacks, E.T. Zellers, Portable Gas Chromatograph with Tunable Retention and Sensor Array Detection for Determination of Complex Vapor Mixtures, Analytical Chemistry. 75 (2003) 1400–1409.
13. S. Zampolli, I. Elmi, F. Mancarella, P. Betti, E. Dalcanale, G. Cardinali, et al., Real-time monitoring of sub-ppb concentrations of aromatic volatiles with a MEMS-enabled miniaturized gas-chromatograph, Sens. Actuators, B. 141 (2009) 322–328. https://doi.org/10.1016/j.snb.
14. S. K. Kim, H. Chang, E. T. Zellers, Microfabricated gas chromatograph for the selective determination of trichloroethylene vapor at sub-parts-per-billion concentrations in complex mixtures," Analytical Chemistry, 2011, 83, 7198-7206.
15. R.-S. Jian, Y.-S. Huang, S.-L. Lai, L.-Y. Sung, C.-J. Lu, Compact instrumentation of a μ-GC for real time analysis of sub-ppb VOC mixtures, J.Microchem. 108 (2013) 161–167.

16. W. R. Collin, G. Serrano, L. K. Wright, H. Chang, N. Nuñovero, E. T. Zellers, "Microfabricated Gas Chromatograph for Rapid, Trace-Level Determinations of Gas – Phase Explosive Marker Compounds," Analytical Chemistry, 2014, 86, 655-663.
17. J. Wang, J. Bryant-Genevier, N. Nuñovero, C. Zhang, B. Kraay, C. Zhan, et al., Compact prototype microfabricated gas chromatographic analyzer for autonomous determinations of VOC mixtures at typical workplace concentrations, Microsystems & Nanoengineering. 4 (2018) 17101.
18. J. Wang, N. Nuñovero, R. Nidetz, S.J. Peterson, B.M. Brookover, W.H. Steinecker, et al., Belt-Mounted Micro-Gas-Chromatograph Prototype for Determining Personal Exposures to Volatile-Organic-Compound Mixture Components, Analytical Chemistry. 91 (2019) 4747–4754.
19. T. Sukaew, H. Chang, G. Serrano, E.T. Zellers, Multi-stage preconcentrator/focuser module designed to enable trace level determinations of trichloroethylene in indoor air with a microfabricated gas chromatograph, The Analyst. 136 (2011) 1664.
20. J. Bryant-Genevier, E.T. Zellers, Toward a microfabricated preconcentrator-focuser for a wearable micro-scale gas chromatograph, Journal of Chromatography A. 1422 (2015) 299–309.
21. Q. Zhong, R. Veeneman, W. Steinecker, C. Jin, S. Batterman, E. T. Zellers, Rapid Determination of ETS Markers with a Prototype Field-Portable GC Employing a Microsensor Array Detector, J. Environ. Monit., 9(2007), 440-448.
22. J. Lee, M. Jung, S. Barthwal, S. Lee, S.-H. Lim, MEMS gas preconcentrator filled with CNT foam for exhaled VOC gas detection, BioChip Journal. 9 (2014) 44–49.
23. G. Serrano, T. Sukaew, E.T. Zellers, Hybrid preconcentrator/focuser module for determinations of explosive marker compounds with a micro-scale gas chromatograph, J. Chrom. A. 1279 (2013) 76–85.
24. Adsorbent Selection Guide, Sigma-Aldrich Inc. https://www.sigmaaldrich.com/analytical-chromatography/air-monitoring/learning-center/adsorbent-selection.html (accessed 20 May 2019.)
25. C. Zhan , M. Akbar, R. Hower, J. Wang, N. Nuñovero, J. A. Potkay, E. T. Zellers, Integrated Multi-Vapor Micro Collector-Injector (uCOIN) for µGC. Proceedings of the 20th International Conference on Solid-State Sensors, Actuators and Microsystems, Transducers 2019, 23-27 June 2019 - Berlin, Germany. In press.
26. K. Ganesan, S. K. Raza, and R. Vijayaraghavan Chemical warfare agents J Pharm Bioallied Sci. 2010 Jul-Sep; 2(3): 166–178.
27. K. Huynh, S. Holdren, J. Hu, L. Wang, M.R. Zachariah, B.W. Eichhorn, Dimethyl Methylphosphonate Adsorption Capacities and Desorption Energies on Ordered Mesoporous Carbons, ACS Applied Materials & Interfaces. 9 (2017) 40638–40644.
28. P. Kowalczyk, P.A. Gauden, A.P. Terzyk, A.V. Neimark, Screening of carbonaceous nanoporous materials for capture of nerve agents, Phys. Chem. Chem. Phys. 15 (2013) 291–298.

29. W.-C. Hung, J.-C. Wang, K.-H. Wu, Adsorption and decomposition of dimethyl methylphosphonate (DMMP) on expanded graphite/metal oxides, Applied Surface Science. 444 (2018) 330–335..

30. R. P. Manginell, G.C. Frye-Mason, R. Kottenstette, P.R. Lewis, C. C. Wong, Microfabricated Planar Preconcentrator, Solid State Sensors and Actuators Workshop, Hilton Head, SC, USA, June 04-June 06, 2000.

31. C.F. Poole, S.K. Poole, Ionic liquid stationary phases for gas chromatography, Journal of Separation Science. 34 (2011) 888–900.

32. M. Kissoudi, V. Samanidou, Recent Advances in Applications of Ionic Liquids in Miniaturized Microextraction Techniques, Molecules. 23 (2018) 1437.

33. Y.-N. Hsieh, P.-C. Huang, I.-W. Sun, T.-J. Whang, C.-Y. Hsu, H.-H. Huang, et al., Nafion membrane-supported ionic liquid–solid phase microextraction for analyzing ultra trace PAHs in water samples, Analytica Chimica Acta. 557 (2006) 321–328.

34. J.-F. Peng, J.-F. Liu, G.-B. Jiang, C. Tai, M.-J. Huang, Ionic liquid for high temperature headspace liquid-phase microextraction of chlorinated anilines in environmental water samples, Journal of Chromatography A. 1072 (2005) 3–6.

35. P.S. Sharma, T. Payagala, E. Wanigasekara, A.B. Wijeratne, J. Huang, D.W. Armstrong, Trigonal Tricationic Ionic Liquids: Molecular Engineering of Trications to Control Physicochemical Properties, Chemistry of Materials. 20 (2008) 4182–4184.

36. T. Payagala, Y. Zhang, E. Wanigasekara, K. Huang, Z.S. Breitbach, P.S. Sharma, et al., Trigonal Tricationic Ionic Liquids: A Generation of Gas Chromatographic Stationary Phases, Analytical Chemistry. 81 (2009) 160–173.

37. N. Lenca, C. F. Poole, System map for the ionic liquid stationary phase tri(tripropylphosphoniumhexanamido) triethylaminebis(trifluoromethylsulfonyl)imde for gas chromatography, Journal of Chromatography A, 1524 (2017) 210–214.

38. S. Rodríguez-Sánchez, P. Galindo-Iranzo, A. Soria, M. Sanz, J. Quintanilla-López, R. Lebrón-Aguilar, Characterization by the solvation parameter model of the retention properties of commercial ionic liquid columns for gas chromatography, Journal of Chromatography A. 1326 (2014) 96–102. doi:10.1016/j.chroma.2013.12.020

39. W.R. Collin, A. Bondy, D. Paul, K. Kurabayashi, E.T. Zellers, μGC × μGC: Comprehensive Two-Dimensional Gas Chromatographic Separations with Microfabricated Components, Analytical Chemistry. 87 (2015) 1630–1637. 39a. D. W. Armstrong Measuring Water: The Expanding Role of Gas Chromatography, LC-GC; http://www.chromatographyonline.com/measuring-water-expanding-role-gas chromatography (accessed May 24, 2019).

40. G.O. Wood, E.S. Moyer, A review of the Wheeler equation and comparison of its applications to organic vapor respirator cartridge breakthrough data, Am. Ind. Hyg. Assoc. J. 50 (1989) 400-407.

41. C.J. Lu, E.T. Zellers, A dual-adsorbent preconcentrator for a portable indoor-VOC microsensor system, Analytical Chemistry, 73 (2001) 3449–3457.

42. W.C. Tian, S.W. Pang, C.J. Lu, E.T. Zellers, Microfabricated preconcentrator-focuser for a microscale gas chromatograph, Journal of Microelectromechanical Sys. 12 (2003) 264-272.

43. T. Sukaew, E. T. Zellers, “"Evaluating the Dynamic Retention Capacities of Microfabricated Vapor Preconcentrators as a Function of Flow Rate,”, Sensors and Actuators B Chemical, 183, 163-171, 2013.

44. F. Rouquerol, J. Rouquerol, K. Sing. Adsorption by Powders and Porous Solids, in K Sinig, F. Rouquerol, J. Rouquerol (Eds.), Classical Interpretation of physisorption Isotherms at the Gas–Solid Interface 2nd edition, Elsevier, 2014.pp160-186.

45. M.H. Abraham, Scales of solute hydrogen-bonding: their construction and application to physicochemical and biochemical processes, Chemical Society Reviews. 22 (1993) 73.

46. K.-U. Goss, R.P. Schwarzenbach, Linear Free Energy Relationships Used To Evaluate Equilibrium Partitioning of Organic Compounds, Environmental Science & Technology. 35 (2001) 1–9.

47. U. Kipka, D. M. D. Toro, A Linear Solvation Energy Relationship Model of Organic Chemical Partitioning To Particulate Organic Carbon In Soils And Sediments, Environmental Toxicology and Chemistry 2011, 30 (9), 2013–2022.

48. S. Endo, K.-U. Goss, Applications of Polyparameter Linear Free Energy Relationships in Environmental Chemistry, Environmental Science & Technology 2014, 48 (21), 12477–12491.

49. M. H. Abraham, A. Ibrahim, A. M. Zissimos, Determination of sets of solute descriptors from chromatographic measurements. J. Chromatogr. A 2004, 1037 (1−2), 29−47.

50. A. Hierlemann, E. T. Zellers, A. J. Ricco, Determination of partition coefficients from surface acoustic wave vapor sensor responses and correlation with gas-liquid chromatographic partition coefficients, Analytical Chemistry, 2001, 73, 3458-3466.

51. Mark Vitha, P. W. Carr, The chemical interpretation and practice of linear solvationenergy relationships in chromatography, Journal of Chromatography A, 1126 (2006) 143–194

52. P. Burg, M. Abraham, D. Cagniant, Methods of determining polar and non-polar sites on carbonaceous adsorbents. The contribution of the linear solvation energy relationship approach, Carbon. 41 (2003) 867–879.

53. C. West, E. Lesellier, A unified classification of stationary phases for packed column supercritical fluid chromatography, Journal of Chromatography A. 1191 (2008) 21–3.

54. M. Schneider, K.-U. Goss, Systematic Investigation of the Sorption Properties of Tenax TA, Chromosorb 106, Porapak N, and Carbopak F, Analytical Chemistry. 81 (2009) 3017–3021.

55. C.F. Poole, S.K. Poole, Separation characteristics of wall-coated open-tubular columns for gas chromatography, Journal of Chromatography A, 1184 (2008) 254–280

56. M.H. Abraham, W. E. Acree Jr., Descriptors for the Prediction of Partition Coefficients and Solubilities of Organophosphorus Compounds, Separation Science and Technology, 48, 884–897, 2013.

Conclusions

This dissertation has described four research projects relating to the development of microfabricated device for aqueous VOC extraction, two μGC instrument prototypes, and materials for graphitized carbon black surface chemistry medications intends a broad application of field/clinical analyses of water contaminants and urinary biomarkers of exposure and disease, industrial hygiene and exposure assessment, industrial process monitoring, homeland security, the explosive sand chemical warfare agents collections. This chapter summarizes the major achievements and conclusions reached, the impacts of the accomplishments, the directions that future efforts for each of the project.

Chapter 2 described that we have designed, microfabricated, and characterized a 2.8×2.3 cm microfabricated vapor extractor (μVE) for VOC extraction from water and biofluids. Fffects of operating conditions including gas flow rate, liquid flow rate, and temperature, on the performance of the μVE were characterized. The μVE was first characterized and optimized by interfacing a gas chromatiography-flame ionization detector (GC-FID) system with a 6-port valve to inject extractor vapors into analytical system. The microsystem, the hybrid μVE-μGC system, was demonstrated using synthetic urine spiked with 4 VOCs from a 700-μL sample in 3.5 min. The extraxcted VOCs were preconcentrated, injected, separated and detected by μGC in ~80 sec with detection limits as low as 660 ppb. Combining response patterns from the μCR array with chromatographic retention times was shown to enhance the reliability of VOC determinations. Although these preliminary results are promising, further work is needed to assess the impact of VOC properties, PDMS membrane thickness, and device operating conditions on performance. With decreases in LODs and sample volumes compared to current techniques, for example, purge and trap, headspace sampling and solid phase microextraction. The μVE-μGC microsystem should

be suitable for on-site analyses of a wide range of VOCs in water and biofluids in environmental, workplace, and clinical settings.

Despite this promising performance, the µVE performance was less than optimal particularly the time required to reach a steady state extraction rate. This larger than expected time constant increases analysis time and the required sample volume. Through a thorough design review, improvements have been identified to reduce the time constant. They are: 1) improved liquid-side fluidic design. The current design has areas of low or stagnant flow in the largest liquid flow channels. These areas of stagnant flow increase device filling time and result in "dead volume", both of which increase the time required to reach steady state. The liquid side could be redesigned to increase flow uniformity throughout and thereby improve analysis time; 2) improved membrane bonding. In the current devices, the bonding of the membrane to the liquid side die was imperfect. Under liquid flow, it was observed that small areas of the membrane became detached from the liquid side. This detachment occurred over some of the extraction channels, thereby effectively increasing the channel height in these areas. This increase in channel height increases resistance to diffusion, which in turn increases the time constant of the system. Bonding will be improved in future devices; 3) decreased membrane thickness. The original design targets called for a 15 µm membrane and µVE devices with 15, 30, and 100 µm membranes were fabricated. 15 µm-membrane devices were damaged during assembly and initial testing. 30 µm-membrane devices were damaged during the testing process. Most of the results presented in this report are thus for 100 µm-membrane devices. Increased membrane thickness will increase resistance to diffusion and thus increase the time to steady state. Membrane thickness will be reduced in future designs. When these improvements are implemented, it is expected that the required extraction time and sample volume will be decreased by approximately an order of magnitude each.

Chapter 3 concerns a benchtop prototype instrument containing a gas chromatographic microanalytical system (μGC) designed for the selective determination of multiple airborne volatile organic compounds (VOCs) at concentrations in the vicinity of recommended occupational exposure limits. The core microsystem consists of a set of discrete Si-microfabricated devices: a dual-cavity, adsorbent-packed micro-preconcentrator-focuser (μPCF) chip that quantitatively captures and thermally desorbs/injects VOCs with vapor pressures between ~0.03 and 13 kPa; tandem micro-column (μcolumn) chips with cross-linked PDMS wall-coated stationary phases capable of temperature-programmed separations; and an integrated array of five μchemiresistors (μCR) coated with different thiolate-monolayer protected gold nanoparticle (MPN) interface films that quantifies and further differentiates among the analytes by virtue of the response patterns generated. Other key components include a pre-trap for low-volatility interferences, a split-flow injection valve, and an onboard He carrier–gas canister. The assembled unit measures 19×30×14 cm, weighs ~3.5 kg, operates on AC power, and is laptop/LabVIEW controlled. Component- and system-level tests of performance demonstrated injection bandwidths <1 s, a μcolumn capacity of ≥8 μg injected mass, linear calibration curves, no humidity effects, excellent medium-term (that is, 1 week) reproducibility, autonomous operation for 8 h, detection limits below Threshold Limit Values (TLV) for 10 mL air samples collected in 1 min, and response patterns that enhanced vapor recognition. The determination of a 17-VOC mixture in the presence of seven interferences was performed in 4 min. Results augur well for adapting the microsystem to an all-MEMS wearable μGC currently under parallel development.

We concluded that the PEMM-1 prototype μGC described in this work is capable of direct, autonomous, multi-VOC determinations at concentrations relevant to workplace applications. The speed, reliability, selectivity, limits of detection, dynamic ranges, low operating power, and types

of VOCs amenable to accurate detection and recognition render the PEMM-1 an effective new addition to the repertoire of quantitative exposure assessment tools available to occupational health scientists. Reconciling the tradeoffs among VOC mixture pre-selection, pre-concentration, separation, and recognition/detection functions was central to realizing effective system-level performance. Collectively, the operational features and performance characteristics of the PEMM-1 prototype demonstrated in this study exceed those demonstrated with other prototype μGCs reported to date. The results obtained from this study have been used to inform the design of a battery-powered, wearable prototype (PEMM-2), from which promising preliminary data to have recently been generated. The results from that effort will be the subject of a forthcoming article. Future work on optimizing sensor coating strategies should yield improvements in peak shapes and reductions in LODs.

Chapter 4 describes a belt-mountable prototype instrument containing a gas chromatographic microsystem (μGC) and demonstrate its capability for near-real-time recognition and quantification of volatile organic compounds (VOCs) in moderately complex mixtures at concentrations encountered in industrial workplace environments. The μGC comprises three discrete, Si/Pyrex microfabricated chips: a dual-adsorbent micropreconcentrator−focuser for VOC capture and injection; a wall-coated microcolumn with thin-metal heaters and temperature sensors for temperature-programmed separations; and an array of four microchemiresistors with thiolate-monolayerprotected-Au-nanoparticle interface films for detection and recognition−discrimination. The battery-powered μGC prototype (20 × 15 × 9 cm, ∼2.1 kg sans battery) has on-board microcontrollers and can autonomously analyze the components of a given VOC mixture several times per hour. Calibration curves bracketing the Threshold Limit Value (TLV) of each VOC yielded detection limits of 16−600 parts-per-billion for air samples of 5−10 mL, well below

respective TLVs. A 2:1 injection split improved the resolution of early eluting compounds by up to 63%. Responses and response patterns were stable for 5 days. Use of retention-time windows facilitated the chemometric recognition and discrimination of the components of a 21-VOC mixture sampled and analyzed in 3.5 min. Results from a "mock" field test, in which personal exposures to time-varying concentrations of a mixture of five VOCs were measured autonomously, agreed closely with those from a reference GC. Thus, reliable, near-real-time determinations of worker exposures to multiple VOCs with this wearable μGC prototype appear feasible

Chapter 4 concludes that the PEMM-2 prototype, employing a core analytical subsystem made entirely from Si-glass microfabricated components, is well-suited for measuring near-realtime worker (personal) exposures to the components of moderately complex multi-VOC mixtures at concentrations encountered in industrial environments. The capability for recognizing and quantifying VOC-mixture components embodied in the PEMM-2 is not available in current wearable monitoring instrumentation and has not been reported in the literature. MPN film quality and stability could be improved with greater care in synthesis, storage, and film deposition. Further reductions in size and weight could be achieved readily by incorporating a smaller (custom) He canister and regulator and a smaller and lighter valve manifold. Reductions in power should be possible by implementing sequential heating of the SC segments. The work can also focused on demonstrating unattended (battery) operation for 8 h and testing in actual workplaces.

Most adsorbent materials used in preconcentrators for trapping and thermally desorbing volatile and semi-volatile organic compounds (S/VOCs) in portable/"micro" gas chromatographic (GC/μGC) instruments preferentially capture non-polar or moderately polar compounds relative to more polar compounds. In Chapter 5, we explored the use of a trigonal-tripyramidal room-temperature ionic liquid (RTIL) as a surface modifier for the graphitized carbons, Carbopack B

(C-B) and Carbopack X (C-X), with the goal of imparting selectivity for polar S/VOCs and against non-polar S/VOCs of similar volatility. Most testing was focused on C-B. After coating the C-B with an amount of RTIL corresponding nominally to a full monolayer, the N_2 BET surface area decreased by ~50% but there was little effect on the pore size distribution. Breakthrough tests were performed by challenging tubes packed with ~2.5 mg of C-B or RTIL-coated C-B with 12 individual S/VOCs, including several organophosphorus compounds and alkyl and aromatic hydrocarbons roughly matched on vapor pressures, at concentrations in the range of 24-130 mg/m^3. The 10% breakthrough volume, V_{b10}, was used as the performance metric. For the RTIL/C-B, the V_{b10} values for the 6 organophosphorus vapors were consistently ~2.5-fold larger than those for the untreated C-B. Furthermore, the V_{b10} of the non-polar reference vapors were 11-26-fold smaller with the RTIL/C-B than for the untreated C-B. Similar results were obtained with C-X and RTIL/C-X on a more limited set of compounds. Tests with a binary mixture of a polar and non-polar compound gave results very similar to those for individual compounds. Humidity did not affect the V_{b10} for the one test performed with a polar compound with the RTIL/C-B. And there was no evidence of bleed and no loss of capacity after 100 cycles from 25 to 250 °C. Among the members of each sub-group of polar or non-polar compounds the trend in breakthrough volumes/masses was strongly correlated with vapor pressure for both adsorbents. Attempts to reconcile the selectivity patterns using linear-solvation-energy relationship models were only partially successful. Nonetheless, it appears that RTIL-coating of carbon adsorbents can be used to impart a high degree of selective trapping of polar vapors.

Appendix 1: Supplementary Information for Chapter 2

A1.1. The channel and membrane of µVE

Table A1 listed the inlet (i), outlet (o), conduction (c), and extraction (e) channels in two different membrane thickness 30 µm and 100 µm, respectively, in this study.

Table A1. 1. The details of channels, membrane thickness and surface area the two device in this study

	i/o (µm)			c (µm)			e(µm)			δ_m (µm)
	w	d	l	w	d	l	w	d	l	
Devices	370	740	15700	60	120	5930	15	30	1000	30/100

A1.2. the modeled SSEE for polar and nonpolar compounds

The following SSEE is modeled based on liquid flow rate, 0.36 mL/min and channel height, 17 µm. using Eq.

Table A1.2. The modeled SSEE for VOC.

Compound	**K_{pw}**	**D_w (cm^2/s)**	**D_p (cm^2/s)**	**SSEE**
Benzene	126	9.8×10^{-6}	5.2×10^{-6}	90
Trichloroethylene	174	9.1×10^{-6}	1.4×10^{-6}	88
Toluene	174	8.6×10^{-6}	1.2×10^{-6}	85
p-xylene	564	8.4×10^{-6}	0.7×10^{-6}	86
Ethylbenzene	513	7.8×10^{-6}	5.0×10^{-7}	83
Methyl ethyl ketone (MEK)	0.79	9.8×10^{-6}	7.6×10^{-6}	37
Acetone	0.28	1.1×10^{-5}	2.9×10^{-6}	8
2-butanol	0.23	9.3×10^{-6}	2.7×10^{-6}	7
Ethanol	0.04	1.2×10^{-5}	1.0×10^{-5}	4
Methanol	0.003	1.6×10^{-5}	1.9×10^{-5}	1

A1.3. Presentative chromatograms from µVE-GC/FID of VOC mixture testing

Figure A2 shows results of testing a mixture of toluene (TOL, 86 ppm), trichloroethylene (TCE, 146 ppm), perchloroethylene (PCE, 162 ppm), and 2-butanone (MEK, 81 ppm) in water with a liquid flow rate of 0.2 mL/min and a gas flow rate of 5 mL/min. Analysis was done sing a downstream GC-FID with a short capillary column between the sampling loop injector and the FID to allow separation of the components. The time-to-steady-state ranged from ~5-12 min; much longer than predicted. Steady-state permeation rates were within +/-50% of model predictions. Discrepancies are ascribed to variations in PDMS thickness and/or gradual/incomplete access to all extraction channels.

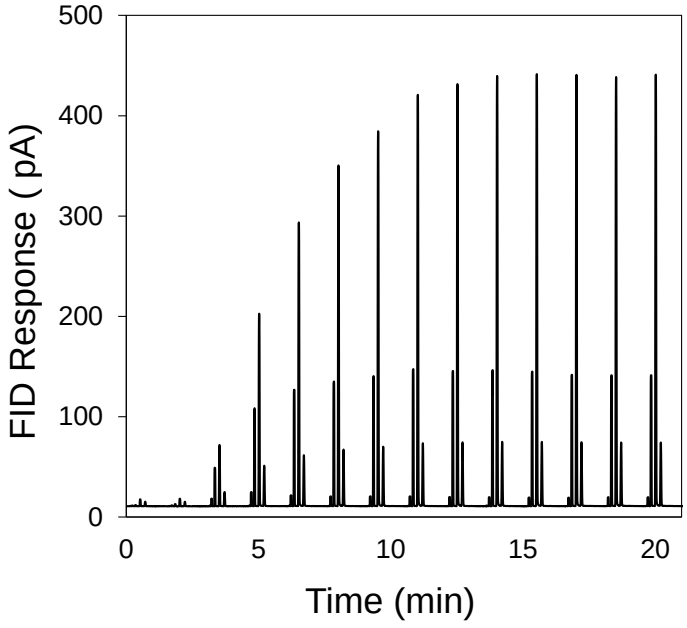

Figure A1.1. Typical VOC mixture chromatograms of periodical injections by 6-port valve into GC-FID analysis system from time 0 to steady state. Characterization data from the FID showing consecutive injections from the sampling loop over time. Sample are TOL, TCE, PCE, and MEK with the concentration of 86, 146, 162, and 81 ppm, respectively, in urine. The injection liquid flow rate is 0.2 mL/min and gas flow rate is 5 mL/min.

Applendix 2: Supplentary Information for Chapter 3

A 2.1. Abstract:

Included in this Supplementary Information file are data and descriptions of various components and aspects of the PEMM-1 prototype design and operation that elaborate on those presented in the main body of the Chapter3. We have organized these into sections (i.e., A1, A2, etc.) as follows, and refer to these, and to the corresponding figures and tables, in the main body of the article:

A2.2. PEMM-1 Electronics and Power/Energy Dissipation Estimates

A2.3 System Design and Operating Specifications

A2.4. Pre-trap Characterization

A2.5. μPCF Characterization

A2.6. μColumn Characterization

A2.7. PEMM-1 Thermal Stability and Interconnect Heaters

A2.8. PEMM-1 Sample Throughput: Effect of Pre-Trap on Quantification

A2.9. Calibration Curves, Sensitivities, and LODs

A2.10. Reliability: Medium Term Stability

A2.11. Response Patterns and Confusion Matrices

A2.2. PEMM-1 Electronics and Power/Energy Dissipation Estimates

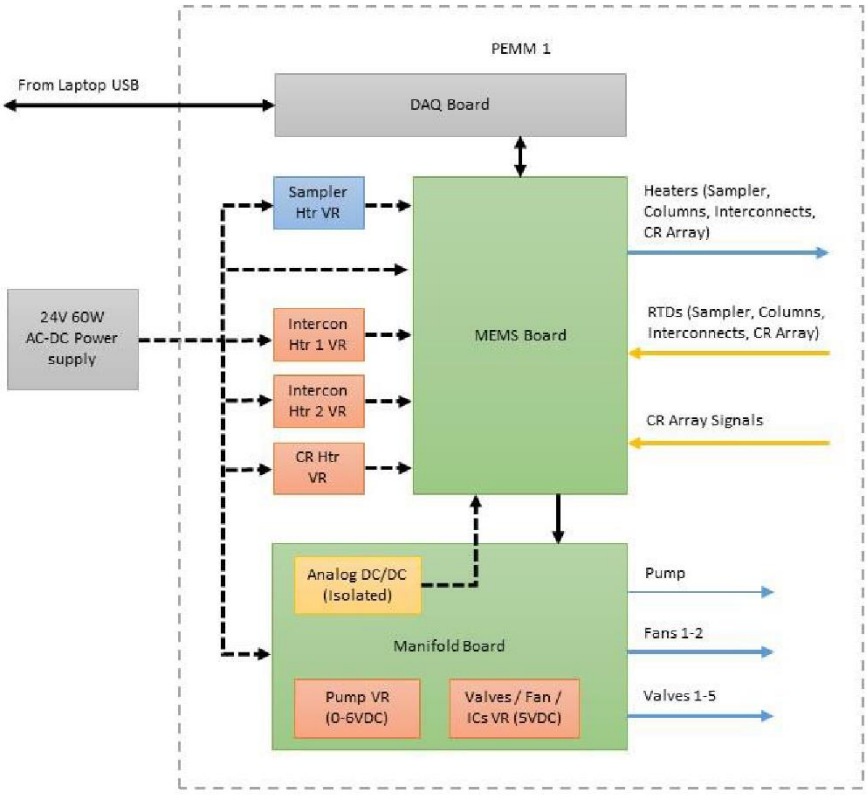

Figure A2.1. Block diagram of the PEMM-1 electronic hardware and associated fluidic hardware and microsystem components to which they are connected.

A2.2.1. Electronic Circuitry

A schematic diagram of the PEMM-1 electronic circuits is presented in Figure A1. Although the PEMM-1 is AC powered, an external AC-DC converter was used to match the DC operating voltage to be used in the PEMM-2 (wearable) prototype. A set of adjustable high efficiency DC-DC converters was employed to supply the range of voltages required for each system component. Two PCBs were fabricated to provide the control signals to and to read output signals from all components. The "Manifold" PCB was dedicated to actuating the pump, valves and fans. The "MEMS" PCB was dedicated to mediating the control and data acquisition functions for µPCF heating, µcolumn heating, and µCR array sensor output signals. Step-down converters

were used for powering the pump, valves, fans, μCR sensors, interconnection heaters and μPCF. Step-up voltage regulators were avoided due to noise affecting the temperature sensors of the micro-devices, and instead a direct feed from the AC-DC converter was used to supply the voltage level required (24VDC) to control the μcolumn heaters. For the μCR array acquisition circuit the DC-DC converter was electrically isolated and additional voltage regulation was employed to achieve low baseline noise on the sensor signals.

A single multifunctional DAQ board (USB-6216 OEM, National Instr., Austin, TX) was identified to meet all acquisition and control requirements. Electronic signal handling circuitry was needed to attain the resolution and dynamic range for the μCR array signals for the wide range of concentrations anticipated for the targeted compounds.

Among the considerations in the PCB layouts was the appropriate use of low-noise design techniques to maintain the integrity of the noise-sensitive signals, most importantly from the μCRs. At the front-end of the μCR interface electronics, a nulling circuit was implemented to cancel the baseline resistance contribution to the sensor output signals. An algorithm was developed to generate the digitally controlled signals for baseline cancellation during initial start-up of the instrument. This implementation also compensated for medium- and long-term drift in sensor resistances, and maximized the signal-to-noise ratio prior to digitization.

In addition, an automated selection feature of appropriate excitation voltages for the μCRs was created, achieving similar circuit sensitivities regardless of sensor resistances, and improving the reproducibility of the response measurements. By monitoring the cancelling signals applied to the aforementioned nulling circuit, it was possible to convert the measured output voltages to changes in relative resistance (i.e., $\Delta R/R$) and to display the responses in such units in real time.

Independent proportional-integral-derivative (PID) feedback loops were designed to achieve control and optimal reproducibility of the device temperature programs at the specified heating rates and set-point temperatures. Solid-state relays, mounted on the PCBs, were used to control the device heaters by pulse-width-modulation (PWM) generated signals. The μCR array signals, device temperatures, and instrument configuration parameters were monitored and stored for subsequent data analysis.

Each CR in the array was connected in series with an on-board bank of four reference resistors having values of 300K, 1M, 3M and 10M, respectively. These resistance values were selected to cover the expected span of MPN-coated μCR baseline resistances, R_b. Each sensor channel on the MEMS board was configured to allow one of these resistors to be selected to serve as a reference. A direct current was applied to each sensor in the μCR array. Then, using a custom LabVIEW program, R_b was estimated for each CR sensor and the reference resistor that most closely matched R_b was automatically selected from the bank. For performance characterization tests, 3 VDC was applied to each μCR in series with its reference resistor. A voltage signal, controlled by LabVIEW, was generated to subtract the baseline voltage (V_b) of each μCR sensor to obtain the voltage drop (ΔV) associated to the sensor response. This voltage was then amplified, collected and finally converted by the LabVIEW software to the preferred output signal, relative resistance change ($\Delta R/R_b$), via the expression:

$$\Delta R/R_b = \frac{3 \cdot \Delta V}{V_b[G(3-V_b)-\Delta V]}$$

where G is the gain of the amplifiers.

A2.2.2. Power and Energy Dissipation

From the anticipated battery requirements of PEMM-2, a 24V, 60W power supply was selected for PEMM-1 on the basis of iterative analyses of the voltage requirements of the Ti/Pt heaters of the μcolumns and μPCF estimated from simulations and experiments. The total cycle time was conservatively assumed to be 8 min, of which 1 min was allotted for sampling, 4 min for separation and detection, and 3 min for cool down and backflushing the pre-trap in preparation for the next sample. On the basis of previous tests, the desorption time from the μPCF (i.e., time of heating) was set at 40 s, which ensures complete desorption of the least volatile analytes. The 4-min separation time is conservative; the temperature program assumed for the μcolumns is the same as that used to assess the temperature stability of the system (see Figure A6 and associated text below). The inter-column interconnect heater and the press-tight heater between the downstream column and the sensor array were included in the budget. The press-tight heater between the μPCF and upstream μcolumn was shown not to be necessary so was not included. In addition, since the internal temperature of the unit was ~30 °C and stable, the μCR array heater was not included in the budget.

As shown in Table A1, the total energy per cycle is 4.1 kJ, corresponding to an average power of 8.5 W for an 8-min cycle. It can be seen that the μcolumns are the largest consumers of energy, using 34% of the total system energy, and 92% of the energy used for the microsystem. Of the total system energy, an additional ~11% is consumed by the interconnect heaters between μcolumns and between the downstream μcolumn and CR array. The control electronics (DAQ, MEMS and Manifold PCBs) account for another 34% of the PEMM-1 energy consumption. The pneumatic components (pump and latching valves) only account for the 0.3% of the total energy. The energy required to cool the PEMM-1 unit and the micro devices represents

~18% of the total system demand. The remaining ~3% is devoted to heating the μPCF and to the drive currents in the μCR array.

A2.3. Comments on System Design and Operational Specifications

Specifying the minimum and maximum volumes of air samples to be captured in a typical (default) analysis requires careful consideration, and will ultimately be case specific. A minimum sample volume is required that is sufficient to capture enough mass of each analyte to accurately quantify its concentration at some specified level. This is related to the LOD in terms of the injected sample mass. Although we assumed a working value of 5 ng on the basis of previous work with μCR arrays,[A1-A4] in order to obtain measurable signals from all sensors (e.g., for pattern recognition), this LOD would be for the least sensitive sensor in the array (i.e., that providing the lowest signal:noise for a given VOC). To relate this to an LOD in terms of air concentration requires a benchmark concentration to be established. Assuming that 0.1×TLV is a suitable minimum concentration, the minimum sample volume would then depend on the target VOC with the lowest TLV value. Assuming that accurate quantification is important up to, say, 4×TLV, which would represent a fairly high concentration, and further stipulating that such a concentration must generate responses that are >40×LOD, then the required sample volumes would be the same as those for 0.1×TLV levels. The maximum sample volume is also subject to several constraints, including the capacity of the μPCF adsorbents, the capacity of the stationary phase in the μcolumns, and the dynamic response ranges of the sensors.

Table A2.1. Power demand of each component in PEMM-1 and net energy dissipation for a typical sampling and analytical cycle.[a]

Component	Voltage (V)	Current[b] (A)	Power[b] (W)	Qty	Time (s)	Energy (J)
µPCF heater	16	0.12	1.9	1	40	76
µcolumn heaters	24	0.12	2.9	2	240	1400
µcolumn interconnect heater	8.5	0.024	0.20	1	480	96
downstream press-tight heater[a]	7.6	0.097	0.74	1	480	360
pump	6.0	0.040	0.24	1	60	14
latching valves	5.0	0.13	0.65	5	0.01	0.03
enclosure fan [c]	5.0	0.17	0.85	1	480	410
MEMS fans [d]	5.0	0.13	0.65	2	240	310
µCR array drive currents	3.0	0.030	0.09	1	480	43
MEMS board	±12	0.010	0.24	1	480	120
manifold board	6.0	0.020	0.12	1	480	58
DAQ board	5.0	0.50	2.5	1	480	1200
Totals			8.5		480	4100

[a] Assumptions: 8-min cycle; 60-s sample; 40-s desorption heating; 4-min separation; unheated µCR array (30 °C internal temp.); press-tight union between µcolumn and µCR array held at 80 °C; latching valves driven by 10 ms pulses; 3-min cooling/purge; voltage conversion losses and laptop power consumption not included; [b] Electric currents of µPCF and µcolumns are avg. values per component over the specified duration; [c] Enclosure fan mainly provide heat dissipation from the electronics boards.[d] MEMS fans promote cooling of µPCF and µcolumns prior to next cycle.

The problem of reconciling sample volumes and/or the required dynamic range of the analytical system with VOC mixtures having widely disparate TLVs was discussed in our previous article,[A5] and remains unresolved – it would need to be addressed on a case-by-case basis. For the testing performed here we assumed a sample volume of 5 or 10 mL. For a representative VOC, like toluene, present at 2.0 ppm, or 7.5 ng/mL, which corresponds to 0.1 × TLV, a 10 mL sample would correspond to a captured mass of 75 ng. At 4 × TLV, the captured mass would be 3 µg.

In practice, it may be necessary to have two operating modes for the PEMM-1, depending on the range of expected VOC concentrations in a given working environment. For cases where high concentrations are expected (e.g., where multiple VOCs are present at, say, 100 ppm or more), our provisional sample volume of 5-10 mL should be adequate such that even in the presence of

co-contaminants, benzene, which has the lowest TLV value of all targets, could still be measured at its TLV with a signal corresponding to 3×LOD (i.e., at 0.5 ppm, which is 1.5 ng/mL of benzene, a 10 mL air sample would capture 15 ng), while maintaining an acceptably low risk of breakthrough due to excessive captured masses of other VOCs, which have higher TLVs, that might be present at concentrations of, say, 4×TLV. For low concentration environments, sample volumes as high as 30 mL could be used without risk of benzene breaking through the μPCF, even in the presence of interferences.[A5]

A2.4. Pre-trap Characterization

Devices were challenged with test atmospheres of one or more VOCs in N_2-filled sampling bags, which were placed in a sealed drum and pressurized to push the atmosphere through the pre-trap at a known rate. A bench scale GC (Agilent 6890, Agilent Technol., Palo Alto, CA) was used downstream to monitor the VOC concentrations directly or via a sampling loop that was periodically injected. Either a short segment of uncoated, deactivated capillary or a short PDMS-coated separation column was used between the GC inlet port and the FID.

Initial tests used packed-tubes containing 5.4 mg of either C-F or C-C (i.e., pre-trap A) and entailed individual challenges with n-alkanes C_{11} to C_{13} at ~200 ppm. Both adsorbents showed significant fractional retention of C_{11} from 10 mL sample volumes and, while the C-F provided a 10% breakthrough volume of ~25 mL for C_{13}, it required heating with backflushing for regeneration. Additional experiments with different bed masses and at different temperatures and concentrations failed to arrive at a viable arrangement with these granular adsorbents. We also tried glass beads, but these did not show sufficient retention of C_{13}.

We then explored capillary-column pre-traps B1 and B2, again using C_{11} and C_{13} as our primary test vapors. With pre-trap B1, the breakthrough volumes of both analytes were

independent of flow rate, from 4 to 11 mL/min, and concentration, from ~0.4 to ~2 ppm, and linearly dependent on the length of the pre-trap, from 4 to 10 cm. Increasing the pre-trap temperature from 20 to 25 °C resulted in a 10% decrease in the 10% breakthrough volume for C_{13}. Both pre-traps B1 and B2 showed similar retention behavior. Pre-trap B2, however, showed slightly better discrimination between C_{11} and C_{13} based on the ratio of 90% and 10% breakthrough volumes, respectively (Figure A2). For mixtures of compounds with p_v values similar to that of C_{11}, the presence of additional compounds did not decrease the breakthrough volume relative to that of any single compound for either pre-trap. Regarding regeneration, after passing 10 mL of a 3 ppm sample of C_{13} through pre-trap B2 and reversing the fluidic connections to allow monitoring with a downstream FID while backflushing at ambient temperature, it required 20 mL before the FID had returned to baseline. As discussed below, we ended up using pre-trap B1 in the final testing of PEMM 1 in this study. Additional results are presented in Section A7.

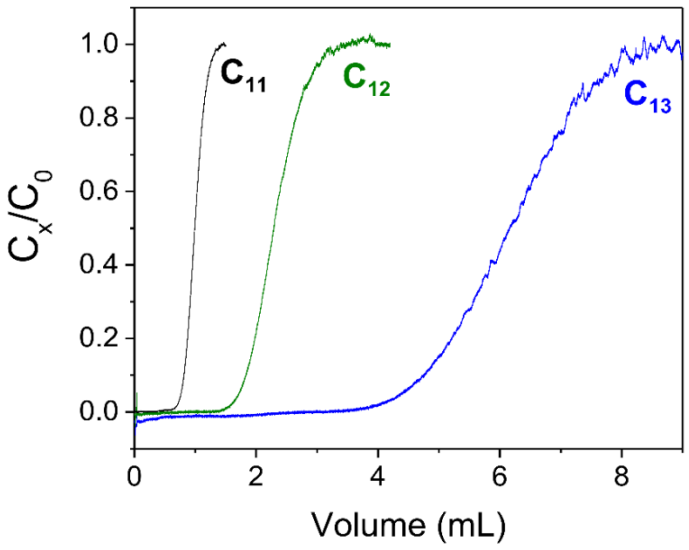

Figure A2.2. Fractional breakthrough of C11, C12, and C13 vapors (individual exposures at ~ 100 ppm each) as a function of sample volume (5 mL/min) for pre-trap B2 (consisting of 6.5 cm long segment of 250 µm i.d. capillary with a 0.1 µm thick wall coating of Rtx-20). Note that the 10% breakthrough volume for C13 was ~5 mL while the 90% breakthrough volume for C11 was 1.2 mL.

A2.5. µPCF Characterization

Figure A3 presents the injection peaks for benzene, toluene, and n-dodecane using a 2:1 split injection (i.e., 9 mL/min desorption flow rate; 3 mL/min analytical flow rate). See text in the main body of the article for discussion.

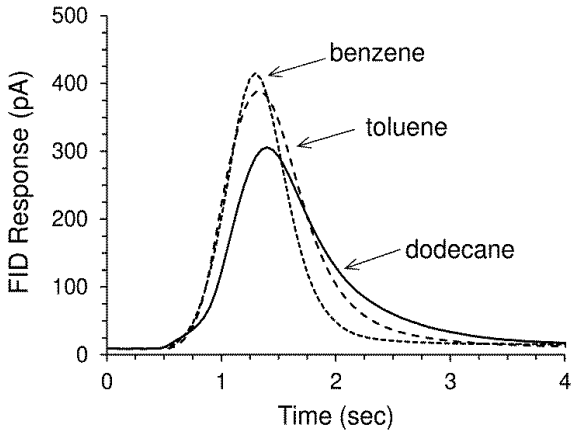

Figure A2.3. Injected peaks for benzene, toluene, and n-C12 from the µPCF prior to system integration. The device was connected across two ports of a 6-port valve, 0.5 µg of each vapor was loaded from individual-vapor static test atmospheres, and thermally desorbed with a 2:1 split directly to the FID; analytical flow rate was maintained at 3 mL/min.

A2.6. µColumn Characterization

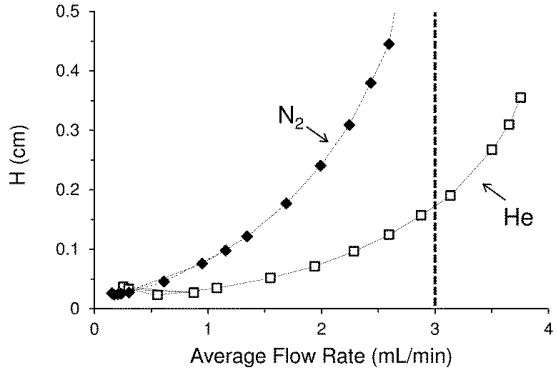

Figure A2.4. Golay plot for the dual µcolumns generated from a mixture of methane (for hold-up time) and n-octane in N2 and He carrier gases as indicated. Gas-tight syringe injections and FID detection were used. The maximum plate count, N, was ~4,300 plates/m with N2 or He at optimal flow rates of 0.17 and 0.56 mL/min, respectively. The vertical dashed line highlights the difference in H values at 3 mL/min, which was the analytical-path flow rate used for most testing.

Prior to system integration, the separation efficiency and sample capacity of the dual μcolumns were characterized. The μcolumns were installed in the oven of the bench scale GC-FID and connected between the inlet and FID via press-tight unions. Analytes were introduced by autosampler syringe or by sample loop connected to a 6-port valve (Model AC6WE, Vici Valco, Houston TX) mounted to the GC. The FID was calibrated with analytes diluted in CS_2. Injections of a vapor-phase mixture of methane and n-octane were made at each of several flow rates in both N_2 and He carrier gases at 30°C. Plate height, *H*, determined by standard methods,[A6] was plotted against flow rate as shown in the Golay plots in Figure A4 for both carrier gases. Results are discussed in the text of the main body of this article.

To evaluate μcolumn capacity, separations were conducted at 50°C and 3 mL/min of a mixture of neat benzene, toluene, and isopropylbenzene (i.e., cumene, p_v = 0.6 kPa) over a range of injected masses from 0.15 μg to as high as 30 μg, and the *fwhm* values of the peaks were used as the metric. [A6] The resulting *fwhm* values are plotted in Figure A5a. For benzene and toluene, the *fwhm* values increased by < 10% up to about ~8 μg and then increased at a somewhat higher rate up to 30 μg. The ratio of *fwhm* values for the highest lowest injected masses was < 1.7 for both compounds. For cumene, with a substantially larger retention factor, the *fwhm* also increased by < 10% up to ~8 μg and then showed a sharp increase with larger injection masses up to 15 μg. In this case, the ratio of *fwhm* values for the highest and lowest injection masses was also < 1.7. Of course, temperature is an important cofactor: higher temperatures reduce the retention factors of all analytes and, thus, the dependence of the *fwhm* on mass injected, because sorption equilibria are shifted in favor of the mobile phase. With temperature programmed separations, the influence of this factor would vary; benzene would probably elute completely before the μcolumns reached

50°C, increasing the chances of overloading, whereas cumene would likely elute at > 50°C, reducing the ultimate impact of this factor on the *fwhm*.

In a follow-up experiment the chromatographic resolution of benzene and trichloroethylene under the same GC conditions was constant up to an injected mass of ~8 μg of each component, and then started to decrease at larger injected masses. Results are presented in Figure A5b. Taken together, these data provide some confidence that injections smaller than ~8 μg of any single component would not result in significant reductions in chromatographic performance due to overloading of the stationary phase.

A2.7. PEMM-1 Thermal Stability and Effect of Interconnect Heaters

Thermal Profiles. The assembled PEMM-1 prototype was then run through a series of sampling and analytical cycles to check for thermal stability and reproducibility. First, a blank static test atmosphere of N_2 was sampled for 1 min at 10 mL/min, valves were actuated and the pump stopped, He was passed at 3 mL/min through the core microsystem, the μPCF was heated to mimic (splitless) injection, and the μcolumn heaters initiated a temperature program typical of that to be used in practice. The full analytical cycle lasted 4 min. Upon reaching the maximum μcolumn temperature, the instrument was allowed to cool for 3 min, during which time two dedicated cooling fans adjacent to the μPCF and μcolumns, respectively, were activated. This 8-min sequence was repeated 22 times over the course of 3 hours; readings from the RTDs in the system and the thermocouple on the fluidic carrier plate were recorded.

Figure A6 shows the data from a representative run. The fidelity of component temperatures to their set point temperatures was excellent. The temperature of the fluidic carrier plate, which reflects the internal temperature of the prototype, rose by only ~3 °C in sync with the

temperatures of the µcolumns. Active cooling (optional) reduced the temperature of the µPCF during sampling to roughly 27-28 °C during the above sequence of runs. There was no cumulative drift over the course of the experiment.

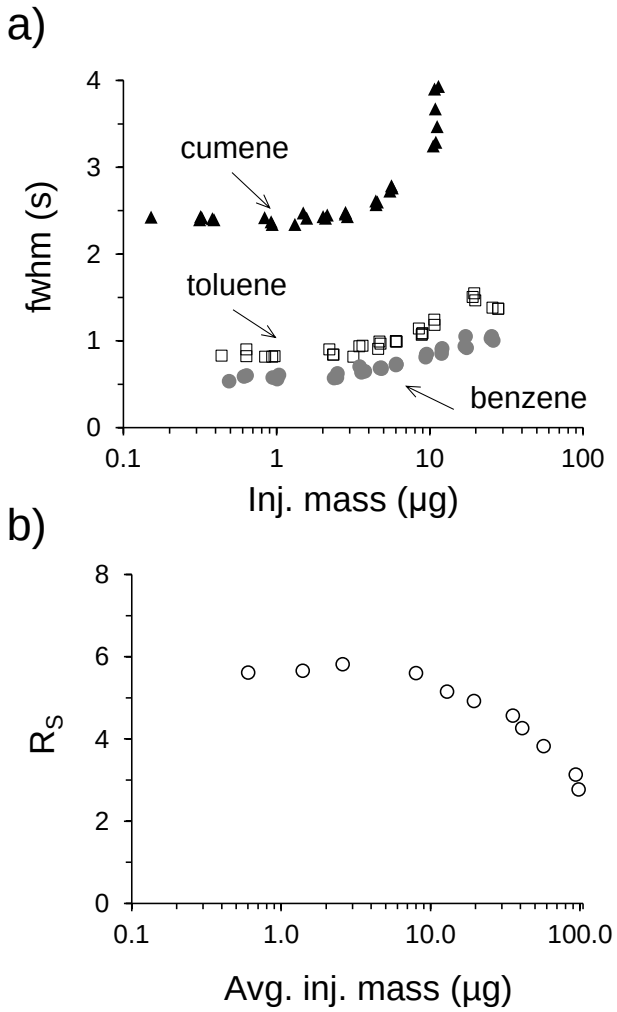

Figure A2.5. Effect of injected mass on chromatographic resolution for the µcolumn ensemble (6 m total length); a) effect of mass on fwhm for three target vapors, benzene, toluene and cumene, and b) effect of injected mass on chromatographic resolution of benzene and trichloroethylene. Mass in b) is the average mass of trichloroethylene and benzene in the injection, and the binary mixture was in a 1.5:1 ratio, respectively, to account for differences in FID sensitivity (i.e., to maintain similar peak sizes).

Although variability was low, deviation from the applied ramp was apparent at the beginning of each new ramp rate. As can be seen in Figure A6, small, transient increases in the

temperature ramp for both µcolumns at 0 and 2 minutes indicate a small over-shoot in the slow ramps. These are apparently an artifact of the voltages used in the PWM algorithm used to control the temperatures of these components. Due to the highly reproducible nature of these deviations, their impact on retention times is low.

For the µCR array, without active heating, the relative standard deviation around the average temperature was 1.7% (temperature ranged from 29.8 to 30.2°C). There was no trend in this variation; it did not track the temperature of the enclosure or the µcolumns. This extremely small shift in temperature is likely attributable to the engineered thermal isolation of the device, which is elevated above its PCB (i.e., suspended by the connecting capillaries) and shielded inside a metallic faraday cage with no circulating air.

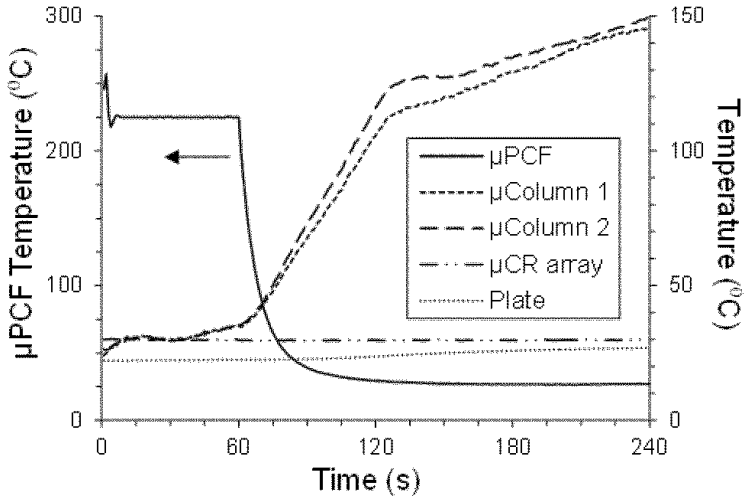

Figure A2.6. Temperature profiles of system components for a representative analytical cycle of PEMM 1 prototype. µPCF temperatures are referenced to the left hand vertical axis, and temperatures of the other components are referenced to the right hand vertical axis. The fluidic carrier "plate" thermistor was used to indicate ambient internal temperature of the system enclosure; all other measurements were taken directly from the fluidic component RTDs; µcolumn 1 was ramped at 5°C/min from an initial 30°C to 35°C (1 min), then at 75° C/min to 110 °C (1 min), then at 20°C/min to 150 °C (2 min); µcolumn 2 was ramped at 5°C/min from an initial 30°C to 35°C (1 min), then 85° C/min to 125 °C (1 min), then 15°C/min to 150 °C (2 min).

2.7.1. Interconnect heaters

The analytical cycle described above was repeated without heating one or the other press-tight unions connecting the μcolumns to the μPCF and μCR array, to evaluate the effect. A test atmosphere containing a homologous series of n-alkanes from C_6 to C_{12} at ~100 ppm each was used. Since these press-tight union heaters demand a large amount of power, it was necessary to evaluate their relevance to the chromatographic performance of the system. When the union between the μPCF and μcolumns was left unheated, no change in *fwhm* was observed for any of the 7 compounds (n-hexane through n-dodecane). This makes sense, because the first μcolumn was held at 30°C for the first 30 sec of the separation. It was concluded that the more volatile fraction of analytes does not adhere to the uncoated union at these temperatures, and the less volatile fraction of analytes undergoes on-column focusing upon reaching the μcolumn, reducing any extra-column band broadening due to the transfer capillary.[A7] When the union between the μcolumn and FID was left un-heated, *fwhm* for n-nonane, n-decane, n-undecane, and n-dodecane increased by 2.8%, 7.0%, 12% and 21%, respectively (no change in *fwhm* was observed for n-hexane, n-heptane or n-octane). The changes in *fwhm* for n-nonane and n-decane were not significant. This suggests that for mixtures containing analytes with vapor pressures < 0.59 kPa, the unheated downstream union introduces a significant source of extra column band broadening.

A2.8. PEMM-1 Sample Throughput: Effect of Pre-Trap on Quantification

To double check the pre-trap retention properties when installed at the inlet of PEMM-1, the B1 pretrap (65 mm, 250 μm i.d. capillary column with 0.1 μm thick PDMS, Rtx-1 phase) was installed at the front of the PEMM-1 prototype. A test atmosphere containing 10 compounds spanning a p_v range from 58.1 kPa (n-C_5) to 0.0075 kPa (n-C_{13}) each at ~100 ppm was prepared in an 8-L Flex-foil bag, and 10 mL of the mixture was sampled through the pre-trap or the same

length of an uncoated capillary and the μPCF was heated to inject the VOCs (splitless). For these tests, the μCR array was bypassed and eluting peaks were quantified with an FID. For quality control, a sample of the same mixture was collected in a sample loop and analyzed by GC-FID in parallel. Triplicates were collected for all tests.

Results are summarized in Figure A7 in terms of each of three ratios of peak areas, R_1, R_2 and R_3: R_1 = PEMM-1 without pre-trap vs. GC-FID; R_2 = PEMM-1 with pre-trap vs. GC-FID; and R_3 = PEMM-1 with pre-trap vs. PEMM-1 without pre-trap. A smaller value of R_1 would reflect either breakthrough of the μPCF, in the case of the more volatile analytes, or retention or entrainment losses on components of the PEMM-1 flow path not related to the pre-trap. A smaller value of R_2 would reflect retention on the pre-trap and retention or entrainment losses relative to the reference method. A smaller R_3 would reflect losses only due to the pre-trap.

The 8-12% loss of the co-eluting pair, C_5 and MEK, can be ascribed to μPCF breakthrough of a portion of the sampled masses of these vapors, since these compounds would not be retained at all by the pre-trap. Since these are less volatile than benzene, and thus were considered interferences, some degree of μPCF breakthrough was expected (see ref A5). All later-eluting target compounds, from benzene to C_{12}, were analyzed with 97-99% throughput (see the R_3 values in Figure A7). For C_{13}, the R_3 value indicates that the pre-trap removed/retained all but 28% of the sample mass compared to operation without the pre-trap. However, the R_1 value indicates that there are other loss mechanisms, since operation without the pre-trap resulted in only 73% throughput compared to the parallel GC-FID analysis. Adsorption on surfaces of other components in the flow path are apparently involved. This reveals an inherent constraint of the PEMM-1, which does not have heated transfer lines upstream of the μcolumns. Thus, the threshold vapor pressure below which quantitative throughput would not be expected is somewhere between

0.027 kPa (C_{12}) and 0.007 kPa (C_{13}), notwithstanding any mitigating effects arising from the polarity of the VOC.

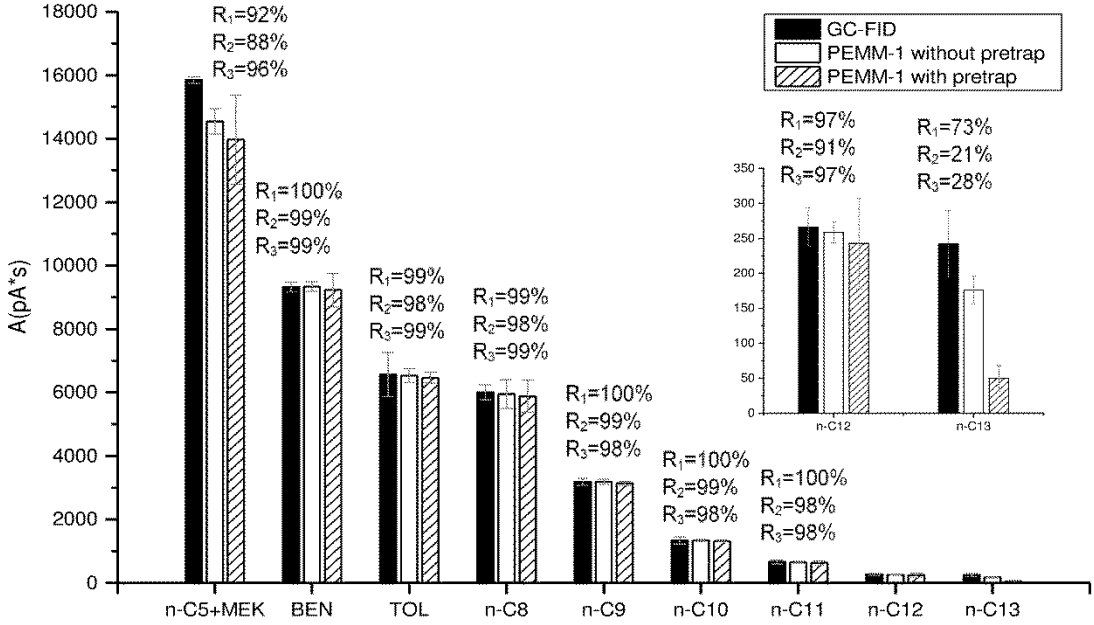

Figure A2.7. Results of tests of PEMM-1 sample throughput for representative compounds using an FID in place of the uCR array for detection. Peak areas (A) with and without the pre-trap are compared to each other and to those generated from samples analyzed by a reference GC-FID. R1=PEMM-1 without pretrap/GC-FID, R2=PEMM-1 with pretrap/GC-FID, R3= PEMM-1 with pretrap/PEMM-1 without pretrap. PEMM-1conditions: 10 mL sample of a mixture of all compounds shown at ~100 ppm of each; splitless injection at 3 mL/min in helium; FID. Pretrap B2 was used (65 mm, 250μm ID with 0.1 μm thick Rtx-20). GC-FID: 100 μL loop injection; He carrier gas. Responses from the GC-FID were multiplied by 100 x to account for smaller sample volume.

A2.9. Calibration Curves, Sensitivities, and LODs

Calibration curves for all VOC-sensor combinations are given in Figure A8. Values of the slope, derived from least-squares linear regression with forced zero are given in Table A2 along with the R^2 values. The corresponding limits of detection (LOD) calculated from injected

masses are given in Table A3. LODs, in ng, were calculated as 3σ/slope, where σ is the RMS noise level.

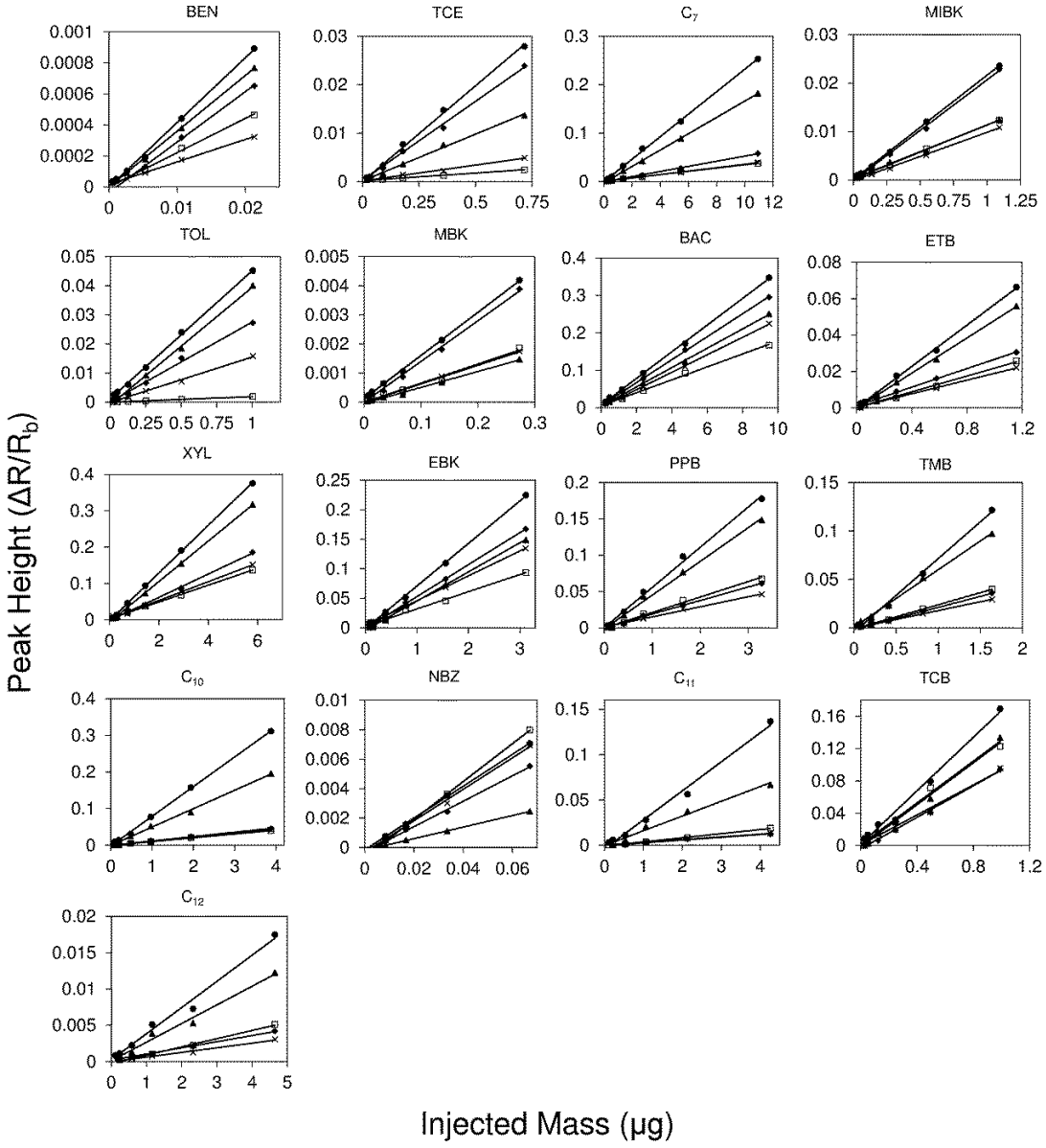

Figure A2.8. Calibration curves for 17 targets from PEMM-1. For each target VOC, the peak height is plotted as a function of injected mass. Peak heights were converted from relative voltage changes to relative resistance changes (i.e., $\Delta R/R_b$) prior to plotting (see Section A1). The range of masses corresponds to a concentration range of 0.1×-4× TLV, assuming a sample volume of 10 mL. All calibrations were performed with He carrier gas using a split injection, with a split ratio of 2:1(vent: analysis), where the flow rate through the analytical path was 3 mL/min. The temperature programs of both µcolumns were as follows: 28 °C for 0.5 min, then 10°C/min to 33°C, then 50°C/min to 125°C, then hold at 125°C for 1.2 min. The CR array temperature was 30 °C. Legend: EOE, filled circles; C8, filled triangles; OPH, filled diamonds; TEG, crosses; HME, unfilled squares.

Although LODs tended to vary directly with vapor pressure for the non-polar C8- and EOE-coated sensors, there were several exceptions, and no such trend was observed among the sensors with more polar MPN coatings. This is because sensitivity also varies with the affinity between the functional groups in the VOCs and MPN thiolates and, evidently, the MPN film thickness, which would affect the rates of VOC sorption and desorption.

Table A2.2. Forced-zero regression slopes and R^2 values of the 17 target VOCs from the calibration curves presented in Figure A8 for the PEMM-1 prototype μGC. [a]

μCR	BEN		TCE		C_7		MIBK	
	Slope	R^2	Slope	R^2	Slope	R^2	Slope	R^2
EOE	0.0416	0.998	0.0395	0.997	0.0232	0.992	0.0217	0.999
C8	0.0360	0.999	0.0195	0.997	0.0165	0.999	0.0115	0.994
OPH	0.0156	0.991	0.0068	0.990	0.0036	0.997	0.0098	0.997
TEG	0.0303	0.993	0.0331	0.996	0.0052	0.998	0.0206	0.998
HME	0.0221	0.994	0.0035	0.981	0.0032	0.994	0.0114	0.998

μCR	TOL		MBK		BAC		ETB	
	Slope	R^2	Slope	R^2	Slope	R^2	Slope	R^2
EOE	0.0457	0.996	0.0155	0.996	0.0367	0.997	0.0568	0.998
C8	0.039	0.996	0.0052	0.990	0.0264	0.998	0.048	0.999
OPH	0.0154	0.997	0.0063	0.995	0.0236	0.998	0.019	0.997
TEG	0.0276	0.996	0.014	0.996	0.0315	0.998	0.0269	0.993
HME	0.019	0.994	0.0065	0.985	0.0181	0.994	0.0218	0.995

μCR	XYL		EBK		PPB		TMB	
	Slope	R^2	Slope	R^2	Slope	R^2	Slope	R^2
EOE	0.0651	1.000	0.0715	0.999	0.0555	0.995	0.0718	0.990
C8	0.0541	0.998	0.0475	0.995	0.0458	0.995	0.0598	0.998
OPH	0.0263	0.997	0.0439	0.995	0.0145	0.992	0.0178	0.998
TEG	0.0315	0.997	0.0536	0.999	0.0188	0.983	0.0213	0.991
HME	0.0238	0.997	0.0304	0.990	0.0212	0.990	0.024	0.995

μCR	C_{10}		NBZ		C_{11}		TCB	
	Slope	R^2	Slope	R^2	Slope	R^2	Slope	R^2
EOE	0.0803	0.999	0.1049	0.989	0.0306	0.987	0.1679	0.989
C8	0.05	0.997	0.0354	0.986	0.0161	0.985	0.131	0.990
OPH	0.004	0.989	0.1005	0.990	0.0031	0.976	0.0939	0.988
TEG	0.0084	0.993	0.0798	0.989	0.0029	0.989	0.0915	0.988
HME	0.0078	0.993	0.1146	0.981	0.0043	0.987	0.1277	0.991

μCR	C_{12}							
	Slope	R^2						
EOE	0.0037	0.986						
C8	0.0026	0.984						
OPH	0.0006	0.985						
TEG	0.0009	0.986						
HME	0.0011	0.986						

[a] *Slope is in units of $\Delta R/R_b/\mu g$, where the mass is 1/3 of the mass captured on the μPCF to account for the 2:1 injection split . See caption of Figure A8 for conditions of analysis. Acronyms for the VOCs in the column headings and for the sensor MPN coatings in the rows are defined in the main body of the article.*

Table A2.3. Limits of detection (LOD) of the 17 target compounds for each μCR in the PEMM-1 prototype μGC on the basis of injected mass using a 2:1 split injection.[a]

Compounds	LOD (ng)				
	EOE	C8	OPH	TEG	HME
BEN	9.5	11	32	19	30
TCE	10	19	73	18	190
C_7	17	23	140	110	200
MIBK	18	33	51	28	57
TOL	8.7	10	32	21	34
MBK	26	73	79	41	100
BAC	11	14	21	18	36
ETB	7.0	7.9	26	22	30
XYL	6.1	7	19	18	27
EBK	5.5	8	11	11	22
PPB	7.1	8	34	31	33
TMB	5.5	6	28	27	27
C_{10}	4.9	8	46	49	63
NBZ	4.8	11	4.9	7.3	5.7
C_{11}	13	23	100	200	150
TCB	2.4	2.9	5.3	6.3	5.1
C_{12}	110	140	820	640	590

[a]*LODs were calculated as 3σ/sensitivity, where σ is the standard deviation of the baseline noise for each sensor and sensitivity is the forced-zero linear-regression slope of peak height versus injected mass. The values of σ, in units of* $(\Delta R/R_b) \times 10^6$*, were as follows: 132(EOE), 126 (C8), 165 (OPH), 193 (TEG), and 218 (HME). The conditions of analysis are given in the caption of Figure A8. Only 1/3 of the mass captured on the μPCF was injected due to the 2:1 split employed. Acronyms for the VOCs and MPN sensor coatings are given in the text of the main body of the article.*

A2.10. Reliability: Medium Term Stability

To assess the reproducibility of analyses performed daily over 7 days, samples from the same static test atmosphere (Flex-foil bag) containing a subset of 9 VOCs at ~100 ppm each were collected by the PEMM-1 prototype (10 mL sample volume) and by a 100 μL sample loop of a bench-scale GC-FID system. The PEMM-1 analyses employed a 2:1 split injection whereas the GC-FID analyses employed a splitless injection. Separation conditions were otherwise the same for both methods, entailing the same temperature program and a He carrier gas flow rate of 3

mL/min in the analytical path. For the PEMM-1, 4 samples were collected each day, with each sample separated in time by at least 1 hr. For the GC-FID, only 1 sample was collected at the end of each day. Results are summarized in Tables A4 and A5.

In Table A4 the RSD (%) around the mean response (peak area) and mean retention time (t_R) obtained from each of two μCR sensors are presented. The C8 sensor gave the lowest variability and the OPH gave the highest variability, on average, among the sensors in the array, and are therefore considered representative of the data set. The peak area data are the same as presented in Table 2 in the main article, and show that the range of intra-day RSD values is quite low for the C8 sensor (range: ~1 to 8 %) and higher for the OPH sensor (range: ~1 to 10%). For the t_R data, the variability is quite low for both sensors, ranging from 0.1 to 1.3% for all VOCs except for n-heptane (C7), which is the earliest eluting mixture component, and which had RSDs ranging from 0.2 to 3.6%. Overall, these data demonstrate a high level of analytical reproducibility by the PEMM 1 prototype, though the variation in sensitivity exhibited by the OPH-coated sensor would argue for replacing this sensor in the future.

Table A5 compares the weekly average values of peak area, *fwhm*, and t_R from the C8 sensor of the PEMM 1 and from the GC-FID, along with the corresponding RSDs for each of the 9 VOCs in the mixture. As shown in Table A5, the mean values of peak area were higher for the GC-FID due to its higher sensitivity. Despite this, the variability in replicate responses, expressed as the RSD (%) around the mean values, were only slightly higher for the PEMM-1 C8 sensor for all 9 VOCs: 2.7-9.6% for PEMM-1 (C8) and 1.3-7.5% for the GC-FID. The relative variation of *fwhm* values was lower for the PEMM-1, in part, because of the larger values of *fwhm* from the C8 sensor. The variation of t_R values was lower for the GC-FID in all cases, but was < 1% for the majority of VOCs with the PEMM-1, which is considered quite acceptable. Overall, the medium-

term stability of analytical performance of the PEMM-1 is judged to be quite good on the basis of these results.

Table A2.4. Stability of peak area and retention time measurements from PEMM-1 on the basis of 4 measurements per day for each of 7 days for a 9-VOC mixture.

Cmpd	μCR	Daily RSD (%)[a]													
		peak area (A)							retention time (t_R)						
		1	2	3	4	5	6	7	1	2	3	4	5	6	7
C_7	C8	1.6	2.1	2.4	2.4	2.4	1.1	1.6	1.5	1.3	1.7	1.5	0.9	0.5	0.4
	OPH	4.1	3.1	4.7	7.3	6.6	3.4	3.0	3.6	1.6	1.2	2.3	2.2	0.2	0.3
BAC	C8	1.3	2.4	2.1	1.5	3.7	2.9	2.0	0.7	1.0	1.6	1.0	0.6	0.4	0.6
	OPH	0.8	2.0	1.2	1.4	1.4	2.6	1.5	1.2	0.8	0.6	1.8	1.4	0.4	0.3
XYL	C8	2.4	3.1	1.8	3.6	4.4	3.0	1.0	0.6	0.8	1.1	0.7	0.4	0.3	0.4
	OPH	2.2	3.5	3.6	5.0	2.1	4.0	2.8	0.7	0.7	0.4	1.3	1.1	0.4	0.2
EBK	C8	2.4	4.1	3.5	3.5	3.5	4.2	4.7	1.0	0.7	1.0	0.7	0.4	0.4	0.4
	OPH	2.3	3.2	1.9	2.4	1.6	3.0	3.5	0.7	0.7	0.4	1.1	1.0	0.3	0.1
PPB	C8	2.7	3.2	3.4	1.9	4.8	3.2	2.0	0.7	0.7	0.8	0.6	0.3	0.2	0.5
	OPH	3.0	5.9	4.1	5.1	5.7	7.9	4.0	0.4	0.7	0.3	0.9	0.9	0.4	0.1
TMB	C8	2.7	3.0	2.8	3.3	2.4	5.9	2.3	0.5	0.6	0.8	0.5	0.2	0.2	0.4
	OPH	6.3	6.6	9.8	5.4	7.3	7.3	5.1	0.4	0.6	0.4	0.8	0.8	0.3	0.1
C_{10}	C8	2.3	1.3	1.6	3.7	4.2	4.8	4.4	0.6	0.6	0.7	0.5	0.2	0.2	0.4
	OPH	6.2	2.3	1.7	5.0	2.0	7.5	6.6	0.3	0.7	0.4	0.8	0.7	0.4	0.2
C_{11}	C8	4.5	4.2	5.8	3.6	4.5	5.8	3.8	0.7	0.6	0.6	0.5	0.2	0.1	0.3
	OPH	8.5	9.8	8.5	8.5	5.1	6.2	6.7	0.2	0.7	0.5	0.6	0.6	0.4	0.1
C_{12}	C8	4.6	7.4	8.0	4.2	5.8	7.0	5.4	0.5	0.5	0.4	0.4	0.2	0.5	0.4
	OPH	9.1	7.8	9.9	9.7	6.3	7.6	9.3	0.5	0.7	0.4	0.6	1.0	0.3	0.2

[a] *Analyses entailed collection of a 10-mL sample of static test atmosphere containing all mixture components at a concentration corresponding to ~2× TLV (see Table 1 in the main body of the article). Separation conditions were the same as those given in the caption of Figures A8. Each RSD value is based on 4 separate determinations collected at least one hour apart each day.*

As shown in Table A6, when operated autonomously over 2 days, the PEMM-1 exhibited small but consistent decreases in retention time, peak height, and peak area for the 6 VOCs included in the test. Within either day or between the two days, these changes were all < 10% and typically < 5%, again, illustrating the stability of performance

*Table A2.5. Comparison of inter-day stability of PEMM-1 and a reference GC-FID on the basis of peak area (A), peak width (*fwhm*), and retention time (t_R) for each component of a 9-VOC mixture. For the PEMM-1, the data from the C8 sensor is presented. Entries are averages of daily values collected for 7 consecutive days (see caption of Figures A8 for conditions).*

Cmpd	PEMM-1/C8 sensor[a]			GC-FID[a]		
	A($\times 10^2$) ($(\Delta R/R_b)\cdot s$)	FWHM (s)	t_R (s)	A (pA·s)	FWHM (s)	t_R (s)
C_7	12 (3.9)[b]	1.4 (3.8)	40.1 (2.0)	121 (1.9)	0.44 (0.7)	24.6 (0.1)
BAC	23 (2.9)	1.9 (2.1)	78.8 (1.3)	173 (1.3)	0.92 (2.8)	49.3 (0.1)
XYL	18 (2.7)	1.2 (0.9)	94.3 (0.9)	109 (2.2)	0.82 (2.5)	66.0 (0.1)
EBK	11 (4.9)	1.2 (1.4)	99.3 (0.9)	94.3 (4.6)	0.93 (3.9)	71.5 (0.1)
PPB	11 (5.2)	1.1 (0.9)	117 (0.7)	59.3 (4.3)	0.81 (4.8)	91.4 (0.1)
TMB	2.2 (6.8)	1.1 (1.5)	127 (0.6)	12.0 (5.3)	0.80 (8.1)	102 (0.1)
C_{10}	11 (5.3)	1.0 (0.7)	132 (0.6)	21.1 (4.4)	0.79 (4.5)	109 (0.2)
C_{11}	6.6 (9.0)	1.7 (1.0)	154 (0.5)	21.1 (6.0)	0.83 (2.1)	135 (0.3)
C_{12}	1.0 (9.6)	2.9 (2.3)	175 (0.5)	8.80 (7.5)	0.85 (5.1)	159 (0.4)

[a] *7-day average where each day's value was the avg of 4 replicates (see Table A4) for the PEMM-1 and was a single value for the GC-FID.*

[b] *Values in parentheses are relative standard deviations (RSD, n=7) expressed as percentage (%).*

Table A2.6. Results (C8 sensor) of continuous, autonomous PEMM-1 operation: analyses of a 6-VOC mixture over 8 hr/day for 2 days.[a]

Cmpd	Intra-day																		
	Day 1									Day 2									
	t_R (s)			H ($\Delta R/R_b \times 10^2$)			A ($\Delta R/R_b \cdot s \times 10^2$)			t_R (s)			H ($\Delta R/R_b \times 10^2$)			A ($\Delta R/R_b \cdot s \times 10^2$)		
	am[b]	pm[c]	Δ%[d]	am	pm	Δ%	am	pm	Δ%	am	pm	Δ%	am	pm	Δ%	am	pm	Δ%
BEN	25.1	24.8	-1.20	3.6	3.6	0	4.1	3.9	-4.9	23.8	23.7	-0.420	3.5	3.4	-2.9	3.9	3.8	-2.6
TOL	48.9	48.3	-1.23	4.4	4.3	-2.3	7.7	7.3	-5.2	46.1	45.9	-0.434	4.3	3.9	-9.3	7.1	6.5	-8.5
MBK	56.7	55.8	-1.59	3.4	3.2	-5.9	6.0	5.7	-5.0	53.4	53.2	-0.375	3.1	3	-3.2	5.7	5.5	-3.5
BAC	69.0	68.1	-1.30	4.3	4.2	-2.3	7.3	6.6	-9.6	65.6	65.2	-0.610	4.0	3.9	-2.5	7.1	6.5	-8.5
ETB	83.9	83.2	-0.83	6.5	6.1	-6.2	8.6	8.1	-5.8	81.2	80.8	-0.493	6.1	5.5	-9.8	8.2	7.5	-8.5
XYL	87.1	86.3	-0.92	6.5	5.9	-9.2	9.7	9.0	-7.2	84.4	84.0	-0.474	6.0	5.5	-8.3	9.0	8.5	-5.6

Cmpd	Inter-day[e]								
	t_R (s)			H ($\Delta R/R_b \times 10^2$)			A ($\Delta R/R_b \cdot s \times 10^2$)		
	Day 1	Day 2	Δ%	Day 1	Day 2	Δ%	Day 1	Day 2	Δ%
BEN	25.0	23.8	-4.80	3.6	3.5	-2.8	4.0	3.9	-2.5
TOL	48.6	46.0	-5.35	4.3	4.1	-4.7	7.5	6.8	-9.3
MBK	56.3	53.3	-5.33	3.3	3.0	-9.1	6.0	5.6	-6.7
BAC	68.6	65.4	-4.67	4.2	4.0	-4.8	7.0	6.8	-2.9
ETB	83.6	81.0	-3.11	6.3	5.8	-7.9	8.0	7.9	-1.3
XYL	86.7	84.2	-2.88	6.2	5.7	-8.1	9.3	8.8	-5.4

[a] *PEMM-1 was operated continuously for 8 hr per day on each of two consecutive days; t_R = retention time; H = peak height; A = peak area; values are based on the responses from the C8 sensor;* [b]*average from 3 consecutive analyses collected at the outset in the morning;* [c]*average from 3 consecutive analyses collected at the end of the afternoon;* [d] *difference (%) = [(pm- am)/am] ×100 or [(Day 2- Day1)/Day 1] ×100;* [e] *inter-day comparisons are based on the averages of am and pm values from a given day. Samples (10 mL) were collected from a static test atmosphere of the mixture in N_2 with each compound at ~100 ppm. Separation conditions were the same as those given in the caption of Figure A8 using the on-board He canister as the carrier gas.*

A2.11. Response Patterns and Confusion Matrices

Figure A9 shows the normalized response patterns for all 17 target compounds. Tables A7 and A8 present the confusion matrices obtained from Monte Carlo simulations coupled with extended disjoint principal components regression (EDPCR) classification models on the basis of arrays of all 5 sensors (Table A7) and 4 sensors (Table A8, OPH removed).[A8] Using the experimental sensitivity (slope) values (Table A2), synthetic responses from each μCR sensor to a selected vapor were generated by randomly selecting a vapor concentration within the range of 5-10×LOD, where the LOD for each compound was that corresponding to the least sensitive sensor in the array to ensure that all sensors contributed to the response patterns. A synthetic response was calculated from the calibration-curve regression equation for each sensor. Then, error was introduced by adding to the response a value obtained by multiplying that response value by a factor derived from randomly sampling a Gaussian distribution with a mean of zero and a standard deviation corresponding to the average RSD determined for each sensor on the basis of repeated measurements (like those presented for C8 and OPH sensors in Table A4, above). The "error enhanced" responses from all sensors were then combined (vector sum in "n-space", where n is the number of sensors in the array) and the location of the resulting response vector was projected onto the principal component corresponding to the original calibrations for each vapor via EDPCR. The identity of the vapor assigned to this synthetic response vector was determined by the shortest Euclidean distance. This procedure was performed iteratively (i.e., 500 samples) to yield a statistical estimate of recognition rate (RR, %) for each vapor.

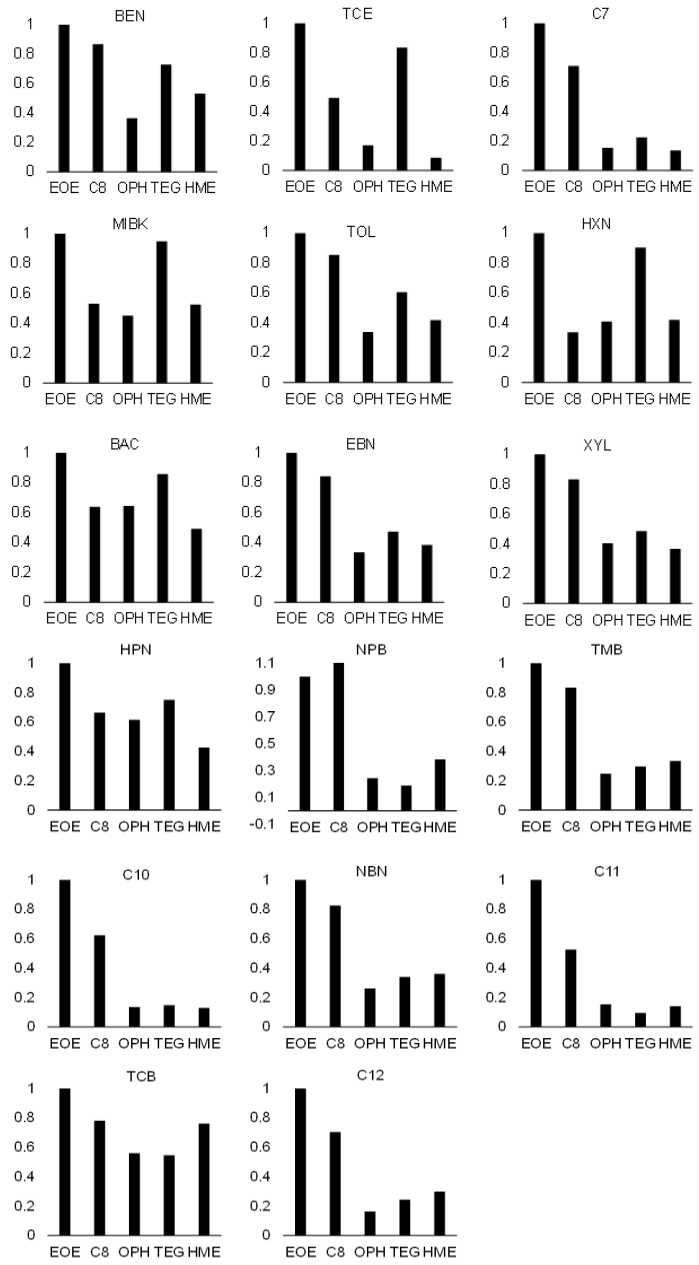

Figure A2.9. Normalized response patterns for 17 targets derived from the slopes of the calibration curves presented in Table S2.

Table A2.7 Confusion matrix showing errors in assigned identities and net recognition rate (RR, %) for the 17 individual target VOCs from MC-EDPCR analyses of response patterns derived from all 5 sensors in the μCR array.[a]

VOCs	BEN	TCE	C_7	MIBK	TOL	MBK	BAC	ETB	XYL	EBK	PPB	TMB	C_{10}	NBZ	C_{11}	TCB	C_{12}
BEN	459	0	0	0	30	0	0	0	2	14	0	0	0	0	0	8	0
TCE	14	481	0	0	0	14	0	0	0	0	0	0	0	0	0	0	0
C_7	0	0	457	0	0	0	0	0	0	0	0	0	35	0	18	0	0
MIBK	0	0	0	479	0	3	4	0	0	0	0	0	0	1	0	0	0
TOL	26	0	0	0	429	0	0	21	22	0	0	0	0	0	0	0	0
MBK	0	4	0	14	0	483	0	0	0	1	0	0	0	0	0	0	0
BAC	0	0	0	4	0	0	413	0	0	70	0	0	0	7	0	0	0
ETB	1	0	0	0	36	0	0	410	47	0	7	18	0	0	0	0	0
XYL	0	0	0	0	5	0	0	52	426	4	0	6	0	0	0	0	0
EBK	0	0	0	0	0	0	77	0	1	411	0	0	0	0	0	0	0
PPB	0	0	0	0	0	0	0	16	2	0	356	105	0	0	0	0	2
TMB	0	0	0	0	0	0	0	1	0	0	107	330	0	0	0	0	38
C_{10}	0	15	36	0	0	0	0	0	0	0	0	0	406	0	49	0	7
NBZ	0	0	0	0	0	0	0	0	0	0	0	0	0	486	0	0	0
C_{11}	0	0	0	0	0	0	0	0	0	0	0	0	51	0	433	0	0
TCB	0	0	0	3	0	0	6	0	0	0	13	0	0	1	0	484	0
C_{12}	0	0	0	0	0	0	0	0	0	0	17	41	8	0	0	0	453
RR[b]	92	96	91	96	86	97	83	82	85	82	71	66	81	97	87	97	91

[a] *Actual identities are listed in the top row and assigned identities are listed in the first column; n = 500 iterations for each VOC; error values assumed in generating synthetic responses are given in the text above;* [b] *recognition rate (%) for correct identity assignments.*
Notes: 5 cases with RR > 95%; 8 cases with RR > 90%; 9 cases with RR from 66-87%.

Table A2.8. Confusion matrix showing errors in assigned identities and net recognition rate (RR, %) for the 17 individual target VOCs from MC-EDPCR analyses of response patterns derived from 4 of the 5 sensors in the μCR array (OPH sensor was omitted).[a]

VOCs	BEN	TCE	C_7	MIBK	TOL	MBK	BAC	ETB	XYL	EBK	PPB	TMB	C_{10}	NBZ	C_{11}	TCB	C_{12}
BEN	470	0	0	0	18	0	13	0	0	11	0	0	0	0	0	5	0
TCE	0	492	0	0	0	0	0	0	0	0	0	0	0	0	0	0	0
C7	2	0	469	0	5	0	0	0	0	0	0	0	41	0	7	0	0
MIBK	0	2	0	490	0	9	9	0	0	4	0	0	0	6	0	0	0
TOL	18	0	0	0	430	0	0	28	34	1	0	0	0	0	0	0	0
MBK	0	0	0	0	0	491	0	0	0	0	0	0	0	0	0	0	0
BAC	0	0	0	0	0	0	389	0	0	2	0	0	0	0	0	0	0
ETB	0	0	0	0	30	0	0	273	153	0	5	2	0	0	0	0	0
XYL	0	0	0	0	11	0	0	181	304	0	0	1	0	0	0	0	0
EBK	10	6	0	10	6	0	89	0	0	482	0	0	0	0	0	0	0
PPB	0	0	0	0	0	0	0	18	9	0	405	76	0	0	0	0	0
TMB	0	0	0	0	0	0	0	0	0	0	74	376	0	0	0	0	59
C10	0	0	26	0	0	0	0	0	0	0	0	0	425	0	28	0	0
NBZ	0	0	0	0	0	0	0	0	0	0	0	0	0	493	0	0	0
C11	0	0	0	0	0	0	0	0	0	0	0	0	34	0	465	0	0
TCB	0	0	0	0	0	0	0	0	0	0	0	0	0	1	0	495	0
C12	0	0	0	0	0	0	0	0	0	0	16	45	0	0	0	0	441
RRb	94	98	94	98	86	98	78	55	61	96	81	75	85	99	93	99	88

[a] *Actual identities are listed in the top row and assigned identities are listed in the first column; n = 500 iterations for each VOC; error values assumed in generating synthetic responses are given in the text above;* [b] *recognition rate (%) for correct identity assignments.*
Notes: 6 cases with RR > 95%; 9 cases with RR > 90%; 8 cases with RR from 55-88%.

A2.12. References

A1. Bryant-Genevier J. Scholten K, Kim SK, *et al.* Multivariate curve resolution of co-eluting vapors from a gas chromatograph with microsensor array detector. *Sens. Actuator B: Chemical* 2014; 202: 167-176.

A2. Wright L, Zellers ET, A nanoparticle-coated chemiresistor array as a microscale gas chromatograph detector for explosive marker compounds: flow rate and temperature effects. *Analyst* 2013; 138: 6860-6868.

A3. Lu CJ, Steinecker WH, Tian WC, *et al.* First-generation hybrid MEMS gas chromatograph. *Lab Chip* 2005; 5:1123-1131.

A4. Kim SK, Burris DR, Chang H, *et al.* Microfabricated gas chromatograph for on-site determinations of trichloroethylene in indoor air arising from vapor intrusion, part 1: field evaluation. *Env. Sci. and Tech*. 2012; 46: 6065-6072.

A5. Bryant-Genevier J, Zellers ET, Toward a microfabricated preconcentrator-focuser for a wearable micro-scale gas chromatograph. *J. Chrom. A.* 2015; 1422: 299-309.

A6. Grob RL, Barry EF, *Modern practice of gas chromatography*. 4th ed. Hoboken: Wiley Interscience, 2004: 114-115.

A7. Lu CJ, Zellers ET. A dual-adsorbent preconcentrator for a portable indoor-VOC microsensor system. *Anal. Chem* 2001; 73: 3449-3457.

A8. Zhong Q, Steinecker W, Zellers ET. Characterization of a high-performance portable GC with a chemiresistor array detector. *Analyst* 2009; 134: 283-293.

Appendix 3: Supplementary Information for Chapter 4

A3.1. Abstract

The following text, figures, tables, and references augment what is presented in the main article on the PEMM-2 prototype, and address the following topics:

- Citations of literature on component devices of potential use in μGC systems
- Determination of μSC separation efficiency
- Components and features related to PEMM-2 prototype control and operating options
- Calibration metrics and response patterns for the nine VOCs
- MC-PCA procedure for assessing VOC recognition/discrimination
- Response stability data
- PC score plot from MC-PCA of the 21-VOC mixture
- Mock field test data
- Power and energy consumption breakout for a typical cycle

A3.2. Literature

Due to constraints on the length of the article imposed by the journal, we have relegated the citations of published work on individual devices of potential use in a μGC system suitable for analyzing mixtures of airborne VOCs to this SI. These comprise microfabricated versions of three critical component devices: a collector/injector for sample capture and introduction;[S1-S5] a chromatographic column for separation;[S6-S11] and a sensor or sensor array for detection and, possibly, identification of eluting VOCs.[S12-S17] Commercial systems employing one or more Si-microfabricated components are also available or becoming available. [S18-S21]

A3.3. µSC Efficiency

The separation efficiency of the µSC was determined by GC-FID at 30 ºC (GC oven) using n-octane as the probe. The headspace of a septum-seal vial containing methane and 2 drops of n-octane was injected by autosampler with a gas-tight syringe (5 µL, 200:1 split). The adjusted retention time (t_R') of n-octane was calculated as the difference of the observed retention time of the n-octane (t_R) and that of methane (t_M). Measured values of t_R' and the full width at half-maxima (*fwhm*) of eluting peaks were collected at different volumetric flow rates of the N_2 carrier by increasing the inlet pressure of the GC. The average N_2 carrier gas velocity, $\bar{u}$, was calculated as $(L+L')/t_M$, where L is the column length and L' is the 30-cm of interconnecting capillary between injector, µSC, and FID. The plate number, N, was calculated as $5.54(t_R'/fwhm)^2$ and then the height equivalent to a theoretical plate, HETP, was calculated as L/N. Values of HETP were plotted against the corresponding values of ū (a Golay plot) to determine the minimum plate height, $HETP_{min}$, and maximum plate count, N_{max}, which occur at the optimal velocity. The range of retention factors for the n-octane was 7.4-9.0.

Based on the data plotted in Figure A-1, $HETP_{min}$ = 0.022 cm at $\bar{u}$ = 11.3 cm/s. For L = 6 m, N_{max} = 27,000 plates (i.e., 4,500 plates/m), which is somewhat greater than that reported in for a previous coated µSC of the same design.[S10]

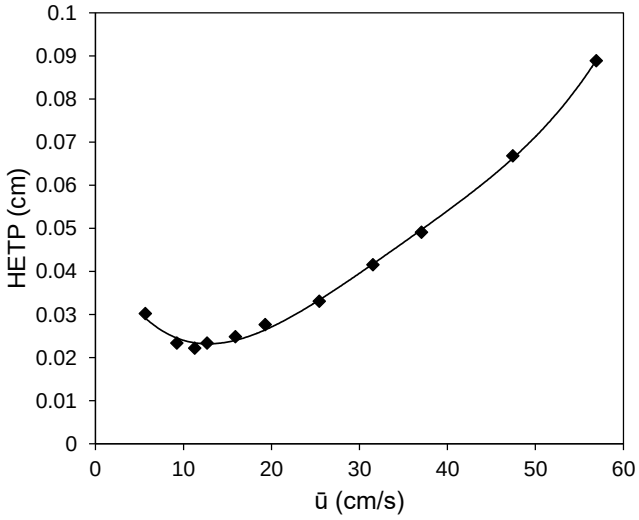

Figure A3.1. Golay plot of the height-equivalent to a theoretical plate, HETP, versus the average linear velocity (ū) for the μSC generated using n-octane as the probe at 30 °C (GC oven) with N2 as carrier gas (GC-FID, 200:1 split injection through heated injection port with glass liner maintained at 250 °C).

A3.4. Prototype Control and Operating Features.

The main hardware components included circuitry for the acquisition and control of the RTDs and heaters, circuitry for acquisition of the μCR array resistance values, and an embedded microcontroller system to provide feedback temperature control, system automation, and configurable operation. A PCB with an STM32F303 microcontroller (ARM) contains an ARM Cortex-M4 CPU and was used for the heating and cooling controls, device digital actuation, event scheduling, and user control execution. A PCB with the PIC32-MX320 micro-controller (PIC32), consisting of an 80 MHz MIPS32 M4K CPU, a 128kB onboard flash memory, and 16kB of RAM was dedicated to data acquisition of the μCR array signals. A μCR amplifier PCB provided amplification, filtering and digitally controlled baseline correction for the μCRs. A relay PCB contained solid state switches for heater, fans, pump and valves control, and provided power supply regulation**.**

For heating the μPCF, independent proportional-integral-derivative (PID) feedback loops were designed to control heating rates and temperatures via solid-state relays. An initial fast ramp of 400 °C s^{-1} was used to heat from 30 to 100 °C, followed by a pulse-width modulated (PWM) ramp of 150 °C s^{-1} to 225 °C, which was maintained for 40 s. For all testing the maximum temperature was 225 °C and it was maintained for 40 s to ensure that even the least volatile VOCs would be completely desorbed.[S2,S22]

To compensate for the large differences in baseline resistances among the μCRs, improve the signal-to-noise ratio (S/N), and maximize the dynamic range of the data acquisition system, a set of socketed 1 MΩ reference resistors was installed that were roughly similar to the resistances of the respective μCRs. Finer tuning and periodic adjustments of eventual drifts were addressed by executing a subroutine residing in the microcontroller to adjust a set of digital to analog converters (DAC), which allowed cancelling of the resulting voltage offsets. Subroutine calls to the micro-controller were performed from the remote computer through a command-line interface, accessed via the RP. This interface also allowed, optionally, manual actuation of component functions during system preparation, instructions on when to start a run and whether a single cycle or a series of multiple cycles were to be executed, and whether or not temperature data were to be stored in the on-board memory.

Measured voltage changes (ΔV) for a given peak on a given sensor was converted to the corresponding resistance change (ΔR) then normalized by the baseline resistance (R_b) via the following equation:

$$\frac{\Delta R}{R_b} = \frac{(1 + \frac{R_b}{R_r})^2 \cdot \Delta V}{\frac{R_b}{R_r} \cdot [G \cdot V - \left(1 + \frac{R_b}{R_r}\right) \cdot \Delta V]}$$

where R_r is the reference resistance (1 MΩ), G is the gain; V is the applied battery voltage (3V).

A3.5. Calibration Metrics and Response Patterns for the Nine VOCs

Table A-1 presents the values of t_R and *fwhm* of each compound and the resolution, R_s, of the peak for that compound from that of the following adjacent compound under the operating conditions established for calibration. Table A-2 provides summary statistics and derived LODs from the calibration curves in Figure A-2, which covered a ~40-fold range of injected mass, corresponding to a concentration range of ~0.1× to 4× TLV-TWA for each compound, assuming a sample volume of 5 mL. Figure A-3 presents the normalized response patterns derived from the forced-zero regression slopes of the peak area vs. injected mass. To normalize the response pattern for a given vapor in its bar chart, the slope for a given sensor was divided by that for the sensor with the highest sensitivity, and the resulting value (ranging from 0-1) was plotted.

*Table A3.1. Retention time (t_R), full width at half maximum (*fwhm*) and resolution (R_s) for the calibration of the PEMM-2 prototype with the initial set of nine VOCs.*

VOC	μCR											
	C8			EOE			HME			TEG		
	t_R (s)	fwhm (s)	R_s	t_R (s)	fwhm (s)	R_s	t_R(s)	fwhm (s)	R_s	t_R (s)	fwhm (s)	R_s
BEN	18.5	1.5	1.9	18.6	1.5	1.8	18.8	1.6	1.8	18.6	1.6	1.8
C_7	23.4	1.6	3.0	23.5	1.7	3.0	23.7	1.6	2.9	23.6	1.6	2.9
TOL	34.6	2.7	2.4	34.8	2.8	2.3	35.2	3.0	2.2	35.0	3.0	2.2
MBK	48.5	4.2	1.7	49.0	4.3	1.6	49.0	4.4	1.6	48.8	4.3	1.6
BAC	58.4	2.7	2.7	58.7	2.9	2.5	59.1	3.0	2.4	58.9	3.0	2.5
XYL	70.5	2.6	3.1	71.1	2.8	2.8	71.5	3.1	2.6	71.3	2.9	2.7
EBK	83.8	2.5	4.0	84.6	2.8	3.4	85.0	3.0	3.1	84.7	3.0	3.2
NPB	99.9	2.3	2.9	101	2.9	2.3	101	3.2	2.1	101	2.9	2.3
TMB	114	3.3	--	115	4.3	--	116	5.1	--	115	4.5	--

Table A3.2. Forced-zero regression slope, R^2 value, and calculated LOD for each of the nine VOCs from the calibration curves of peak height vs. injected mass of each μCR sensor in the PEMM-2 prototype.

VOC	μCR											
	C8			EOE			HME			TEG		
	Slope[a]	R^2	LOD[b]	Slope	R^2	LOD	Slope	R^2	LOD	Slope	R^2	LOD
BEN	53.4	0.996	2.4	87.7	0.996	2.2	39.5	0.996	9.5	24.2	0.993	8.8
C_7	35.5	0.997	3.6	87.0	0.997	2.2	105	0.999	3.6	34.8	0.996	6.1
TOL	60.9	0.993	2.1	98.7	0.999	2.0	43.8	0.997	8.6	26.4	0.997	8.1
MBK	69.6	0.985	1.8	159	0.999	1.2	317	0.998	1.2	61.2	0.997	3.5
BAC	82.2	0.997	1.6	168	0.991	1.2	175	0.993	2.1	39.9	0.997	5.3
XYL	63.3	0.993	2.0	115	0.999	1.7	53.1	0.997	7.1	30.0	0.997	7.1
EBK	52.3	0.995	2.4	165	0.993	1.2	279	0.992	1.4	42.3	0.998	5.0
NPB	102	0.997	1.3	116	0.993	1.7	174	0.997	2.2	87.0	0.999	2.5
TMB	104	0.995	1.2	122	0.995	1.6	162	0.996	2.3	87.0	0.997	2.5

[a] *unit = $1000(\Delta R/R_b)/\mu g$*

[b] *Limit of detection, in ng, calculated as 3σ/sensitivity, where σ is the standard deviation of the baseline noise for each sensor and sensitivity is the forced-zero linear-regression slope. The values of σ, in units of $(\Delta R/R_b) \times 10^6$, were as follows: 42 (C8), 65(EOE), 125 (HME), and 70 (TEG). See main article text for acronym definitions.*

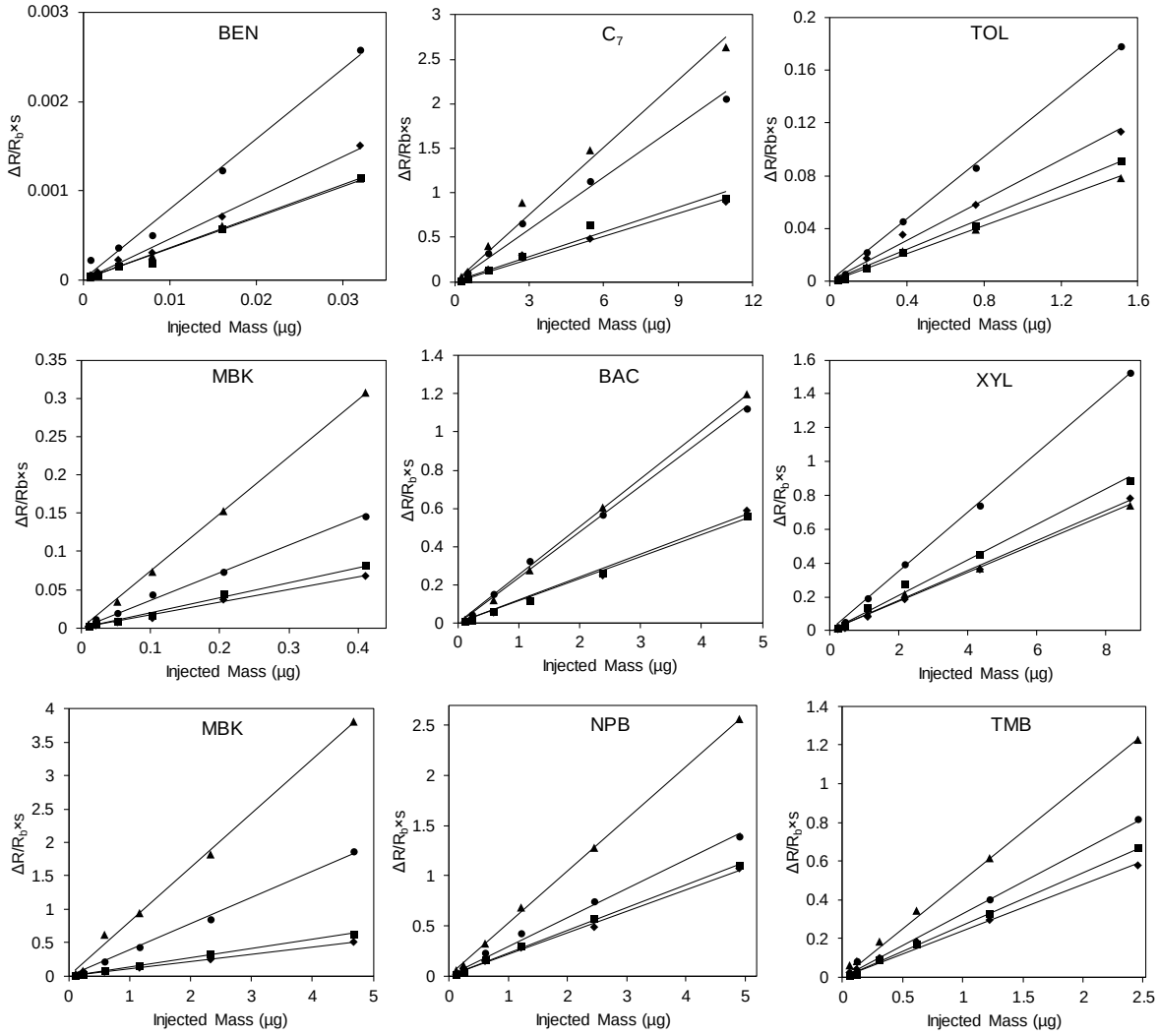

Figure A3.2. Calibration curves for the nine VOCs. Peak area is plotted vs. injected mass for each sensor in the µCR array. Lines are from regression with forced-zero y-intercept. The range of loop-injected masses corresponds to a conc. range of ~0.1 - 4×TLV-TWA, assuming a sample volume of 5 mL. µSC temp. program: 30 °C for 35 s, then 40 °C/min to 105 °C; µCR array was at 30 °C. Legend: C8, squares; EOE, circles; HME, triangles; TEG, diamonds.

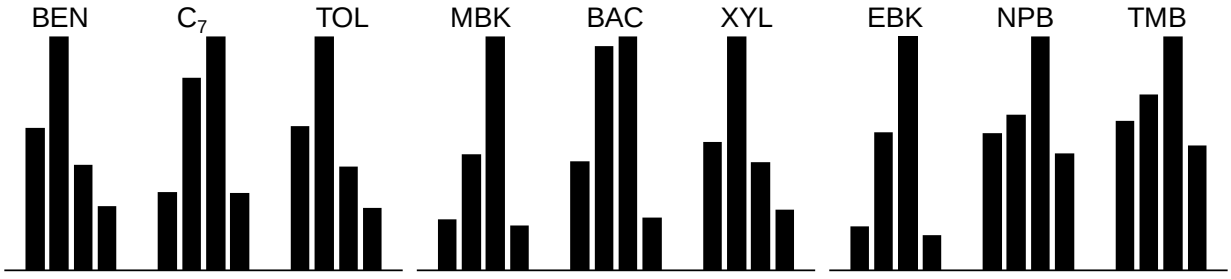

Figure A3.3. Normalized response patterns for nine VOCs derived from the slopes of the calibration curves (Figure A-2). For each bar chart the order (from l to r) is C8, EOE, HME and TEG.

A3.6. Monte Carlo Simulations Coupled with Principal Components Analysis (MC-PCA)

PCA was coupled with and Monte Carlo simulations were used to quantify the pattern-based recognition/discrimination of VOCs and to evaluate the stability of response patterns over time in the data sets generated in this study. In PCA the response vector in 4-space resulting from the sum of the responses of the four μCR sensors for each vapor is calculated. The collection of all such vectors is then analyzed to find the axis in 4-space that maximizes the variance among the vectors. This is the first PC. The second PC is the orthogonal axis that accounts for most of the remaining variance in the vectors. Normally, the first two PCs account for > 95% of the total variance in the data set. Projecting the point corresponding to the vectors onto the plane defined by the two PCs, called a score plot, therefore adequately conveys the degree of separation in 4-space in two dimensions.

To quantify the extent of separation among the vectors, i.e., the uniqueness of the response patterns, we have used Monte Carlo (MC) simulations that entail superimposing error onto the responses of each sensor and then using the error enhanced responses to create an error-enhanced vector for a given VOC. Assuming responses are > 5×LOD, previous work has shown that baseline noise does not contribute significantly to an pattern distortion and can be ignored.[S23] Any "common mode" errors arising from small changes in sample volume, flow rate, or temperature should affect sensor responses equally and therefore would have no effect on the response pattern (note that this may not be strictly true for temperature but it is good enough to a first approximation to assume so for the purposes of simulation). Thus, the only source of response variation we include in the MC simulations is that arising from random error in sensor responses. By convention, and based on previous studies of this factor, an error of 5% is adopted. In fact, as

shown in Table A-3 this is a fairly good, if not conservative, estimate of variation in peak areas for the sensor used in this study.

Thus, a Gaussian distribution having a mean of "1" and a standard deviation of 0.05 is created and then sampled to extract a value from this distribution. This value is then multiplied by the calibration response to create the error enhanced response. This is repeated, separately, for all sensors in the array. The collective error-enhanced responses are summed to create the error-enhanced vector or pattern. By repeating this procedure 500 times we get a probabilistic estimate of the variation in the response pattern for that VOC. From this distribution of response vectors we obtain a distribution of Euclidean distances from which we can calculate a 95% confidence interval (CI_{95}), or boundary, around the initial response vector in "4-space" which can be used to assess the uniqueness of the pattern for one VOC relative to those of all other VOCs. By plotting the CI_{95} in a PC score plot, we can get a visual indication of the separation of the vectors (uniqueness of the patterns) for evaluating vapor recognition and discrimination. In general, if the CI_{95} for one vapor derived from the MC-PCA does not overlap that of another then there is < 5% likelihood of confusing one VOC for another on the basis of the response pattern.

In the case of binary mixtures, we assume that responses are additive,[S24] and can create composite response vectors corresponding to the mixture in any fractional combination of the two components. We can then perform the same type of MC-PCA procedure to estimate the CI_{95} around the mixture vector in order to assess its uniqueness from those of the individual components. This, then, allows an evaluation of whether we can discriminate the mixture from the components based on the patterns.

For evaluating pattern drift over time, a similar procedure is used to create the CI_{95} around the initial response vector. Subsequent samples are then evaluated and plotted with respect to this

initial CI_{95} to determine if the pattern has drifted outside of this boundary. This could be used as a way to set a limit on pattern drift, say, for determining when re-calibration would be needed. However, even if the pattern drifts outside of this boundary, it may still be possible to recognize and discriminate the VOC in question as long as its Euclidean distance between the vector for the sample in question and the "correct" CI_{95} boundary is shorter than that to nearby CI_{95} boundaries for other VOCs.

A3.7. Response Stability

Table A-3 presents the variation in responses, expressed as the relative standard deviation (RSD, %), to a test-atmosphere of the nine VOCs (~100 ppm each) from the (representative) EOE sensor averaged over 0.5 hr (i.e., 6 consecutive 5-min measurements), 8 hr (i.e., 3 measurements at the start of the day and 3 at the end of the day; intraday), and five days (i.e., 5 daily averages, interday). For reference, the averages of measurements collected once per day for five days with a GC-FID (sample loop) are also presented in Table A-3.

Figure A-4a shows daily average peak areas of the 9 VOCs from the representative EOE sensor in PEMM-2 over five consecutive days. Figure A-4b presents PC score plot that includes data for the 3 VOCs whose response patterns (vectors) on day 5 showed a statistically significant deviation from those on day 1. The ellipses in Figure A-4b are the projected CI_{95} boundaries on the response vectors derived from MC-PCA with 5% random error assumed in the sensor responses. The details of MC-PCA procedure are given in the preceding section.

Table A3.3. Stability of peak areas, peak heights, and retention times over different time periods. Data for the EOE sensor are shown.

Relative Standard Deviation (RSD, %)												
VOC	PEMM-2 (EOE sensor)									GC-FID		
	0.5 hr (n=6)			intraday (n=6) [d]			interday (n=5) [e]			interday (n=5) [f]		
	A[a]	H[b]	t_R[c]	A	H	t_R	A	H	t_R	A	H	t_R
BEN	1.6	1.7	1.5	1.1-2.7	2.1-3.8	0.3-2.1	4.7	2.3	3.2	2.6	1.5	0.1
C7	2.1	2.4	0.7	1.8-2.6	2.0-3.2	0.3-1.4	5.4	3.5	1.3	3.2	1.3	0.2
TOL	2.0	1.4	0.6	1.1-1.9	2.5-4.0	0.2-1.5	7.7	2.8	4.9	3.2	0.81	0.2
MBK	1.0	1.2	0.5	0.58-1.9	3.0-5.0	0.2-1.2	4.1	4.5	5.9	6.1	2.4	0.1
BAC	1.2	1.7	0.6	0.71-1.8	2.1-5.0	0.2-0.9	3.1	5.0	5.0	7.6	2.6	0.1
XYL	1.0	1.3	0.7	0.59-1.7	1.4-3.7	0.2-0.5	4.9	4.0	5.1	4.7	2.9	0.2
EBK	1.4	0.68	0.8	0.15-0.88	0.76-3.1	0.0-0.3	3.0	4.5	4.5	4.8	2.3	0.8
PPB	0.80	0.96	0.8	0.44-1.6	0.77-1.8	0.1-0.3	2.7	5.6	4.8	8.3	4.0	0.2
TMB	1.2	2.4	1.0	0.33-1.8	0.97-1.4	0.1-0.3	2.8	5.3	5.8	6.3	2.8	0.2

[a] A = peak area; [b] H = peak height, [c] t_R = retention time; [d] ranges of RSD values express the variation on each day (n=6) for the 5 consecutive days for which measurements were collected; [e] based on 5 daily average values (n = 6 per day) collected over 5 consecutive days; [f] based on a single daily analysis on each of 5 consecutive days (250 µL loop injection). All samples were collected from the same (bag) test atmosphere.

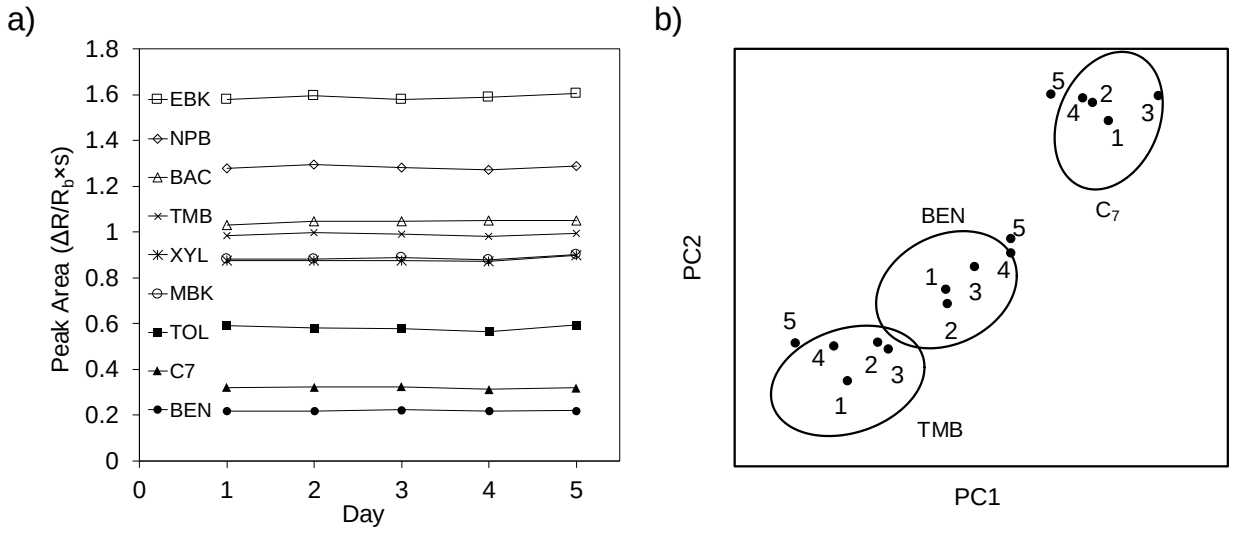

Figure A3.4. Stability of PEMM-2 responses (EOE sensor data shown) to the components of a 9-VOC mixture as reflected by the daily average peak area (6 replicates/day) over 5 consecutive days; (b) PC score plot of the daily pattern vectors for the three VOCs showing some pattern drift on day 5. Ellipses represent the projected CI_{95} established on the basis of day 1 vectors and MC simulations assuming a 5% random error in responses. VOC acronyms are defined in the main article.

A3.8. 21-VOC MC-PCA

Figure A-5 presents the PC score plot for the 21 VOCs with the CI_{95} boundaries from MC-PCA (5% superimposed error, see preceding section) included. Without regard for separation, it can be seen that, while numerous individual VOCs could be recognized and discriminated from one another based on their array response patterns alone, a large fraction of them could not.

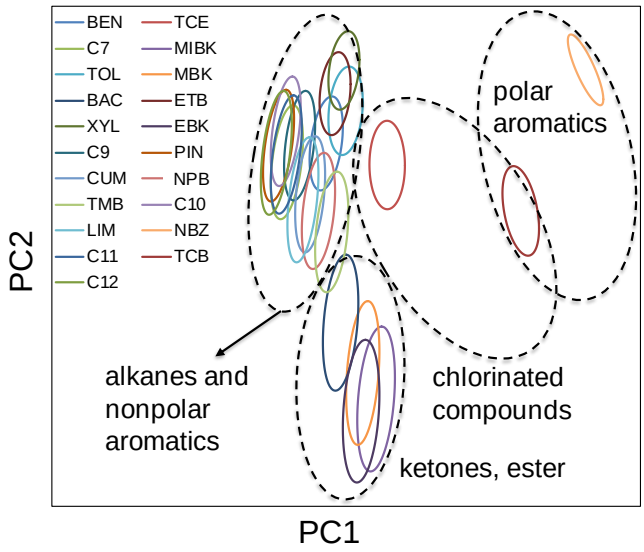

Figure A3.5. PC score plot of 21 VOCs with respective CI95 ellipses (from MC-PCA with 5% superimposed error on responses). Black dashed lines are included as a visual aid only to designate different functional group classes. VOC acronyms are defined in the main article.

A3.9. Mock Field Test Results

Figures S-6a-e show the time-exposure profiles for the five VOCs measured with the PEMM-2 and the reference GC-FID over the 60-min test period while the PEMM-2 was being worn by one of the research team members (note: the TCE profiles are also presented in Figure 6 of the main article and are included here for completeness). Agreement between the two sources of concentration measurements is excellent with the exception of MIBK (Figure A-6d) which

shows a consistent positive bias in the PEMM-2 data, suggesting a possible calibration error. Various solvent transfer activities were performed to vary the concentrations (see caption).

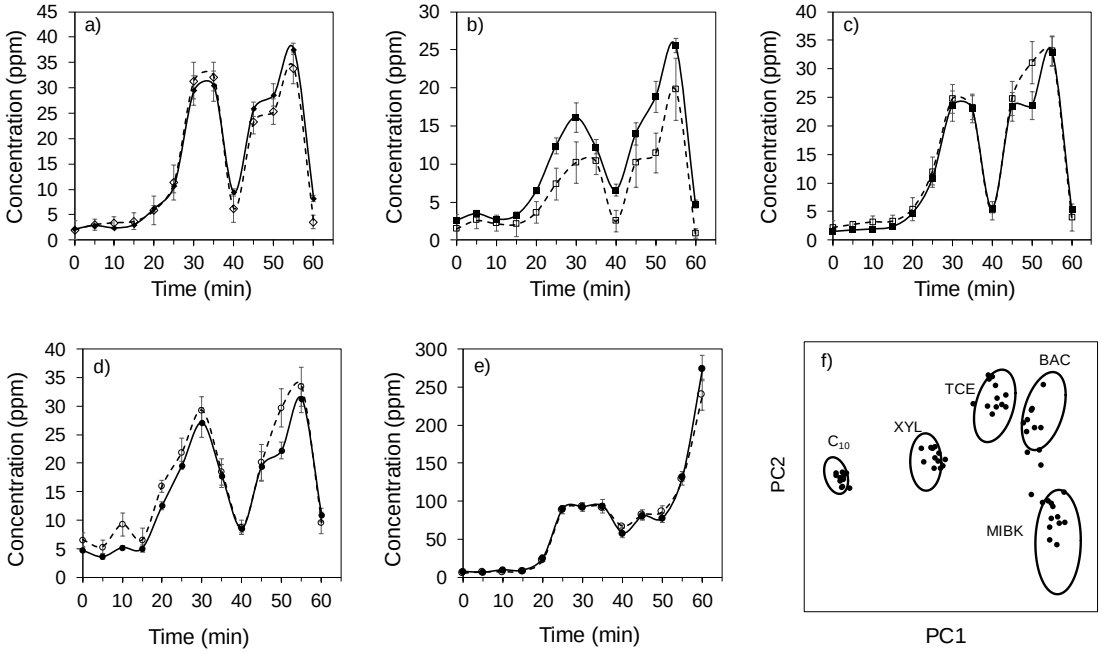

Figure A3.6. Mock field test results. Representative time-exposure profiles for the 5-VOC mixture of a) TCE; b) MIBK; c) BAC; d) XYL; e) C10 over 60 min of continuous, unattended operation of PEMM-2 (solid lines) while worn on the belt of one of the research team members, along with the reference measurements by GC-FID (dashed lines). Two GC-FID samples were collected (250 µL loop) and analyzed during each of the 1-min sampling periods of the PEMM-2. Activities: 0-10 min, no activities; 10-20 min, solvent transfer (room temp.); 20-30 min, solvent transfer to a 2nd beaker held at 80°C; 30-40 min, solvent transfer (room temp.); 40-55 min, solvent transfer (100°C); 55-60 min: no activities. Each data point from the PEMM-2 is the average from the four sensors. Each data point from the GC-FID is the average from the two samples. Error bars are the standard deviations around each average. Panel f) reflects the stability of response patterns of the 5 VOCs during the mock field tests. Individual CI95 ellipses were created from the data at t = 0 min (MC-PCA with 5% random error on sensor responses) and the data points (vectors) for subsequent measurements were plotted. As shown, although some pattern drift is apparent the vast majority of vectors fall within the CI95 boundaries and none of the patterns would result in an error in the assignment of identities of the vapors.

Figure A-3.6f shows the PC score plot of the 12 response vectors generated for each VOC over the test period. Using the initial vector at t = 0 min as the basis for the CI_{95} regions represented as ellipses in Figures A-3.6f (from MC-PCA with 5% average random error assumed), the stability

of responses can be assessed. As shown, the stability of the response patterns is excellent and there would be no errors in assigning identities to the VOCs based on their Euclidean distances from the CI_{95} boundary surfaces (or centroids of the elliptical regions).

A3.10. Power/Energy Consumption.

Table A-4 provides the breakout of power and energy consumption for a typical 6-min cycle along with the average power and total energy.

Table A3.4. Power/Energy budget for PEMM-2 for a typical operating cycle.[a]

Source	Voltage (V)	Current (A)	Power (W)	Quantity	Time (s)	Energy (J)	Avg. Power (W)
µPCF	16	0.126	2.01	1	40	80.4	0.22
µSC	24	0.124	2.97	1	150	446	1.24
µCR array	3	0.03	0.09	1	300	27	0.08
Pump	6	0.05	0.3	1	60	18	0.05
Latching valves	5	0.65	3.25	3	0.04	0.39	0
Cooling fans	12	0.05	0.6	3	150	270	0.75
Electronics[b]	12	0.29	3.5	1	360	1260	3.50
					Total	**2,101**	**5.84**

[a] *Based on a 6-min operating cycle consisting of a 60-s sample, 40-s desorption/injection; 150 s separation (overlaps the desorption/injection period); 150-s cooling and reset period;* [b] *includes microcontrollers, µCR circuits, temperature sensing circuits, relay drivers, voltage regulators, etc.*

A3.11. References

A1. Nachef, K.; Marty, F.; Donzier, E.; Bourlon, B.; Danaie, K.; Bourouina, T. Micro Gas Chromatography Sample Injector for the Analysis of Natural Gas. *J. Microelectromech. Sys.* **2012**, *21*, 730–738.

A2. Bryant-Genevier, J.; Zellers, E. T. Toward a Microfabricated Preconcentrator-Focuser for a Wearable Micro-Scale Gas Chromatograph. *J. Chrom. A.* **2015**, *1422*, 299-309.

A3. Voiculescu, I.; McGill, R.; Zaghloul, M.; Mott. D.; Stepnowski, J.; Stepnowski, S.; Summers, H.; Nguyen, V.; Ross, S.; Walsh, K.; Martin, M. Micropreconcentrator for Enhanced Trace Detection of Explosives and Chemical Agents. *IEEE Sens. J.* **2006**, *6*, 1094–1104.

A4. Manginell, R.P.; Adkins, D.R.; Moorman, M.W.; Hadizadeh, R.; Copic. D.; Porter, D.A.; Anderson, J.M.; Hietala, V.M.; Bryan. J.R.; Wheeler, D.R.; Pfeifer, K.B.; Rumpf, A. Mass-Sensitive Microfabricated Chemical Preconcentrator. *J. Microelectromech. Syst.* **2008**, *17*, 1396–1407.

A5. Camara, E.H.; Breuil. P.; Briand, D.; Rooij. N.F.; Pijolat. C. A Micro Gas Preconcentrator with Improved Performance for Pollution Monitoring and Explosives detection. *Anal. Chim. Acta* **2011**, *688*, 175–182.

A6. Frye-Mason, G. C.; Kottenstette, R.J.; Heller, E.J.; Matzke, C. M.; Casalnuovo, S. A.; Lewis, P. R.; Manginell, R. P.; Schuber, W. K.; Hietala, V. M.; Shul, R.J. *Micro Total Anal. Syst.'98, Proc. μTAS '98 Workshop,* **1998**, 477–481.

A7. Lambertus, G.; Elstro A, Sensenig K, Potkay J, Agah M, Scheuering S, Wise K, Dorman F, Sacks, R. Design, Fabrication, and Evaluation of Microfabricated Columns for Gas Chromatography. *Anal. Chem.* **2004**, 76: 2629–2637.

A8. Shakeel, H.; Agah, M. High Density Semipacked Separation Columns with Optimized Atomic Layer Deposited Phases.*Sens. Actuators, B* **2017**, 242, 215–223.

A9. Chen, B.X.; Huang, T.Y.; Jian, R.S.; Lu, C.J. A Multidimensional Micro Gas Chromatograph Employing a Parallel Separation Multi-Column Chip and Stop-Flow μGC×μGC Configuration. *Lab Chip* **2013**, *13*, 1333–1341.

A10. Lin, Z.; Nuñovero, N.; Wang.J.; Nidetz R.; Buggaveeti, S.; Kurabayashi, K.; Zellers, E.T. A Zone-Heated Gas Chromatographic Microcolumn: Energy Efficiency. *Sens. Actuators, B* **2018**, *254*, 561-572.

A11. Akbar, M.; Restaino, M.; Agah, M. Chip-Scale Gas Chromatography: From Injection Through Detection. *Microsyst. Nanoeng.* **2015**, *1*, 15039.

A12. Scholten, K.; Collin, W. R.; Fan, X.; Zellers, E. T. Nanoparticle-Coated Micro-Optofluidic Ring Resonator as a Detector for Microscale Gas Chromatographic Vapor Analysis. *Nanoscale*, **2015**, *7*, 9282-9289.

A13. Collin, W. R.; Scholten, K. W.; Fan X.; Paul, D.; Kurabayashi K.; Zellers, E. T. Polymer-Coated Micro-Optofluidic Ring Resonator Detector for a Comprehensive Two-Dimensional Gas Chromatographic Microsystem: μGC × μGC-μOFRR. *Analyst*, **2016**, *141*, 261-269.

A14. Narayanan, S.; Rice G.; Agah M. Characterization of a Micro-Helium Discharge Detector for Gas Chromatography. *Sens. Actuators, B* **2015**, *206*, 190-197.

A15. Zhu H.; Nidetz, R.; Zhou M.; Lee, J.; Buggaveeti, S.; Kurabayashi, K.; Fan, X. Flow-Through Microfluidic Photoionization Detectors for Rapid and Highly Sensitive Vapor Detection. *Lab Chip* **2015**, *15*, 3021–3029.

A16. Archibald, R.; Datskos, P.; Devault, G.; Lamberti, V.; Lavrik, N.; Noid, D.; Sepaniak, M.; Dutta, P. Independent Component Analysis of Nanomechanical Responses of Cantilever Arrays. *Anal. Chim. Acta* **2007**; *584*, 101–105.

A17. Chen, F.Y.; Chang, W.C.; Jian, R.S.; Lu, C.J. Novel Gas Chromatographic Detector Utilizing the Localized Surface Plasmon Resonance of a Gold Nanoparticle Monolayer inside a Glass Capillary. *Anal. Chem.* **2014**, *28*, 5257–2564.

A18. APIX Analytics. Miniaturized and Modular Gas Analyzers for Industrial Analysis and OEM Use. https://www.apixanalytics.com/ (accessed February 2019).

A19. Zebra Analyticx. Zebra-GC™ Model L-- Low-Cost, Complete, Zebra MicroGC system with PC. https://zebraanalytix.com/technology/ (accessed February 2019).

A20. TCM Global Targeted Compound Monitoring. www.tcmglobalinc.com (accessed February, 2019)

A21. Omniscent. https://omniscent.com/ (accessed February 2019).

A22. Wang J.; Bryant-Genevier, J.; Nunovero, N.; Zhang, C.; Kraay, B.; Zhan, C.; Scholten, K.; Nidetz, R.; Buggaveeti, S.; Zellers, E.T. Compact Prototype Microfabricated Gas Chromatographic Analyzer for Autonomous Determinations of VOC Mixtures at Typical Workplace Concentrations. *Microsyst. Nanoeng.* **2018**, *4*, 17101

A23. Hsieh, M. D.; Zellers, E. T. Limits of Recognition for Simple Vapor Mixtures Determined with a Microsensor Array. *Anal. Chem.* **2004**, *76*, 1885-1895.

A24. Bryant-Genevier, J.; Scholten, K.; Kim, S. K.; Zellers, E. T. Multivariate Curve Resolution of Co-Eluting Vapors from a Gas Chromatograph with Microsensor Array Detector. *Sens. Actuators, B* **2014**, *202*, 167-176.

Appendix 4: Supplementary Information for Chapter 5

A4.1. RTIL Synthesis

The core of tri(2-hexanamido) ethylamine was synthesized by mixing 1 mol of tris(2-aminoethyl)amine and 5 mol of triethylamine in CH_2Cl_2 at -78 ℃ and 3.5 mol of 6 bromohexanoylchloride injected through a syringe under a vigorous stream of N_2. The reaction mixture was stirred for 3h at -78 ℃ and then continued be stirring additional 12 hrs at 80°C. Then the solution was transferred to 100 ml of cold water. The aqueous layer was extracted 3 times with 50 ml of CH_2Cl_2 and the combined organic layer was concentrated by the rotavap. The pale-yellow liquid was then placed into a vacuum oven to dry for overnight at 100 ºC. The core was orange color solid and its structure was confirmed by H^1NMR. The core was then dissolved in THF and tripropylphosphine was added into THF solution. The mixture was refluxed for 2 days under N_2 atmosphere. The solvent was removed by rotavap and the thick liquid was dissolved in 100 ml of water and the aqueous layer was washed with 100 mL of ethyl acetate 6 times. The aqueous layer was evaporated to dry and resulted ionic liquid was dried under vacuum for 24 hr to get bromide form of tricationic salt. The final RTIL product were obtained through a metathesis reaction of the bromide salts with lithium trifluorlmethanesulfonimide (NTf_2^-). The details of the metathesis were reported in the reference A1.

A4.2. Characterization of RTIL

All results agreed with those reported in reference A2 and A3. And details of each characterization results were summarized in the following:

4.2.1. Elemental analysis

Analyses for C, H, N, and F were performed by Atlantic Microlab Inc. (Norcross, GA). Duplicate measurements of C, H, and N were performed. Table A1 shows the results. Experimental values agree closely with theoretical values.

Table A4.1. Elemental analysis of the RTIL (values are % mass).

Element	Theory	Found		Error[a]
C	38.93	39.07	38.96	0.08
H	6.19	6.09	5.99	-0.15
N	5.57	5.20	5.23	-0.36
F	19.44	17.87	--[b]	-1.6

[a] difference of average measurement from theoretical; [b] duplicate was not collected.

A4.2.2. ^{1}H NMR analysis

The ^{1}H NMR spectrum of the RTIL in DMSO-d6 was collected on a Varian MR400 spectrometer (400 MHz). Chemical shifts (δ, ppm) are relative to tetramethylsilane (TMS). Chemical shifts and integrated intensities are consistent with those reported in the literature[A1-2]:

^{1}H NMR (400 MHz, DMSO): δ(ppm) = 3.06 (br s, 4H), 2.11 (m, 28H), 1.47 (m, 40H), 0.98 (t, 27H). Multiplicities are reported as follows: singlet (s), triplet (t), multiplet (m), broad (b). All NMR spectra were recorded at room temperature.

A4.3. Thermal stability

Thermogravimetric analysis (TGA) was used to determine the thermal stability of the RTIL using a Perkin Elmer Pyris 1 instrument. The sample (~ 2.91 mg) was loaded into the Pt sample pan of the TGA instrument and heated from 30 to 600°C at 10°C/min in N_2 sheath gas. Results are presented in Figure A4.1 as mass loss vs. temperature. As shown there was 1% mass loss at 283

ºC and 5% mass loss at 351 ºC. The latter temperature is 10% lower than that reported by Payagala et al. [A2] and 5% lower than that reported by Collin et al.[A3] The latter study also tested with an air sheath gas and found similar results. These results confirm that the RTIL is thermally stable well above our target desorption temperature of 250 ºC.

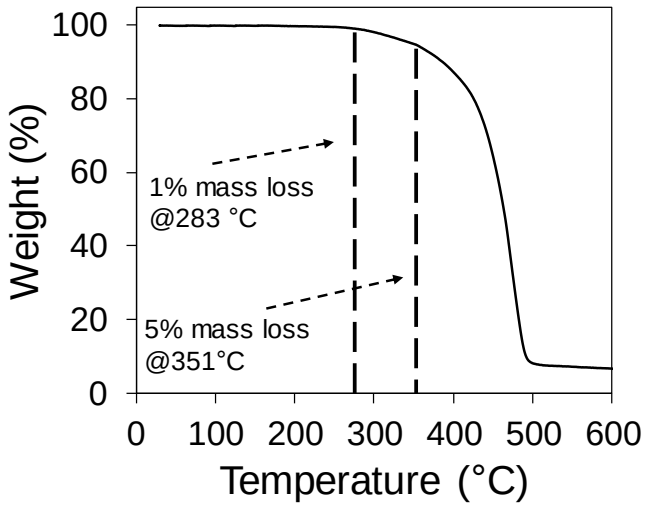

Figure A4.1. TGA curves for the RTIL sample (2.91 mg) heated from 30 °C to 600 °C at 10 °C /min with a sheath gas of N2 (20 mL/min).

A4.4. The mass ratio of RTIL over C-B/-X calculation for monolayer surface coverage

For monolayer coverage, the RTIL molecule was assumed an ideal spherical ball. The monolayer of RTIL molecules spread out over the C-B or C-X surface with each molecule tightly close to adjacent molecules and the center of four closest molecules in two adjacent rows form a unit rhombus. Forming each of the unit rhombus unit, 4 RTIL molecules were needed and each of the molecule of RTIL was shared by 4 unit rhombus. The diagram in Figure A4.2 demonstrated the unit rhombus of RTIL over the C-B/-X surface. Thus, the number of unit rhombuses and the number of RTIL molecules was equal to each other. Thus the total number of RTIL molecules for the monolayer surface coverage of C-B and C-X can be obtained by calculating the total number of unit rhombus was needed to cover the surface of C-B and C-X. This total number of unit

rhombus can be calculated by dividing the surface are of C-B (100 m^2/g) and C-X (240 m^2/g) by the unit rhombus area. The unit rhombus can be calculated if the side length was known. The side length of the unit rhombus equals to the diameter of the RTIL molecule. The diameter (D) of the RTIL was 2 times of the radius (R) of the RTIL molecule. The molecular weight (MW) of RTIL was 1758.8 g/mol, and the density (ρ) of RTIL was 1.48 g/mol.[A2] Thus, the molar volume (V_m)of the RTIL could be calculated using $V_m=MW/\rho$. Thus the single RTIL volume can be calculated by $V_{RTIL}=V_m/N_A$. Once the VRTIL was calculated, R of RTIL molecule could be calculated by the relationship of $V_{RTIL}=4/3\pi R^3$. Thus, D could be obtained. Once D was calculated, the number of unit rhombus or the number of RTIL molecules could be calculated by the above description for the monolayer surface coverage of 1 g of C-B/-X. Thus, then the mass of RTIL can be calculated corresponding to the monolayer of surface coverage of 1g of C-B or C-X. The Table A4.2 showed the example of calculation for RTIL monolayer coverage mass ratio between RTIL and C-B. The surface area of 1g of C-X was 2.4 times larger than 1 g of C-B. Thus the mass ratio of between RTIL and C-X was 2.4 times of the mass ratio between RTIL and C-B for monolayer surface coverage.

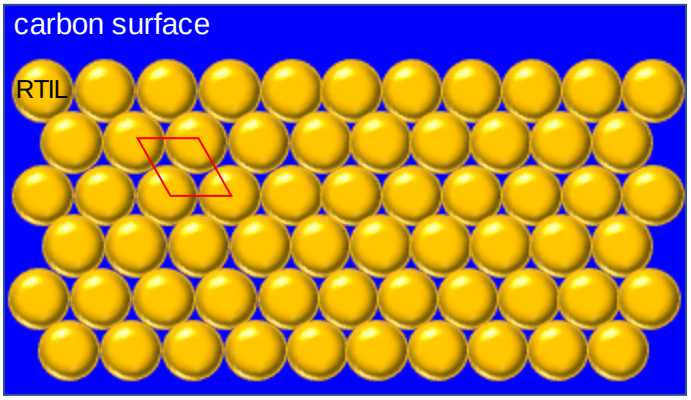

Figure A4.2. The diagram of RTIL molecules over the surface of C-B/-X. The unit rhombus was the smallest rhombus in the figure formed by the closest four RTIL molecules in the adjacent rows.

Table A4.2. The mass ratio between RTIL and C-B calculation details for the monolayer surface area coverage.

molecular weight (MW) of RTIL	1758.8 g/mol
the density of RTIL. ρ	1.48 g/mL
molar volume of RTIL, V_m	1188.38 mL/mol
Avogadro number, N_A	6.02×10^{23}
volume of single RTIL molecule ,V_{RTIL}	1.97×10^{-21} mL
R^3 (R=radius of RTIL molecule)	4.71×10^{-22} cm
or R	7.78×10^{-8} cm
diameter of single RTIL molecule, D	1.6×10^{-7} cm
or D	1.56 nm
Area of each smallest rhombus	1.82 nm^2
surface area of C-B	1.0×10^{20} nm^2/g
number of rhombus need	5.5×10^{19}/g
number of RTIL-A molecule	5.50×10^{19}/g
moles of RTIL	9.14×10^{-5} mole
RTILA/C-B	0.16 g/g

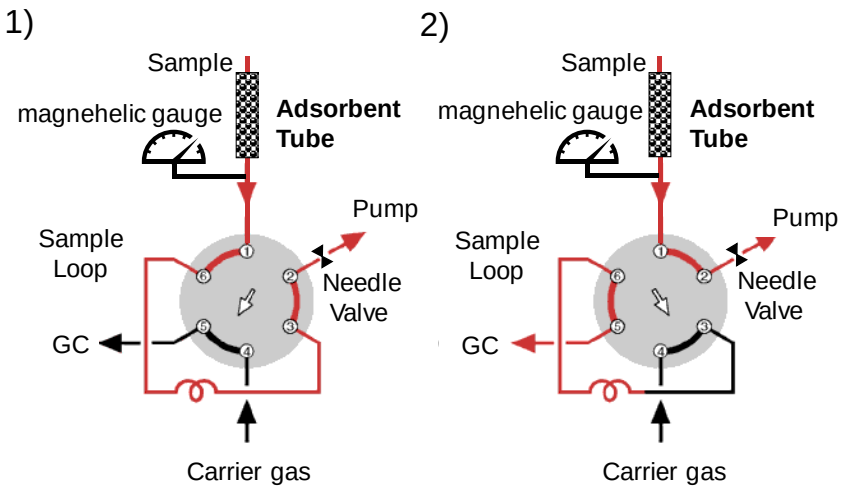

Figure A4.3. Diagram of the breakthrough test system. 1) any vapor that breakthrough tube will be passed through the sample loop; 2) the vapors in the fix volume loop are passed to GC system for quantification. The temperature of 6-port valve was controlled by an external heating box.

Table A4.3. Solute descriptor values for tested compounds and interaction parameters of RTIL and carbotrap used for LSER modeling in this study

	e	*s*	*a*	*b*	*l*
RTIL	0.048	2.0	2.1	0.80	0.66
carbotrap	0	0	0	0	2.4
	E	*S*	*A*	*B*	*L*
DMMP	0.21	1.6	0	1.0	3.9
DEMP	0.15	1.5	0	1.0	4.8
DIMP	0.11	1.4	0	1.0	5.7
TETP	0	1.1	0	1.1	5.0
DMPI	0.22	0.89	0.10	0.87	2.9
NBZ	0.87	1.1	0	0.28	4.5
XYL	0.62	0.52	0	0.16	3.8
C9	0	0	0	0	3.7
C10	0	0	0	0	4.7
C11	0	0	0	0	5.2
CEOH	0.42	0.59	0.47	0.57	2.6
CHNO	0.40	0.86	0	0.56	3.8
BTOH	0.22	0.42	0.37	0.48	2.6

Table A4.4. Intermolecular interactions quantified by LSER model; dipole and dispersion interactions are major forces between vapors and adsorbents.

Compounds	RTIL					carbotrap
	eE	*sS*	*aA*	*bB*	*lL*	*lL*
DMMP	0.0099	3.2	0	0.81	2.6	9.4
DEMP	0.073	2.9	0	0.81	3.2	12
DIMP	0.052	2.7	0	0.81	3.8	14
TETP	0	2.2	0	0.84	3.3	12
DMPI	0.011	1.7	0.21	0.69	1.9	6.9
NBZ	0.042	2.2	0	0.22	3.0	11
XYL	0.030	1.0	0	0.13	2.6	9.3
C9	0	0	0	0	2.4	8.9
C10	0	0	0	0	3.1	11
C11	0	0	0	0	3.4	13
CEOH	0.020	1.2	0.97	0.45	1.8	6.3
CHNO	0.019	1.7	0	0.45	2.5	9.1
BTOH	0.011	0.82	0.76	0.38	1.7	6.3

A4.5. LSER Parameter Modeling

A4.5.1. RTIL Solvation Coefficients at 26 °C

The solvation coefficients of RTIL reported by Payagala in ref. A2 were generated based on the testing at 70 °C and 100 °C, which are higher than that we used for out testing. Since the five types of the interactions described by the LSER greatly depend on the temperature, the solvation coefficients of RTIL were modeled based on the Pool's solvation coefficients from 80 ℃ to 240 ℃. [A4] The best fit trendlines and the equations were generated to predict the respective values at 26 ℃ where our testing was conducted. The equations and R^2 with predict values at 26 ℃. were summarized in Table SA4.5.

Table A4.5. RTIL solvation coefficients.

Solvation coefficients	Equation	R^2	@26 °C
e	y = 0.0008x+0.0275	0.88	0.048
s	y = -0.0041x+2.058	0.98	1.95
a	y = -0.0056x+2.21	0.98	2.06
b	y = -0.36ln(x)+1.98	0.96	0.80
l	$y = 0.80\ e^{-0.007x}$	1	0.66

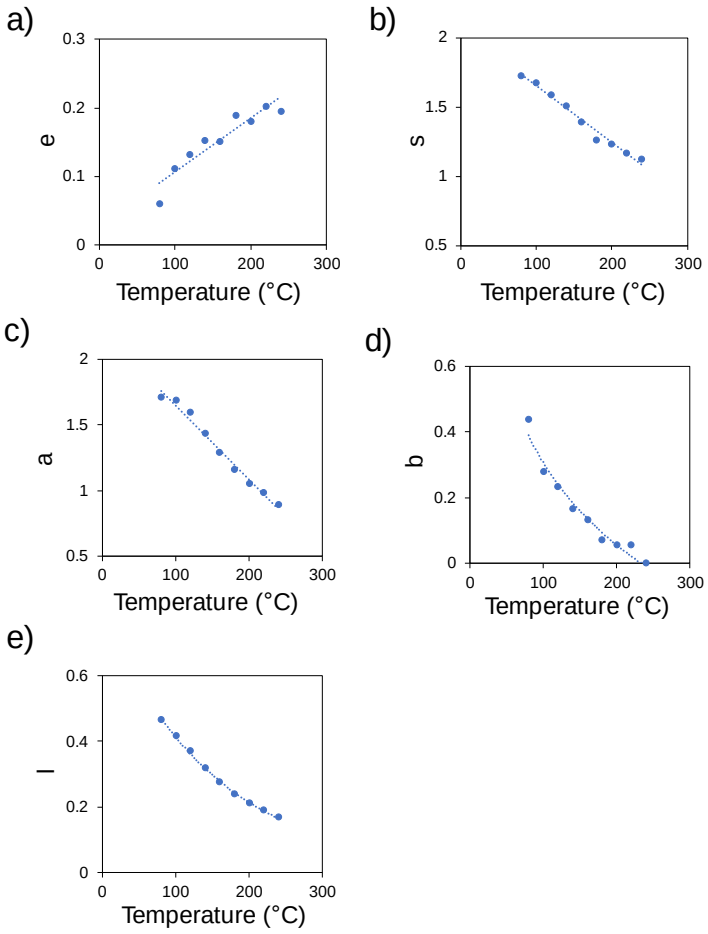

Figure A4.4. RTIL solvation coefficients under different temperatures from 80 °C to 240 °C. The best fit line trendline and equation was generated to predict the value of each parameter at 26°C.

A4.5.2. DEMP and DIMP Solute Descriptors Modeling

Abraham and his co-worker found the solute descriptors altered regularly among the organophosphate compounds.[A5] Thus, we explored the relationship of the solute descriptors relationships with the alkyl carbon numbers for the reported in ref. A5. Ref A5 also reported dimethyl methylphosphate (DMMP) solute descriptors. Thus, with the trend found in Figure SY, and DMMP descriptors, the descriptor values of diethyl methylphosphonate (DEMP) and diisopropyl methylphosphonate (DIMP) can be predicted. In the Figure A4.5, *S* was linearly decreased with the increase of the alkyl carbon number, while *L* was linearly increase with the increase of the alkyl carbon number. *A*and *B* were not affected by the carbon number of alkyl group. Although *E* was exponentially decreased with the alkyl carbon number from 4-18, it is more likely decrease linearly from alkyl carbon number of 4-12. For a better estimation of DEMP and DIMP, a linear relationship between E and alkyl carbon number was used. Table A4.6.

Table A4.6, estimated DEMP and DIMP descriptors based on DMMP descriptors from ref. A5.

	E	S	A	B	L
DMMP	0.21	1.6	0	1.0	3.9
Δ(C4-C2) [a]	-0.044	-0.11	0	0	0.86
DEMP	0.15	1.5	0	1.0	4.8
Δ(C6-C2) [b]	-0.098	-0.24	0	0	1.8
DIMP	0.11	1.38	0	1.0	5.7

[a.] solute descriptor changes from DEMP to DMMP ; [b.] solute descriptor changes from DIMP to DMMP

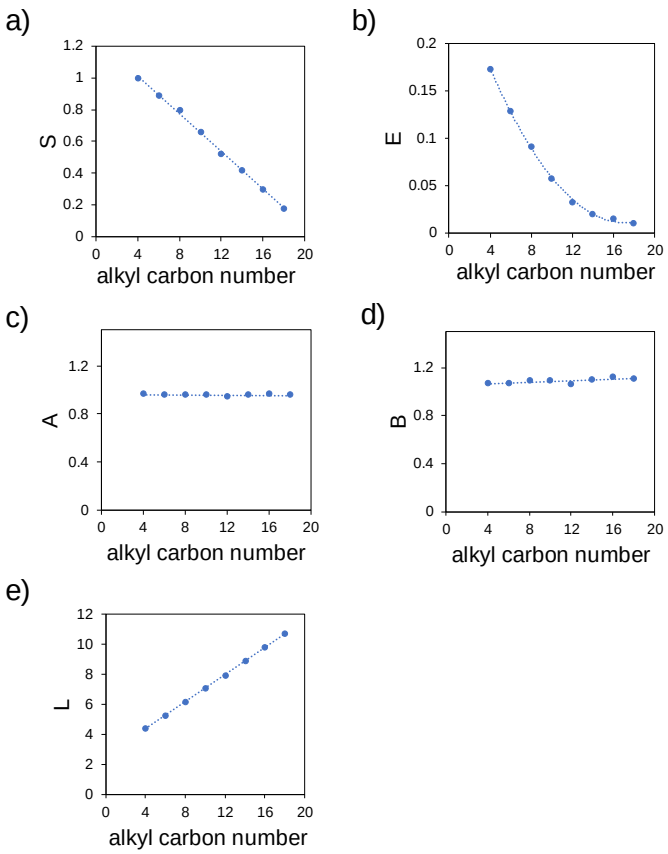

Figure A4.5. solute descriptors of dialkylphosphates change regularly with the carbon numbers in the alkyl group.

A4.6 References

A1. P. S.Sharma, T. Payagala, E. P. Wanigasekara, A. B. Wijeratne, J. Huang, D. W. Armstrong, *Chem. Mater.* **2008**, *20*, 4182–4184.

A2. T. Payagala, Y. Zhang, E. Wanigasekara, K. Huang, Z. Breitbachm, P. Sharma, L. Sidisky, D. W. Armstrong, *Anal. Chem.*, **2009**, *81*, 160-173.

A3. W. Collin, A. Bondy, D. Paul, K. Kurabayashi, E.T Zellers, *Anal. Chem.*, **2015**,*87*, 1630–1637.

A4. N. Lenca,, C. F. Poole, *J. Chromatogr. A.* **2017**, *1524*, 210–214.

A5. M.H. Abraham, W.E. Acree, *Sep. Sci. Technol.* **2013**, *48*, 884–897.